AED R-3553F
April 30, 1970

ITOS D and E
System Design Report

Prepared for
Goddard Space Flight Center
National Aeronautics and Space Administration
Washington, D.C.
Contract No. NAS5-10306

Volume I

RCA | Defense Electronic Products
Astro Electronics Division | Princeton, New Jersey

345

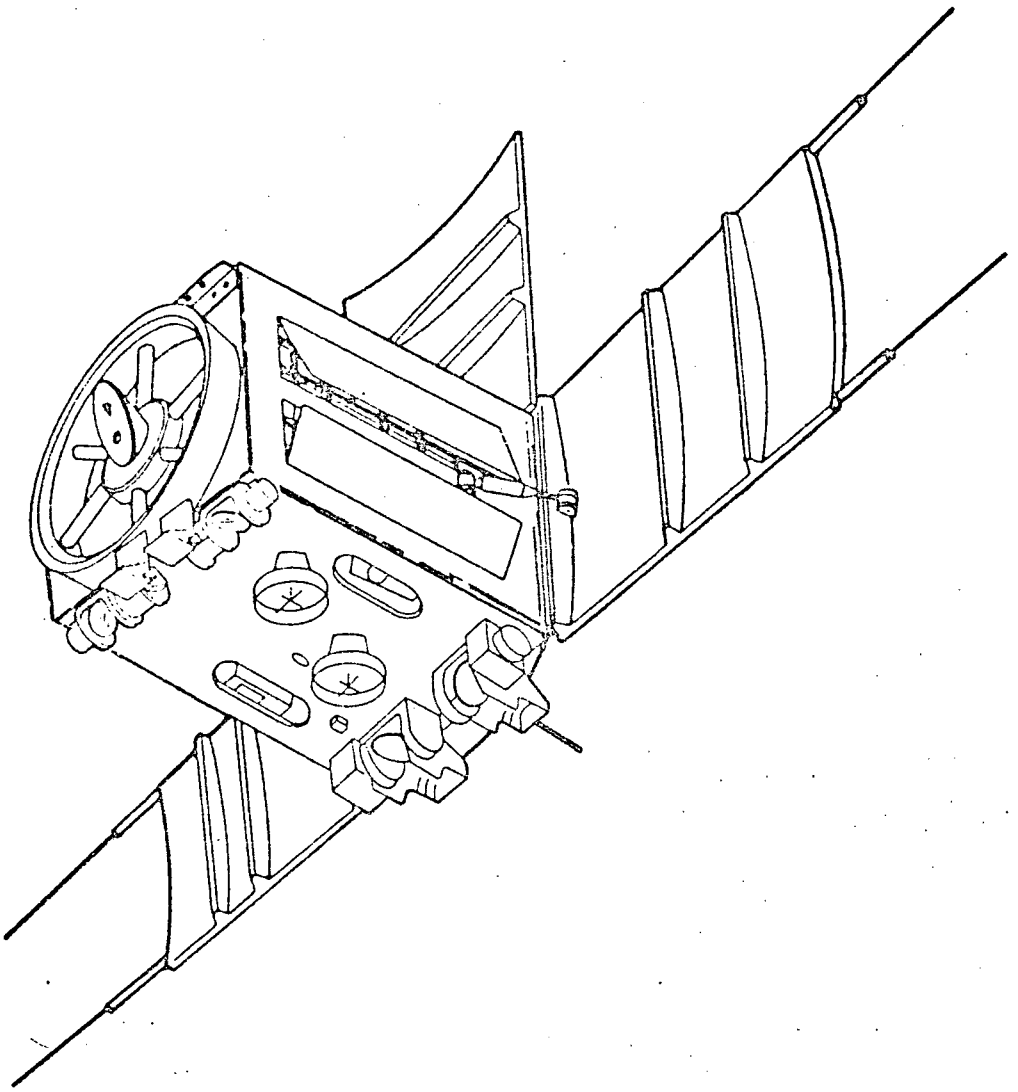

Preceding page blank

The ITOS D and E Spacecraft

PREFACE

This report describes the system, spacecraft, and ground installation design, as well as related studies, for the ITOS D and E meteorological satellite system. The ITOS D and E design study program has been conducted by the Astro-Electronics Division of RCA Corporation for the Goddard Space Flight Center of the National Aeronautics and Space Administration, under contract NAS5-10306.

TABLE OF CONTENTS

TABLE OF CONTENTS (Continued)

TABLE OF CONTENTS (Continued)

TABLE OF CONTENTS (Continued)

TABLE OF CONTENTS (Continued)

TABLE OF CONTENTS (Continued)

TABLE OF CONTENTS (Continued)

TABLE OF CONTENTS (Continued)

TABLE OF CONTENTS (Continued)

TABLE OF CONTENTS (Continued)

APPENDICES

LIST OF ILLUSTRATIONS

LIST OF ILLUSTRATIONS (Continued)

LIST OF ILLUSTRATIONS (Continued)

LIST OF ILLUSTRATIONS (Continued)

LIST OF ILLUSTRATIONS (Continued)

LIST OF TABLES

LIST OF TABLES (Continued)

LIST OF TABLES (Continued)

LIST OF TABLES (Continued)

SECTION I
SYSTEM DESIGN

SECTION I

SYSTEM DESIGN

A. INTRODUCTION

The ITOS D and E system described in this report will expand the operational capability of the basic TIROS M/ITOS system. The ITOS D and E mission will utilize the capabilities of the two-stage DSV 3N-6 Delta launch vehicle to place the ITOS D and E spacecraft into a circular, near-polar, sun synchronous orbit at 790 nautical miles altitude.

1. Mission Requirements

In fulfilling its mission, the ITOS D and E system will provide the following primary data for use by meteorologists and other scientists:

- Daytime observations of cloud cover as detected in the visible spectrum for direct transmission to users located around the world.
- Daytime and nighttime observations of cloud cover as detected from radiance in the infrared spectrum for direct transmission to users located around the world.
- Daily observations of global cloud cover in the visible and the infrared spectrums for processing at the National Environmental Satellite Center (NESC) of the Environmental Science Services Administration (ESSA).
- A vertical temperature profile of the atmosphere on a global basis for processing at the NESC of the ESSA.

In addition, the ITOS D and E system will provide secondary data comprising solar proton density measurements obtained throughout the orbit for processing at the NESC and the Space Disturbances Laboratory (SDL) of the ESSA.

2. System Summary

a. GENERAL

The ITOS D and E operating system comprises a stable, earth-oriented spacecraft, two command and data acquisition (CDA) stations, the TOS Evaluation Center and TOS Checkout Center (TEC/TCC), the TOS Operations Center (TOC), the Data Processing and Analysis Facility (DAPAF), the Scanning Radiometer Ground Station, and the Very High Resolution Radiometer Ground Stations (VHRRGS). The external configuration of the ITOS D and E spacecraft is shown in Figure I-1. The general relationships of the system elements are illustrated in Figure I-2.

b. SPACECRAFT

The spacecraft is a rectangular prism with a deployable solar array and a momentum wheel which provides gyroscopic stabilization of spacecraft attitude. The spacecraft is three-axis stabilized to provide an earth-oriented platform for the sensors. Reaction between the earth's magnetic field generated within the spacecraft provides control over the yaw/roll attitudes of the spacecraft and the total system momentum. A sampled data servo system with an error input derived from the attitude relationship between the spacecraft and the earth's horizon provides the required control of spacecraft pitch motion by means of momentum interchange between the wheel and spacecraft.

Thermal control of the spacecraft is provided by both active and passive elements. The passive elements comprise a thermal fence and appropriately distributed radiator surfaces. The thermal fence provides a variable absorptivity characteristic which changes with sun angle. The passive system is augmented by active thermal controllers (ATC's), which maintain temperature control by the variation of radiator surface area.

The power supply subsystem is a solar cell/battery/regulator system very similar to the TIROS M/ITOS system. This subsystem will provide power for operation of the spacecraft throughout its minimum mission life of 6 months.

The primary environmental sensor subsystems provide the means for both direct readout and remote recording of earth cloud cover in the visible and infrared regions, and for remote recording of temperature profile data. The sensor subsystems are operated continuously to provide global coverage.

Direct readout of daytime and nighttime cloud cover data in both the visible and infrared regions is accomplished by operating both very high resolution radiometers (VHRR) in the phased-mirror mode. The time-multiplexed data is transmitted directly to VHRR ground stations (VHRRGS). Up to 9 minutes of time multiplexed VHRR data may be stored on a VHRR recorder for subsequent transmission to a CDA station. Direct readout of both nighttime and daytime cloud

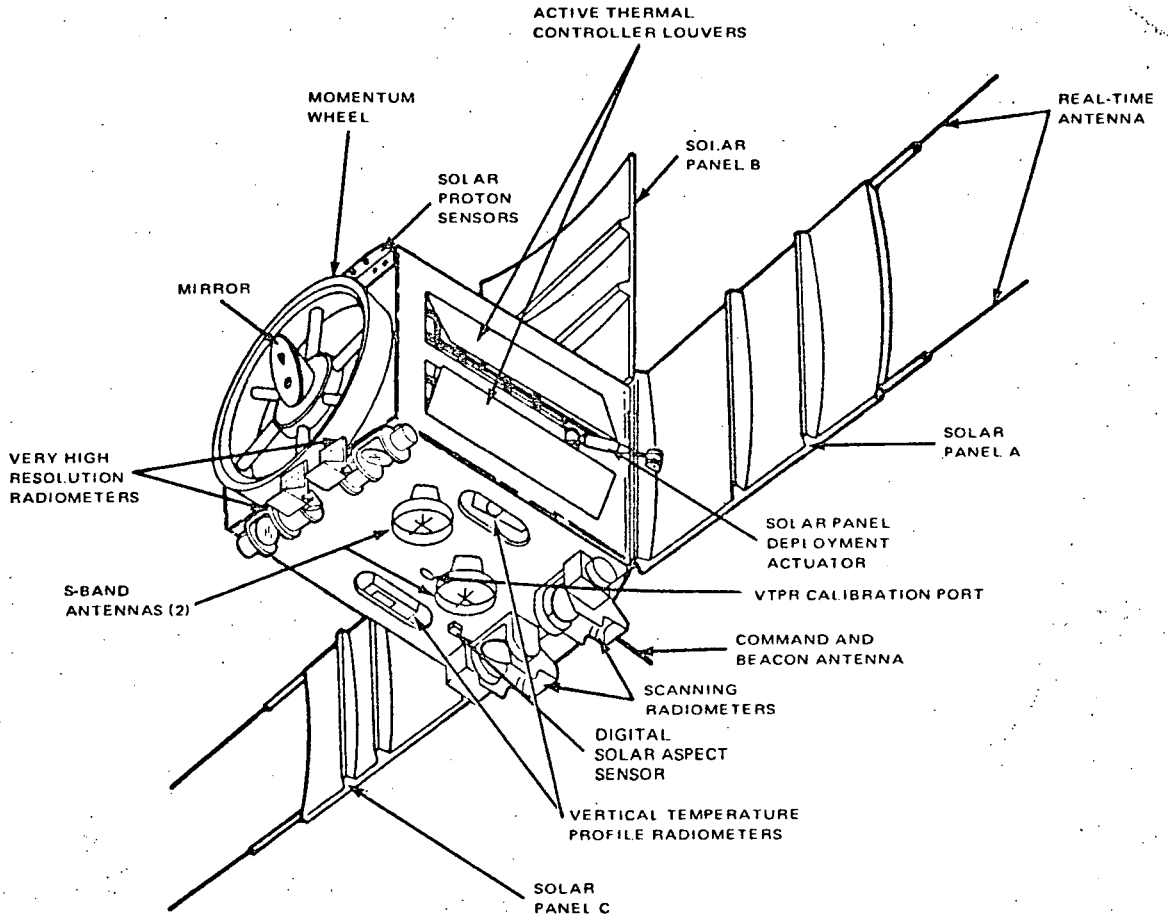

Figure I-1. ITOS D and E Satellite, Identification of External Features

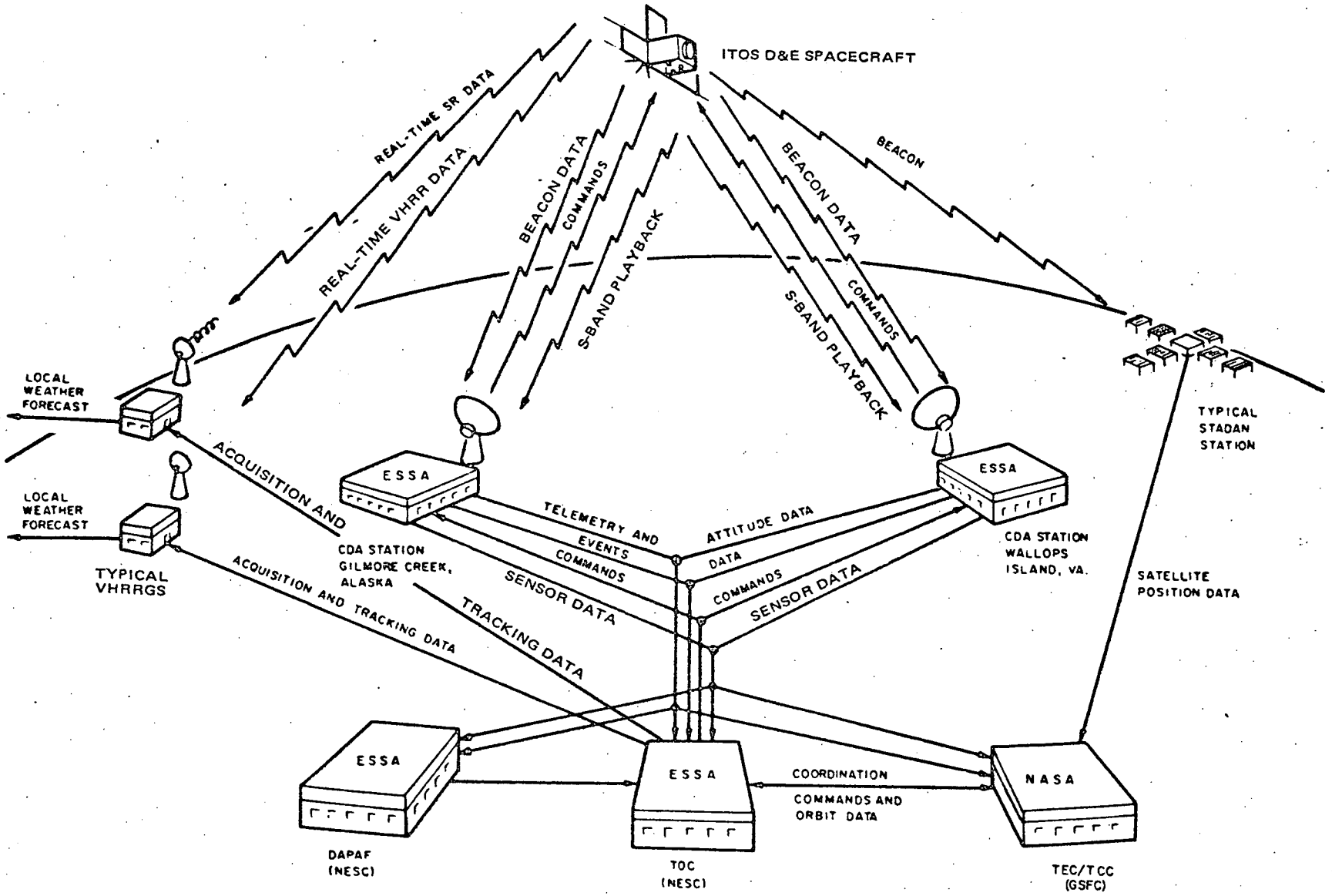

Figure I-2. The ITOS D and E System

cover and cloud-top temperature data is accomplished by one of the redundant scanning radiometers (SR). The SR output, both in the visible and the infrared regions, is transmitted in real time and is stored aboard the spacecraft on redundant SR tape recorders to obtain global data that will be played back and transmitted to one of the CDA stations. Both the real-time and stored data will be transmitted in a time-multiplexed mode.

A vertical temperature profile of the atmosphere is obtained from the vertical temperature profile radiometer (VTPR) and recorded, on a global basis, on a track of the scanning radiometer recorder (SRR) for subsequent transmission to a CDA station.

The solar proton monitor (SPM) data is transmitted continuously in real time and also recorded globally, along with the VTPR data on a track of the SRR.

The CDA station relays the recorded SR, VHRR, telemetry, SPM and VTPR data to the NESC for processing and analysis. The real time transmission of the SPM data is via the beacon telemetry link.

The ITOS D and E command subsystem is identical to that used on TIROS M/ITOS. The communications links between the satellite and ground stations include: a beacon telemetry link, a command link, and a real-time data link (SR), all in the VHF band; a real-time data link (VHRR) and a playback data link (SR, VTPR, SPM, and VHRR) in the UHF band, (S-band).

c. ORBIT

The ITOS D and E spacecraft system design is predicated on the assumption that the spacecraft will be placed in a 790 nmi, circular, near polar, sun-synchronous orbit. Recently, the possibility of increasing the orbit altitude to 900 nmi has been proposed. The system changes required for operation at a higher orbital altitude are comparatively minor if the primary sensor operating parameters are not changed.

Presuming there will be no changes in unit design, the effects of operating the spacecraft in a 900 nmi altitude circular orbit, instead of the present 790 nmi, are as follows:

(1) Radiation damage to the solar cells increases by a factor of 1.8.

(2) Radiation damage to other spacecraft semiconductors increases by a factor ranging from 1.6 to 2.0, depending on the shielding.

(3) The scan-to-scan overlap of radiometer data increases.

(4) The margin and signal to noise ratios in all communication links decreases by 1 dB.

(5) The roll sensor scan angle and the index pickoff position must be changed.

The SR will have a scan-to-scan overlap, at the subpoint, of 28 percent at 900 nmi. In comparison, the overlap at 790 nmi is 8 percent.

The VHRR will have a scan-to-scan overlap, at the subpoint, of 20 percent at 900 nmi. In comparison, the overlap at 790 nmi is 0.8 percent.

The VTPR will have a spot overlap of 10 percent from scan to scan, at the subpoint, and 33 percent at a 30-degree nadir angle. The geocentric arc length will increase from 15° at 790 nmi to 18° 14' at 900 nmi. The angular relationship from spot to spot, within a scan, will remain the same. However, the distance between spots, within a scan, increases. In addition, the VTPR sun shields and image motion compensation would require reexamination and probable redesign.

If the overlap from scan line to scan line is unacceptable for the VTPR, a modification to the delay between scans will have to be incorporated. If the VTPR is modified, the digital data processor (DDP) may require redesign. At the least, it would require an analysis to determine the effect of the VTPR modification. If the DDP were to be changed, the following items would have to be done: (1) filter modifications in the spacecraft multiplexer and ground station demultiplexer; (2) analysis of the long lines and associated modems; (3) analysis of the time base unit (TBU); (4) analysis of the SRR for increased storage density on the digital data track; (5) the SPM may require modification; (6) analysis of the beacon telemetry link, and (7) analysis of the S-band playback link.

The radiation environment corresponding to a sun-synchronous orbit will increase the damage effect on the solar cells by a factor of approximately 1.8. This factor is based on the environmental data, published in NASA SP 3024, "Models of the Trapped Radiation Environment," by J. Vette, et al, for the number of protons above 4 MeV at different altitudes and angles of inclination. Protons in the energy range above 4 MeV account for nearly all of the anticipated radiation damage to ITOS solar cells. The damage contribution from electrons is almost negligible. The effect on system performance may be roughly evaluated by referring to Section V, Power Supply, Figure V-11. For a 900-nmi altitude orbit, the 6-month curve is a 3-month curve and the 12-month curve is a 6-month curve.

A preliminary evaluation of the effect of the radiation at the higher altitude, on components other than solar cells, was made. The safety factor for ionization damage was reduced from 5 to 3 for the exposed location (i.e., shield thickness equivalent to 170 mils of aluminum), and from 2 to 1 at the average location (i.e., shield thickness equivalent to 270 mils of aluminum). The safety factor described is the radiation dose used in the TIROS M/ITOS-1 design (6 months, 1965 data, 750 nmi), divided by the predicted radiation dose for 1 year, 1968 data, at 900 nmi. Bulk damage effects require further analysis. However, only a few of the transistor types used in the ITOS units are susceptible to this type of damage.

d. GROUND COMPLEX

The ITOS D and E system utilizes the capability of the existing automatic picture transmission (APT) ground stations for receiving SR data. Modifications of the APT ground station were made to receive the 48-lines-per-minute SR data. A new local user ground station will be required to receive the real-time data from the VHRR.

The present TIROS M/ITOS CDA stations will be used with the addition of new demultiplexing equipment. The CDA stations will transmit the commands that originate at TEC/TCC and TOC to the spacecraft and transmit the data received from the spacecraft to TEC/TCC, TOC, or NESC, as required.

TEC/TCC will control the operation of the spacecraft during launch and throughout initial checkout and will evaluate the operational performance of the spacecraft. TOC will provide programming and control of the spacecraft during its operational phase.

The processing of the data, both primary and secondary, will be performed at NESC by the Data Processing and Analysis Facility (DAPAF).

B. SYSTEM FUNCTIONAL DESCRIPTION

1. Spacecraft

a. PHYSICAL DESCRIPTION

(1) CONFIGURATION

The ITOS D and E spacecraft is shown in Figure I-1 which depicts the equipment module (main body), the deployable three-panel solar array, the passive thermal-control fence, the ATC's, and the momentum wheel with scanning mirror assembly. The total weight of the spacecraft, including a spacecraft separation ring for mating the spacecraft to the launch-vehicle second-stage attach fitting, will be approximately 735 pounds. Figure I-3 shows the spacecraft orientation and defines the various panels that make up the spacecraft.

Figure I-4 shows the earth sensor fields of view in relationship to each other with the spacecraft in an operational configuration. Sufficient clearance is provided so that the sensor fields of view are not encroached upon by other elements on the spacecraft. The scanning mirror for the pitch and roll sensors of the pitch control loop is shielded by the equipment module proper.

(2) CENTRAL EQUIPMENT MODULE

The central equipment module or main body of the spacecraft is a rectangular prism. The base of the prism is approximately 40 by 40 inches and the overall height is approximately 57 inches. This module houses the data-gathering subsystems required for performance of the mission, such as VTPR's, VHRR's, SR's, and the SPM, and the associated support subsystems, such as power, command, communications, etc.

As shown in the component layout diagram of Figure I-5, the baseplate and two side panels serve as mounting surfaces for the subsystems.

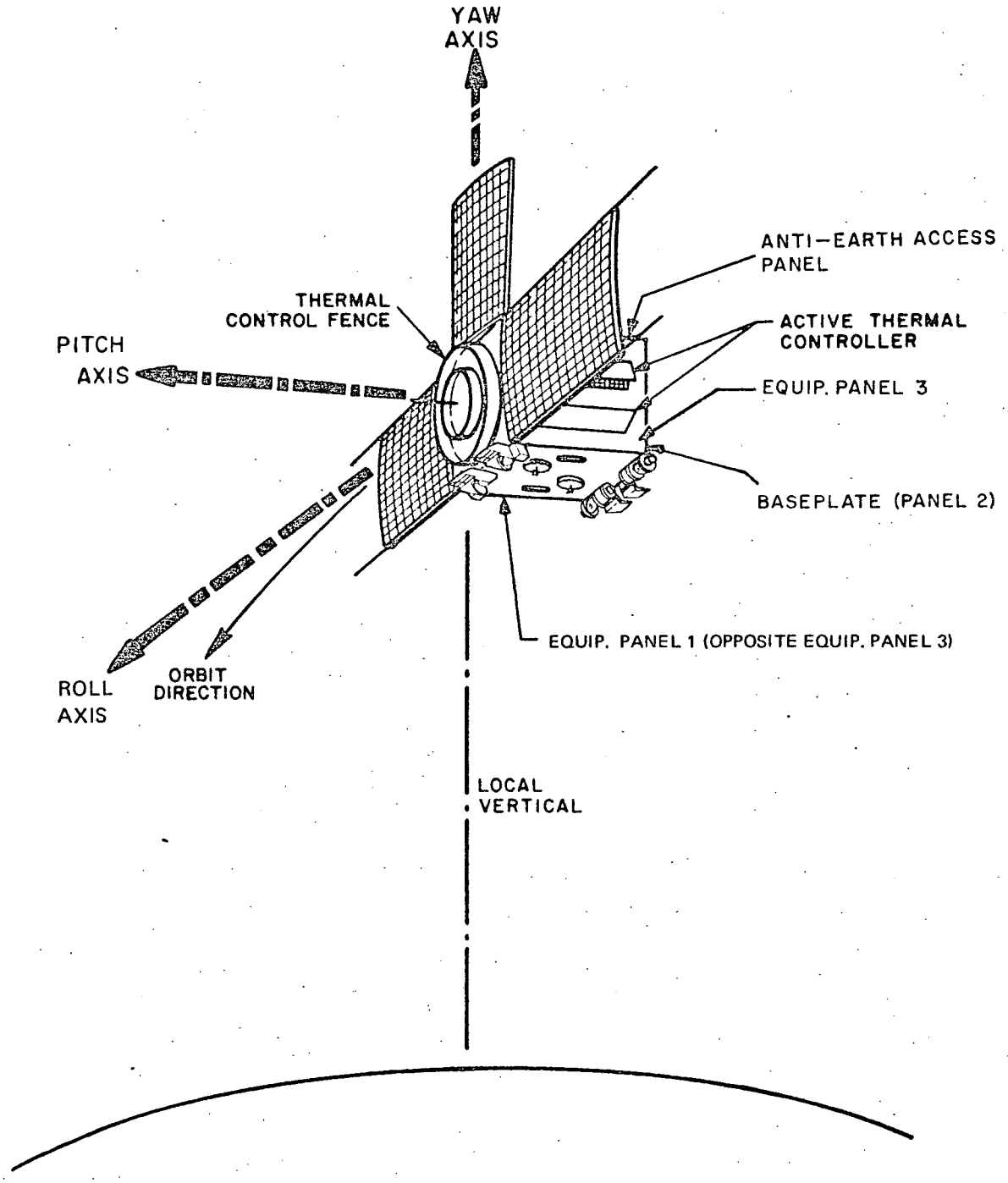

Figure I-3. ITOS D and E Spacecraft Orientation

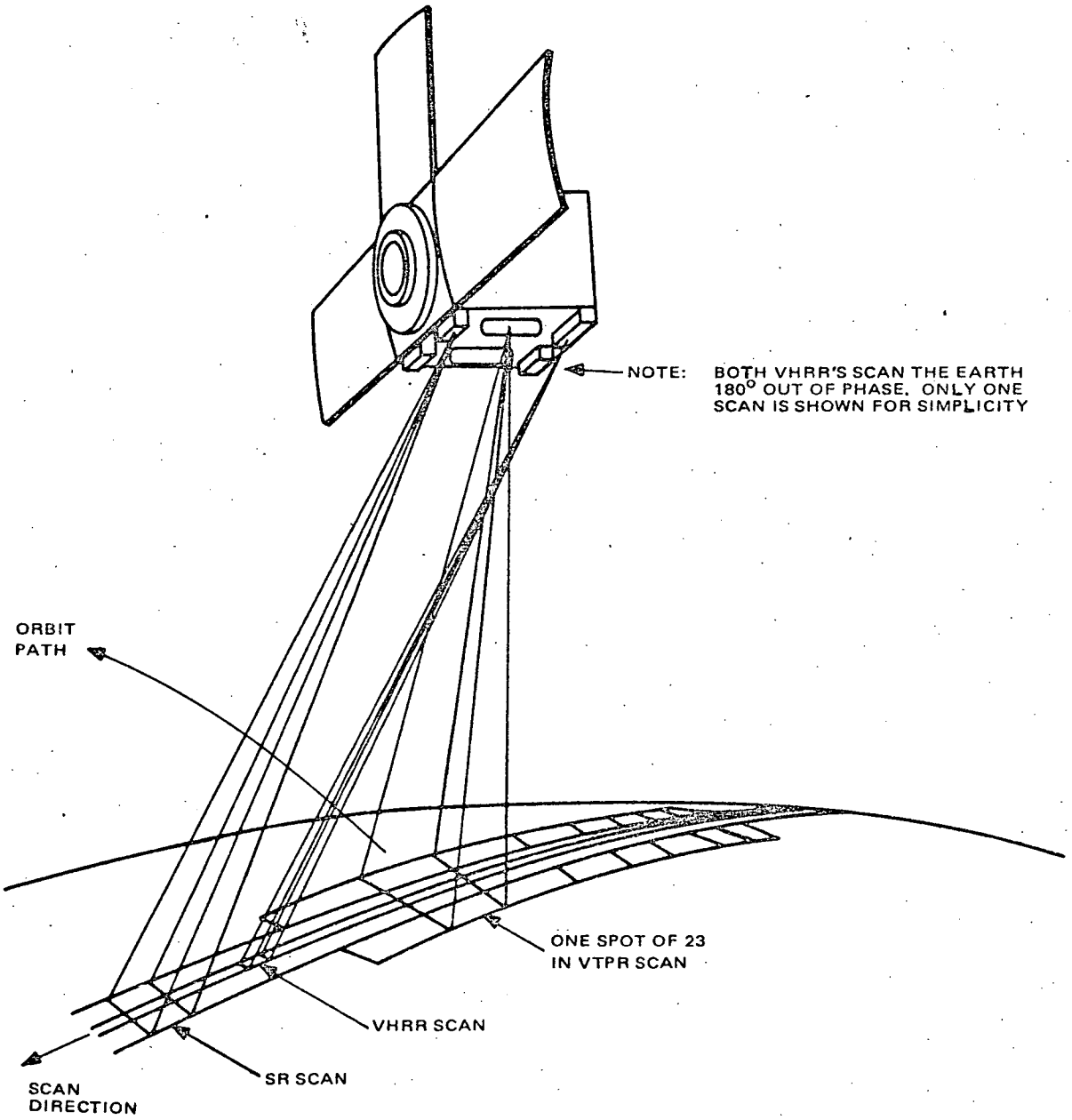

Figure I-4. ITOS D and E Spacecraft in Operational Mode, Showing Sensor Field of View

Constraints imposed by sensor fields of view, thermal considerations, single unit equipment removal, and electrical harness requirements were major factors in establishing the component layouts. (Figures II-6 through II-10 of Section II show the component layout for all panels of the spacecraft.)

To facilitate spacecraft integration, panels 1 and 3 are hinged to the baseplate such that the three surfaces can be laid flat and the components assembled and electrically checked out in the configuration prior to completion of the structural assembly. Any minor repairs or adjustments required after final assembly can be performed through access ports provided in the earth-viewing and anti-earth-viewing panels of the spacecraft. The S-band antennas, which are positioned over the access hole in the earth-viewing panel, are mounted on hinged structures, and can be rotated out of the way, when access into the interior of the spacecraft is required.

(3) SOLAR ARRAY

The ITOS D and E spacecraft is designed to operate over a range of orbit sun angles (gamma angles) from 30 to 60 degrees.

The ITOS D and E solar array is the same as the TIROS M/ITOS design and consists of three identical panels which are independently hinged to panels 1, 3, and the anti-earth panel of the spacecraft. Each panel is 36.4 x 65.2 inches and in mission mode lies in the orbit plane. The panels are slightly curved (as can be seen in Figure I-3); this design provides adequate clearance between the panels and the Marmon clamp of the spacecraft separation mechanism, thus precluding any danger of interference under adverse separation tip-off conditions.

In the launch configuration, the panels are folded 90 degrees, and held against the sides of the central equipment module. Following the initial orientation maneuver, squibs are actuated, allowing a spring/hydraulic damper-type actuator to deploy each array panel until it is positioned normal to the spacecraft pitch axis. This array configuration permits an unimpeded field of view for all the earth-viewing sensors.

(4) THERMAL CONTROL

The thermal design of the ITOS D and E spacecraft is the result of modifications made to the TIROS M/ITOS spacecraft.

Thermal control of the spacecraft is achieved by using passive and active control elements. The passive elements include a variable solar absorptance thermal fence and fixed radiator surfaces; see Figures I-6 and I-7. All radiator surfaces and thermal fence fins are finished with 3M 400 series black velvet coating to prevent degradation of the optical properties of the radiators due to space radiation.

Page intentionally left blank

Active control is accomplished with temperature-controlled, moving louvers, two per equipment side, which cover or expose radiator surface as required. Radiator and louver sizes are shown in Figure I-6. (General location with respect to the overall spacecraft configuration is illustrated in Figure I-3).

Internal temperature distribution is controlled by a balance of conduction and radiation coupling to the thermal control surfaces of the fence and radiators. By proper location of the baseplate radiation surfaces, high thermal dissipation units are controlled within specifications. Distribution of the radiator area controls the internal gradients. Figure I-6 illustrates this distribution.

The spacecraft surface not used for temperature control is blanketed with insulation to limit the radiation heat transfer from these areas. The effective emissivity of the blanket has been empirically determined to be 0.02.

(5) PITCH-CONTROL LOOP

The pitch-control loop consists of a momentum wheel assembly (MWA), comprising a wheel, a dc drive motor, a scanning mirror, pitch and roll sensors, and an associated pitch control electronics unit. As shown in Figure I-1, the MWA is mounted on the spacecraft baseplate, with the momentum wheel and scanning mirror exterior to the equipment module. The momentum wheel, operating in mission mode at a nominal speed of 150 r/min, provides gyroscopic stiffness and acts as a momentum source and sink. At the nominal orbital altitude of 790 nautical miles, one surface of the spacecraft is maintained normal to the local vertical through the action of the pitch control loop. The pitch control loop is a first-order, sampled-data servo system, the error input for which is derived from redundant IR sensors mounted on the tee-plate within the shaft of the MWA. The scanning mirror is attached to the momentum wheel and provides the necessary optical scanning motion, allowing the canted pitch sensors to be body-fixed. Roll sensors are also included in this assembly and likewise derive their scanning motion from the mirror. The wheel, motor, and sensors are packaged as an integral unit.

(6) SEPARATION RING

A separation ring is attached to the baseplate to mate the baseplate of the spacecraft to the spacecraft-to-launch vehicle attach fitting. This ring is 37 inches in diameter and 5.6 inches deep, and is bolted to the underside of the baseplate. Its lower edge forms one-half of the "Vee-seating" of the separation interface and serves as the reference surface for sensor alignment purposes. Mounting pads for the four springs of the separation mechanism and the separation switches are attached to the separation ring.

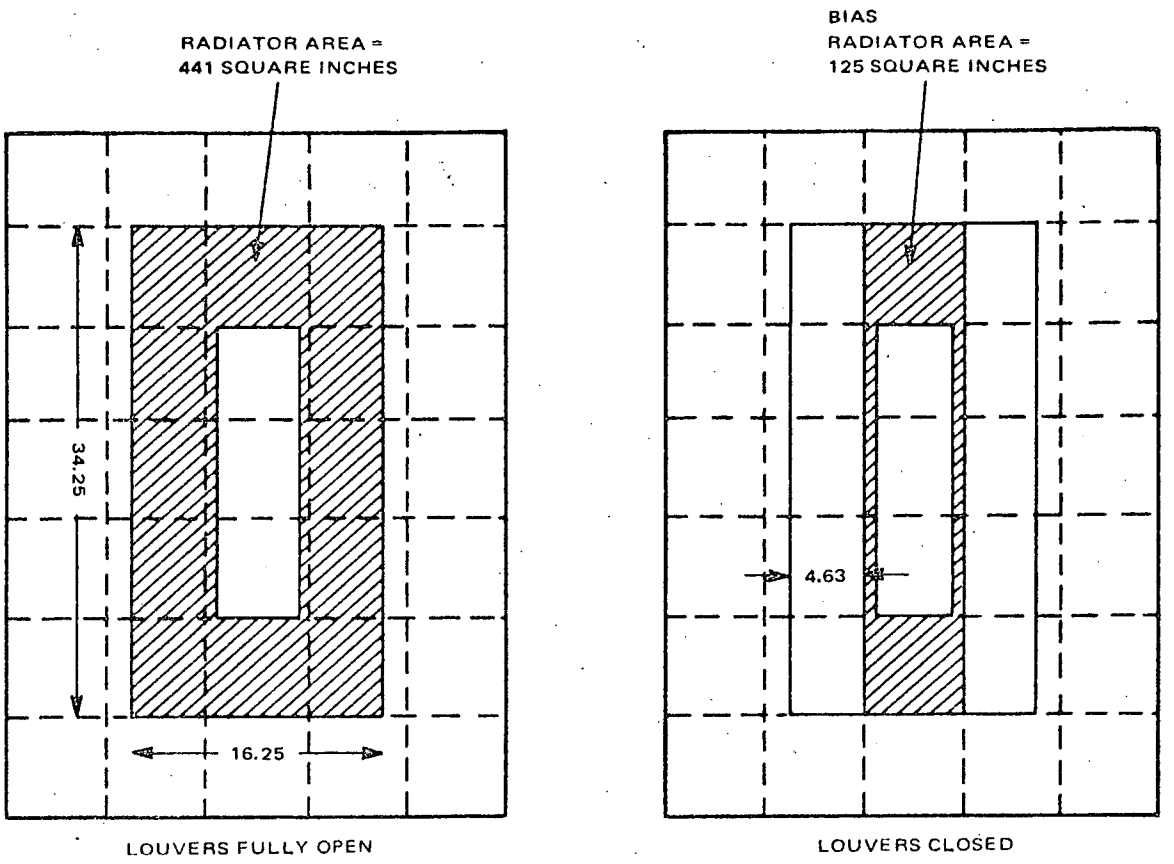

Figure I-6. ITOS D and E Thermal Radiators

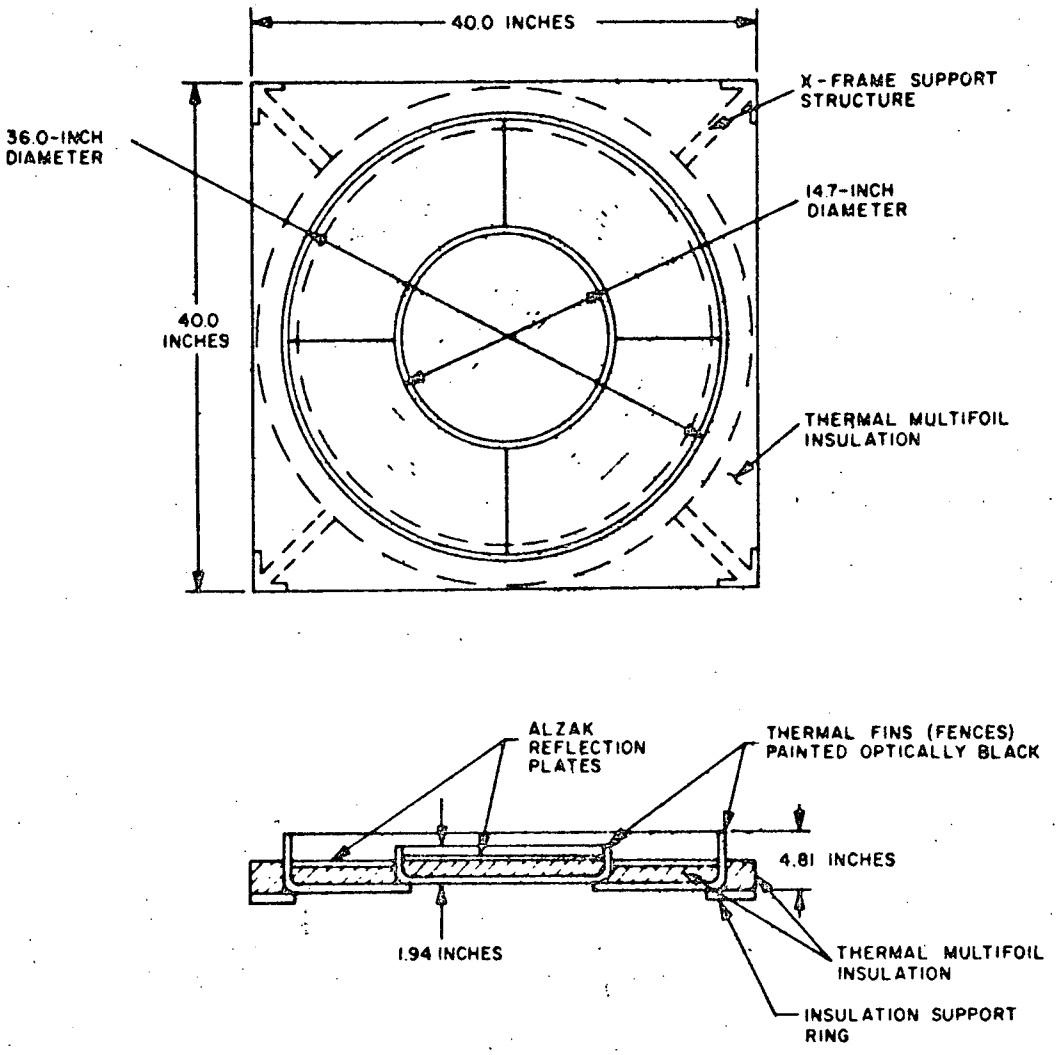

Figure I-7. Thermal Control Fence

b. LAUNCH VEHICLE COMPATIBILITY

The ITOS D and E spacecraft is scheduled to be launched by a two-stage long tank DELTA launch vehicle which has the following improved features above the present DELTA N configuration:

- Long tank DELTA 1st stage
- Universal boattail section capable of handling 3, 6, or 9 solid motors for thrust augmentation
- Improved second stage (AJ-10-118F) with the N_2O_4 higher thrust propellant and restart capability

Compatibility of the spacecraft with this booster and the improved DELTA fairing is shown in Figure II-3. Allowable payload weight for the three-solid motor launch vehicle configuration for a Western Test Range launch into a 790-nmi sun-synchronous orbit, is 1,000 pounds. This includes the 60-pound weight of the attach fitting. The present estimated weight of the ITOS D and E spacecraft is 735 pounds.

The launch vehicle will inject the payload into its operational orientation with the pitch axis normal to the orbital plane. In addition, just prior to separation, the launch vehicle roll jets will impart to the spacecraft, the angular momentum necessary to ensure operational dynamic stability (i.e., 212 ±10% inch-pound-second).

The same 37-inch spacecraft-to-launch vehicle attach fitting developed for TIROS M/ITOS will also be used for the ITOS D and E spacecraft. Access holes are provided in the attach fitting to allow check-out of pitch and roll sensors. The spacecraft is mated to the attach fitting by means of the Marmon clamp. Four springs, equispaced around the periphery of the adapter, provide a separation velocity of between 5 and 8 feet per second. A breakaway connector at the spacecraft-to-launch vehicle separation plane provides spacecraft battery charging from the block house; and upon spacecraft separation, it disables the telemetered accelerometer data.

View-angle and envelope constraints of the SR's and the VHRR's made it necessary to exceed the "permissible" 57-inch diameter spacecraft constraint envelope of the shroud. By agreement from the NASA-DELTA office, the static spacecraft constraint envelope, specifically, the inside dimensions of the fairing, has been redefined as a 0.75-inch annulus at the separation plane, linearly increasing to 1.38-inch at the top of the spacecraft (STA 643.47), as shown in Figure II-3. Along the thrust axis of the launch vehicle, a nominal 1-inch clearance with respect to spacecraft-to-shroud hardpoints, is mandatory.

The envelope of the VHRR's will require relocation of the fairing rib located at STA 672.98 to STA 670.18 and the fairing rib presently located

STA 638.98 requires relocation to STA 642.48 in order to clear the constraint envelope of the two SR's.

In view of the insensitivity to payload imbalance of the three-axis control system of the launch vehicle, the spacecraft will be neither dynamically nor statically balanced. The sizeable weights of the new ITOS D and E sensors mounted to the earth-viewing panel of the structure, impart a "front-heaviness" to the integrated structure for which the rest of the electronic boxes cannot compensate. Computer balance and placement studies show the magnitudes of the imbalance to be:

- Static - 1,705 in-lbs
- Dynamic:

I_{12} (Yaw-Roll) = + 6.6 in-lbs-sec^2

I_{13} (Yaw-Pitch) = -10.7 in-lbs-sec^2

I_{23} (Roll-Pitch) = - 6.0 in-lbs-sec^2

Concurrence has been received from the NASA-DELTA office that imbalances in these orders of magnitude can adequately be handled by the launch-vehicle three-axis control system. However, the four separation springs will have to be force-matched to compensate for the static center of gravity offset. This precaution must be taken in order to minimize the coning of the spacecraft during its separation from the launch vehicle.

c. FUNCTIONAL DESCRIPTION

(1) GENERAL

The ITOS D and E spacecraft, shown in the block diagram of Figure I-8, is functionally divided into the command, vehicle dynamics, primary sensor, SPM, thermal, communications, and power subsystems. The communication subsystem includes telemetry as well as all transmitters, antennas, and associated circuits.

(2) COMMAND SUBSYSTEM

The dual command receiver and the enable-tone detectors of the dual decoder are powered continuously. The command receivers amplify and detect the received signals. The outputs of the receivers are applied to their respective associated decoders. Decoder selection is implemented by transmission of the appropriate command enable tone by the ground station. Detection of the correct enable tone energizes the remainder of the selected decoder. Receipt and detection of the correct command address applies power to the circuitry of the

selected decoder permitting subsequent command reception and decoding. As the commands are received, verification data are retransmitted to the CDA station via the beacon transmitter to confirm correct receipt of a command.

Outputs of the decoder are used to select a programmer and a time-base unit. The dual programmer provides the signals for all remote sequencing of spacecraft subsystems such as the recorders and attitude correction. The dual time-base unit provides all the timing signals and frequencies required to operate the spacecraft subsystems.

The detected command signals are routed to the command distribution units (CDU's) where the commands are converted to the appropriate action. In addition to inputs from the decoder, the CDU's also receive inputs from the programmers.

(3) PRIMARY SENSORS

(a) Real-Time Data

Two types of real time data are sent to local users:

- VHRR data via the S-band link,
- SR data via the VHF link.

The VHRR sensors in two spectral regions: 0.6 to 0.7 micron and 10.5 to 12.5 microns. The local user will obtain VHRR data when the spacecraft is at least 5 degrees above the horizon. The ground resolution at the local vertical is 0.5 nautical mile square.

The SR provides coverage similar to that of the VHRR but with a resolution at the local vertical of 4 nautical miles for the IR channel and 2 nautical miles for the visible channel. Both radiometers, in the normal operating mode, will provide time-multiplexed IR and visible earth scans. In the backup operating mode, the VHRR provides frequency multiplexed IR and visible information from one radiometer; the SR provides either IR or visible information depending upon ground command. Details of the multiplexed format are in Section IX.

(b) Stored Data

A nine-minute portion of the orbit may be selected by ground command for recording VHRR data. This recording will contain both the visible and IR data from the operating radiometers. However, only one channel can play back.

REPRODUCIBILITY OF THE
ORIGINAL PAGE IS POOR

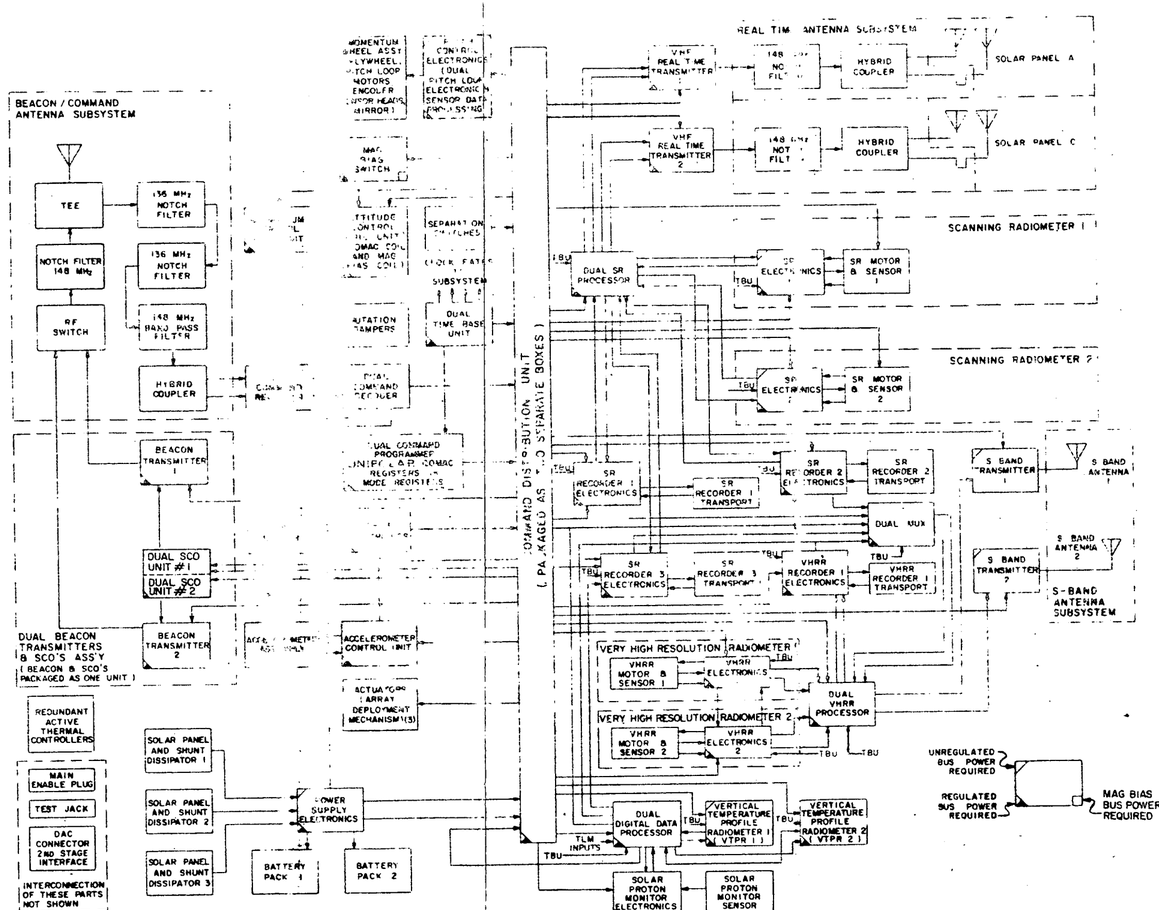

Figure I-8. ITOS D and E System Block Diagram

FOLDOUT FRAME 1

FOLDOUT FRAME 2

SR data is recorded continuously on one of three SRR's. Any two of the three recorders may be selected at a time with only one recorder in the record mode at any given time. The end-of-tape signal on one recorder causes the second one to start recording. By this means, continuous recording of SR data can be accomplished even through "missed" revolutions.

In addition to SR data, the SRR stores digital data from the VTPR and from the SPM. Interleaved with the data from these sensors is digital housekeeping telemetry data.

The stored data is played back to either the Wallops Island or Gilmore Creek CDA stations upon their command. The playback function causes erasure of the recorded data.

(4) SOLAR PROTON MONITOR

The SPM consists of an array of solid-state detectors and an electronics unit to encode the data in digital form. The subsystem detects solar protons in several energy ranges. An electron detector is used to determine the extent of contamination of the proton data due to the electrons. The control of the timing and monitor is accomplished by the DDP. In addition to recorded data, SPM data can be transmitted in real time over the beacon telemetry link.

(5) COMMUNICATIONS SUBSYSTEM

(a) S-Band Link

The S-band link is used for both real-time VHRR data and transmission of the remote data stored on magnetic tape recorders. Real-time and remote data cannot be transmitted simultaneously. The real-time VHRR signals are placed on subcarriers by the VHRR processor. The outputs of the VHRR processor are connected to the redundant S-band (1.7 GHz) transmitters. The remote data is processed by the dual multiplexer.

The dual multiplexer contains redundant multiplexers which can accept simultaneous inputs from one or two SRR (two SRR data signals and two SRR flutter-and-wow signals), and a VHRR recorder (one VHRR data signal and one VHRR flutter-and-wow signal). The signals are translated to appropriate channels and combined. The outputs of the redundant multiplexers are connected to the VHRR processors for cross-coupling to the S-band transmitters. Selection of the redundant subsystem is made by powering the selected unit rather than by external signal switching. Each of the two S-band transmitters has an S-band

antenna connected directly to it. The S-band array provides right hand circularly polarized radiation and has a pattern shaped to maximize the gain at the points which correspond to maximum communication ranges. Each S-band antenna consists of crossed dipoles over a ground plane.

(b) Real-Time Link

The VHF real-time transmitter handles the SR real-time data. The transmitter frequency is nominally 137.5 MHz. One of the redundant transmitters is selected by ground command. The output of the energized transmitter is applied to the real-time antenna coupler which provides a quadrature feed for two half-wavelength dipoles mounted on the end of one of the solar panels. The two dipoles are configured to provide a linear polarized directive pattern in a 110-degree cone centered on the local vertical.

(c) Command and Beacon Link

The command RF carrier, in the 148-MHz band, is received on the command and beacon antenna, a monopole configuration which accepts signals over a look angle of 4π steradians. The command-receiver coupler provides isolation, couples the received power into both channels of the dual command receiver, and maintains an impedance match.

Telemetry data is transmitted to the CDA ground stations by the beacon transmitter. Beacon transmitter 1 and set 1 of the dual subcarrier oscillator (SCO) are associated permanently as a unit as are beacon transmitter 2 and set 2 of the dual SCO. The two SCO frequencies are IRIG channel 9 and IRIG channel 7 (modified). These channels are used to transmit the pulse amplitude modulated (PAM) housekeeping telemetry from the DDP, real-time SPM data, analog VTPR data, attitude data, command verification, vibration data during launch, and DSAS signals. Data is switched to the SCO channels by the CDU in response to ground commands. The beacon transmitter output passes through the beacon filter network to the monopole antenna.

(6) POWER SUBSYSTEM

The power subsystem comprises a solar array, power-supply electronics, batteries, and external shunt dissipators. The solar array consists of solar cells mounted on one side of three panels, with the cells wired in series-parallel combinations to provide component redundancy. The electronics unit has a control amplifier which, in conjunction with the shunt dissipator, dissipates the array power in excess of the spacecraft requirements. Tapered charge controllers regulate the charge rate of two batteries as a function of battery charge condition and temperature. The series regulator provides the regulated -24.5-volt power which most of the spacecraft

subsystems use. The dual command receiver, SR's, VTPR's, S-band transmitters, pitch control motors, and the dual decoder operate from the unregulated output of the power subsystem. The batteries are used to supply power during the night portion of the orbit and when spacecraft demands exceed the power available from the solar array during the daytime. The battery capacity has been increased from the TIROS M/ITOS value of 8 ampere hours to 12 ampere hours.

d. SUBSYSTEM REDUNDANCY

(1) OPERATING GOALS

The ITOS D and E spacecraft has been designed to satisfy the requirements of the operational system. It will be in use full-time, providing complete data capability from the VTPR, SR, and SPM every revolution. Programming capability has been included for use with the VHRR at high sun angles to conserve electrical power. The design mission life-time of the spacecraft is a minimum of 6 months. To meet this requirement, design factors have been incorporated to allow for degradation of transistor characteristics due to aging and radiation bombardment. Premature termination of the mission because of subsystem failures has been minimized by the use of cross-strapped redundant units. Redundant units have generally been included for those subsystems which are primary to the mission. Where it has not been feasible to include a redundant unit for a primary subsystem, the unit has been designed to include redundant circuits or functions, as in the CDU, or the design includes a backup mode with a performance degradation, as in the VHRR subsystem design.

As a further aid to improved reliability, the signals from redundant units are generally cross-strapped by resistive coupling. Thus, it is not necessary to provide signal switching; the selection and powering of the desired redundant units automatically produce the desired subsystem combinations.

Table I-1 indicates the spacecraft subsystems and units, and the number of each type.

TABLE I-1. SPACECRAFT SUBSYSTEM COMPLEMENT

Unit	Quantity
1. Structure or Bus	1
2. Active Thermal Control	4
3. Harness	1
4. VHRR	2
5. VTPR	2
6. Scanning Radiometer (Sensor and Electronics)	2
7. VHRR Recorder	1
8. SR Recorder	3
9. Dual SR Processor	1*
10. Dual Command Receiver	1*
11. Beacon Transmitter	2
12. S-Band Transmitter	2
13. Real-Time VHF Transmitter	2
14. Dual Multiplexer	1*
15. Dual SCO Unit	1*
16. VHRR Processor	1
17. Digital Data Processor	1*
18. Command Receiver Coupler	1
19. Beacon and Command Antenna	1
20. Beacon RF Switch	1
21. S-Band Antenna	2
22. VHF Real-Time Antenna Array	2
23. VHF Real-Time Antenna Coupler	2
24. VHF Real-Time Filter	2
25. Momentum Wheel Assembly	1
26. Pitch Control Electronics	1*

*Redundant units housed in single box

TABLE I-1. SPACECRAFT SUBSYSTEM COMPLEMENT (Continued)

Unit	Quantity
27. Attitude Control Coil Unit	1
28. Momentum Control Coil	2
29. Nutation Damper	2
30. Magnetic Bias Switch	1
31. Separation Switch	2
32. Digital Solar Aspect Sensor	1
33. Dual Decoder	1*
34. Command Distribution Unit	1**
35. Dual Programmer	1*
36. Dual Time-Base Unit	1*
37. Solar Array	3
38. Battery	2
39. Power Supply Electronics	1*
40. Solar Proton Monitor	1

*Redundant units housed in single box

**Packaged in two boxes

2. Spacecraft/CDA Station Interface

Four communication channels are provided between the CDA stations and the spacecraft. One channel, the command link, transmits data from the ground to the spacecraft; the remaining three channels transmit data from the spacecraft to the ground.

a. COMMAND LINK

The command transmission takes the form of enable tones and FSK signals which ampltiude-modulate the CDA-station command transmitter. Table I-2 lists the command link characteristics.

TABLE I-2. COMMAND LINK CHARACTERISTICS

Characteristic	Parameter
Frequency	148.56 MHz
Transmitter Power - CDA	1000 watts, minimum
Ground-Station Antenna Gain	12 dB
Spacecraft Antenna Gain	-14.0 dB, minimum
Spacecraft Receiver RF Threshold	-107 dBm
Margin	+3.0 dB, minimum

The modulation input to the transmitter is obtained from one of two tone pair oscillators, designated tone pair A and tone pair B. Each oscillator pair contains an enable-tone oscillator and an FSK voltage-controlled oscillator. Transmission from the CDA station antenna is circularly polarized. The monopole antenna on the spacecraft is linearly polarized for command reception.

b. BEACON LINK

The beacon channel is used to transmit preseparation accelerometer spacecraft attitude, DSAS data, real-time SPM data; telemetry; and command verification data from the spacecraft to the ground. This information modulates two voltage-controlled oscillators, the outputs of which are combined to phase-modulate the beacon transmitter. Table I-3 lists the beacon link characteristics.

TABLE I-3. BEACON LINK CHARACTERISTICS

Characteristic	Parameter
Frequency	136.77 MHz
Transmitter Power	250 mW (24 dBm) minimum
Spacecraft Antenna Gain, including losses	-14.5 dB, minimum
Ground-Station Antenna Gain	27.6 dB
IF Bandwidth	30 kHz

TABLE I-3. BEACON LINK CHARACTERISTICS (Continued)

Characteristic	Parameter
Received Carrier Power	-115.3 dBm (minimum)
Phase-Lock-Loop Noise Power	-142.7 dBm
Phase-Lock-Loop S/N Ratio	27.4 dB
Phase-Lock-Loop Threshold	-136.7 dBm
Phase-Lock-Loop Margin above Threshold	21.4 dB (minimum)
Signal Modulation Characteristics	
(a) 3.9 kHz subcarrier ±7.5% RF phase deviation: Margin Baseband S/N ratio	59 Hz baseband 0.50 radian 0.3 dB (minimum) 47.7 dB p-p/rms (min)
(b) 2.3 kHz subcarrier ±20% RF phase deviation: Margin Baseband S/N ratio	160 Hz baseband 0.70 radian 1.2 dB (minimum) 42.1 dB p-p/rms (min)

The beacon antenna is the same monopole antenna used for command reception.

c. REAL-TIME VHF LINK

The real-time VHF link transmits SR signals to the local readout stations. The output of one of the SR's amplitude-modulates a 2.4-kHz subcarrier, which in turn frequency-modulates one of the redundant VHF transmitters. The transmitter output is coupled through a notch filter to a pair of half-wave dipoles mounted at the ends of the solar panels.

The real-time VHF link characteristics are listed in Table I-4.

TABLE I-4. REAL-TIME VHF LINK CHARACTERISTICS

Characteristic	Parameter
Frequency	137.5 MHz
Transmitter Power	5 watts, (+37 dBm) minimum
Spacecraft Antenna Gain, Including Losses	-5.3 dB, minimum (over ±60° about local vertical)
Polarization of Transmission	Linear
Ground-Station Antenna Gain	+12.5 dB
Received Carrier Power	-107.2 dBm (minimum)
RF Carrier Margin Above Threshold	+0.1 dB (minimum)
Signal Modulation Characteristics:	
Peak deviation:	9 kHz
Video baseband:	
Visible Channel	900 Hz
IR Channel	450 Hz
Subcarrier bandwidth:	3.6 kHz
Baseband S/N Ratio	
Visible Channel	36.4 dB p-p/rms
IR Channel	39.5 dB p-p/rms

d. S-BAND PLAYBACK LINK

The S-band playback link transmits the reproduced outputs of the spacecraft tape recorders on command from the ground station and is the principal data link from the spacecraft to the CDA stations. The data transmitted over the link are as follows:

- SR Video (two channels)
- SR Flutter and Wow (two channels)

- VHRR Video (one channel)
- VHRR Flutter and Wow (one channel)
- Digital Data (two channels)

The VHRR and SR signals, from either of their respective subsystems, modulate subcarrier oscillators whose output is recorded. The DDP data are in digital form which is directly recorded; upon playback, each channel, as appropriate, is frequency translated and then combined in one of the redundant multiplexers to produce a composite 10- to 500-kHz signal which frequency-modulates one of the redundant S-band transmitters. Each transmitter feeds a crossed-dipole S-band antenna array.

The S-band playback link characteristics are listed in Table I-5.

TABLE I-5. S-BAND PLAYBACK LINK CHARACTERISTICS

Characteristic	Parameter
Center Frequency	1697.5 MHz
Transmitter Power	5 watts
Spacecraft Antenna Gain (including losses)	1.2 dB min at ±55° from local vertical
Ground-Station Antenna Gain	+47.7 dB
Receiver Threshold	-96.2 dBm
Worst-case Margin	+11.9 dB

The S-band signal is received by the 85-foot antenna at the CDA station, demodulated by an FM receiver, demultiplexed and shifted to original frequency bands, and recorded. The signals are then played back into telephone-type long lines and transmitted to NESC at Suitland, Maryland.

e. S-BAND REAL-TIME LINK

The S-band real-time link transmits the VHRR data to the local readout stations equipped for the reception and display of VHRR data.

The S-band real-time link characteristics are listed in Table I-6.

TABLE I-6. S-BAND REAL-TIME LINK CHARACTERISTICS

Characteristic	Parameter
Frequency	1697.5 MHz
Transmitter Power	5 watts, minimum
Spacecraft Antenna Gain (including losses)	1.2 dB min at ±55° from local vertical
Polarization of Transmission	right hand circular
Ground-Station Antenna Gain	32.0 dB (10-ft dish)
Received Carrier Power	-102.3 dBm (minimum)
RF Carrier Margin Above Threshold	1.2 dB (minimum)
Signal Modulation Characteristics	normal mode
Peak Deviation	300 kHz
Video Baseband	35 kHz
Subcarrier Bandwidth	140 kHz
Baseband S/N Ratio	45.6 dB p-p/rms

3. Local Ground Stations

a. GENERAL

Two different local ground stations will be in use for the recovery of real-time data from the ITOS D and E spacecraft. The displayed data are used locally for meteorological purposes. One station will be used for the SR data, while the other will be used for the VHRR data.

b. SPACECRAFT/APT GROUND-STATION INTERFACE

The spacecraft/APT ground station data link is used to transmit SR data from the spacecraft to local ground stations equipped for the reception and display of APT and SR data. The output of one of the spacecraft SR's amplitude-

modulates a 2.4-kHz subcarrier, which in turn frequency-modulates one of the redundant real-time transmitters. The transmitter output is coupled through a notch filter to a pair of half-wave dipoles mounted at the end of one of the solar panels.

The spacecraft elements of the APT ground station data link are the same elements included in the real-time link to the CDA stations. The ground receiver is also the same. The ground antenna, however, is unique to the field stations while the CDA stations use the beacon-receiving antenna to receive all real-time transmissions from the satellite. The APT ground station facsimile recorders have been modified to permit display of the SR signals (48 lines per minute).

c. SPACECRAFT/VHRR GROUND-STATION INTERFACE

The spacecraft/VHRR ground station data link is used to transmit VHRR data from the spacecraft to local ground stations equipped for the reception and display of VHRR data.

4. Orbit Characteristics

a. THE ITOS ORBIT

The ITOS spacecraft is launched from the Western Test Range (WTR), Vandenberg AFB, California, by a two-stage Delta launch vehicle. The nominal orbit is sun synchronous, * with an altitude of 790 nautical miles and an inclination of 101.7 degrees. Mission mode orientation of the spacecraft as well as its injection into orbit is accomplished by the launch vehicle. The final attitude of the spacecraft, in which the pitch axis is aligned with the positive orbit normal, is attained after injection by a programmed yaw maneuver of the second-stage launch vehicle. (See Figure I-3 for details of the spacecraft orientation during mission mode.) The launch time is selected by NESC, within the spacecraft design constraints, to best meet operational requirements. Nominal launch time is chosen such that the ascending node crossing** occurs at 1500 hours or the descending node crossing at 0900 hours, local mean time (LMT).

The initial orbit, which begins with the powered flight at launch and ends at the first ascending node crossing is designated Revolution 0000. Successive revolutions about the earth start at the ascending node crossing and are numbered

*In a sun-synchronous orbit, the orbital plane precesses about the earth's polar axis in the same direction and at the same average rate as the earth's annual revolution about the sun.

**The point at which the orbit track intersects the equatorial plane, as the spacecraft travels from south to north, shown in Figure I-9.

serially, Revolution 0001, 0002, 0003, etc. A day in the lifetime of the spacecraft is denoted by a Julian Day count, Julian Day 000 being launch day. Julian Day 001 begins at the following midnight, Greenwich Mean Time (GMT). Other orbital particulars are given in Table I-7.

The sun-synchronous orbit provides the least annual variation in spacecraft sun angle for mission mode operation. (The term "sun angle" is used here to designate the angle between the spacecraft pitch axis and the sun line.) In such an orbit, the annual fluctuations in spacecraft termperature, solar energy conversion, and duration of eclipse time are kept to a minimum. The orbit o'clock angle, which, among other things, determines the level of scene illumination encountered, is usually referred to as the "mean sun", * because of the variability in the apparent motion of the true sun; see Figure I-9 for geometric particulars. In essence, the o'clock angle of the orbit gives the local mean time (LMT) of the nodal crossing of reference. For example, a 1500-hour ascending node (AN) orbit (or what is commonly referred to as a 3 PM ascending node orbit) is a sun synchronous orbit for which the time of the ascending node crossing is 3 PM, LMT. The orbit o'clock angle may also be defined as the difference in right ascensions of the ascending node and sun.

TABLE I-7. PARTICULARS OF THE ITOS NOMINAL ORBIT

Parameter	Design Value
Altitude	790 nautical miles (circular)
Inclination	101.7 degrees
Anomalistic Period	115.2 minutes
Nodal Regression	Westward, 28.8 degrees in longitude/orbit
Time of Ascending Node	1500 LMT (approx)
Orbit Precession Rate	0.9857 degree per day (eastward)
Orbits per Day	12.5
Injection Coordinates (Geographic)	Latitude 0.71°S (nominal)
	Longitude 36.1°E (nominal)

*To afford a uniform reference, a fictitious sun, referred to as the "mean sun", was postulated. This "mean sun" moves eastward around the celestial equator at a perfectly uniform rate, completing its circuit in one year. The apparent motion of the true sun about the equator is not precisely uniform.

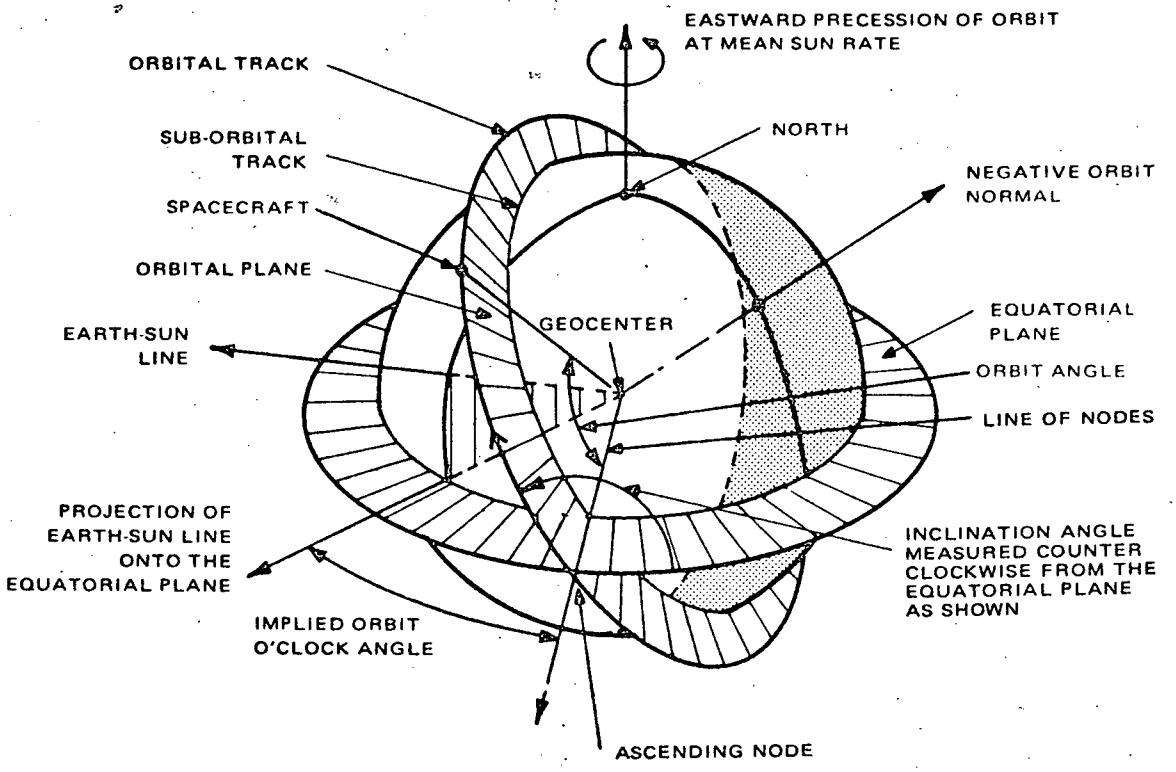

Figure I-9. Geometry of the Sun-Synchronous Orbit

Orbital precession is caused by the oblateness of the earth. The bulge of the earth's equator will cause the orbit plane to rotate at a fixed rate with respect to inertial space. For a circular orbit, the precession rate depends on altitude and inclination. The line of nodes moves westward if the orbital inclination is less than 90 degrees and eastward if it is more than 90 degrees, regardless of the altitude.

For a given altitude, the desired rate of orbital precession is obtained by the proper choice of orbital inclination angle. For the nominal altitude of 790 nautical miles of the ITOS spacecraft, an orbit inclination angle of 101.7 degrees is required for sun synchronism. For these conditions, the orbit plane rotates in an easterly direction at a rate of 360/365.24 or 0.9857 degree per day, which is the value required to maintain a constant angle between the orbit plane and the mean sun (i.e., that necessary to offset the average angular motion of the earth in orbiting the sun). In geographic coordinates, this corresponds to a westward drift in longitude at about 0.25 degree per minute, which causes successive ascending nodal crossings to occur some 28.8 degrees farther westward.

b. OPERATIONAL EFFECTS OF ORBIT CHARACTERISTICS

As has been indicated, the sun-synchronous orbit has the property of maintaining a nearly constant orientation with respect to the earth-sun line,

thereby preventing large fluctuations in the solar-radiation-dependent phenomena, such as picture illumination and solar array power. However, even for an orbit strictly synchronous with the mean sun, orbital and seasonal variations in these properties occur that influence the operation of the spacecraft.

(1) SPACECRAFT SUN ANGLE AND ECLIPSE TIME

Unlike scene illumination angle, which exhibits an orbital as well as a seasonal variation, the sun angle of the spacecraft shows only a seasonal variation. This is indicated in Figure I-10, which also shows the effect of orbit o'clock angle. It can be seen that, for afternoon ascending node (AN) orbits, the earlier the local mean time of the AN, the higher the sun angle for a given date.

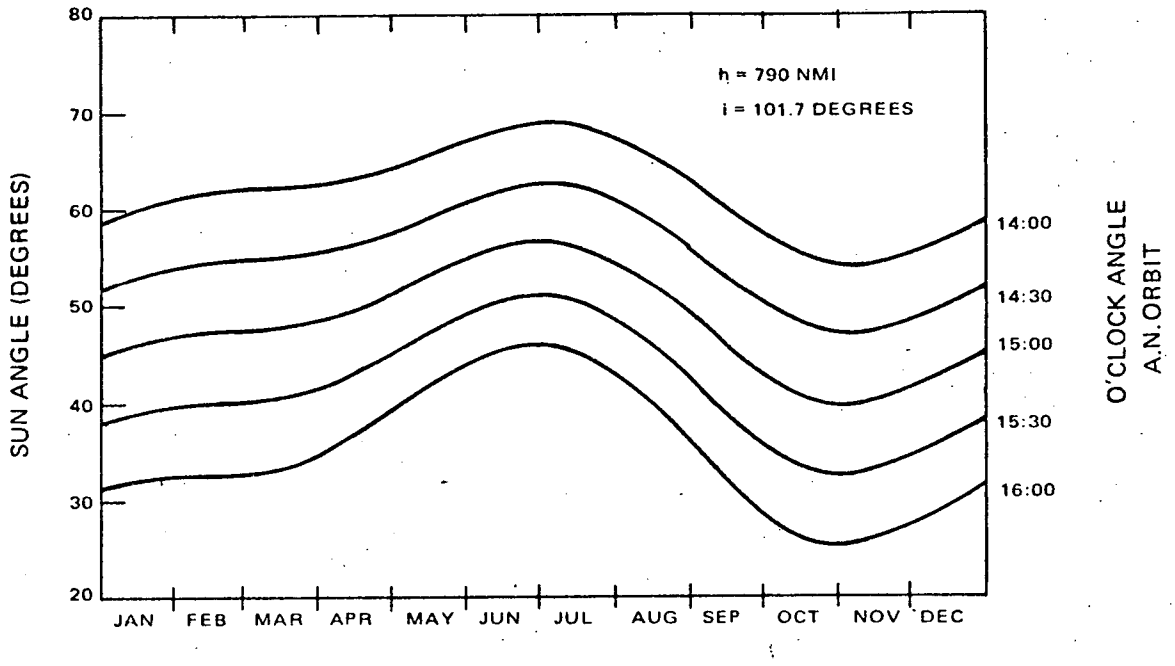

Figure I-10. Seasonal Variation of Spacecraft Sun Angle for Afternoon AN Orbits

The percent of time the spacecraft spends in the sun on each orbit also varies with calendar date orbit o'clock angle. Figure I-11 shows that for those orbits in which the ascending node occurs earlier than 1522 LMT, the spacecraft will not experience 100-percent sun time at any time during the course of a year. The mission mode constraint on sun angle (30 to 60 degrees) and the date selected for launch set the time of launch and the duration of the launch window.

(2) EFFECT OF DATE AND TIME OF LAUNCH

In addition to matching orbit inclination angle to altitude in order to achieve sun synchronism, it is necessary to select the proper launch time to obtain the desired orbit o'clock angle. The launch time for a particular orbit fixed to the mean sun will always fall at the same hour, regardless of calendar date. However, the date of launch will determine where in the cyclic variation of sun angle the spacecraft will find itself at the beginning of mission mode. For the sun synchronous orbit under discussion, an early July launch will result in a mission mode sun angle of 57 degrees, whereas for an early November launch, the sun angle will be only 39 degrees at the outset (see Figure I-10).

(3) EFFECTS OF INJECTION ERRORS

In general, there are two types of injection errors that affect mission operation. These are errors in orbital inclination and in spacecraft altitude, each of which affects sun synchronism. The individual effects may be separately evaluated and algebraically combined to determine the overall departure from the synchronous condition.

The effects on the nodal drift rate of variations in inclination and altitude are shown in Figures I-12 and I-13, respectively. The drift rates given are departures from the synchronous rate for the stated nominal values. Also listed are the 1 σ tolerances on the respective errors.

A number of different quantities change with injection errors. Orbital period, which is important in unipolar torquing cycles, depends upon spacecraft altitude. The value of the orbital period can be obtained either from the orbital elements or from nodal crossings printed in the (spacecraft) ephemeris. An altitude error will also give rise to an angular offset in pitch attitude as shown in Figure I-14. This offset is also influenced by departures of the earth radiance level and system temperature from nominal values. The combined effect of the two error sources for the operating region defined by the tolerance extremes is shown in Figure I-14.

Orbital altitude and inclination, by controlling nodal drift, affect sun angle history. Figure I-15 shows the effect on sun angle history over a calendar year of an asynchronous nodal drift rate of 0.02 degree per day. Also shown is the effect of a 20-minute launch window, which has been centered about the launch time of a 1500 AN orbit. It can be seen that an extended launch window and an asynchronous nodal drift may combine to cause the sun angle to diverge beyond the mission extremes of 30 and 60 degrees.

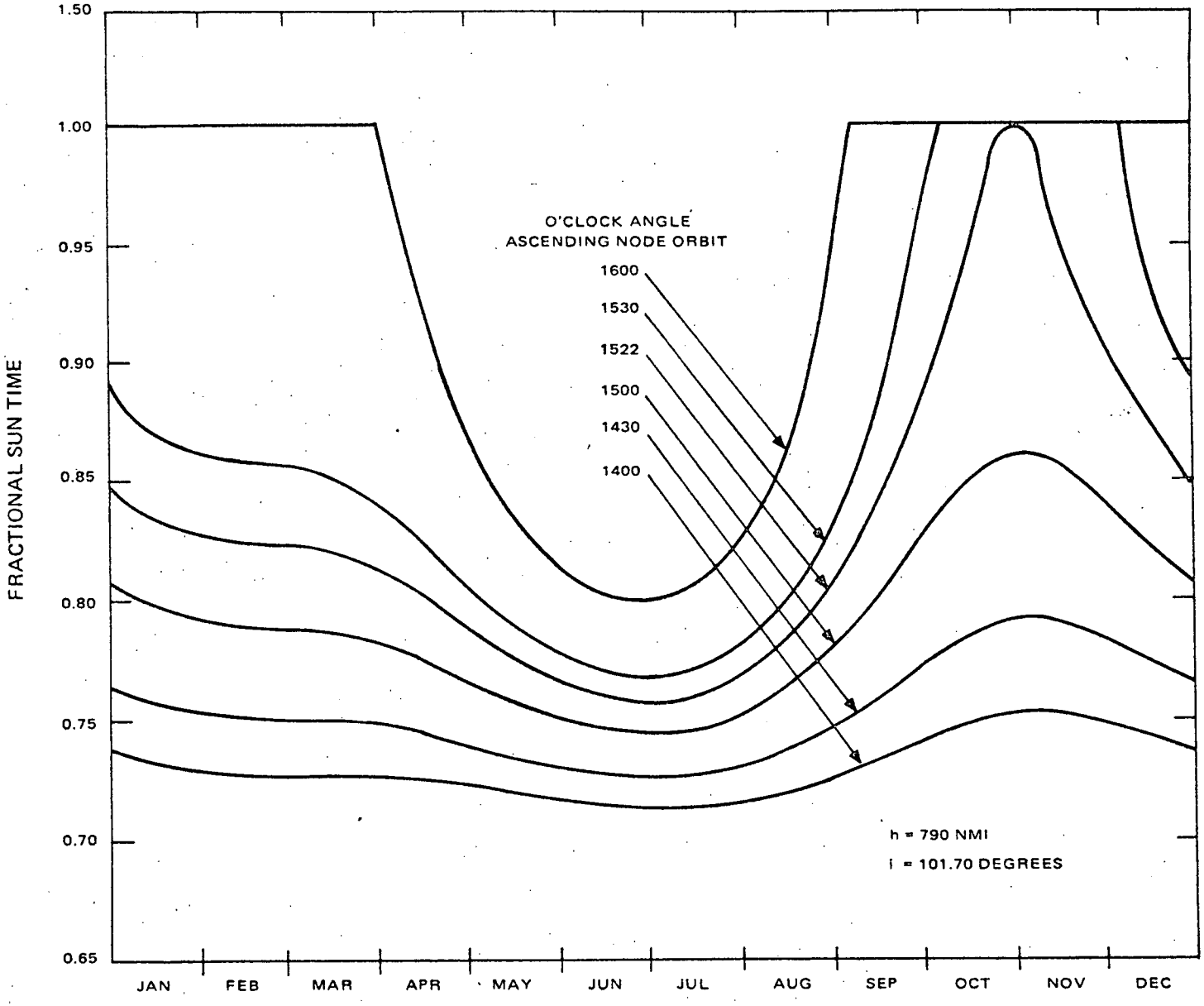

Figure I-11. ITOS Spacecraft Time in Sunlight

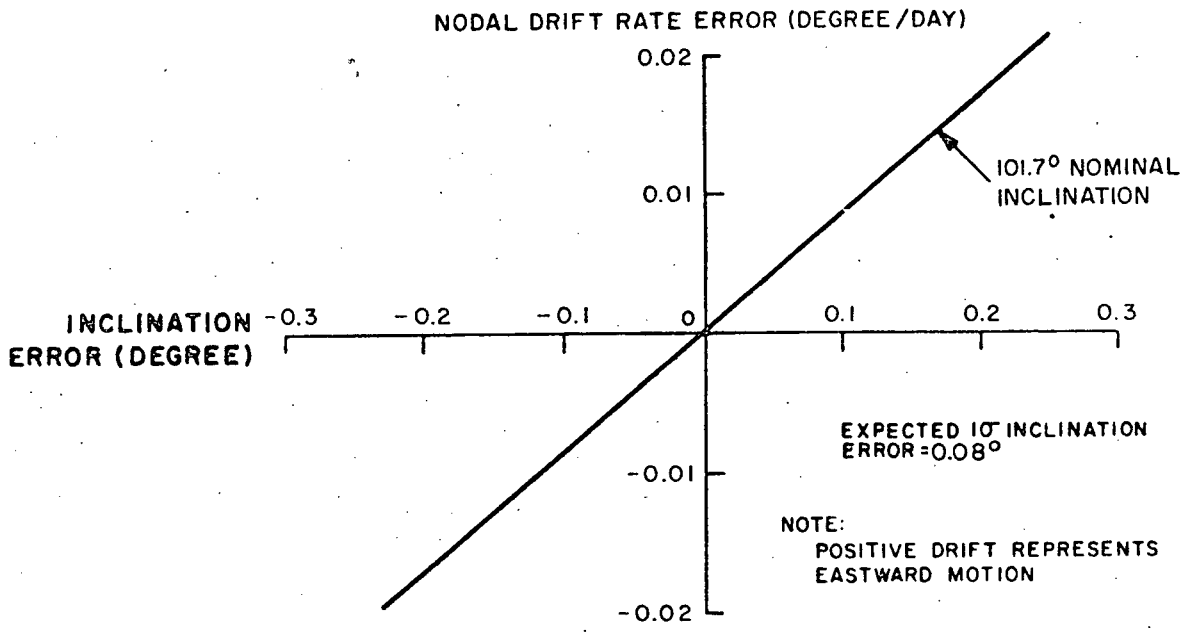

Figure I-12. Nodal Drift Rate Error vs Inclination Error

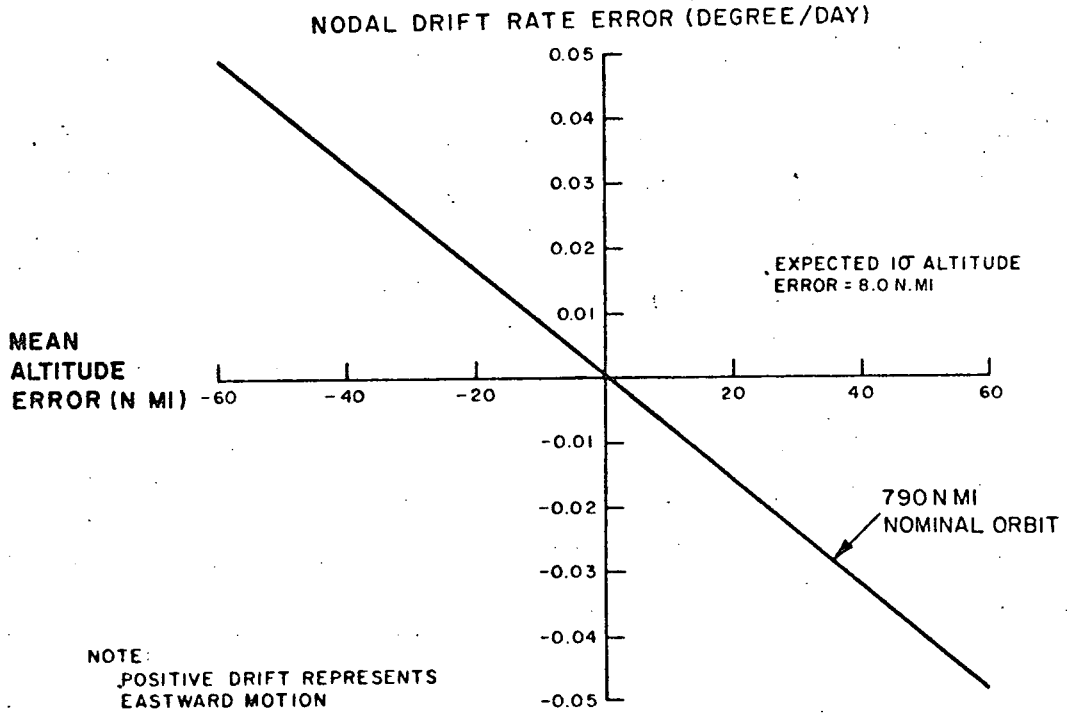

Figure I-13. Nodal Drift Rate Error vs Mean Altitude Error

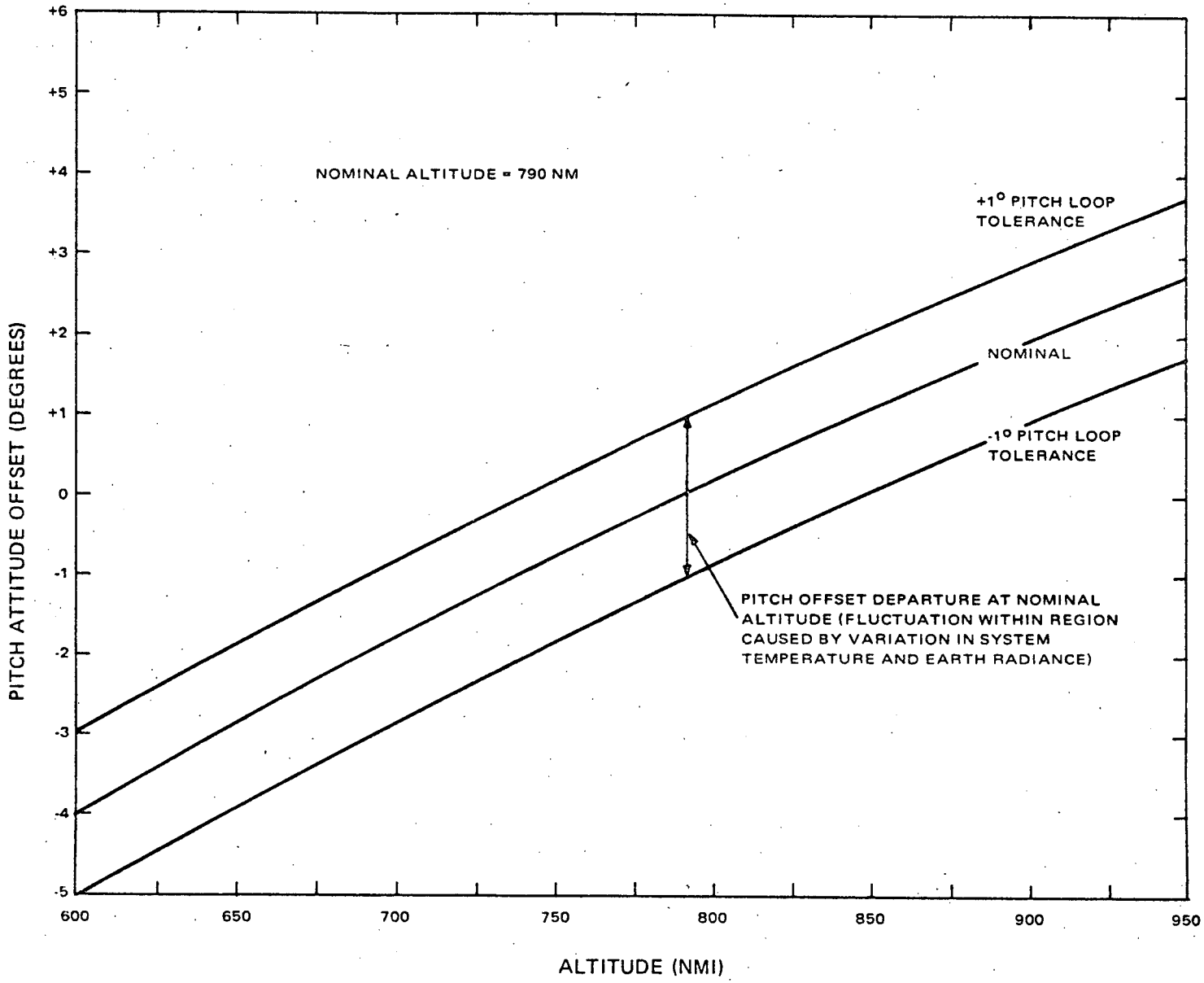

Figure I-14. Spacecraft Pitch Attitude Offset vs Altitude

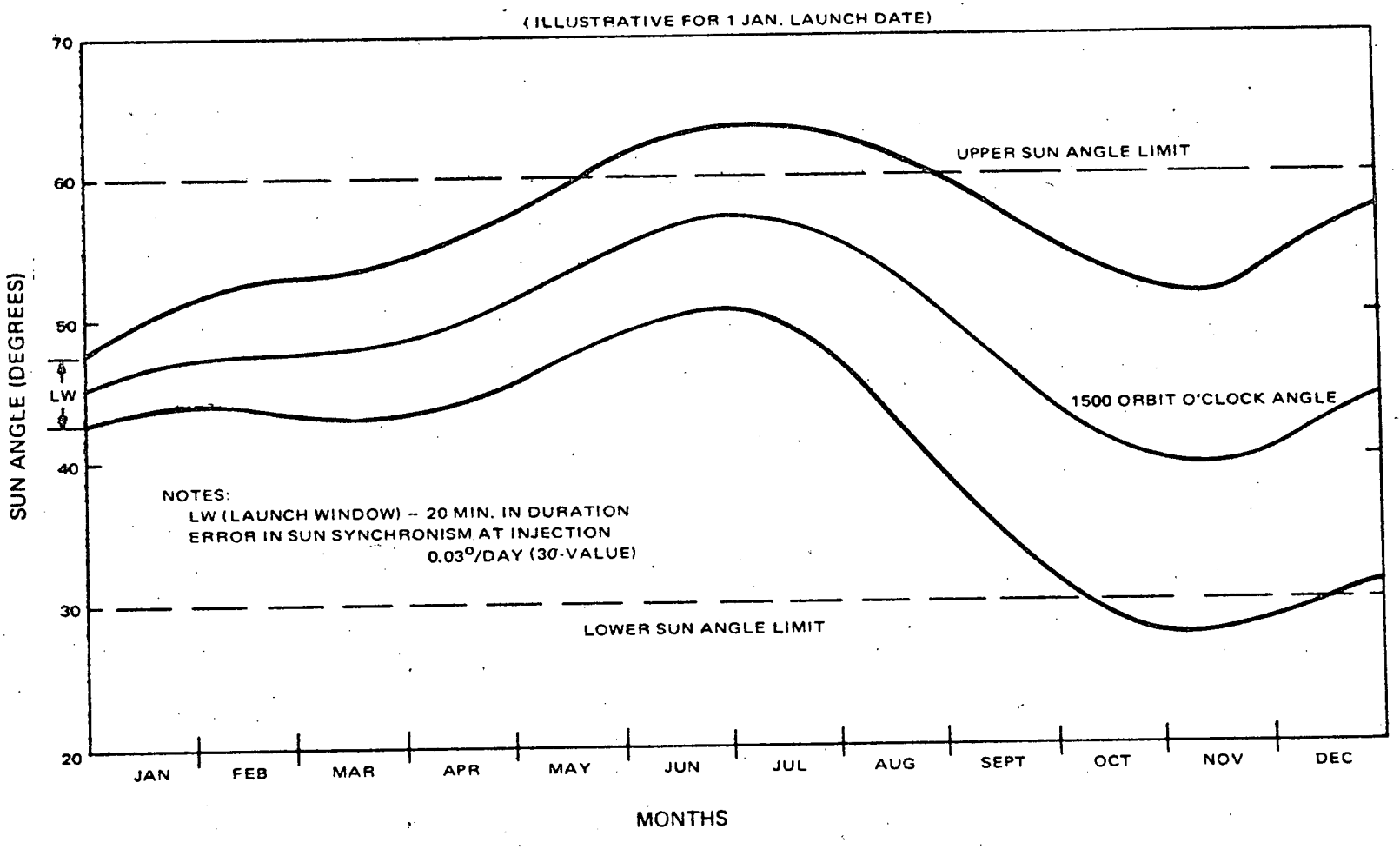

Figure I-15. Effect of Launch Window and Injection Error on Mission Mode Sun Angle (Worst Case)

5. Sensor Coverage

a. SR RADIOMETRY

(1) GENERAL

The SR will provide earth-cloud-cover data in the 10.5 to 12.5 micron spectral region during the entire orbit. The visible channel (0.52 to 0.73 microns) senses cloud cover during the daylight portion of the orbit. The radiometer will be calibrated to operate over a range of scene temperatures from 180 to 315°K. A typical transfer function of the IR channel is given in Figure I-16.

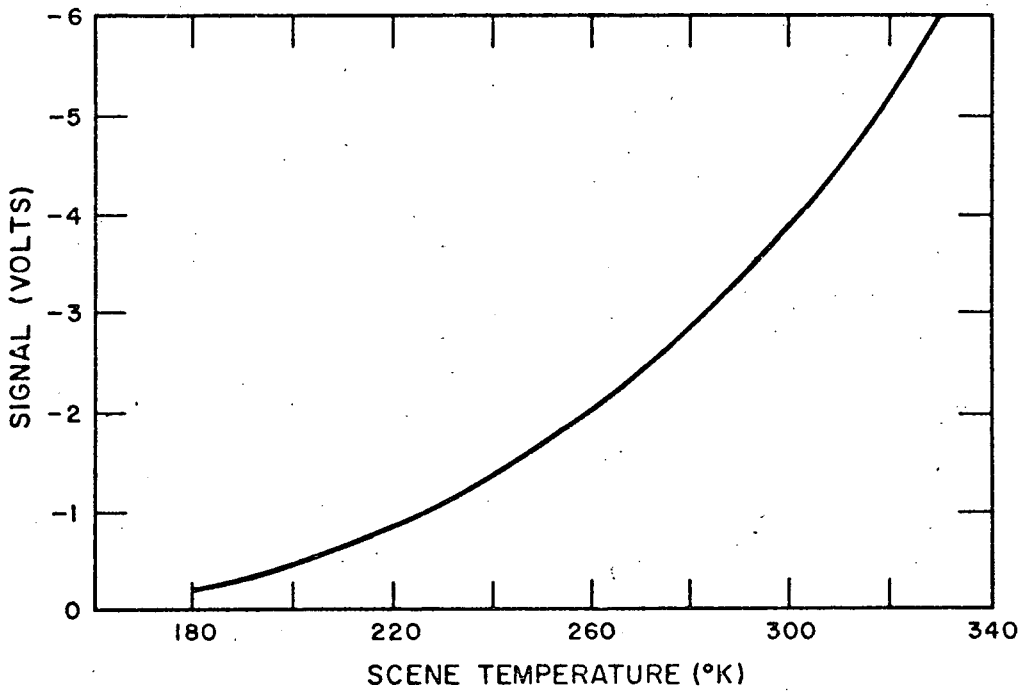

Figure I-16. Typical SR Transfer Function

(2) SPECTRAL RESPONSE

The spectral response of the radiometer IR channel (10.5 to 12.5 microns) was selected because atmospheric conditions allow high transmission of surface radiance with a very low level of reflected solar radiation to contaminate it.

The visible channel spectral region (0.52 to 0.75 microns) closely approximates the region used successfully by the cameras on TIROS and TOS spacecraft.

(3) RESOLUTION

The ability of a scanning mechanism to resolve details is limited by the effective beam width (5.3 milliradians) and the relationship of the scanned surface and the beam. When the beam of the radiometer is at local vertical (perpendicular to the scanned surface), the effective beam cross section sensed on the ground is square and the resolution (4.1 nmi in the IR channel) is optimum. As the displacement of the beam from local vertical increases, the effective beam cross section becomes elongated, and resolution decreases.

The resolution in the direction of spacecraft travel is optimized when the area sensed on the ground is equal to the forward motion across the ground which occurs during one scan period. The 48-rpm scan rate of the SR gives a close to optimum relation between scan rate and field of view of the IR channel.

The 2.8 milliradians field of view of the visible channel is selected to give optimum resolution for data collection at 45° off each side of the nadir. This results in about 50 percent under scan at the subsatellite point.

(4) SR IMAGE CHARACTERISTIC

Since the SR is a line scan device, the pictorial display has different aspect characteristics along the direction of scan in comparison to the direction of spacecraft motion.

The forward motion of the spacecraft produces an undistorted image in the direction of travel as shown by the 5-degree pattern of horizontal lines in Figure I-17. The sidewise scan shows marked foreshortening close to the horizon. Furthermore, the constant angular scan rate reduces the effective expanse time of each element.

The seven vertical lines on the left are the real time sync signal which is present in both real time and remote global data. Space is shown on each side of the earth scan.

The earth scan is gridded with a pattern of lines spaced 5-degree geocentric arc lengths apart. The pattern is for a 790-nautical mile orbit. The orbital period was taken as exactly 115 minutes. The horizon will be at 35° 24' geocentric arc length from the subsatellite point.

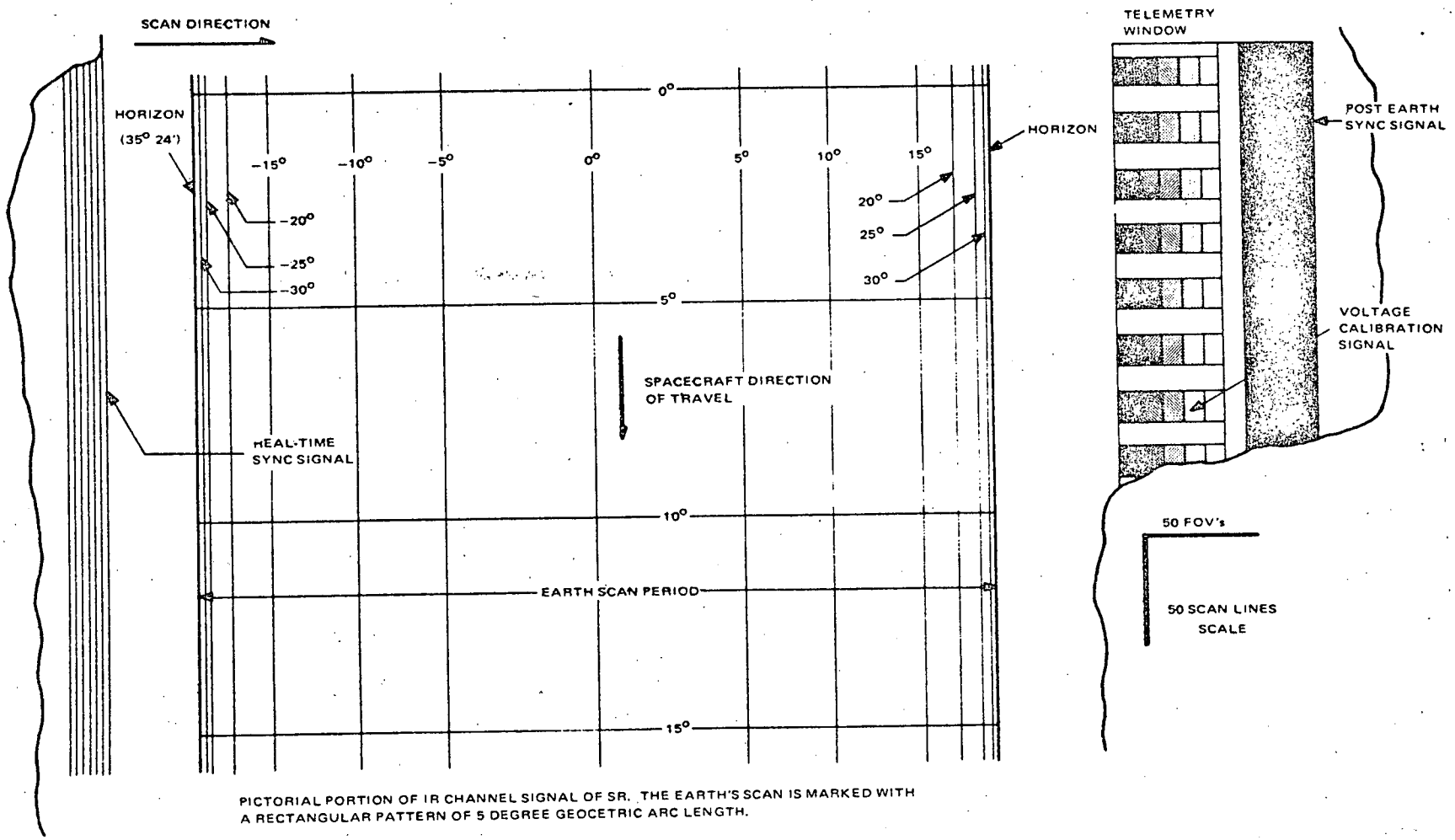

PICTORIAL PORTION OF IR CHANNEL SIGNAL OF SR. THE EARTH'S SCAN IS MARKED WITH A RECTANGULAR PATTERN OF 5 DEGREE GEOCETRIC ARC LENGTH.

Figure I-17. SR Image Characteristics

The telemetry window is shown on the right. The voltage calibration signal is repeated on 14 successive scans to produce a "control patch" for adjusting the gain of local readout equipment.

The post-earth sync signal is to the extreme right. This signal is used as sync for data played back from the spacecraft tape recorder.

The aspect ratio of the display is controlled by the user selection of the relationship between the vertical and horizontal display expansion. Figure I-17 was calculated assuming that instantaneous field of view (FOV) equals the distance between scans (i.e., distance equal to 50 resolution elements (FOV) was set equal to the distance of 50 scan lines).

b. VHRR RADIOMETRY

(1) GENERAL

The VHRR will provide high resolution earth-cloud-cover data to the real time user. The radiometer senses in two spectral regions 0.6 to 0.7 micron and 10.5 to 12.5 microns. One selected portion, of about 9 minutes duration, may be recorded remotely for subsequent readout by the CDA station.

The local user will obtain VHRR visible channel data once a day and infrared data twice daily.

(2) RESOLUTION

The ability of the scanning mechanism to resolve ground details is limited by the effective beam width (0.6 milliradian) and the relationship of the scanned surface and the beam. When the beam of the radiometer is at local vertical (perpendicular to the scanned surface), the effective area sensed on the ground is 0.47 nmi^2.

In addition, the resolution in the direction of spacecraft travel is optimized when the area sensed on the ground is equal to the forward motion across the ground which occurs during one scan period. The 400-rpm scan rate of the VHRR yields a close to optimum relation between scan rate and beam width (field of view) of both channels.

(3) SPECTRAL RESPONSE

The spectral response of the radiometer's IR channel (10.5 to 12.5 microns) was selected because atmospheric conditions allow high transmission of the surface radiance with a very low level of reflected solar radiation to contaminate it.

The visible channel spectral response (0.6 to 0.7 micron) is selected towards the red end of the visible spectrum to increase the contrast between earth surface and clouds by reducing the effect of haze.

(4) VHRR IMAGE CHARACTERISTIC

The line scan image construction of the VHRR produces different aspect characteristics along the direction of scan as compared to the characteristics in the direction of spacecraft motion. The forward motion of the spacecraft produces an undistorted reproduction of the scene as shown by the pattern of horizontal lines in Figure I-18. The distortion in the scan direction is caused by both the constant angular rotation rate of the scan mirror and the foreshortening caused by the earth curvature.

To the left, the precursor signal precedes the black to white transition which provides the line synchronization. The sampled data from the 300°K and 240°K targets are introduced into part of the space scan area.

The earth has a 5-degree geocentric pattern superimposed to illustrate the differences in aspect ratios caused by the line scan sensor system.

Two subsync markers are generated by the radiometer during the earth scan portion of the display.

To the right of the earth scan is the voltage calibration signal. The increasing amplitude of the signal produces bars which start with a full black and shade off to a pure white.

A post-earth sync pulse (full black then switching to pure white) is used as sync for data played back from the spacecraft tape recorder.

The 180° mark shows where the sync pulse for the visible channel portion of the scan would occur. In the normal mode of operation, this visible channel will be interleaved with the IR data. It may be identified by the tone of the precursor.

c. VTPR RADIOMETRY

(1) GENERAL

The VTPR will provide sounding of the temperature profile from the surface of the earth to about 100,000 feet. The temperature sounding is made in the 15-micron Q branch region of the carbon dioxide spectrum.

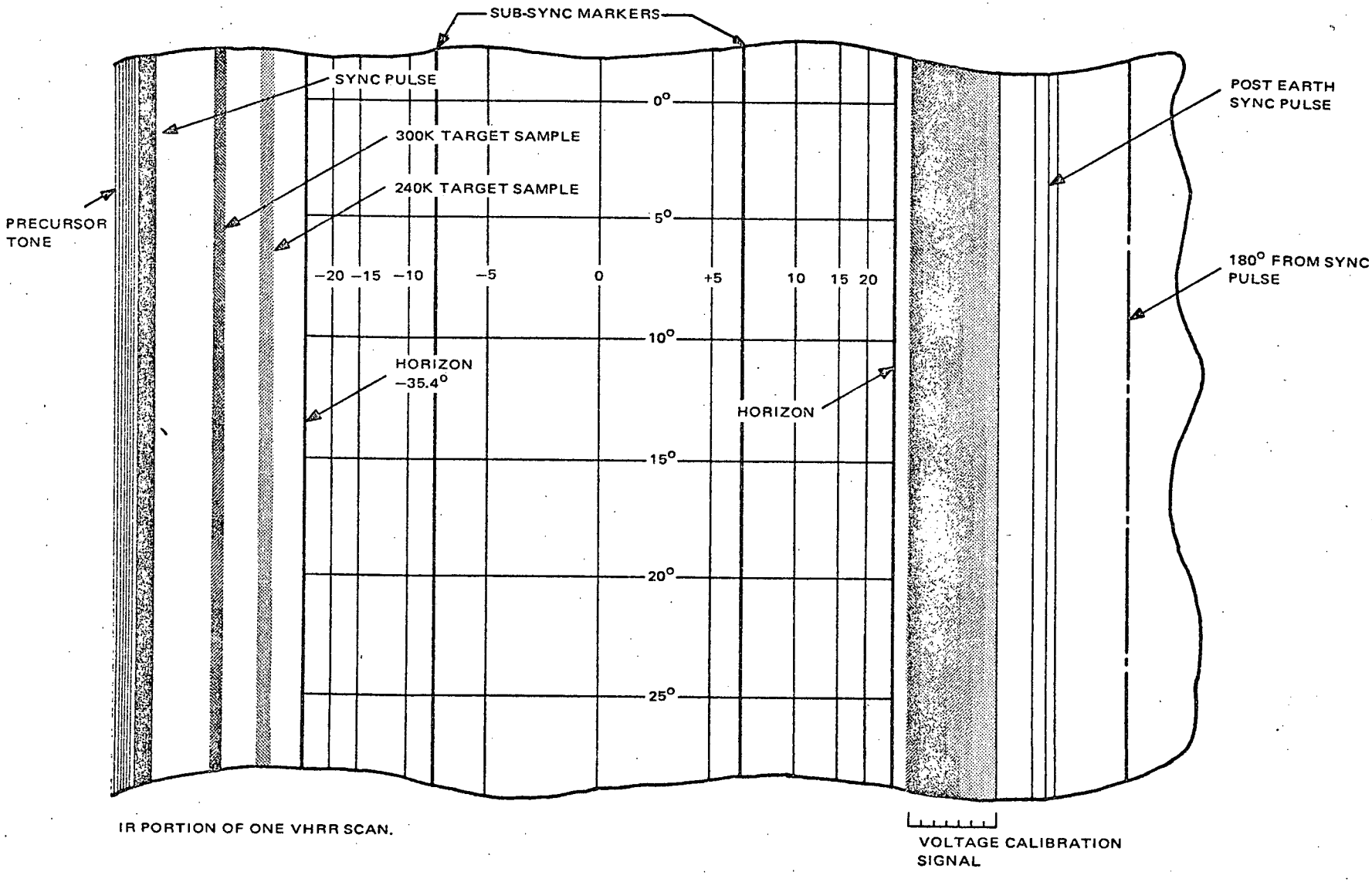

Figure I-18. VHRR Image Characteristics

The soundings are made over every part of the earth at least twice daily. The data is only available to the remote user.

(2) SPECTRAL CONSIDERATIONS

The VTPR senses the radiance from carbon dioxide gas in six narrow spectral regions centered at 668.5, 677, 695, 708, 725, and 747 cm^{-1}. The surface radiance is measured in a window (low atmospheric absorption) located at 835 cm^{-1}. A gross water content measurement is made at 535 cm^{-1}. This latter measurement is used to correct the effect of water vapor on the carbon dioxide radiance measurement.

(3) ANGULAR RESOLUTION

The angular resolution of the VTPR defines the ground area sensed. The eight successively sampled spectral regions must view the same ground area to an accuracy of one percent. The overlays of sampled area, either adjacent in scan or along the spacecraft track contain less than 5 percent redundant information.

The ground area covered by one sample is approximately 30 by 30 nautical miles.

(4) VTPR IMAGE CHARACTERISTICS

With the 2° 38' field of view of the radiometer, the VTPR sampled areas from one scan line to the next underlap 7-1/4 percent at the subsatellite point. As the instrument scans off to either side, the underlap decreases and becomes zero at 24.5° nadir angle. From this scan angle, the overlap increases rapidly, giving about 11 percent overlap at 30 degrees from the nadir. Thirty degrees is the center of the FOV for the maximum cross-track scan angle.

The percent of overlap from adjacent samples along the scan is normally zero at the one-percent response points. This percentage does not increase as the angle from nadir increases, because it is controlled by the mechanical scanning mechanism.

The swath sampled by scanning is approximately a 15-degree great circle in total width.

d. SPM RADIOMETRY

(1) GENERAL

The SPM is designed to measure the protons and high-energy electron flux at the spacecraft altitude. The SPM data is recorded on board the spacecraft for transmission to the CDA stations. When other functions do not require the beacon transmission link, the SPM will be transmitted to real-time users.

(2) SENSORS

Six sensors are used in the SPM subsystem. Sensors 1, 2, and 3 are omnidirectional units which detect protons with energies above 60, 30, and 10 MeV, respectively. Sensor 4 measures electrons with energy between 100 and 750 keV. Sensors 5 and 6 detect protons coming from a preferred direction with energy levels from 0.27 to 60 MeV.

6. ITOS Ground Complex

a. GENERAL

The ITOS system operations are monitored and controlled by a ground complex comprising three major groups of facilities:

- Command, programming, and analysis centers,
- Command and data acquisition (CDA) stations, and
- Spacecraft checkout facilities.

In addition to the above, the ITOS system utilizes the facilities of the NASA Space Tracking and Data Acquisition Network (STADAN). APT field stations throughout the world also participate in the program as SR data users. Local read out stations will also be developed to utilize the real time VHRR data.

b. COMMAND, PROGRAMMING, AND ANALYSIS CENTERS

The command, programming, and analysis centers comprise three facilities; the name, location, and primary functions of each are given below:

(1) TOS Evaluation Center and TOS Checkout Center (TEC/TCC), Goddard Space Flight Center (GSFC), Greenbelt, Maryland. TEC/TCC functions as the control center for all operations concerned

with the prelaunch checkout and launch operations of new or replacement spacecraft, and for operations of the spacecraft during the in-orbit checkout performed following the launch.

(2) TOS Operation Center (TOC), National Environmental Satellite Center (NESC), Suitland, Maryland. TOC is the control center for the ITOS system, and is responsible for overall system operations. It receives requests for weather data from NESC and formulates programs of commands for the satellite instrumentation, which are teletyped to the CDA stations and transmitted from the CDA stations to the satellite. TOC monitors all significant CDA events and provides instructions pertaining to courses of action to be taken by CDA personnel. The facility receives, in real time, all engineering data, including attitude information, telemetered from the satellite to the CDA station via the beacon link, evaluates this data, and, where applicable, formulates corrective command programs for transmission to the satellite(s).

(3) Data Processing and Analysis Facility (DAPAF), NESC, Suitland, Maryland. DAPAF is the installation that processes satellite meteorological data for presentation to the requesting agencies. VHRR, SR, VTPR, and SPM information received at the CDA stations are transmitted to DAPAF where computer equipment is used to locate, format, and digitize the input data, and produce scale-rectified maps and other summaries of meteorological data. DAPAF processes telemetered data in support of TEC/TCC and TOC. (Real-time SR data is processed by the modified APT ground stations.)

c. COMMAND AND DATA ACQUISITION (CDA) STATIONS

The CDA stations are located at Gilmore Creek, Alaska, and Wallops Island, Virginia. The CDA stations and the command, programming, and analysis centers are interconnected by a microwave communications system, which has characteristics to which the required data was tailored.

Each of the two CDA stations functions primarily as a relay station between TOC and the satellites. The CDA stations receive the command programs teletyped from TOC. When the satellite comes within communications range on the revolution specified in the program, these stations transmit the commands in the form of FSK audio-frequency tones modulating an RF command carrier frequency. In all operations, the stations receive and record on magnetic tape the video and telemetered data transmitted by the satellite, relaying the telemetered data in real time (i.e., as it is received at the station) to TOC for evaluation. The recorded data are played back after the satellite pass and transmitted to DAPAF over the communications network for processing by that facility.

d. SPACECRAFT CHECKOUT FACILITIES

The spacecraft checkout facilities include three complete sets of ground equipment suitable for performing a full functional checkout of the spacecraft, as well as test equipment required during fabrication and assembly of the spacecraft.

Two of these sets of ground equipment are the factory sets located at RCA Astro-Electronics Division, Princeton, New Jersey, while the third set is installed in a transportable air-conditioned van, for use at the factory or at the launch site, as required for the prelaunch checkout of the spacecraft.

In addition to the facilities included in the CDA stations, each checkout facility includes equipment for RF signal handling (i.e. for the conversion of the signals transmitted from the spacecraft into the appropriate frequency bands at the proper interface signal levels and for the transmission of command data to the spacecraft) for simulating the operation of the DAF station for display of both direct and recorded radiometric information and for processing and displaying digital data.

e. SCOPE OF GROUND EQUIPMENT COVERAGE

Much of the ground equipment that is used for the ITOS system was installed as part of the TOS ground complex. A brief description of the ITOS ground complex equipment is presented in Section II of this report. Further information concerning that equipment is presented in the Instruction and Operating Handbook for the ITOS and TOS ground equipment, Volumes 1 through 5, prepared for the Environmental Science Services Administration under NASA contracts No. 5-10306 and No. 5-9034, dated April 3, 1969, revised December 3, 1969.

C. SYSTEM OPERATION

1. ITOS Mission Profile

The ITOS mission is divided into four phases, the last of which is the mission mode operational phase, in which the satellite performs its normal primary and secondary sensing functions. Preceding the operational phase are the launch sequence phase, the acquisition phase which under expected conditions, encompasses the first five orbits and the spacecraft system checkout phase. These three phases are depicted in Figure I-19.

The prime objective of the launch and acquisition phases is to orient the spacecraft in mission mode attitude. When mission mode attitude has been achieved, the following conditions exist.

- Solar panels are deployed,
- Momentum vector is aligned to within ±1 degree of the positive orbit normal,
- Nutation halfcone angle is less than 0.3 degree,
- Momentum wheel is spinning at a rate of 150 ±2 rpm, and
- Pitch control subsystem is operating in the closed loop mode, and the pitch attitude is within ±1 degree of the earth reference peculiar to its altitude (i.e., local vertical if the spacecraft is at nominal altitude.)

A programmed series of launch vehicle and spacecraft events occurs in the interval between lift-off and the achievement of mission mode attitude. The launch vehicle, a Delta booster, besides providing the thrust necessary to achieve the desired orbit, orients the spacecraft into an approximate mission mode attitude by the execution of a 90-degree yaw maneuver; it also imparts to the spacecraft the required angular momentum by means of a programmed spinup.

The objective of the programmed operations following the separation event is to establish the spacecraft in earth-lock, with the solar panels deployed, by the time of completion of the CDA contact on revolution 0005. Certain conditions may make it necessary to use alternate operational sequences to achieve this same end. Some of these alternatives require that the lock-on attempt be delayed until a CDA contact later than that of revolution 0005. The constraints requiring alternative commanding operations are related to "moon conflicts" with proper operation of the pitch loop during the period of establishing lock-on and to variations from nominal performance of the second stage launch vehicle in the performance of spinup, resulting in variations from desired system momentum values. Constraints in both of the categories cited

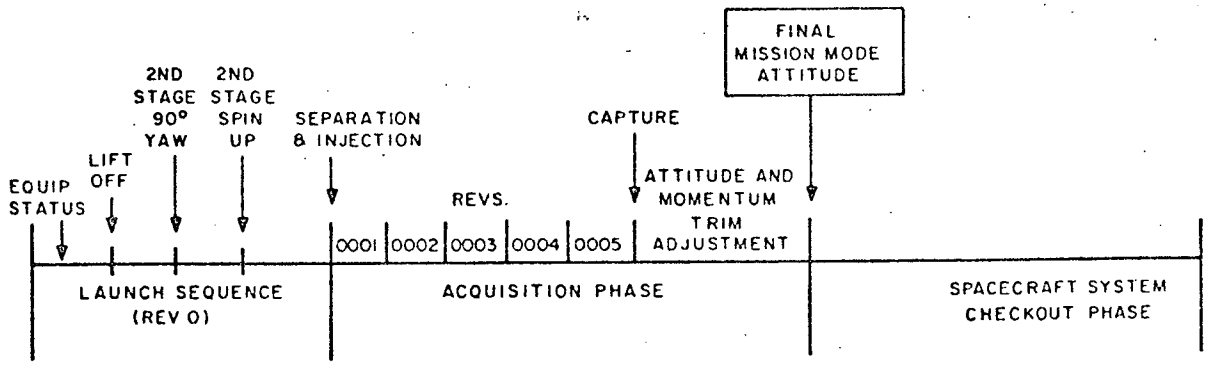

Figure I-19. Launch to Mission Mode Events

can be foreseen, and the required alternative operations predicted, prior to the time of their execution.

The sequences of events and the changes in spacecraft status that are undergone from lift-off to earth lock-on are listed below.

- Establishment of equipment launch status,
- Lift off
- First stage separation
- First burn of second stage
- Second stage programmed pitch maneuver
- Second stage coast
- Burn No. 2 cutoff of second stage, (i.e., orbital rejection)
- 90-degree yaw maneuver,
- Spinup to desired roll rate,
- Separation event:

  power applied to pitch loop motor,

  momentum wheel accelerated to nominal rate,

  spacecraft module decelerated to appropriate body rate,

  telemetered accelerometer data removed and replaced by spacecraft roll data, and sun-angle data.

Subsequent spacecraft operations are initiated by ground command and are directed toward trimming the attitude, deploying the solar array panels, and achieving earth lock via the pitch control system. Operations are based on a 3 PM ascending node orbit with the ascending node of the first revolution located at approximately 35 degrees East longitude. While a satisfactory power and thermal condition exists with the spacecraft in this post separation orientation, since the three solar panels are still folded back along the sides of the spacecraft body, a reduced amount of power is available for the spacecraft. It is, therefore, desirable to achieve the mission mode orientation as soon as possible. Revolution 0005 is the "target" revolution for this operation, because it provides for "long" contacts at both the Wallops Island and the Gilmore Creek CDA ground stations and is preceded by a sufficient number of revolutions during which the attitude trimming operations can be performed.

Following the achievement of the mission mode attitude, the spacecraft is subjected to a performance verification program, referred to as the "system checkout phase". The purpose of this program is to establish that all of the spacecraft equipment has satisfactorily survived the launch and that the spacecraft is capable of satisfying the mission objectives. During this phase, the functional performance of the equipment is evaluated by checking operating parameters. Once satisfactory operation of a unit of equipment has been verified, it is not exercised further until all spacecraft equipments have been similarly checked out.

The mission of the spacecraft is such that simultaneous operation of the various data-gathering and control equipment is required. The end objective of the system checkout phase is to demonstrate that the basic operational combinations of the spacecraft equipment perform together in a satisfactory manner.

The first equipment to be checked is that which monitors the status of the telemetry, command, power, and stabilization equipment and permits subsequent parameter measurements. The secondary and primary data systems are next checked individually to verify satisfactory operation. Next, the equipment combinations are selected. To ensure that spacecraft operation will meet the mission requirements with the combinations of redundant equipment, several of these operational combinations are exercised in parallel during the operational mode checkout.

When spacecraft system checkout has been completed, demonstrating the operational capability of the spacecraft, mission mode operations may begin. These operations are performed on a routine basis subsequent to the attainment of mission mode attitude and are continued throughout the operational life of the satellite.

Mission mode operations include the programming of the primary data sensors, attitude control operations, power supply monitoring, telemetry processing, SPM processing, and the exercising of redundant satellite equipment.

2. VHRR, SR and VTPR Radiometers, and QOMAC Programming

a. GENERAL

The programming of the radiometers is independent of QOMAC programming. QOMAC is used to control the attitude of the spacecraft. QOMAC programming will be operated in a full quarter-orbit mode during the initial orientation maneuver, and for large attitude changes. A unipolar torquing mode will be programmed operationally to compensate for smaller attitude deviations resulting from disturbances such as solar pressure.

b. RADIOMETER PROGRAMMING

One SR, one VTPR, and both VHRR's will normally be on throughout the orbit. As such, all radiometer programming will be by ground command. The SR and VHRR real-time outputs can be programmed to be inhibited for N of 8 segments of an orbit, either independently or together. The spacecraft programmer, when loaded by a ground command, will automatically control the inhibition. Orbital SR data is recorded despite the inhibition.

c. QOMAC PROGRAMMING

The QOMAC units are programmed to control the magnitude and polarity of the current to the QOMAC coil. During the initial orientation maneuver, the coil is energized for the whole orbit, with the coil current polarity switched at quarter-orbit intervals as determined by the programmer. To increase the rate of precession of the spin axis to 10 degrees per orbit, the magnetic bias coil is utilized in parallel with the QOMAC coil.

In mission mode, a maximum precession rate of 1.1 degrees per orbit can be realized with QOMAC torquing. Lesser rates can be obtained by programming a fractional duty cycle for the coil current. Polarity switching still takes place at quarter-orbit intervals. The duration of the "quarter-orbit pulses" can be programmed up to 11 minutes, in 16-second increments.

The orbital phasing of the current pulses can be adjusted by programming a time delay which retards the initiation of the "quarter-orbit" sequencing. The start can be delayed up to one-half orbit from the time the QOMAC portion of the programmer is loaded by ground command. Quarter-orbit timing can be adjusted to a value consistent with the actual orbit achieved by ground programming.

d. SR RECORDER PROGRAMMING

Any two of the three SRR's can be selected for use. Any one of the two selected SRR's can be directed to record first. The other selected recorder is put into the record mode at the following times: (1) the recorder in the record mode is put into the playback mode, or (2) the first recorder reaches the end of tape in the record direction.

3. CDA Station Contact Time

The approximate contact times of the Alaska and Wallops Island CDA stations with the satellite are shown in Figures I-20 and I-21. Figure I-20 shows the contact in minutes after the ascending node as a function of the longitude of the ascending node. The contact begins and ends 5 degrees above the horizon at the Wallops Island station and 5 degrees above the terrain at the Alaska station. The position of the terminator at the winter and summer solstices is also indicated. Figure I-21 is a plot of net contact time as a function of the longitude of the ascending node.

A ground station contact time of 12 minutes has been established as the minimum time required to perform satellite acquisition, playback-command transmission, and SR-data playback (9 minutes is required for data playback and 3 minutes for ground commands and telemetry.)

For ascending-node longitudes in the 160-degrees West to 136 degrees East range, neither the Wallops Island nor the Gilmor Creek CDA station will be in contact with the satellite for the specified minimum time. Since the nodal regression between consecutive ITOS orbits amounts to 28.8 degrees of longitude, the situation of two successive revolutions with marginal ground station contact will, in time, occur. Normally, one revolution with ground station contact less than the assumed minimum will occur every 12 to 13 revolutions. When this "blind orbit" condition exists, data playback will be performed during the next revolution when adequate ground station contact time is available.

4. Effect of Date and Time of Launch

In addition to matching orbit inclination and altitude in order to achieve sun synchronism, it is necessary to select the proper launch time to obtain the desired orbit o'clock angle. The launch time for a particular orbit in synchronism with the mean sun will always fall at the same hour regardless of calendar date. However, the date of launch will determine where in the cyclic variation of orbit sun angle the spacecraft will find itself at the outset of the mission. For the sun synchronous orbit under discussion, an early July launch will result in an initial mission mode sun angle of 57 degrees, whereas for an early November launch the sun angle will be only 40 degrees at the outset.

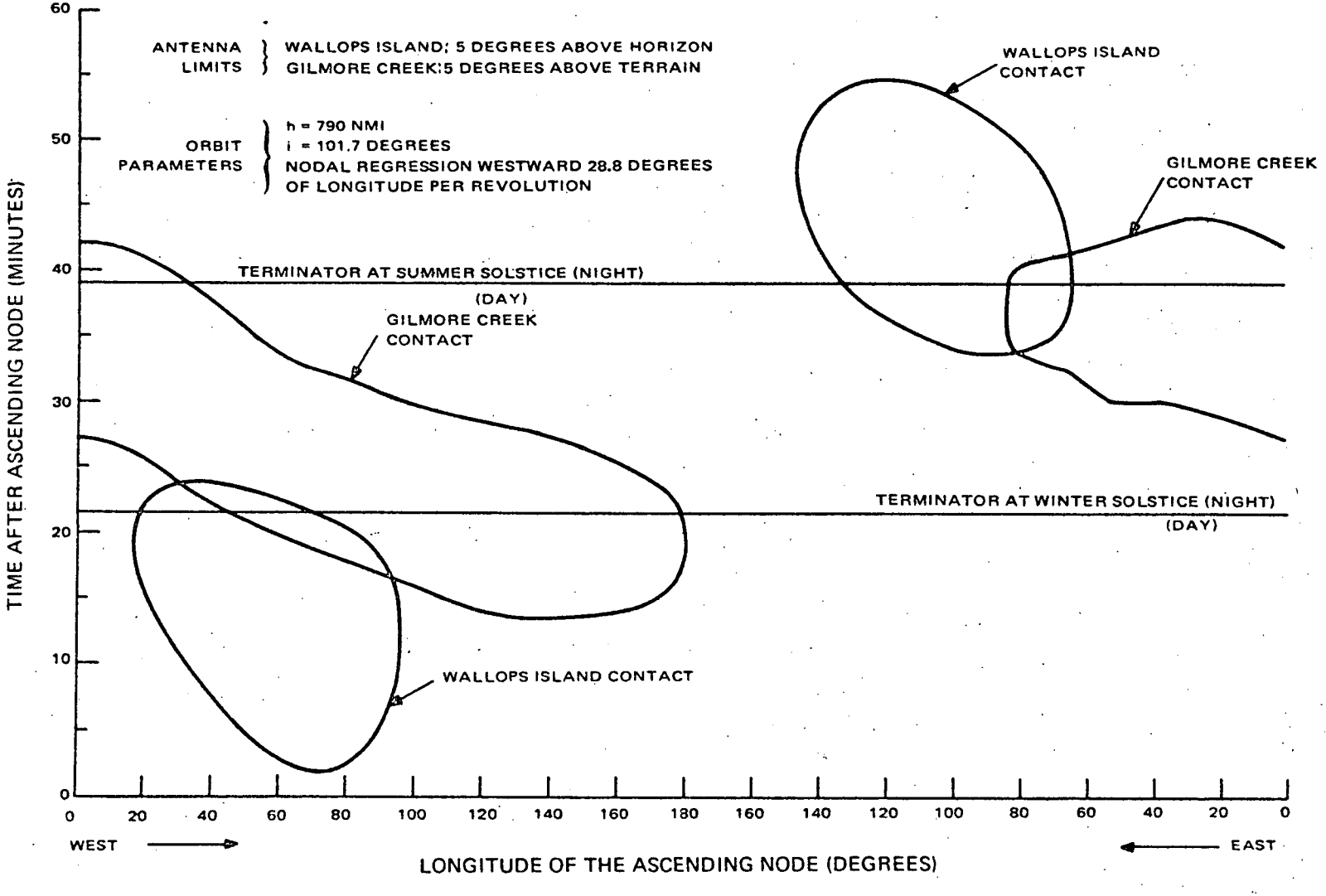

Figure I-20. Typical Ground-Contact Boundaries for Wallops Island and Alaska CDA Stations

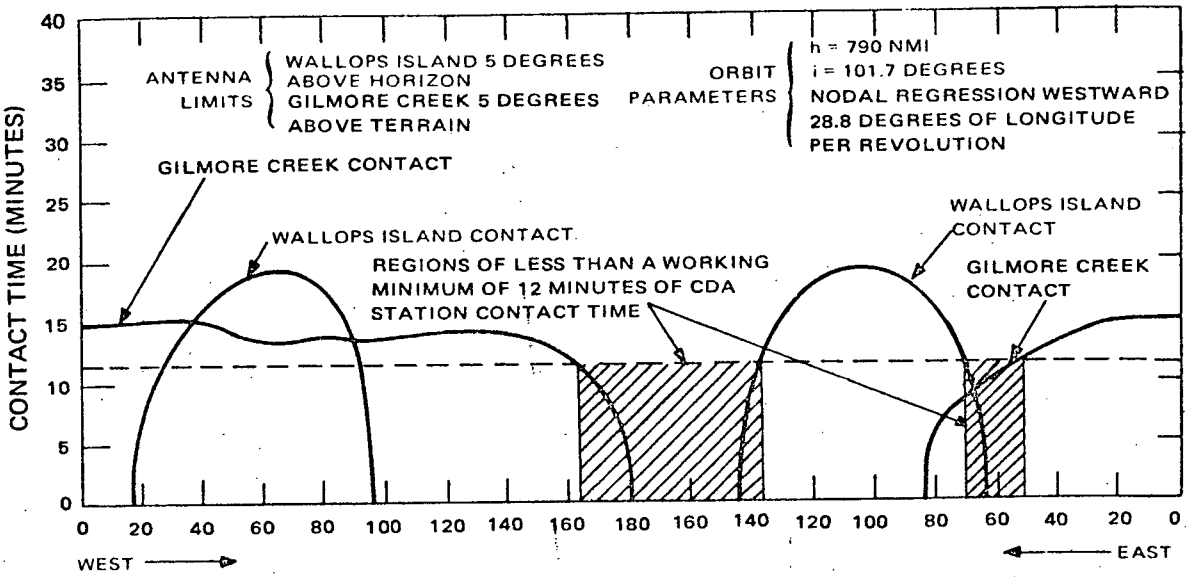

Figure I-21. Typical CDA Station Contact Time

The Greenwich Mean Time of the launch (GMT_L) is given by the expression:

$$GMT_L = LMT_N \left[L_I \pm \sin^{-1}(\tan\rho / \tan i)\right] /15 - \left(t_{PF}/60\right)^*$$

where:

LMT_N is the local mean time of the node nearest to the final injection point, designated in hours from 0 to 24,

L_I is the geographic longitude of the injection point in degrees for which the convention eastward-positive applies,

ρ is the latitude of injection in degrees for which the convention northward-positive applies,

i is orbital inclination, in degrees, and

t_F is time of flight from liftoff to final injection, in minutes.

*Within the brackets, use: + for descending nodes; - for ascending nodes.

SECTION II

MECHANICAL AND STRUCTURAL DESIGN

SECTION II

MECHANICAL AND STRUCTURAL DESIGN

A. GENERAL

The ITOS D and E spacecraft is illustrated in Figure II-1. It is a modification of the TIROS M spacecraft. It consists of a main body, three deployable solar panels, a passive thermal control fence, and active thermal control louvers. The main body of the spacecraft measures 40 by 40 by 48.5 inches. The passive thermal controller is comprised of a thermal fence which is 4.5 inches high by 36 inches in diameter. Each of the three curved solar panels is approximately 36.4 inches wide and 65.2 inches long. When folded, the solar panels extend 11 inches beyond the separation plane. All of the above elements, except the earth-facing panel of the main body, are exactly the same as those used on the TIROS M spacecraft.

The spacecraft was designed such that it is compatible with the Delta launch vehicle and the improved Delta fairing. In the launch configuration, the spacecraft is mounted to the 37-inch diameter by 31-inch high Delta attach fitting and coupled to it with a Marmon clamp. Four separation spring pads, two separation switches, a launch operations connector, and a separation ring keyway on the spacecraft interface with elements on the attach fitting. The spacecraft main body consists of externally reinforced aluminum panels bolted together to form a rectangular prism. The sensors are mounted on the earth-facing panel. The remaining electronic equipment is located on three panels; i.e., equipment panels 1 and 3, and the baseplate. Panels 1 and 3 are hinged to the baseplate and can be laid flat for integration and electrical checkout of spacecraft components.

Large openings in the access panels, shown in Figure II-2, facilitate component repair or replacement after the main body of the spacecraft is assembled. The S-band antennas which are positioned over the front access hole are mounted on hinged structures. These structures can be rotated out of the way, when access into the interior of the spacecraft is required. The scanning radiometer (SR), the SR electronics, the very high resolution radiometer (VHRR) and the digital solar aspect sensor (DSAS) mount on the earth-facing panel. Slots in this panel permit clear fields of view for the vertical temperature profile radiometer (VTPR) sensors.

The cross brace at the top of the structure supports the thermal control fence and the beacon antenna. The three curved solar panels are independently hinged to the top of the two equipment panels and the anti-earth access panel. The solar panels are constructed of bonded-honeycomb, with sheet metal reinforcing channels bonded to the backside skin. All the other structural members are constructed of skin-stringers, fabricated of riveted sheet metal.

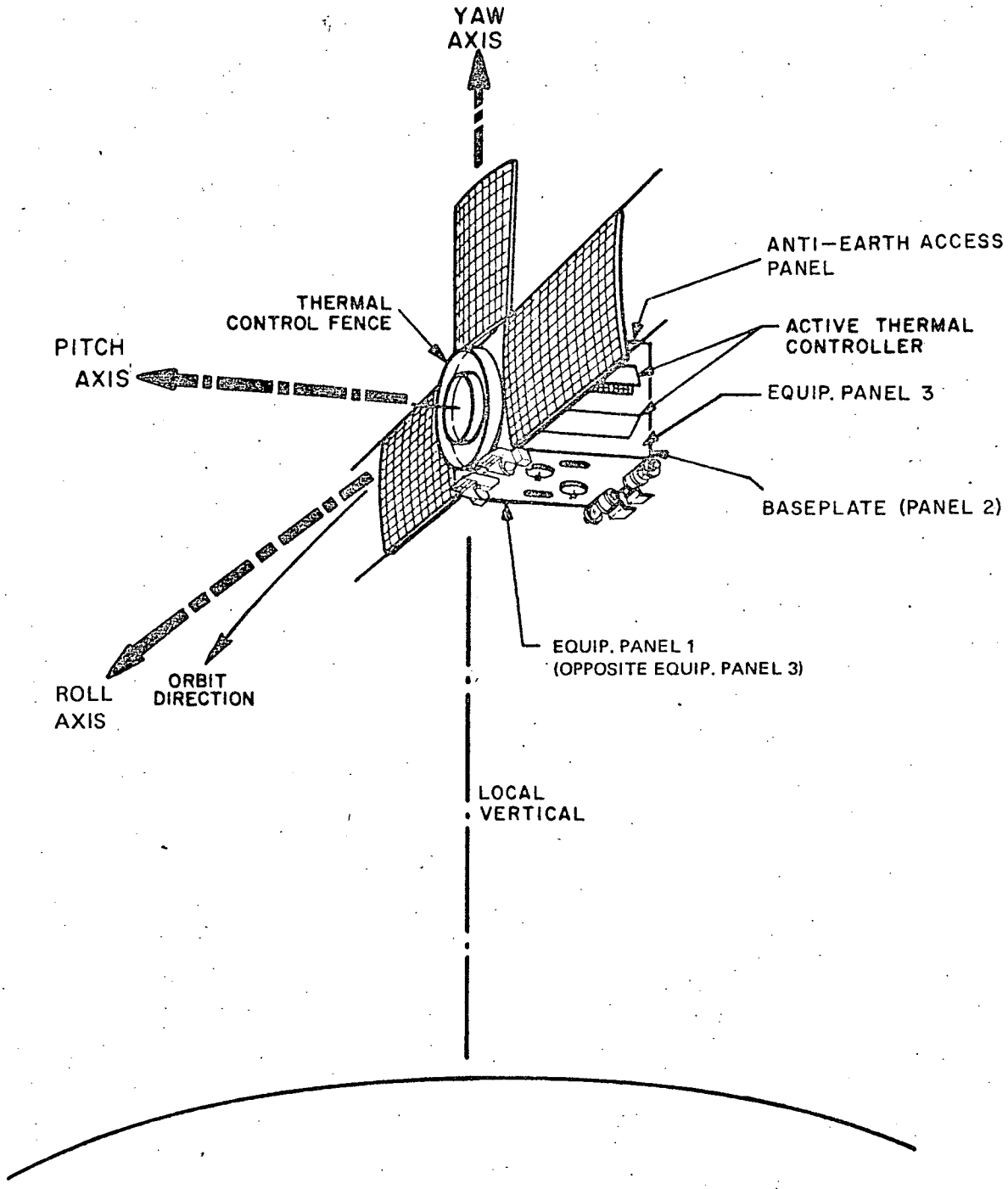

Figure II-1. ITOS D and E Spacecraft Orientation

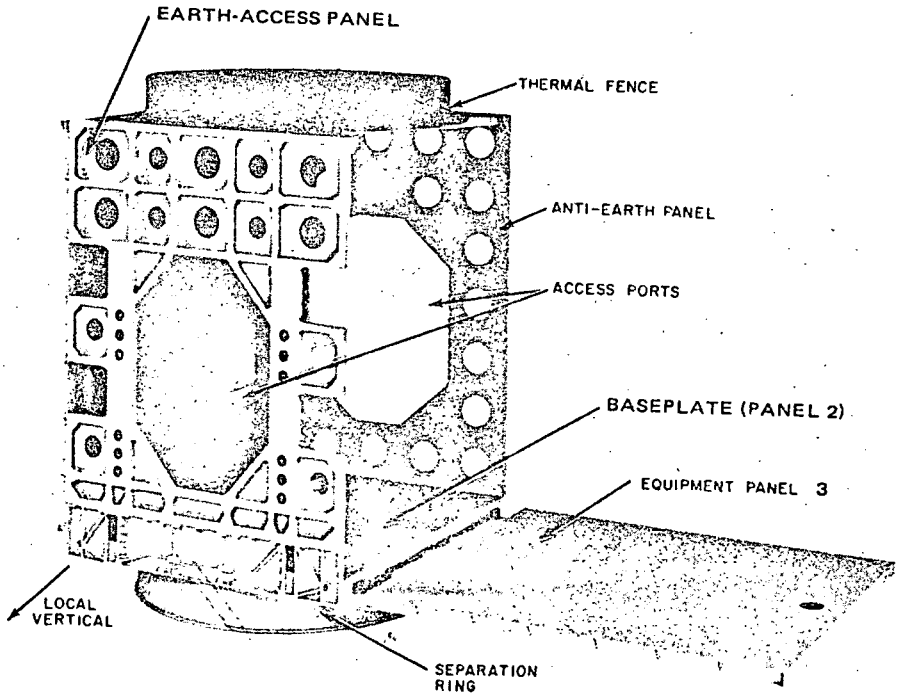

*Shown here is the TIROS M access panel which will be modified for ITOS D and E.

Figure II-2. Basic Structure, Showing Panel Access Ports (Cutouts) and Hinged Equipment Panel Opened

B. DESIGN APPROACH

1. Requirements and Constraints

A major requirement of this program was to use as many TIROS M components and structural elements as possible and still perform the basic mission. The ITOS D and E configuration requires redesign of one structural element, the earth-facing access panel. The sensors [two SR's, two VTPR's, two VHRR's, and a solar proton monitor (SPM)] require a clear field of view, unobstructed by any part of the spacecraft structure, by other sensors, or by the antennas. Positioning of the antennas on the spacecraft was influenced by their radiation pattern requirements.

The ITOS D and E spacecraft will mate with the same MDAC attach fitting used on TIROS M. Only one interfacing element, the breakaway connector, requires moving from the earth-facing position to a rear position. This connector and its brackets were moved to vacate its former space for mounting the VHRR cold temperature calibration target.

Minor modifications are required on the Standard Improved Delta Fairing used with TIROS M to accommodate the ITOS D and E. Two annular ribs in the fairing must be moved to provide adequate clearance between the two SR and two VHRR sensors and the fairing. The rib at station 638.98 must be moved to station 642.48, and the rib at station 672.98 must be moved to station 670.10.

The spacecraft structure has been designed to survive the environmental vibration requirements of TIROS M in RCA Specification TP-V-1975000.

2. Modifications to the TIROS M Design

A single front panel designed for the ITOS D and E mission replaces the present two-piece front panel configuration used on the TIROS M spacecraft. This new panel supports the two SR's, the SR electronics, the two S-band antennas and their brackets, and the two VHRR's. This panel has two slots which provide clear fields-of-view for the VTPR's mounted on the equipment panels. An additional field-of-view clearance hole is required for each VTPR for its space calibration look which occurs once in approximately every 10 minutes of operation. From its normal operation, the VTPR mission interrupts its earth-scanning, rotates 60°, and calibrates with cold space. To accommodate this, a clearance hole is cut into the skin of the number 3 equipment panel and another hole cut in the access hole thermal blanket (see Figure II-3).

The solar panels, the solar panel deployment and latching mechanism, thermal fence, active thermal controllers (ATC's), S-band antennas, DSAS, beacon and command antenna, and real-time antennas of TIROS M are used on the ITOS D and E spacecraft.

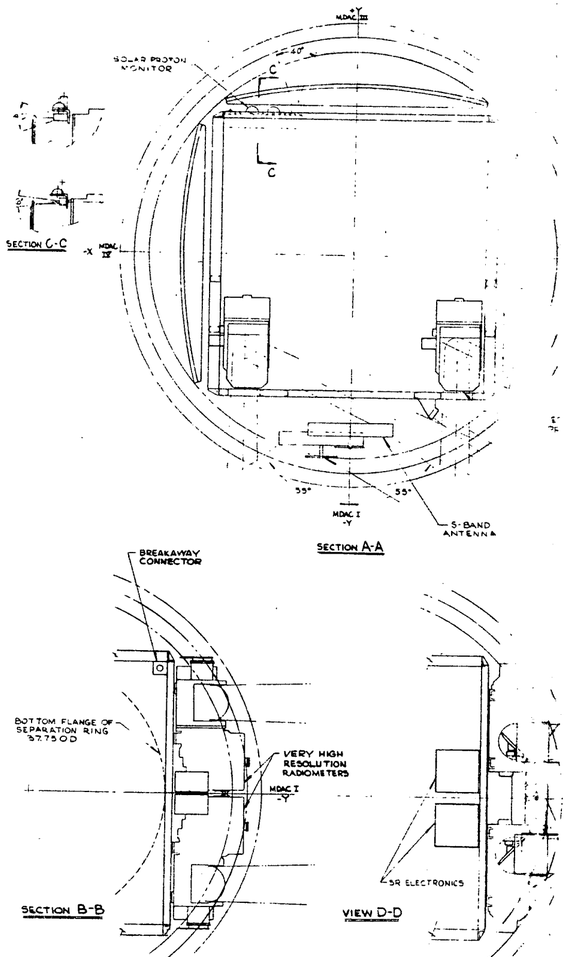

FOLDOUT FRAME 1

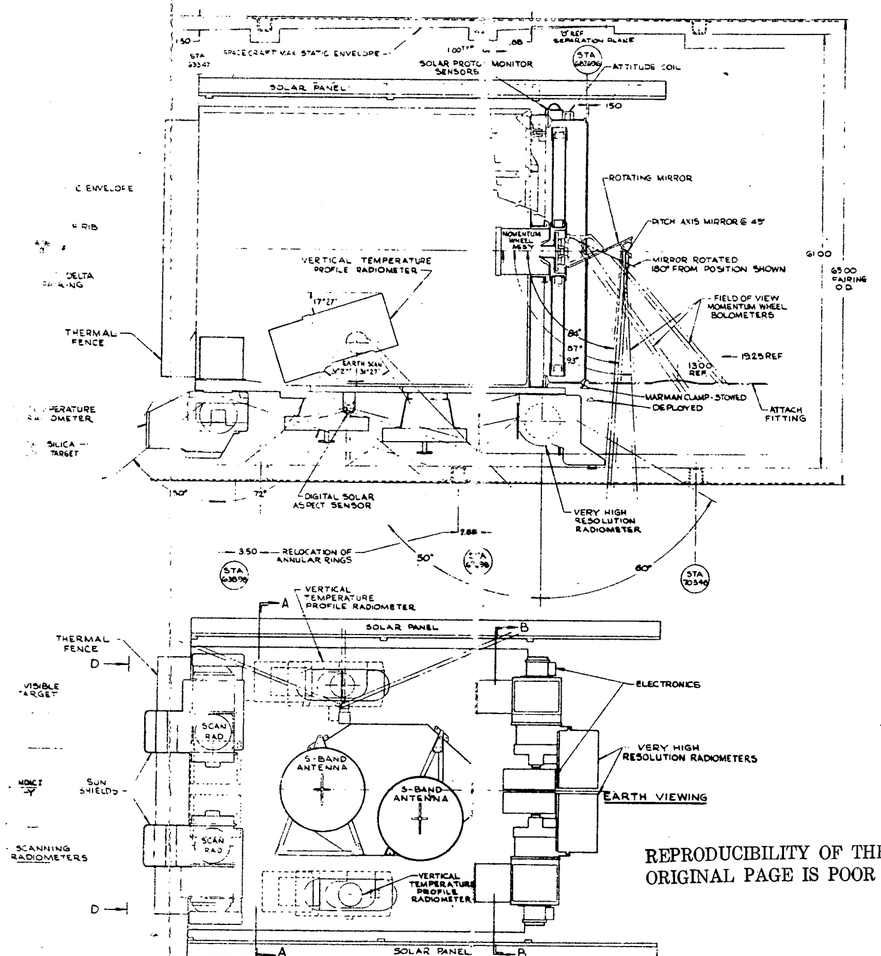

Figure II-3. ITOS D and E Spacecraft Launch Compatibility

FOLDOUT FRAME 2

All components of the TIROS M vehicle dynamics subsystem are used without modification in the ITOS D and E spacecraft. However, two dynamic elements, the nutation damper and the momentum control coil, were relocated to preserve the calibration field-of-view of the VTPR on the number 3 equipment panel. The nutation damper was placed on the anti-earth panel and the momentum control coil was moved to the number 1 equipment panel. Also, a cutout was required in the skin of the equipment panel.

Since the weight of the ITOS D and E spacecraft is more than the 720-pound TIROS M maximum, the support corners on the spacecraft structure were reinforced to handle the additional weight. As shown in Figure II-4, a "bathtub" fixture was added to the structure so that the handling hardware could be attached without opening up the thermal blanket.

The accessibility, interchangeability, manufacturability and alignment properties of the TIROS M design have been retained in the ITOS D and E spacecraft.

Placement of the interior electronics followed as closely as possible the TIROS M configuration and philosophy. Systems were grouped together and placed on individual panels. Where possible, groups of boxes which have not changed in size or configuration were not moved from their TIROS M locations. This is in keeping with the design philosophy of minimizing the changes between the TIROS M and the proposed ITOS D and E configuration.

3. Spacecraft Structure

The design of the earth-facing access panel for the ITOS D and E structure followed closely in concept the philosophy adopted for the TIROS M structure. The original design goals established for TIROS M were load sharing of members, simplicity and uniformity of elements, alignment of load carrying members with each other, and use of continuous notchless members along the highest load paths.

The separation of the natural frequencies of structural components established for the TIROS M structure has been retained for the ITOS D and E structure.

The ITOS D and E spacecraft uses the standard TIROS M/ITOS "bus" structure already procured under the existing contract. Only the existing front access panel will be removed, and the new ITOS D and E panel substituted into the structure. All attachment holes for the new panel will be line reamed from the existing holes in the main structure. This assures that the modified structure is as accurate and as stable as the original (TIROS M) unit.

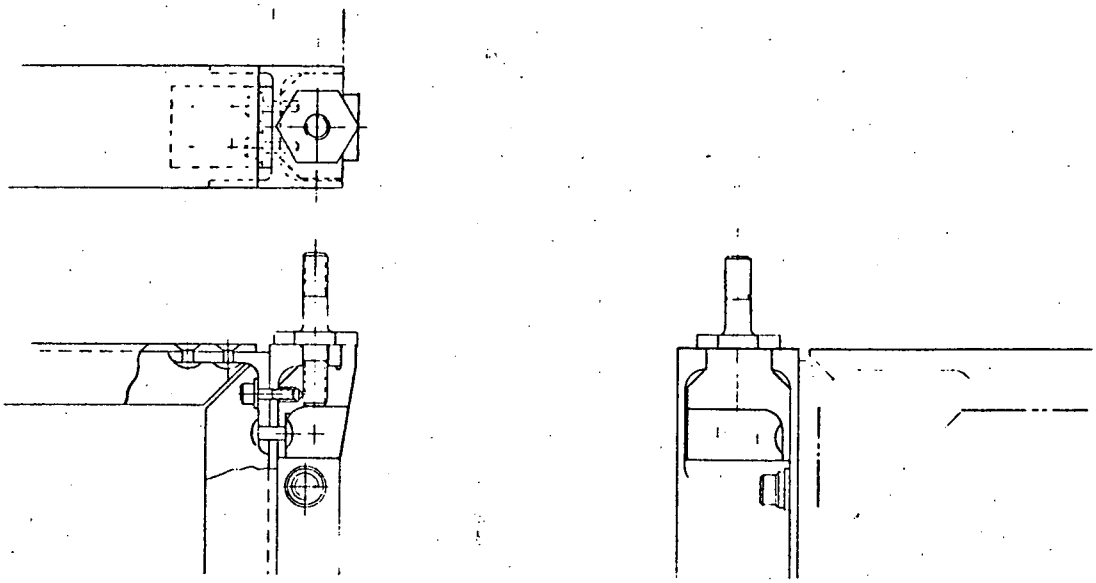

Figure II-4. Stud Mounting for Spacecraft Handling

4. Mechanisms

Two major goals of the mechanical design were (a) to minimize the number of moving parts and (b) to reduce the complexity of the moving parts without jeopardizing their functions. Wherever possible, existing space-qualified hardware was incorporated to minimize the amount of qualification testing required. Redundancy to reduce the possibility of system failure was also considered where applicable.

The hinge alignment problems usually encountered with rigid units and bored holes were avoided by using spherical, self-aligning, reinforced Teflon bearings in all hinge members. The screws used in the bearings were coated with dry-film lubricant to provide redundant bearing surfaces. Most of the linkage joints were provided with the same type of spherical bearings to eliminate binding and misalignment. Spherical joints were designed into bumper pad assemblies and solar panel restraining elements to ensure complete seating of these items. Threaded members in these assemblies afforded sufficient adjustment so that tolerances of the major assemblies could be relaxed without jeopardizing their functions. The components were designed so that differential thermal expansion between major elements of the spacecraft would not result in jamming or increased friction in the mechanisms.

Moving parts between metal-to-metal contacting surfaces and abutting metal surfaces which separate in space were either interfaced with dielectric spacers or adjacent metal surfaces were treated with dry-film lubricants. These surface treatments were primarily to prevent the possibility of vacuum cold-welding. Contact forces, surface roughness, and similarity of contacting metals are

parameters that contribute to the possibility of vacuum cold-welding. Therefore, to forego any possibility of metal seizing, all interfacing metal surfaces on the ITOS D and E spacecraft were treated with dielectric surface treatments or used dielectric spacers.

5. Stress Analysis

A stress analysis was performed to verify that the ITOS D and E structure can safely withstand the design load levels. Details of this analysis are presented in Appendix A.

C. DESIGN PHILOSOPHY

1. General

The ITOS D and E structure is the same type of box type structure used in TIROS M. This structural shape, with its sides fastened to each other along their edges, is an efficient arrangement since each side supports the adjacent sides. Load sharing provides a rigid and lightweight structure.

Unlike TIROS M, the ITOS D and E earth-facing panel was designed as a load carrying member rather than primarily a shear tie between the equipment panels. Continuous taper beams span between the top edges of the equipment panels and support the two SR sensors and their electronics. The added depth of the top two beams was required to provide the strength to carry the weight of the SR sensors and their electronics. The new panel was shaped and configured to eliminate changes to other reusable TIROS M structural elements.

The bottom section of the redesigned access panel which supports the VHRR sensors was reinforced (see Figure II-5). This modification, along with the addition of shear clips in all joints, made the lower portion of this panel a load carrying member.

2. Mechanical Alignment

The major structural components, such as the baseplate, equipment panels, and access panels, are designed to achieve and maintain squareness and parallelism of the structure. Accurate jigs and fixtures accomplish positioning of the machined edge members, and the use of body-bound bolts maintains the alignment. No weight penalty is imposed for this alignment control feature.

Final machining of the baseplate and the use of close-tolerance bolts at the interface of the baseplate ring and the separation ring achieve and maintain

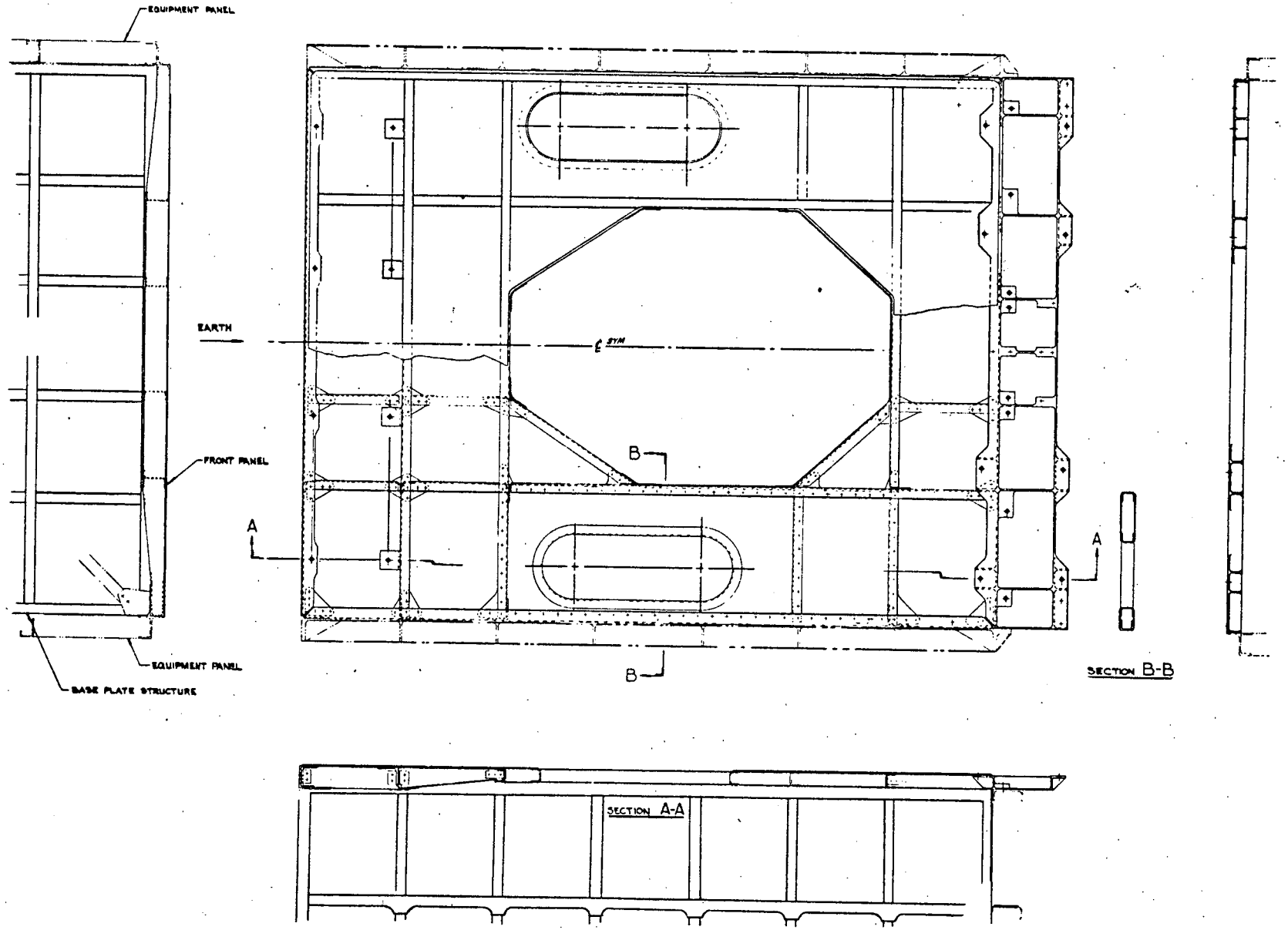

Figure II-5. Front Access Panel

control of the alignment of the spacecraft with the launch vehicle. The mating surface of the baseplate ring is perpendicular to the spin (pitch) axis within 0.01 degree, and flat to 0.005 inch TIR.* The upper and lower mating surfaces of the separation ring are parallel and flat within 0.005 inch TIR.*

The mounting plate for the momentum wheel assembly is machined perpendicular to the pitch axis within 0.05 degree and flat to 0.005 inch TIR. This maintains the total nonperpendicularity from the separation ring mating surface to the mounting surface of the momentum wheel assembly within the 0.1 degree of the system requirement for alignment. The lower mating surface of the separation ring could therefore be used as a reference for momentum wheel assembly and sensor alignment procedures when the separation ring was bolted to the baseplate ring.

Close control of the sensor mounting surfaces (to 0.03 inch TIR) minimizes the number of shims required for the final alignment of the sensors. The use of body-bound bolts, to join the major assemblies of the structure, maintains alignment during environmental tests and in the launch environments.

3. Component Accessibility

The integration of the electronic components into the spacecraft structure was accomplished as described earlier. The equipment panels are equipped with removable hinges for attachment to the baseplate and are coplanar with the baseplate in the folded-down position. With the structure in this open configuration and the earth-oriented panel attached to the baseplate, all integration and initial testing of the subsystems can be accomplished with excellent accessibility to all subsystem elements. With the structure assembled to its final box configuration, with the access panels in place and hinges removed, access to the interior of the spacecraft is provided through the large cutouts in the earth-oriented and anti-earth access panels. These access holes, approximately 25-1/2 by 20-3/4 inches in the anti-earth panel and 18-1/2 by 25-1/2 inches in the earth panel, are large enough to admit a man's shoulders so that the electronic equipment can be repaired or removed from the spacecraft without disassembly of the structure. The two S-band antennas, which are mounted on hinged panels over the access holes, can be rotated out of the way. Two men can reach into the assembled spacecraft at the same time through the two access panels. Since no subsystem component is more than 20 inches from the access holes, inspection can be made without disturbing the spacecraft structure.

*TIR - Total indicator runout.

One nutation damper, the momentum control coil, and active thermal controllers are mounted on the exterior of the No. 1 equipment panel. The other nutation damper is mounted on the exterior of the anti-earth access panel. Accessibility to these elements is not a problem; however, in the completely assembled spacecraft, the solar panels have to be deployed and the thermal blanket removed if inspection of the elements is required.

4. Weight

The total estimated launch weight of the spacecraft is 735 pounds. The weight breakdown is shown in Table II-1.

5. Fabrication and Assembly

Fabrication and assembly procedures were analyzed to provide assurance of structural alignment and interchangeability. To ensure the maintenance of tolerances on dimensions, squareness, parallelism, and the flatness of mating or mounting surfaces, the controlling surfaces were machined so that they could be held accurately in jigs and fixtures during riveting. The base of the spacecraft structure has a short, permanently attached ring (the baseplate ring) that mates with the separation ring. After fabrication of the baseplate, the baseplate ring was final-machined, using the skin of the baseplate as a reference surface. This eliminated distortions in riveting the ring to the baseplate and ensured parallelism between the baseplate skin and the mounting surface for the baseplate ring. During this operation, the mounting plate for the momentum wheel assembly was final-machined, ensuring the maintenance of an accurate reference between the baseplate ring and the momentum flywheel assembly. After machining, the baseplate-ring-to-separation-ring mating holes were jig-drilled. Close-tolerance, high-strength bolts were used to provide alignment and concentricity control and to carry shear loads. The separation ring is interchangeable and easily replaced if damaged.

Since the mounting surfaces for the equipment panels are the edges of the baseplate and the two access panels, these three parts must present a flat, smooth, continuous surface for the equipment panels. If the baseplate and one or both of the access panels differed in width within normal tolerances, the equipment panels could be stressed locally when these panels are bolted to the baseplate and access panels. To maintain close enough tolerances on the width of the parts to prevent such damage to the equipment panels would be difficult, expensive, and unnecessary. It was more advantageous to assemble the baseplate and access panels in accurately made fixtures of a matched dimension than to specify a close tolerance in width between the access panels and the baseplate.

The baseplate and access panels were assembled first, with the earth-oriented access panel and baseplate jig-drilled from a single jig. The drilled holes

TABLE II-1. ITOS D AND E SPACECRAFT, ESTIMATED WEIGHT SUMMARY

Group	Estimated Weight (Pounds)
Structure (includes thermal fence and bracketry)	135
Power (array, batteries, and power supply electronics)	125
Thermal (incl. ATC's and thermal blankets)	18
Sensors (SR, VHRR, VTPR, DSAS)	130
Recorders	83
Communication, Antennas and RF Cables	49
Dynamic Controls	70
Command	62
Experiment Equipment (SPM)	8
Miscellaneous (harness, separation switches, hardware, and accelerometer package)	55
Total Spacecraft Weight	735

were then reamed to final size for close-tolerance bolts and the access panel was joined to the baseplate. The anti-earth access panel was joined to the baseplate similarly, but because of a different pattern of mounting holes, a different drill jig was used.

After the access panels were joined to the baseplate, the bolt holes for the equipment mounting panels were drilled. The baseplate and access panel subassembly was clamped in a square configuration and a drill jig used to drill holes in the edges of the baseplate and access panels. Using the other side of the same drill jig, matching holes were drilled in the equipment panel. Again using the same jig, the same procedure was then followed for the second equipment panel. Following this, the holes were all reamed to final size and precision bolts installed, thus completing the major assembly of the structure. Body-bound bolts were used for two reasons: they provide control for satisfactory alignment and also perform a shear function at the joint between adjacent panels. The crossbrace assembly (opposite the baseplate) was the

last structural assembly to be integrated into the structure. All the members except the four pieces were assembled in a fixture, then the corner pieces were joined to the main structure. The crossbrace or X-frame was then fitted, drilled, and riveted to the corner pieces. The thermal fence was attached to the X-frame at this time, with the holes in the thermal fence spotted from the X-frame. Standard hardware was used to join the crossbrace fittings to the panels and to attach the thermal fence. In addition, the thermal fence is conductively isolated from the crossbrace by means of fiberglass standoffs.

6. Integration of Electronic Equipment

Several conditions had to be satisfied in integrating the electronic equipment into the spacecraft. Due to their functions, certain components such as sensors, antennas, and the momentum flywheel are required to be placed in specific areas of the spacecraft. The remaining equipment could be placed anywhere on the structure, providing the spacecraft stability requirements are satisfied. The location of a particular unit was also influenced by other considerations such as thermal requirements, proximity of like or related units, space, geometry, and harnessing.

It was found desirable to locate the mounting feet of the "black boxes" over the flanges of main structural ribs. Where this was not possible, brackets were added to the underside of the structure to support the heavier components. These brackets consisted of intercostal beams or angle clips, and were located under the mounting holes of the black boxes and the box fastened to the brackets through the skin of the structure. The rivets are thus placed in shear during vibration.

After assembly of the structure, hinges were attached to the lower edges of the equipment panels. One half of a hinge was attached to each side of each equipment panel; the other halves of the hinges were attached to the baseplate. These hinges enabled the equipment panels to be lowered from their assembled position to a horizontal position for testing or replacement of components mounted on the panels without complete disassembly of the structure.

The three solar panels were finally joined to the structure. A fixture and drill jig located the hinges on the solar panels and the structure. The fixture controlled the position of the interface between the halves of the hinges rather than the mounting holes for the hinges.

7. Interchangeability

The same approach of major structural component interchangeability used on TIROS M will again be used on the ITOS D and E structure. One approach was to make all major subassemblies of the structure interchangeable with the same subassemblies from another structure or with spare subassemblies.

A second approach was to make none of the subassemblies interchangeable. A compromise philosophy of interchangeability was adopted based on considerations of cost, design and fabrication, possibilities of electronic failures, and possibility of extensive physical damage to major structural assemblies.

The equipment panels are interchangeable to facilitate replacement. For the same reason, each solar panel is made identical and is therefore interchangeable. The separation ring is also interchangeable since its holes were located from a common drill jig.

None of the other subassemblies (baseplate, access panels, thermal fence, or crossbrace assembly) is considered interchangeable. If necessary, however, these components can be replaced by assembling the replacement part in the same assembly fixture as that used for the original part; however, the mounting holes are not drilled at assembly. The part is then mounted in (or on) the structure and the mounting holes are drilled from the holes in the mating parts of the structure. This concept will be used to mount a redesigned earth-oriented access panel.

D. STRUCTURAL COMPONENTS

1. Separation Ring

The separation ring serves as the means of connection between the spacecraft baseplate and the launch vehicle attach fitting. The ring was purchased as a forged ring of type 7075-T73 aluminum alloy and machined to the final dimensions of approximately 38 inches outside diameter, 35.5 inches inside diameter, and 5.6 inches high. Type 7075-T73 alloy was chosen to provide minimum weight since this material is 50-percent stronger in tensile yield strength than type 6061-T6 and, therefore, permits the use of a thinner cross section. The present design has no pilot diameter on the baseplate ring flange. Analysis showed that the pilot diameter section would not withstand the shear loads imposed by the launch environment. More weight would have been needed to increase the section strength; therefore, from a weight economy standpoint, another means of carrying the shear load was necessary. This load is now carried by high-strength, close-tolerance bolts joining the base ring and the separation ring. Control of the alignment and concentricity of the separation ring is maintained by these bolts.

The outer wall of the cylindrical portion of the separation ring has a double taper. The wall is thickest at the flanges and thinnest at the midpoint between the flanges. The taper is a compromise between the weight and the stiffness necessary in the flange areas. The straight inner wall of the cylinder provides a convenient mounting for the separation spring pads, spring pad brackets, and

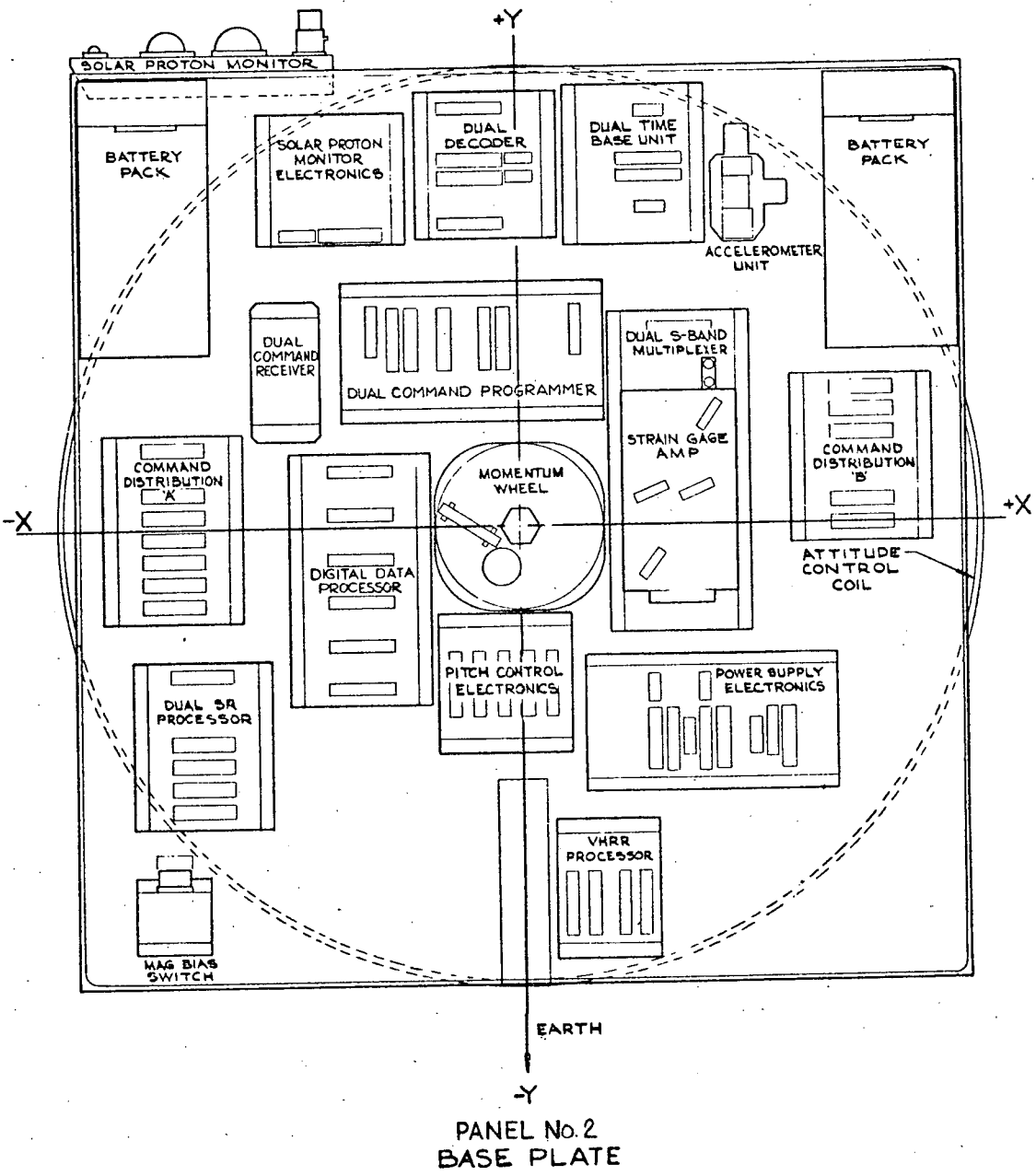

Figure II-6. Baseplate (Panel No. 2) Layout

separation switches. When attached to the baseplate, the separation ring allows removal of the momentum wheel if the separation switch brackets and spring pad brackets are removed. The launch operations connector, which contacts a mating half of the connector pair on the launch vehicle attach fitting, was attached to a separate mounting bracket which was exterior to the separation ring. The connector bracket was jig drilled and aligned to the underside of the baseplate.

2. Baseplate

The baseplate assembly (Figure II-6) will be fabricated from sheet metal and machined components. The edge members of the baseplate are four machined 2024-T4 aluminum channels, with 0.09-inch-thick web and flanges. Bosses are located in the bolt-clamping areas and machined webs will be used to join continuous channel ribs and intercostal channel stringers. The edge channels will be joined together at the corners with type 6061-T6 aluminum angle clips. The mounting plate for the momentum wheel assembly will be machined from 0.19-inch-thick 2024-T4 aluminum plate and riveted to the continuous channel ribs and intercostal channel stringers.

All the continuous channel ribs and intercostal stringers will be fabricated from 0.05-inch-thick, type 2024-0 aluminum and then heat-treated to the T4 or T6 condition. This procedure allows these parts to be fabricated while the material is easily workable; maximum-strength capabilities will be then achieved through solution heat treatment and aging. The skin will be 0.05-inch-thick type 2024-T4 aluminum alloy; all gussets are of the same material, but are 0.08-inch thick. The skin will be finished with a blue epoxy paint on the equipment-mounting side and with 3M Black Velvet paint on the underside (radiator side). The non-radiating area of the underside of the baseplate will be left in the Iridite finish state which undersurfaces all paint finishes. The equipment-mounting surface will be appropriately masked off for the electronic equipment so that metal-to-metal grounding exists.

In the design of the baseplate, the continuous channel ribs were oriented in one direction and are continuous between the equipment panel mounting (edge) channels of the baseplate. This design aids thermal conductivity from the baseplate to the equipment panels since it reduces the number of joints between the electronic equipment located on the baseplate and the active thermal controllers located on the equipment panels. The continuous ribs also provide more efficient support for the equipment panels and momentum wheel assembly, which is the heaviest unit on the baseplate. The intercostal channel stringers will be riveted between the continuous channel ribs and run perpendicular to them. Angle clips of the same material will be used at the joints because bending the intercostal end 90 degrees to form a riveting area may cause rib distortion.

The baseplate skin will be riveted to the edge channels, ribs, and intercostal stringers. The skin and intercostal stringers are dimpled to accept the flat-head rivets and provide a flat (within 0.03 inch TIR) surface for mounting electronic equipment. Gussets will be riveted at all intersections of structural members of the baseplate on the lower side. A ring which joins the separation ring to the baseplate will be riveted to the ribs, intercostals, and edge members.

3. Equipment Mounting Panels

The equipment mounting panels (Figure II-7, panel 1; Figure II-8, panel 3), like the baseplate, will be fabricated from sheet metal and machined components. Continuous ribs and intercostal stringers make up an "egg-crate" structure within the edge members and the skin serves as the mounting surface for the electronic equipment. The edge members will be machined, with 0.09-inch-thick web and flange, from type 2024-T4 aluminum alloy. These members have a cross section that may be described as an "I" beam with part of one flange removed to form a "J" section. The open portion has gussets to provide stiffness to the outer flange for joining to the access panels.

The continuous ribs and the clips that tie the intercostal stringers to the ribs will be formed of 0.04-inch type 2024-0 aluminum alloy. These will be subsequently solution heat-treated, then precipitation-hardened to the T4 condition. The intercostal stringers will be formed of 0.04-inch type 7075-0 aluminum alloy and then solution heat-treated to the T6 condition. The ribs are continuous, oriented vertically, and riveted to the upper and lower edge channels. This orientation provided a better strength-to-weight ratio than an arrangement of the ribs in a horizontal direction. The ribs on these panels will be located to join the baseplate at the same location as the baseplate ribs, providing continuous stress-load paths to the separation ring. Intercostal members will be located between the ribs and perpendicular to them. The intercostal members will be riveted directly to the ribs at one end and tied to the adjacent ribs at the other end by angle clips to reduce the possibility of rib distortion during riveting. The pitch of the ribs and intercostal members on the equipment panels and baseplate was selected to provide the strongest structure for the least weight within the space and equipment constraints and still allow reasonable accessibility to attach component reinforcing brackets.

The skin of the equipment mounting panels will be 0.04-inch-thick type 2024-T4 aluminum, riveted to the ribs, intercostal members, and edge channels with flathead rivets. The skin and structural members will be either countersunk or dimpled, depending upon the section thickness, to recess the rivet heads below the surface of the skin to provide a flat (within 0.03 TIR) surface for mounting equipment. The skin thickness favors structural rather than thermal requirements; a thermal analysis indicated the adequacy of a thinner skin.

Gussets of 0.06- and 0.08-inch-thick type 7075-T6 aluminum will be riveted to each intersection of ribs, intercostal members, and edge members to provide section continuity on the rib side of the panels.

The equipment mounting surfaces of the equipment panels will be finished with a blue epoxy paint; areas will be masked to provide metal-to-metal electrical grounding contact with the electronic equipment. The radiation surfaces,

under the active-thermal-control (ATC) louvers, will be finished with 3M Black Velvet Paint. The rest of the exterior surfaces of the equipment panels will be left in their Iridite finish.

4. Earth-Facing Access Panel

A new earth-facing access panel (Figure II-5) will be constructed for the ITOS D and E spacecraft. The construction will be the same as the other elements of the structure; such as, the baseplate and the equipment panels. Its design consists of machined channels around the perimeter, with a system of metal ribs and intercostal stringer members within the area bounded by the edge channels. A sheet metal skin covers the exterior of the panel. Around the VTPR view ports, the structure will be reinforced by formed channels and secondary skins on the interior of the panel.

The edge channels will be machined from 2024-T4 aluminum bar stock. The webs of the channels are 0.09 inch thick and the flanges are 0.06 inch thick.

The ribs and the intercostal stringers will be formed from type 2024-0 aluminum, and then solution-heat-treated, quenched, and age-hardened to the T4 condition. The rib and intercostals stringers, which are 0.06 inch thick, are tied together by a system of clips and gussets. Clips are used at one end of each intercostal stringer to reduce the possibility of distortion during fabrication.

Both the interior and exterior skins will be fabricated from 0.04-inch thick, type 2024-T3 aluminum. The interior of the structure will be painted with blue epoxy and exterior will be left with its Iridite finish.

The access hole will be the same size as that used on TIROS M which is 8-1/2 by 25-1/2 inches. The two S-band antennas are mounted over the access hole on hinged structures. Each of these structures consists of a sheet metal spun cup mounted onto a riveted sheet metal door. These doors will be mounted over the access panel thermal blanket.

5. Anti-Earth Access Panel

The anti-earth access panel will be constructed the same as the baseplate and equipment panels. It is formed of machined channels around the perimeter with a system of sheet metal ribs and intercostal stringer members within the area bounded by the edge channels. A metal skin will cover the interior structural area.

The edge channels will be machined from type 2024-T4 aluminum bar stock. The web of the channels is 0.09 inch thick and the flanges are 0.06 inch thick.

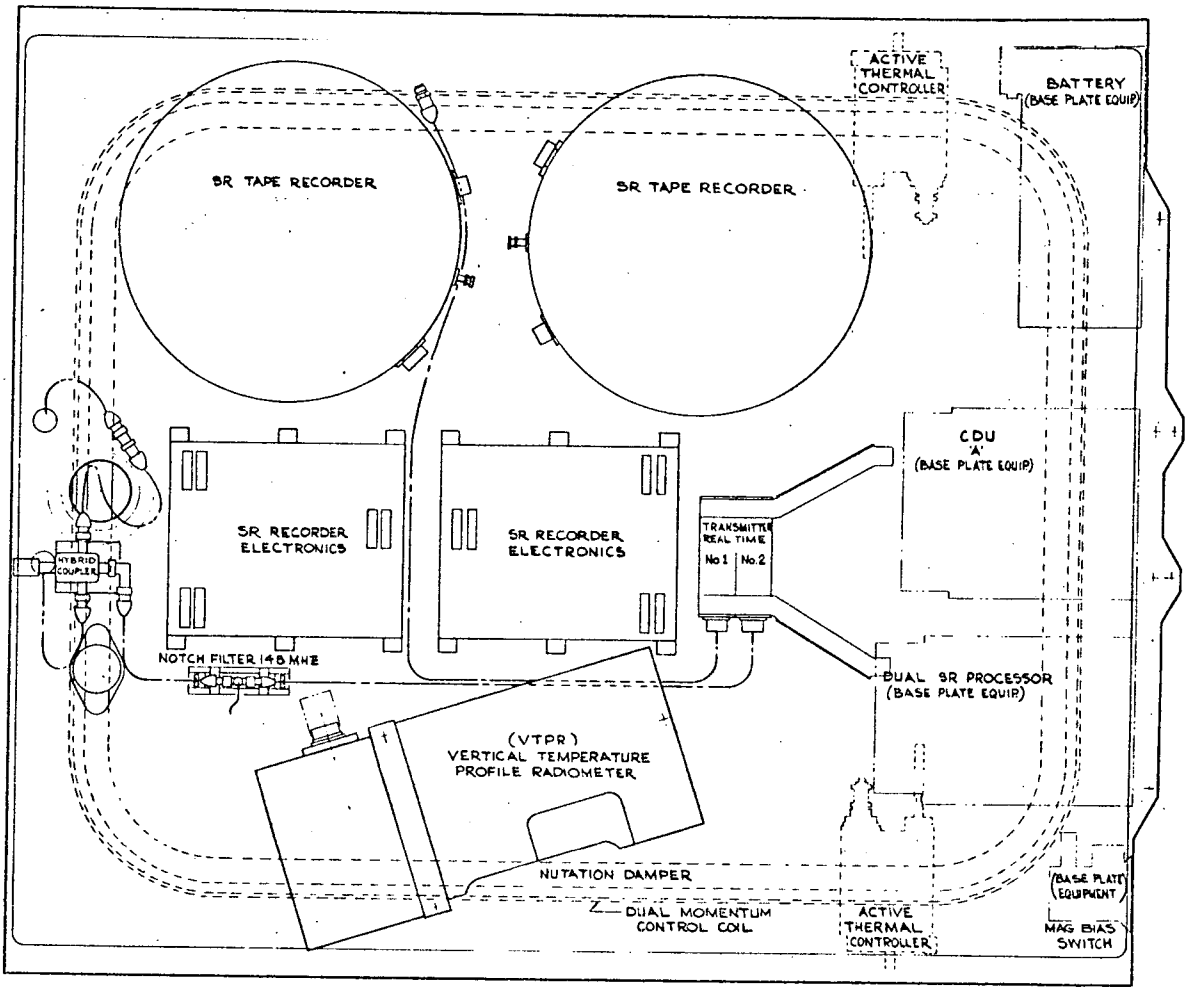

Figure II-7. Equipment Panel No. 1

The ribs and the intercostal stringers will be formed from type 2024-0 aluminum, and then solution-heat-treated, quenched, and age-hardened to the T4 condition. Rib and intercostal stringers are 0.03 or 0.06 inch thick, depending upon local strength requirements. These ribs are tied together by a system of intercostal stringers and edge members perpendicular to the ribs. Clips will again be used at one end of each intercostal stringer to reduce the possibility of distortion during fabrication.

The skin consists of two separate sheets of type 2024-T4 aluminum, with an overlap joint between the two pieces. The lower and upper pieces will be 0.04 and 0.03 inch thick, respectively. The two-piece skin provides maximum shear strength on the lower portion where it is required and preserves the minimum weight concept in the upper area. Both areas will have blue epoxy paint on the side opposite the ribs.

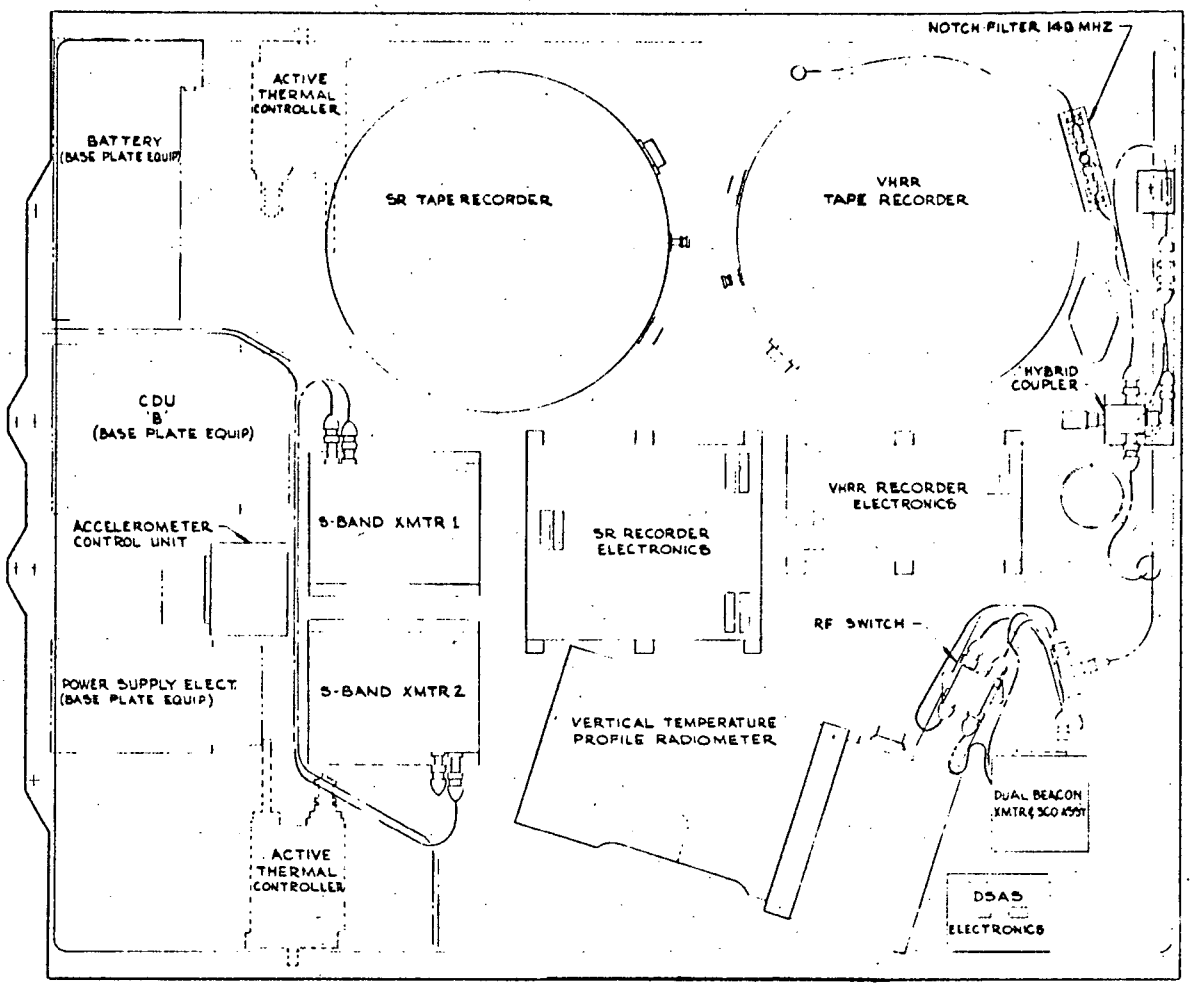

Figure II-8. Equipment Panel No. 3

Gussets of type 2024-T3 aluminum, either 0.04 or 0.08 inch thick, will be used to provide maximum strength, where necessary, and minimum weight, where possible.

Large aircraft-type lightening holes with formed lips will be used in the skin. These holes are centrally located between rib and intercostal intersections to reduce the panel weight without jeopardizing panel strength.

The access cutout is basically a rectangle with gusseted corners. The gussets will be formed by the skin and a rib-type member at each corner. Small standard gussets carry the stress load from the corner rib to the main standard structural ribs.

6. Crossbrace Assembly

The crossbrace assembly (see Figure II-9) is located at the top of the structure. This assembly stabilizes the top of the spacecraft structure and supports the thermal fence.

The X-frame portion of the crossbrace will be fabricated from 0.04-inch-thick type 7075-0 aluminum sheet, which is formed into a channel, then heat-treated to the T6 condition. The shape of the beam was designed for uniform strength.

The corner fittings will be machined from type 2024-T4 aluminum, with flanges to join them to the X-frame beams. The center of the X-frame, where the two channels intersect, is strengthened on the top and bottom with 0.08-inch-thick type 2024-T4 aluminum gussets, which were riveted to the channels. The upper plate has studs to fasten a shaft for checking runout of the spacecraft from the separation plane.

7. Thermal Fence

The thermal fence configuration is the same as was used on TIROS M. The device consists basically of two concentric cups spun of 0.050-inch-thick type 6061-0 aluminum alloy, as illustrated in Figures II-9 and II-10. The outer cup is 36 inches in diameter and 4.81 inches high. The outer flat mounting ring was made from 0.050-inch-thick type 6061-T4 aluminum alloy with an inner diameter of 34 inches and an outer diameter of 40 inches. These three main members were riveted together with indium foil in the joints to provide thermal conduction between the members. The walls of the cups were finished in black to absorb heat; the mirrors were supported above the flat surfaces of the cups by epoxy glass standoff insulators. The mirrors, fabricated of 0.025-inch-thick Alcoa Alzak lighting sheet, Type I, with specular finish and H18 temper, were also insulated from the cups by thermal blankets. The assembled thermal fence was mounted to the crossbrace assembly by 24 standoff insulators. Details of this mounting are shown in Figure II-10.

8. Solar Array Structure and Deployment Mechanism

The solar array structure and deployment mechanism are the same as was used on TIROS M. The solar array consists of three identical curved solar panels 36.38 inches wide (measured on a chord of the 75.61-inch-radius circle described by the outer surface of the panel) and 65.15 inches maximum length from the upper machined channels of the structure to a point 10.9 inches below the separation plane (Figure II-11).

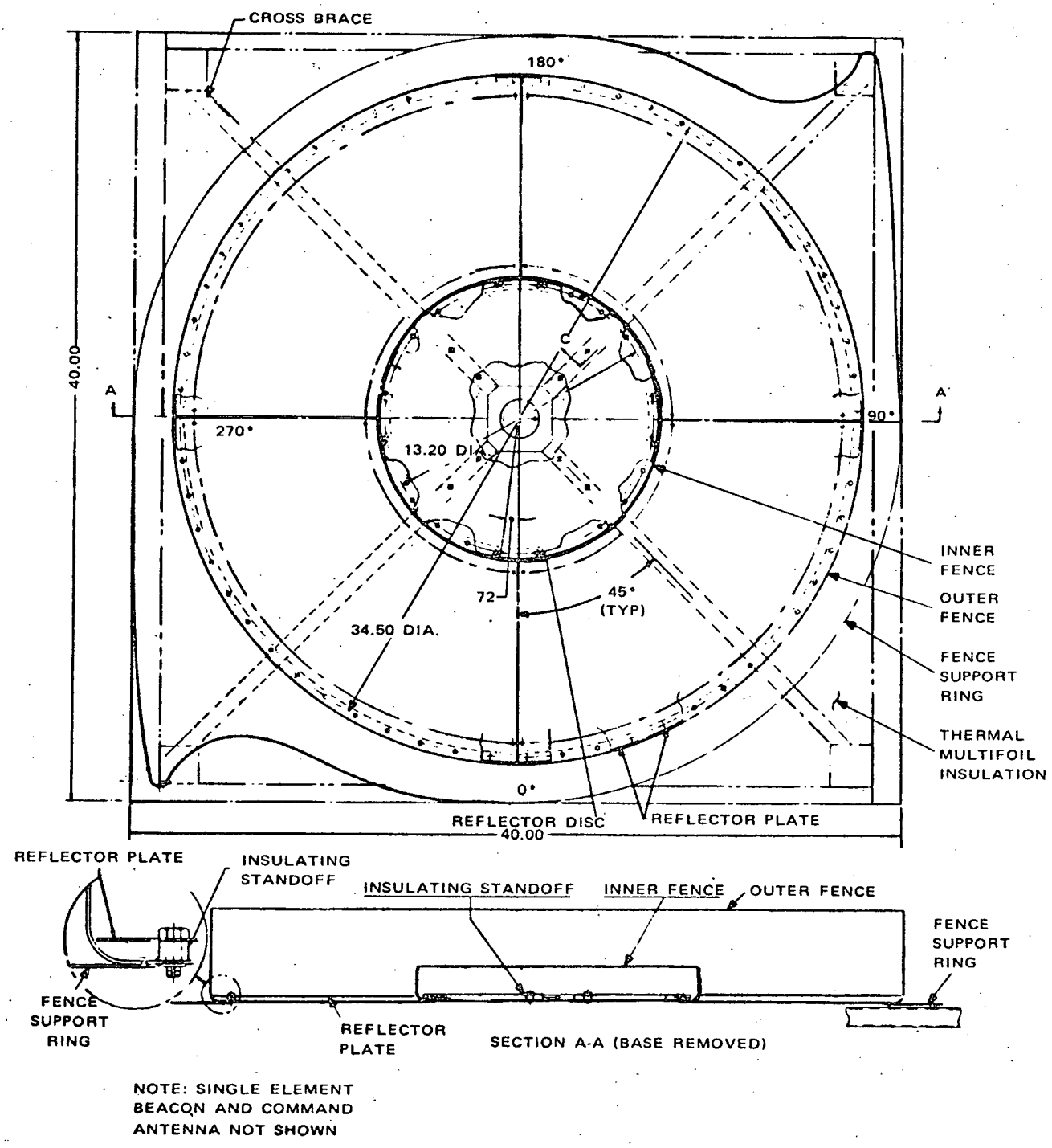

Figure II-9. Cross Brace Assembly and Thermal Fence

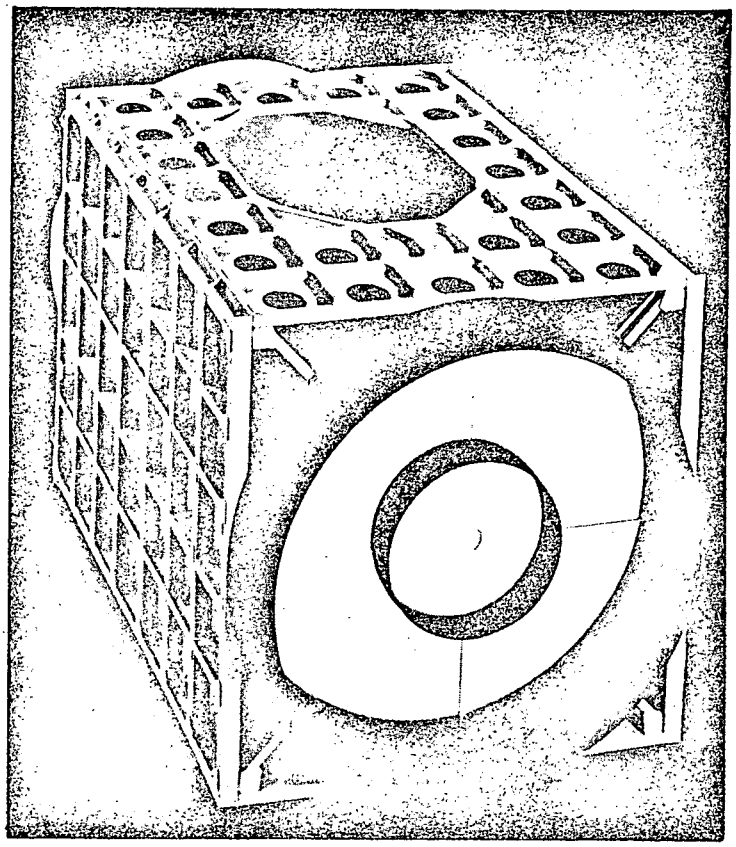

A. Structure Top View, Showing Thermal Fence Assembly
(This is the TIROS M Structure)

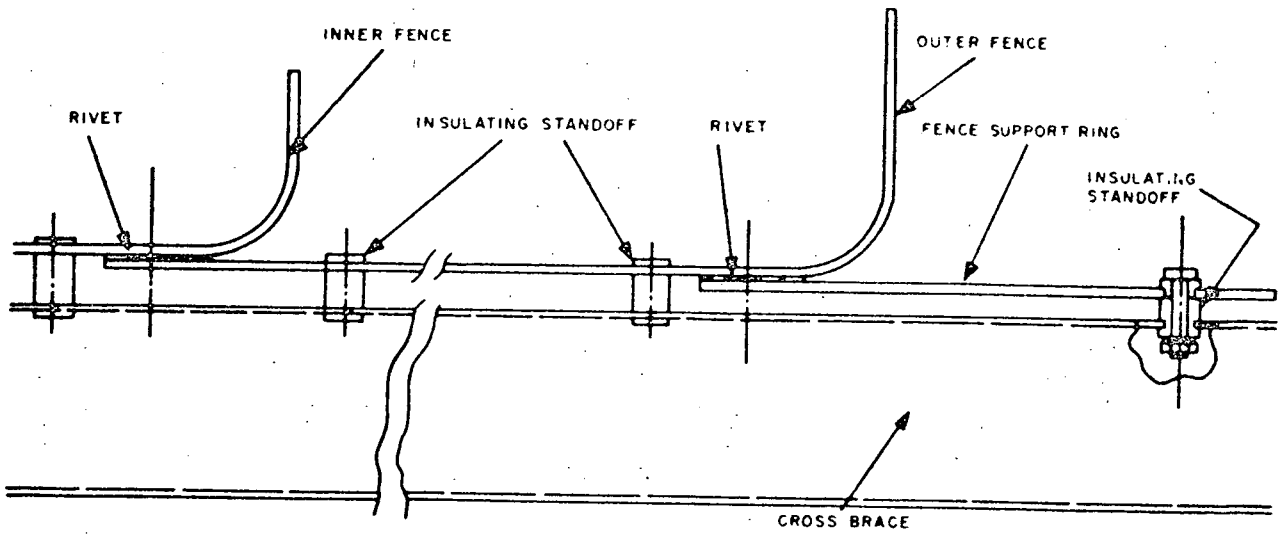

B. Thermal Fence Assembly Mounting Technique, Detailed

Figure II-10. ITOS D and E Thermal Fence Assembly Configuration

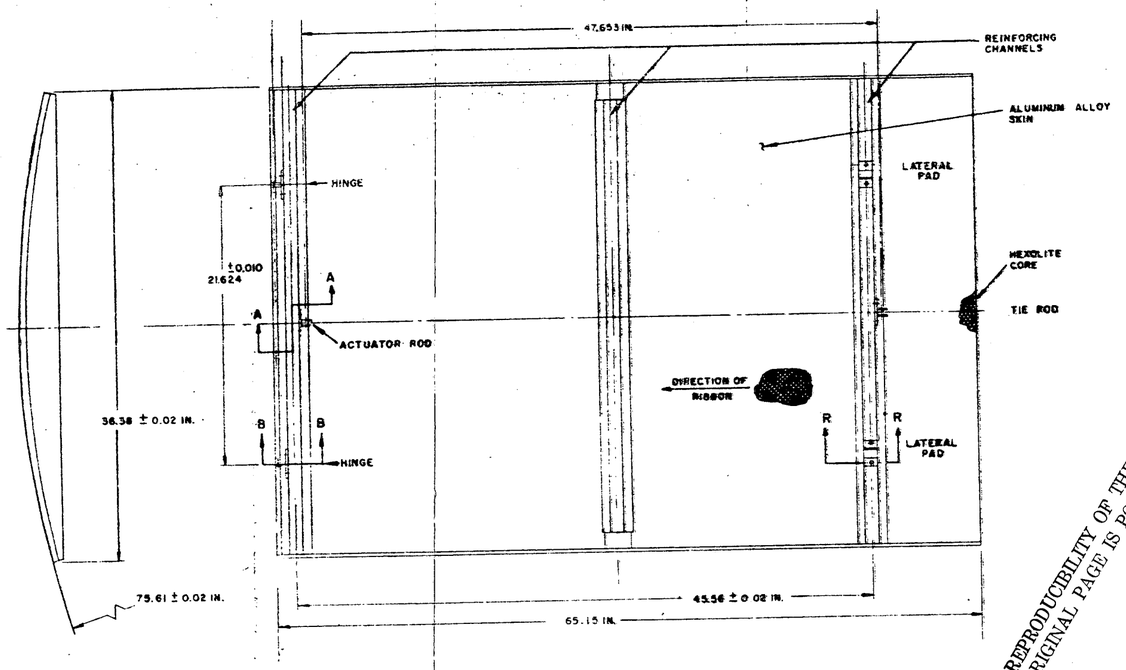

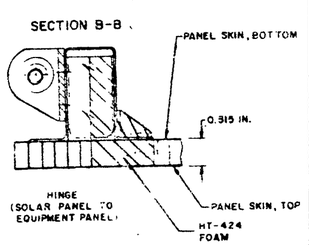

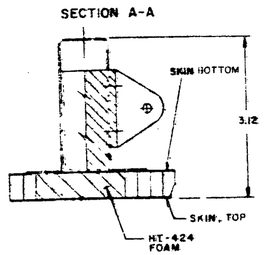

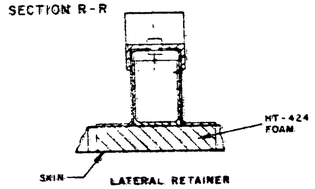

Figure II-11. Solar Panel, Mechanical Configuration

FOLDOUT FRAME 1

FOLDOUT FRAME 2

The solar panels are of a sandwich construction consisting of an aluminum honeycomb core 0.50-inch-thick (type 5052-H19) and 0.0047-inch-thick aluminum skins (type 5056-H191). The panels have high torsional stiffness and high natural frequency combined with low inertia and low weight. The curved design provides a high section modulus plus the necessary clearance during separation. The convex side of each panel has one continuous surface for the mounting of solar cells. Bonded to the concave face were three reinforcing channels (hat sections) fabricated from 0.032-inch-thick type 2024-0 aluminum alloy, which were heat-treated to T4 condition after forming. In addition to their structural function, these hat sections provided mounting surfaces for the array isolation diodes and shunt dissipators. Formed "C"-channel members were bonded to the long edges of the panel to serve as a closeout structure. The last row of honeycomb core cells at each end of the panel were compressed to obtain a suitable surface for filling with type HT424 foam-type adhesive to close the edges.

Three adhesives were selected for use on the solar panel structure. Type FM-1000 was used for bonding the honeycomb core to the aluminum skin; type M-688/CH-16 was chosen as the adhesive for bonding the three structural reinforcing channels to the honeycomb skin; type HT-424 foam adhesive was used as the bonding agent between the honeycomb core and the edge-closure structural members. These adhesives received a thorough evaluation and were used on the solar panels of the Lunar Orbiter spacecraft.

The three solar panels are attached to the spacecraft by a set of hinges at the top reinforcing channel of the anti-earth access panel and the two equipment mounting panels. This permits the solar panels to be stowed in the launch configuration. A spring actuator, hydraulically damped (Figure II-12), is attached to this same channel of each mounting panel to deploy the solar array from the stowed position to the operating position.

Two secondary restraints are also employed. A pair of vibration snubbers located on the outer edges of the center reinforcing channel of each solar panel interface with screw jacks on the spacecraft structure. A set of pads on the outboard (bottom) reinforcing channel of the solar panels restrain the lateral movement of the solar panels and also interface with the spacecraft structure through jacks. One of the pads has the jacks so angled from a line normal to the panel-reinforcing channel and the spacecraft structure that the intersections of the lines of force of the two jacks meet at a point within the structure. The other pad has a jack normal to the rib to provide restraint to inward motion of the panel. This produces a two-directional stabilizing effect upon the panels; the panels are stabilized in the third direction by the hinges and hinge pins.

Two additional interfaces, associated with the actuating mechanism, exist between the solar panels and the spacecraft structure. A clevis fitting to accept the deployment actuator is located in the center of the top reinforcing channel

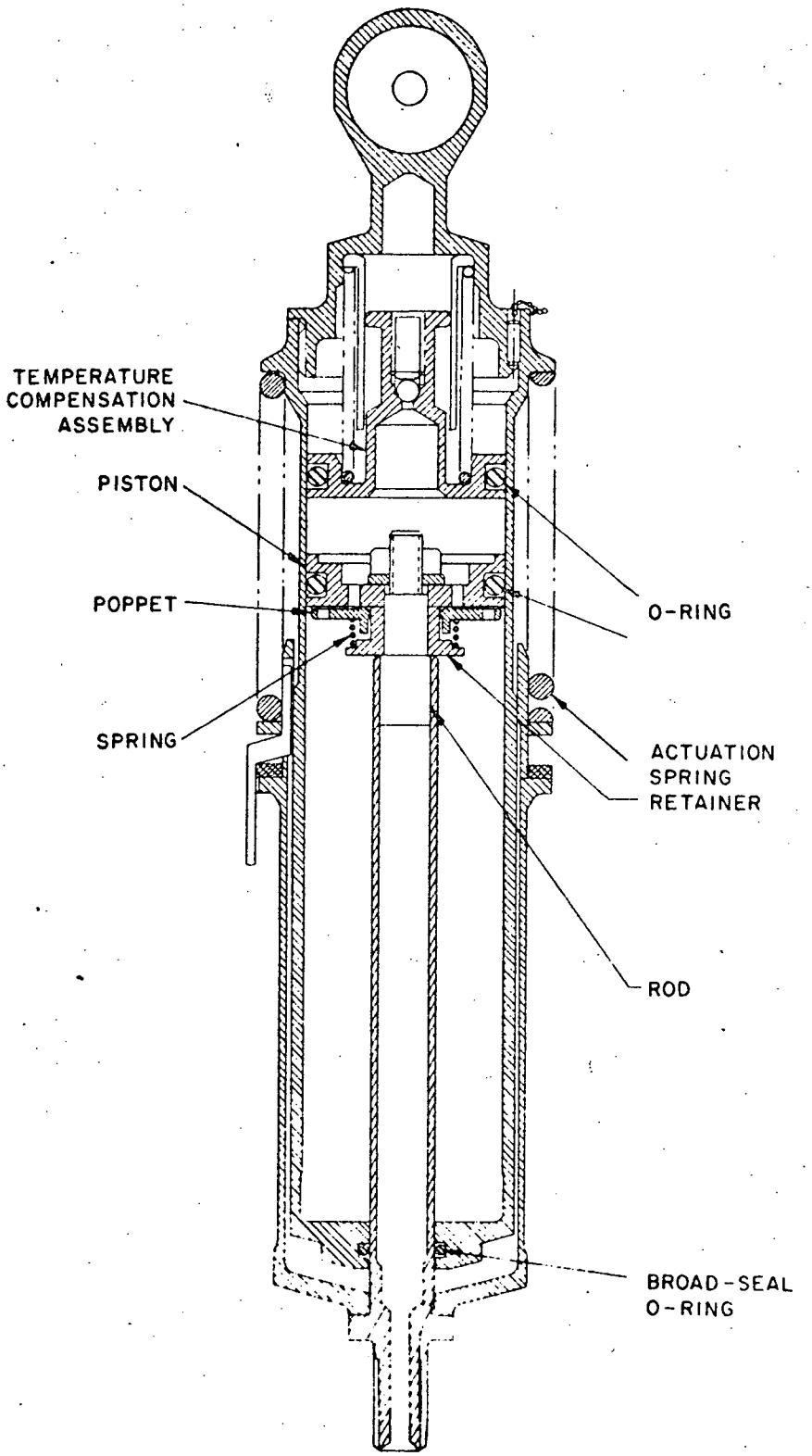

Figure II-12. Solar Panel Hydraulic Actuator

of the structure. A restraining link is attached to a clevis fitting on the lower reinforcing channel through a pin-puller mechanism. This link consists of a turnbuckle link fastened by a bolt at one end to the solar panel and at the other end to two pyrotechic pin pullers on the spacecraft structure.

In operation, either pin puller (see Figure II-13) releases the lower edge of the solar panel on ground command and the deployment actuator rotates the solar panel 90 degrees upward to its deployed position (see Figure II-14). An end-of-stroke shouldered piston stop provides the 90-degree positioning. A hydraulically dampened actuator develops 158 pounds of axial force at the beginning of the panel deployment and 30 pounds at the end of the stroke.

All rotating interfaces between the solar panels, spacecraft structure panels, and deployment mechanisms are through Teflon-lined spherical bearings, permitting up to 10 degrees of misalignment between the solar panel and its interfaces.

9. Momentum and Attitude Control Coils

The momentum coil will be fastened to the ribs of one of the equipment panels beneath the thermal blanket and the attitude control coil will be mounted on the separation ring attached to the baseplate. The concepts used in mechanical design of the coils are identical, although the finished sizes and shapes differed due to specific size, position, and electrical requirements. These coils will be of the same design and fabrication as was used on TIROS M.

10. Nutation Dampers

The two nutation dampers will be of the same design and construction as those used on TIROS M. They will be fastened to the outside of the spacecraft beneath the thermal blanket. One will be on panel 1 and the other will be on the anti-earth access panel.

11. Active Thermal Controller (ATC)

The ATC provides thermal control by varying the effective area of the radiative surface on the equipment panels. Two louvers are located on each equipment panel. Each louver is driven by a thermal actuator sensor that responds to the spacecraft temperature to maintain the equipment panels within given temperature limits.

a. ACTUATOR SENSOR UNIT

This unit is the sensing and actuating device that opens or closes the louver over the radiative surface of the equipment panel. The actuator sensor operates on the principle of controlled thermal expansion of a confined fluid. Its output is a linear motion as a function of the sensed temperature. Figure II-15 is a cross section of the assembly. The actuator sensor characteristics are listed in Table II-2. The actuator sensor unit is the same as that used on TIROS M.

The unit comprises two parts, the drive system and the adjust-relief system. The two systems are hydraulically coupled to a reservoir.

The drive system consists of a drive bellows, drive spring, and drive piston. The piston has two Teflon piston rings, which also act as bearings. The piston is not keyed to the housing, but can rotate, allowing its threaded end to be adjusted in the linkage without disassembly. The drive bellows is an accurate, electrodeposited, nickel element with a precise spring rate, stroke, and pressure capability. To package the device in the minimum space, the bellows is used in both the compressed and extended modes. The drive spring was sized so that it can completely compress the bellows and also supply force to the external linkage. As the temperature increases, the fluid expands, forces the bellows outward against the drive spring, and moves the piston outward. As the temperature decreases, the fluid contracts and the drive spring forces the bellows to contract; the excess force of the drive spring supplies the external driving force. The preload in the drive spring is such that the minimum external drive force of the drive spring and bellows combination is never less than 4 pounds, available when the piston is full in. As the fluid expands, the available force increases until it reaches 7 pounds at the maximum outward position of the piston. Since the drive necessary for the louver is approximately 1 pound, an adequate force margin is maintained throughout the stroke of the piston.

The adjust-relief system includes a bellows, spring, and piston, quite similar to the drive system. In this case, the piston rod is attached to the bellows and an adjusting nut that positions it relative to the housing. This arrangement fulfills two functions: the adjustment of the operating range and the provision of overtemperature relief. The combined spring rate was sized for compatibility with that of the drive system. The relief system was designed so that the minimum pressure required to move it is greater than the maximum pressure developed in the drive system. Incorporated in the adjust-relief system is an adjustment with a 20°C nominal range that can be adjusted anywhere between -10° to +55°C. This adjustment is made by turning the adjusting nut to increase or decrease the internal volume for the fluid.

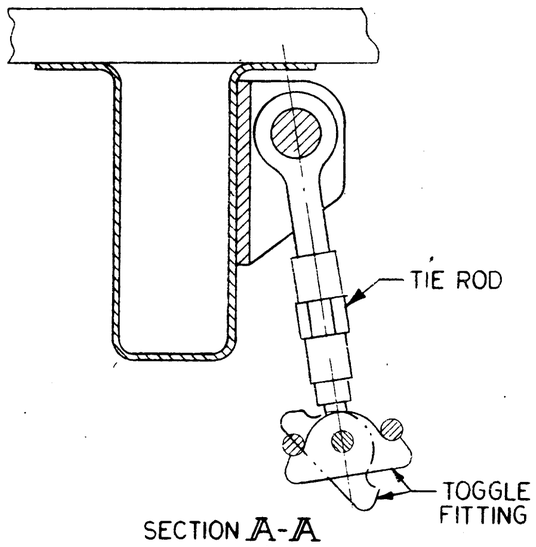

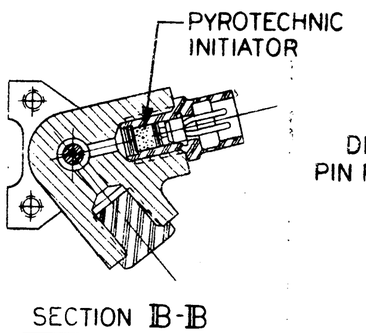

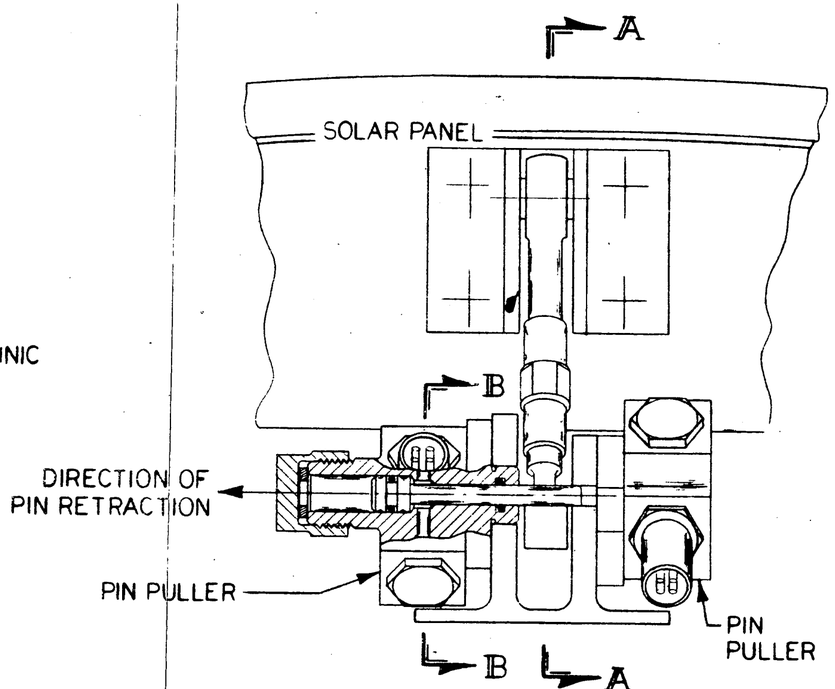

Figure II-13. Solar Panel Retention and Release Mechanism

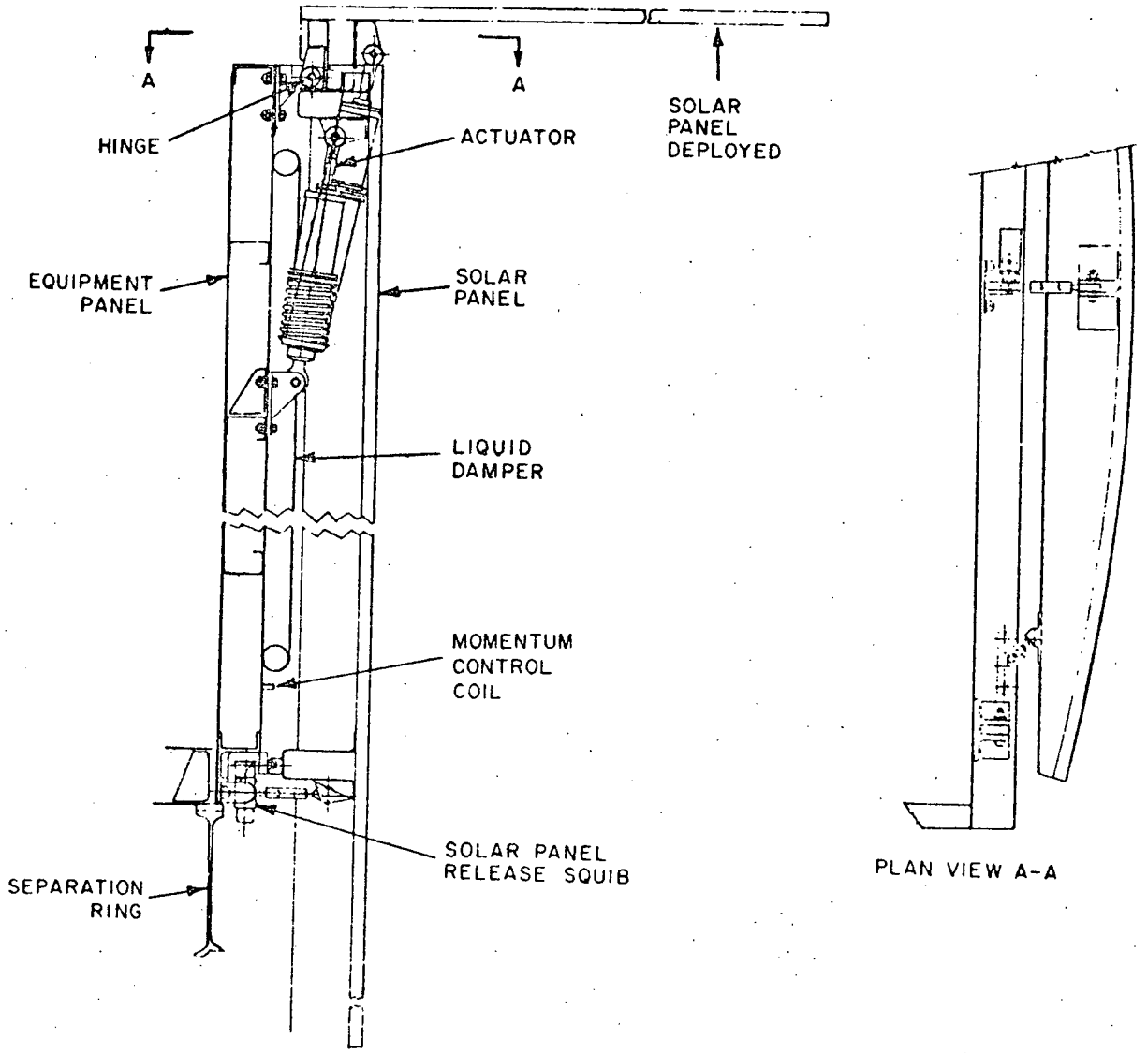

Figure II-14. Deployment of Solar Panel

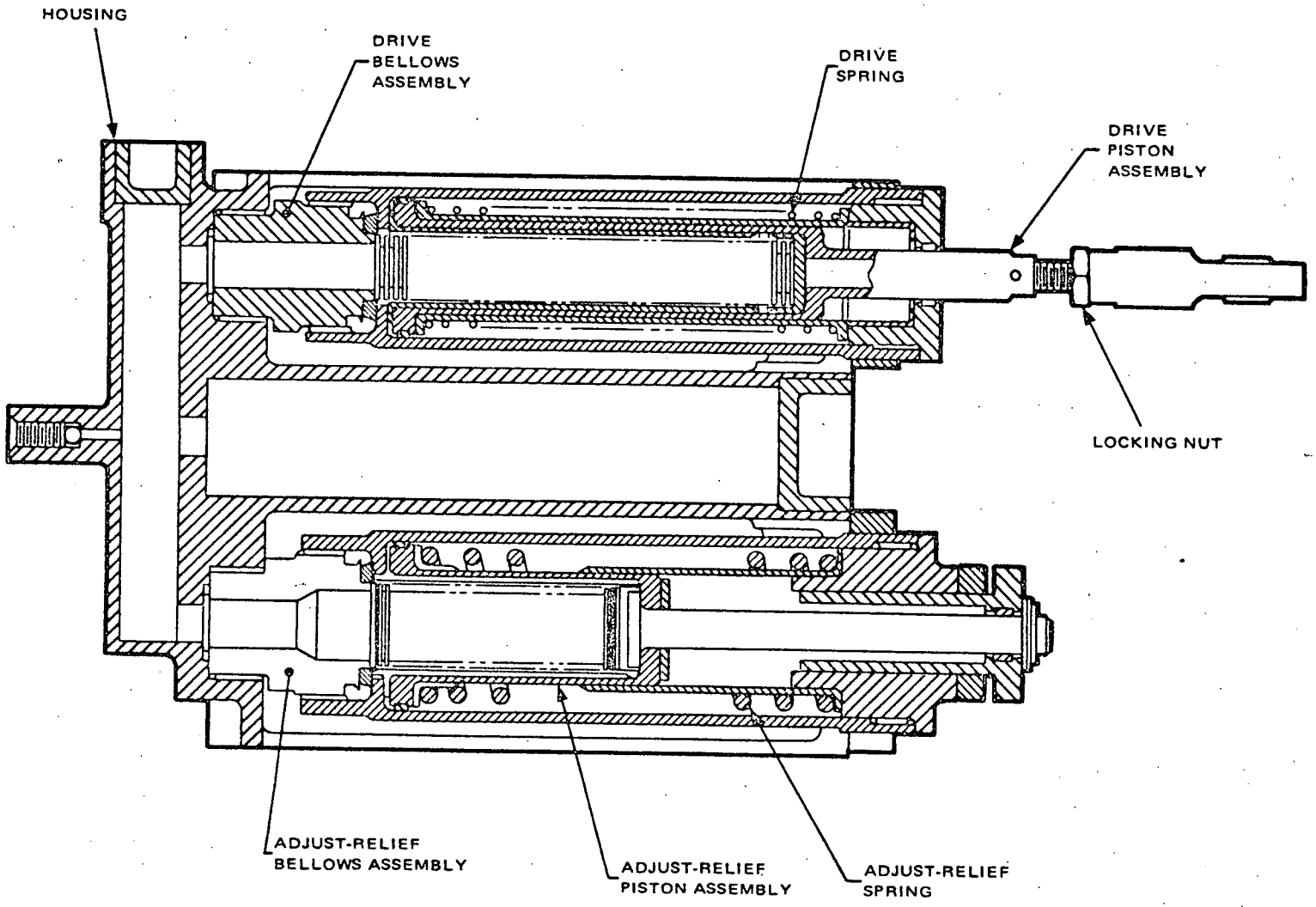

Figure II-15. ATC Actuator Sensor Unit

TABLE II-2. ACTUATOR SENSOR CHARACTERISTICS

Item	Characteristic
Operating Range	20°C
Range Selection	Any 20°C range between -10° and +55°C
Range Setting:	
a) 6°C	Louver closed
b) 26°C	Louver open
Overtemperature Relief (regardless of selected range)	+60°C
Period of Reliable Operation	1-year space life (equiv. to 5×10^3 cycles)
Stroke	0.6 inch
Force Output	4 to 7 pounds
Linearity	±2 percent of full stroke
Sensitivity	0.03 linear inch per °C
Weight	2 pounds

The unit actuator sensor is sealed and the absolute volume of the fluid is constant at a given temperature. The fluid will not exert any force until it is expanded by an increase in temperature to fill the selected volume. Additional incremental increases in temperature cause the expanding fluid to impart force (and motion) to the drive piston. This continues until the drive piston reaches the end of its stroke. At this point, increases in temperature beyond the selected range cause the adjust-relief shaft to move outwards so that the internal pressure caused by the overtemperature does not cause failure of the bellows.

b. LOUVER AND HINGE ASSEMBLY

The louver is a honeycomb structure 34-1/4 by 4-3/8 inches with hinges bonded at each end of its long edges. The assembly is illustrated in Figure II-16, together with the drive linkage and the actuator sensor unit. It is the same as that used on TIROS M.

The thermal requirements of the spacecraft dictate that the radiation surfaces of the equipment panels be exposed during the injection mode. It was also required that the ATC louver system must function normally when the spacecraft is in the operating mode.

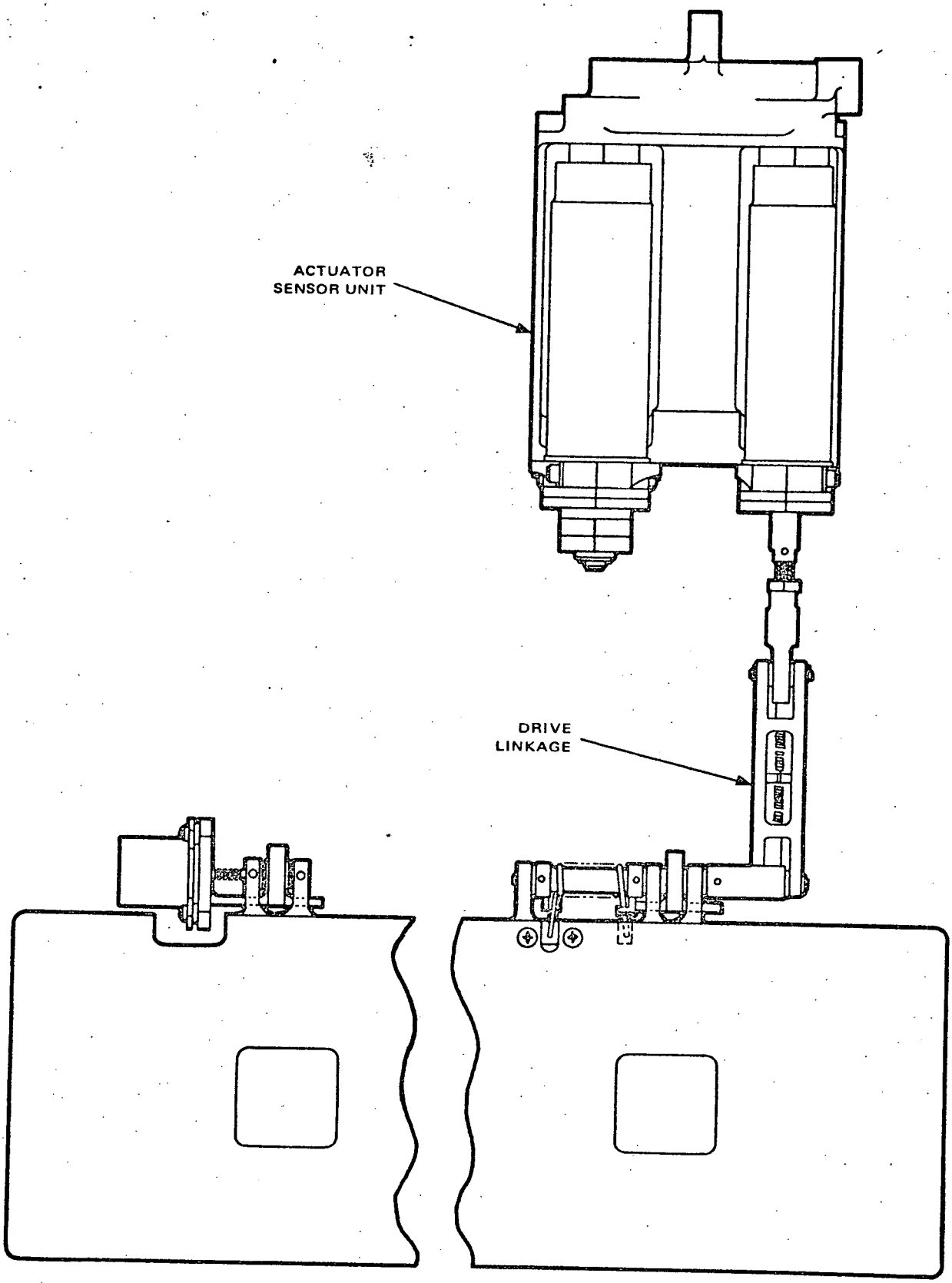

Figure II-16. ATC Louver and Hinge Assembly

For the first condition, the louvers had to be rotated 180 degrees from the completely closed position to a folded back condition when the solar panels are folded. Two nylon hold-downs on the solar panel hold the louver open and release it during the solar panel deployment. The released louver then assumes a position required by the particular temperature of the spacecraft as determined by the position of the output shaft of the actuator sensor unit. This was accomplished by a spring-linkage system.

The actuator sensor is connected through a linkage system to the lower hinge. The linkage, which transforms the linear motion of the actuator unit to a rotary motion, consists of a drag link, a bell crank, a shaft, and two collars with fingers to engage a torsion spring. The shaft provides a bearing surface for the louver hinge and acts as a drive member for the torsion spring, which has protruding ends. The bell crank and the two collars are pinned to the shaft, which is driven by the drag link connected to the output shaft of the actuator sensor unit. The fingers of the collars engage the protruding ends of the torsion spring. The spring is so positioned that the force output of the actuator is transmitted to the louver through the torsion force of the spring, which is limited by the collar fingers. When the louver is folded back to the launch position, the spring tends to return it to a position against the finger of the collar, so that it will then assume a position compatible with the temperature of the actuator sensor unit. A fast decaying vibration of the louver takes place but the final position of the louver is determined by the position of the actuator sensor output shaft. The pin of the second hinge is connected to a bellows, which is a coupler to a potentiometer. The louver is connected to the hinge pin such that the position of the louver is sensed by the potentiometer for use in telemetering this information. An anti-backlash spring was incorporated into the louver drive linkage that eliminated build-up of mechanical clearance tolerances and inaccuracies of louver position vs. temperature.

The louver is 1/4 inch thick, constructed of 3/8- by 0.0016-inch type 5052-H39 honeycomb aluminum alloy core, with skins of 0.0037-inch-thick aluminum alloy. The same adhesive system was used for the louvers as for the solar panels. FM-1000 was used to bond the skins to the core; the edges were closed off with HT424 foamed adhesive; bumper areas were reinforced internally by filling with HT424 foamed adhesive; bumper plates of 0.14-inch-thick 5052-H34 aluminum alloy were bonded on the skin over the bumper areas with M688 A and B adhesive.

A system of hinge clearance was devised to provide for the temperature-differential expansion between the louvers and the equipment panels; this same system was used on the solar panel hinges. The clearance between the tangs on one set of hinges was kept close so that free rotational motion was provided but lateral motion was inhibited. This hinge assembly was designed to sustain the total lateral load of the louver. The clearance between the tangs of the other hinge was large enough so that contact would not occur at the extremes

of differential temperature between the two structures, allowing for the expansion and contraction of the louver without impeding its rotational capability. As in the solar panels, all rotating interfaces are through Teflon-lined spherical bearings, allowing for misalignment of up to 10 degrees without any appreciable binding.

E. INTERIOR ELECTRONICS ARRANGEMENT

1. General

The ITOS D and E spacecraft like the TIROS M spacecraft has three mounting panels for the electronic equipment. These panels are the two equipment panels and the baseplate. In addition, the earth-facing access panel was reinforced to support the VHRR, the SR, and the SR electronics.

The equipment was laid out to maintain the subsystem module concept. Most of the spacecraft housekeeping equipment is mounted on the baseplate. Since the same type sensors are mounted on both sides of the spacecraft, no advantage could be obtained in assigning each equipment panel a payload subsystem as was done with TIROS M.

During integration of the electronic equipment on the ITOS D and E spacecrafts, the two equipment panels will be hinged down into the plane of the baseplate. The earth-facing access panel is fastened to the baseplate and fastened with auxiliary diagonal tie struts during spacecraft "debug and test" phase while the equipment panels are in their hinged down position. ITOS D and E integration requires this configuration due to location of the sensors on the earth-facing access panel. This slight decrease in accessibility should not appreciably affect the efficiency of the integration program.

2. Accessibility of Components

The layout of the interior electronics (shown in Figures II-6, II-7 and II-8) provides adequate space for not only the black boxes but for the harness and RF cable assemblies. The electronic boxes are placed on the structure such that the corner boxes, including the batteries, can be removed from the completely assembled spacecraft without removing other electronic boxes or without disassembly of the equipment panels.

Since the dynamic and static balance requirements of both the spacecraft and the launch vehicle do not require a balanced spacecraft, balance weights were not added to the inertia calculations. This configuration has its lateral cg in

the launch configuration approximately 2.2* inches from the geometric center of the structure. This is caused by the positions of the SR and VHRR sensors on the earth-facing panel which is not naturally balanced out by other electronic boxes on the interior of the equipment module. The weights and the inertia data for the ITOS D and E spacecraft are given in Table II-3, and identification of the major axes is given in Figure II-17.

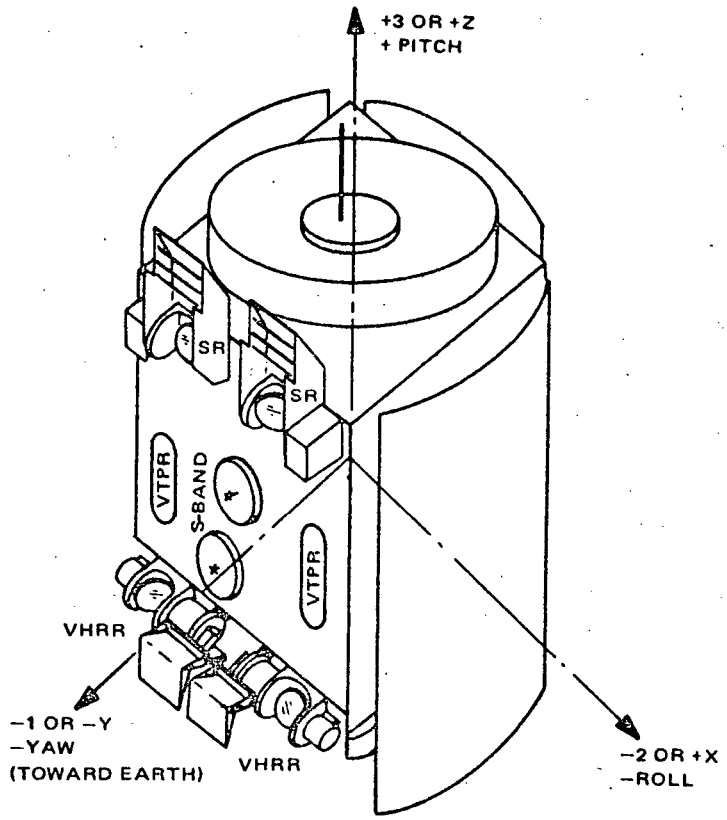

Figure II-17. Spacecraft Alignment Reference Axes

*This does not reflect a change to a lighter VHRR.

TABLE II-3. MECHANICAL AND PHYSICAL PARAMETERS OF ITOS D AND E

Parameter	Launch Configuration (Panels Folded)	Operational Configuration (Panels Deployed)
Spacecraft Weight	735 lbs	735 lbs
Moment of Inertia*		
(a) About Yaw Axis I_{11}	936 lbs-in-sec^2	1307 lbs-in-sec^2
(b) About Roll Axis I_{22}	935 lbs-in-sec^2	1178 lbs-in-sec^2
(c) About Spin (Pitch) Axis I_{33}	780 lbs-in-sec^2	1200 lbs-in-sec^2
Product of Inertia*		
(a) In Yaw-Roll Plane I_{12}	+6.6 lbs-in-sec^2	+6.0 lbs-in-sec^2
(b) In Yaw-Pitch Plane I_{13}	-10.7 lbs-in-sec^2	+71.6 lbs-in-sec^2
(c) In Roll-Pitch Plane I_{23}	-6.0 lbs-in-sec^2	-8.0 lbs-in-sec^2
NOTE: Orbital moments-and-products-of-inertia are values about a set of coordinate axes which have been shifted parallel from the initial launch coordinates.		
Center of Gravity $\bar{z}$* (Above Separation Plane)	21.7 inches	24.1 inches
Center of Gravity $\bar{x}$	-0.1 inch	-0.15 inch
Center of Gravity $\bar{y}$	-2.2 inches	-1.56 inches
*Inertia and cg locations do not reflect decrease in the weight, which reduces the spacecraft weight from 775 to 735 pounds.		

SECTION III
THERMAL DESIGN

SECTION III
THERMAL DESIGN

A. GENERAL

The thermal design of the ITOS D and E spacecraft is the result of modifications made to the thermal design of the TIROS M flight spacecraft.

Thermal control of the spacecraft is achieved through the combined use of passive and active thermal control surfaces. The passive thermal control of the spacecraft is accomplished by means of a variable solar absorptance thermal fence in conjunction with fixed radiators (see Figures III-1 and III-2). All radiator surfaces and thermal fence fins are finished with 3M 400 Series Black Velvet Coating to prevent degradation of the optical properties of the radiators due to space radiation.

The active control is accomplished with temperature controlled moving louvers, two per equipment side, which cover or expose the radiator surface as required. Radiator and louver sizes are shown in Figure III-1. The general location of the thermal control elements, with respect to the overall spacecraft configuration, is illustrated in the frontispiece.

Internal temperature distribution is controlled by a balance of conduction and radiation coupling of the internal components to the thermal control surfaces of the fence and radiators. By proper location of the fixed radiator area, high thermal dissipation units on the baseplate are controlled within specifications.

The spacecraft surface not used for temperature control is blanketed with insulation to limit the radiation heat transfer from these areas. The effective emissivity has been empirically determined to be 0.02 for the insulated area.

The thermal control system design specifications, summarized in Table III-1, have been met for both the acquisition and operational mode. The thermal analysis assumes the sun angle (i.e., the angle between the sun and the spacecraft momentum spin axis) will be between 30 and 60 degrees. This analysis was performed with a very high resolution radiometer (VHRR) which had an electronics unit, located on the baseplate, which dissipated 15 watts. During the hardware design phase, the baseplate radiating areas will be sized to accommodate this VHRR change.

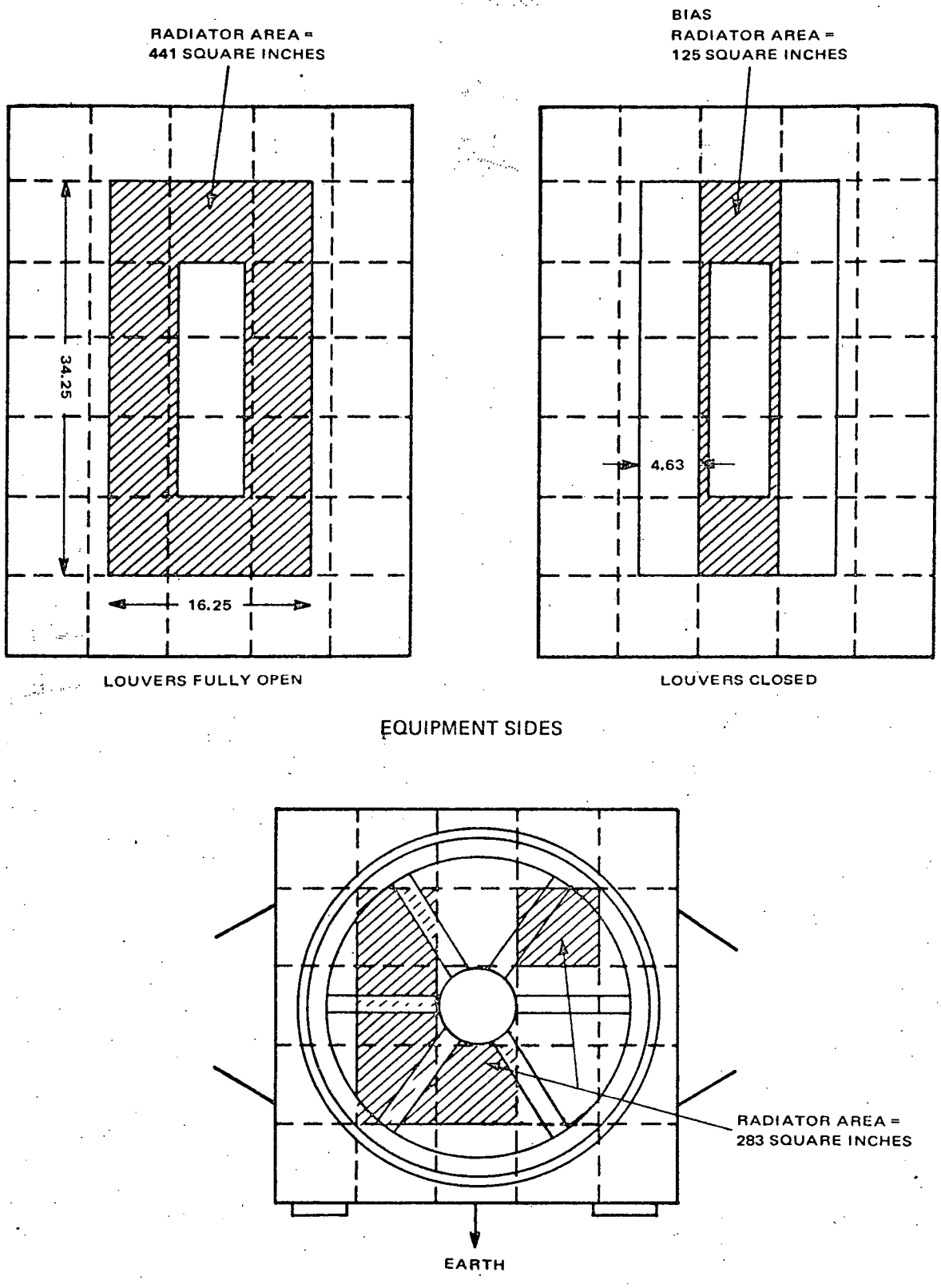

Figure III-1. Thermal Radiators

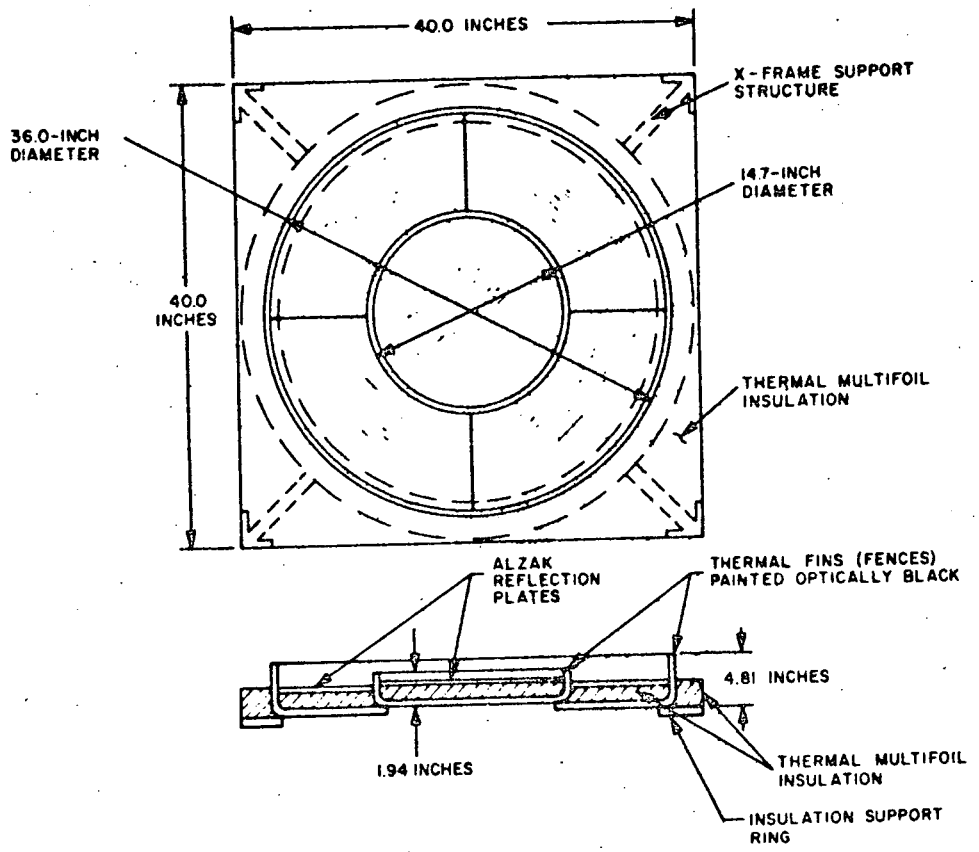

Figure III-2. Thermal Control Fence

B. FUNCTIONAL DESCRIPTION

1. Thermal Fence

The thermal fence is composed of two spun sheet metal cylinders, concentrically riveted to form a common sheet metal plate, as illustrated in Figure III-2. The horizontal surface of the assembly, called the fence plate, is covered with a multilayer insulation blanket at the outer or space viewing surface. A thin, flat, solar reflector is placed over the insulation blanket in the area enclosed by the vertical portions of the two cylinders. The vertical portions of the cylinders, called fence fins, project through the insulation and are exposed to space. The surface finish on the fins and plate is optically black. while the solar reflectors are Alzak aluminum, a high-emissivity, high-specular solar reflectance material.

The thermal fence is attached to an X-frame support member by thermal insulation spacers. The X-frame attaches to the spacecraft at four diagonal corners and is not insulated for structural reasons. Conductive heat losses from the fence to the spacecraft structure are minimal. Exchange of radiant energy between the thermal control fence and the interior of the spacecraft

TABLE III-1. SPACECRAFT THERMAL CONTROL SYSTEM PERFORMANCE REQUIREMENTS

Mode	Parameter	Component Mean Housing Temperature °C Based on an Orbit Avg. Power Dissipation**	
		max.	min.
Acquisition	Components Internal to Spacecraft Structure, Except Batteries & Vertical Temperature Profile Radiometers (VTPR's)	50	0
	Batteries	35	10
	VTPR's	35	-5
	Momentum Wheel Assembly (MWA)	30	5
	Scanning Radiometers (SR's)	45	-5
	VHRR's	40	-5
	Solar Proton Monitor (SPM)	55	-50
	Shunt Limiter:		
	(a) Transistors (Junct.)	123	-55
	(b) Resistors (Core)	175	-100
	Antennas:		
	(a) Beacon	120	-30
	(b) S-Band	90	-47
	(c) Real-Time	110	-5
	Solar Panel Actuators	45	-5
	Solar Panels* (Cells)	85	-110
Operational	Components Internal to Spacecraft Structure, Except Power Supply Electronics (PSE), Batteries & VTPR's)	40	5
	PSE	50	5
	Batteries	35	10
	VTPR's	30	0
	MWA	30	10
	SR's	40	0
	VHRR's	40	0
	SPM	15	-40
	Shunt Limiter:		
	(a) Transistors (Junct.)	123	-55
	(b) Resistors (Core)	175	-100
	Antennas:		
	(a) Beacon	120	-30
	(b) S-Band	90	-47
	(c) Real-Time	110	-95
	Solar Panels* (Cells)	85	-110
	Solar Panel Actuators	NA	NA

*These values are not orbit average but rather the maximum/end-of-eclipse minimum temperature extremes defined for 100% sun-time and 73% sun-time orbits respectively. (In a circular orbit of 790 mni altitude, 100% sun-time implies an orbit sun angle of 35.6 degrees or less and 73% sun-time, an orbit sun angle of 61.6 degrees.)

**These analyses were performed using a VHRR which had an electronics unit, located on the baseplate, which dissipated 15 watts.

occurs at the inner surface of the fenceplate. Areas on the top endplate beyond the periphery of the circular fenceplate are covered with a multilayer insulation blanket (see Figure III-2) to shield the view to space from the interior of the spacecraft.

The desired thermal performance is achieved as follows. At a given solar angle of incidence, (γ), solar energy is absorbed by the exposed black fins from two sources; namely, by direct illumination and by specular reflection from illuminated portions of the reflector plate. As the solar angle of incidence increases from 0 to 60 degrees, more fin absorption results due to the combined effects of increases in projected area and indirect specular reflections. The resulting fenceplate temperatures are used to control the spacecraft temperatures by means of radiation heat exchange with the spacecraft interior. Incorporating theoretically predicted and experimentally derived values, the net heat exchange between the thermal fenceplate and a representative 20°C spacecraft is portrayed graphically as a function of sun angle in Figure III-3.

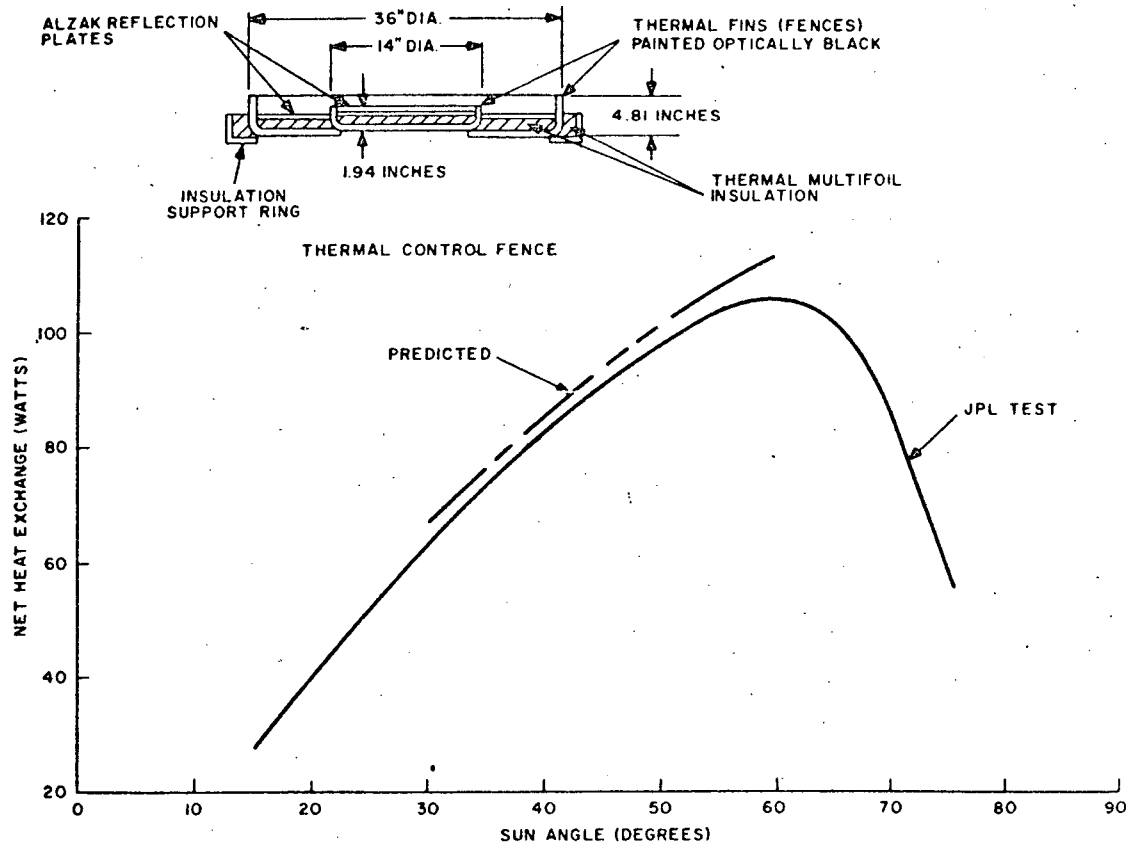

Figure III-3. Net Heat Exchange Between Thermal Fenceplate and 20°C Spacecraft

2. Active Thermal Controller

The active portion of the thermal control system consists of four independent active thermal control (ATC) units (two per equipment side), each consisting of a fluid expansion actuator/sensor mechanically linked to a single vertically hinged louver.

The actuator/sensor responds to local temperature changes at its mounting surface and develops motion through the controlled volumetric expansion of a confined fluid. The unit is located on, but is external to, the equipment panel between the panel and the insulation blanket, and is adjacent to the lower end of its associated louver. Each ATC is designed to provide a 90 degree louver rotation (i.e., fully closed to 90 degrees open) for an actuator/sensor box temperature change of 20°C. Further, as needs dictate, the 20°C operating range can be selected anywhere in the -10° to +55°C regime. Survival under a qualification soak temperature range of -15° to +60°C is a design requirement. A change in the temperature at the hydraulic reservoir causes a related change in the volume of the liquid; the volumetric differential is manifest in the bellows as a rectilinear expansion or contraction which is coupled to the mechanism used to open or close a louver on the side of the spacecraft. The relationships among ATC temperature differential, louver position and radiator surface effective emissivity are displayed graphically in Figure III-4.

The ATC's are operable only when the solar panels are deployed. Acquisition temperature requirements must be satisfied when the louvers are fixed in a forced open condition (i.e., 180 degrees from the closed position). Return of the louvers from the forced open condition is accomplished by means of spring loading.

3. Thermal Insulation

As determined under test, the insulation material provides an effective emissivity of approximately 0.02 in spacecraft areas which do not act as thermal control surfaces. In theory, the effective emissivity of a multilayered aluminized film insulation can be expressed as:

$$\frac{1}{\epsilon_e} = \frac{1}{\epsilon} + \frac{1}{\epsilon_1} + \frac{1}{\epsilon_2} + \frac{1}{\epsilon_3} + \ldots + \frac{1}{\epsilon_{2n}} - n$$

where

ϵ_e is effective emissivity,

ϵ is emissivity of spacecraft structure,

$\epsilon_1, \epsilon_2, \epsilon_3 \ldots$ is emissivity of subsequent film surface, and

n is number of film layers

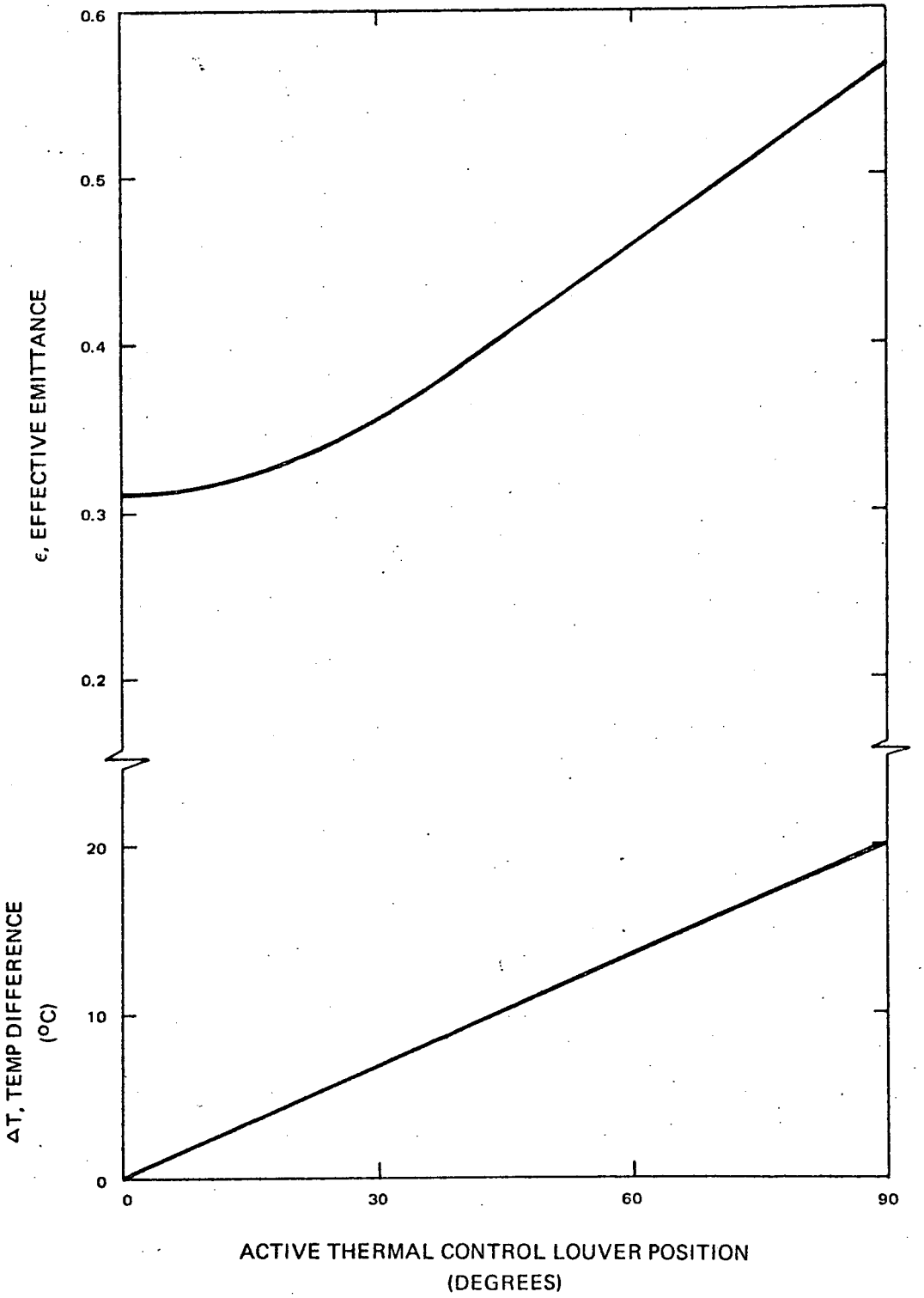

Figure III-4. Active Thermal Control, Functional Characteristics

The theoretical value is elusive in actual practice since other factors become prominent. Conduction from layer-to-layer, where contact between subsequent surfaces occurs, will reduce the insulating qualities of the material. Edge losses by radiation and face-to-face conduction by bonding, stitching, or fastening devices are also factors which increase the effective emissivity of the insulation, thereby reducing the insulating quality.

The insulation used consists of ten layers of aluminized film, each separated with nylon netting. As determined empirically in laboratory tests and substantiated in the TIROS M TTM and flight spacecraft tests, the effective emissivity meets the 0.01 to 0.02 requirement.

4. Thermal Painting

The paint used on the radiators and thermal fence is the 3M 400 series black velvet coating, selected for characteristically high values of emissivity and absorptivity which will be stable over the full orbit life of the spacecraft.

A detailed investigation of this series of 3M paint was performed by the AED Materials Engineering Activity. The specifications, pertinent to the ITOS D and E design, are listed in Table III-2.

TABLE III-2. THERMAL PAINT SPECIFICATIONS

RCA Specification	Subject
2021064 Manufacturing Specification	Thermal Control Coatings
1960416 Materials Specification	3M400 Series Black Velvet Coating
1960706 Materials Procedure	Thermal Control Coatings
1960707 Materials Procedure	Protective peelable coating for polished aluminum

5. Temperature Sensors

The temperature sensors measure the inflight temperatures at various locations within the spacecraft. This is done in analog fashion by resistance thermometry voltage divider action. A sensor output voltage is developed as a function of temperature and applied, via an electronic commutator which time-shares the sensor signal with those signals from other sensors and functions, to the input of the analog telemetry subsystems.

To achieve uniform temperature resolution over the various estimated temperature ranges predetermined for the selected locations of the sensors, there is, ideally, a linear relationship between the output voltage and sensor temperature.

A three-terminal passive element, using ceramic thermistors and fixed resistors, has been developed which provides an output voltage that is nearly a linear function of temperature when supplied with a low impedance, regulated voltage of -24.5 volts dc. This is accomplished by a unique combination of semiconductor and metallic resistance materials which have different temperature coefficients of resistance. The circuits and assemblies were qualified on the TIROS M program and have demonstrated reliability.

The sensors have a linear repeatability and intercept temperature insensitivity better than 10 percent, but individual calibration is required to achieve a readout accuracy of 1°C.

C. DESIGN HISTORY

1. Flight Correlation for TIROS M

Correlation between telemetered data from the in-flight TIROS M spacecraft and the analytical flight predictions has been obtained to within ±3°C at operational conditions. The sun angle for the period during which the correlation was attempted was 48°. The 45° sun-angle predictions were considered a valid basis for comparison, since the temperature vs. sun-angle curves proved to be almost flat (i.e., within 0.5°C) for values in the midrange region. Correlation of the acquisition mode in-flight temperatures with predictions was not possible since the electrical loads were increased from the acquisition level before a steady-state spacecraft temperature was attained.

2. Modification of the TIROS M Thermal Design for ITOS D and E

Utilizing the same Analytical Thermal Model that was employed in the final design exercise for the TIROS M thermal subsystem, the ITOS D and E modifications were applied without change to the thermal control elements. Based on the results of this analysis, equipments were relocated, the baseplate radiator area was enlarged, and the side radiator bias area (Figure III-1) was increased, thereby providing the thermal design configuration for the ITOS D and E spacecraft.

The factors necessitating an increase in the baseplate radiator included:

- Relocation of the SR's, which acted as heat leaks for the baseplate equipment. (These radiometers were shifted to the thermal fence end of the earth facing panel in order to accomodate location of the VHRR's at the baseplate end of the same panel. The VHRR's are to be thermally isolated from the spacecraft structure.)
- An increased electrical load, in comparison to that of the TIROS M spacecraft in the 30° sun angle BOL case.

Optimization of equipment location to limit the thermal gradients within the structure, in combination with an increase in the side radiator bias area near the fence end of the spacecraft, tends to compensate for the VTPR's field-of-view holes in the earth-facing panel.

3. Prediction of Flight Temperatures*

Flight predictions were computed using a 127 body analytical thermal model. A diagram indicating the nodal definitions for both the structure and the components is shown in Figure III-5.

For the purpose of bracketing the temperatures in the ITOS mission, an operational case characterized by a 30° sun angle orbit (i.e., a 100% sun-time orbit) with a BOL power supply and an acquisition mode case characterized by a 45° sun angle orbit (i.e., an 80% sun-time orbit) were postulated to define worst-hot and worst-cold performance.

Temperatures determined for these orbital conditions are orbit average steady-state values. The flight temperature predictions are shown in Table III-3 where the nodal designations are consistent with those of Figure III-5.

It can be observed that the range of predictions for the ITOS D and E spacecraft is wider than those for the TIROS M spacecraft. This is due primarily to the wider range in power dissipation from the 30° sun angle BOL operational case to the 45° acquisition case. Whereas the power dissipation has increased by 62 watts from 166 watts to 228 watts in operation at 30° BOL, during acquisition, the increase is but 22 watts from 47 watts to 69 watts, thereby spreading the range of predicted temperatures. The range is within the mission requirements, however, and presents no problems to the design.

---

*These analyses were performed with a VHRR which had an electronics unit, located on the baseplate, dissipating 15 watts. This extra dissipation does not change the minimum temperature condition because the VHRR electronics will be off in that mode. However, the maximum dissipation case that is shown has higher temperatures than will be achieved in practice. During the hardware design phase, the baseplate radiating areas will be sized to accommodate this VHRR change.

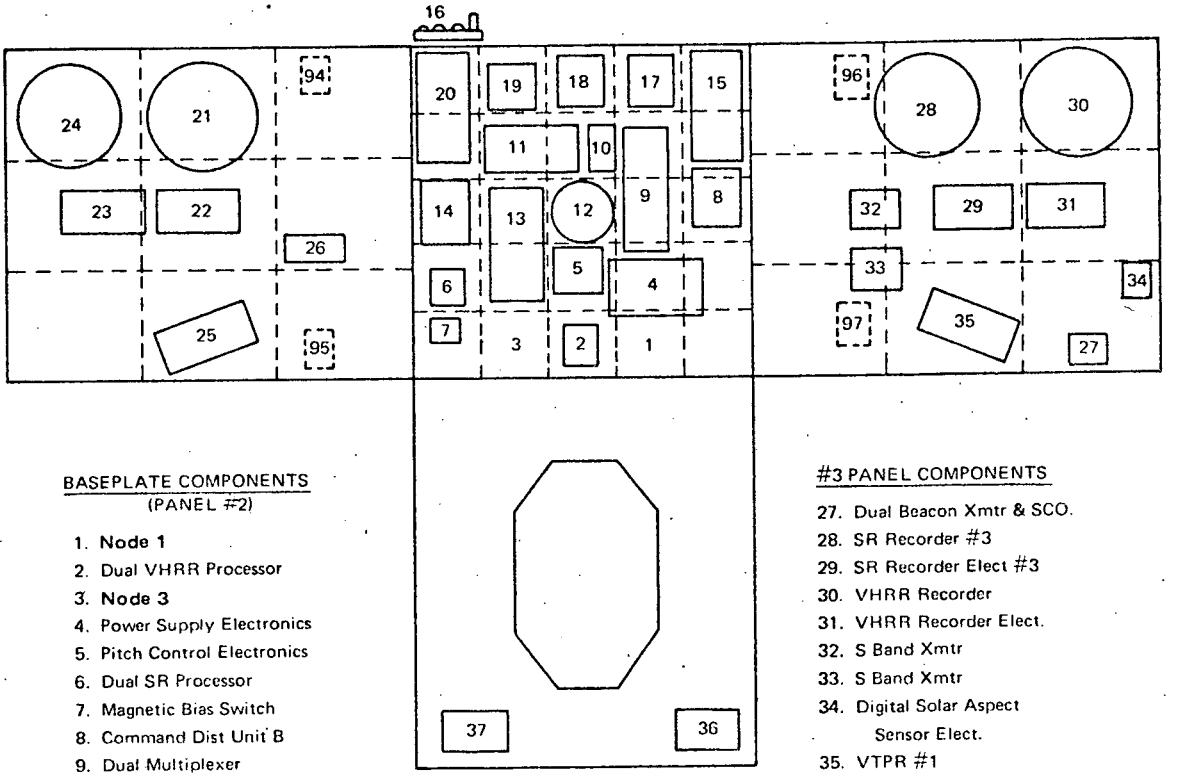

BASEPLATE COMPONENTS
(PANEL #2)

1. Node 1
2. Dual VHRR Processor
3. Node 3
4. Power Supply Electronics
5. Pitch Control Electronics
6. Dual SR Processor
7. Magnetic Bias Switch
8. Command Dist Unit B
9. Dual Multiplexer
10. Dual Command Rcvr
11. Dual Programmer
12. Momentum Wheel Assembly
13. Digital Data Processor
14. Command Dist Unit A
15. Battery #2
16. Solar Proton Monitor Sensors
17. Dual Time Base Unit
18. Dual Decoder
19. Solar Proton Monitor Electronics
20. Battery #1

#1 PANEL COMPONENTS

21. SR Recorder #1
22. SR Recorder Elect #1
23. SR Recorder Elect #2
24. SR Recorder #2
25. VTPR #2
26. Real-Time Xmtr (VHF)

#3 PANEL COMPONENTS

27. Dual Beacon Xmtr & SCO.
28. SR Recorder #3
29. SR Recorder Elect #3
30. VHRR Recorder
31. VHRR Recorder Elect.
32. S Band Xmtr
33. S Band Xmtr
34. Digital Solar Aspect Sensor Elect.
35. VTPR #1

EARTH PANEL COMPONENTS

36. SR #1 Electronics
37. SR #2 Electronics
38. Sunshield #1
39. Sunshield #2
40. SR #1
41. SR #2
42. S-Band Antenna #1
127. S-Band Antenna #2

ACTIVE THERMAL CONTROLLERS

94. Panel #1 ATC #2
95. Panel #1 ATC #1
96. Panel #3 ATC #3
97. Panel #3 ATC #4
123. Avg of 94 and 95
124. Avg of 96 and 97

Figure III-5. Nodal Definitions for Analytical Thermal Model (Sheet 1 of 2)

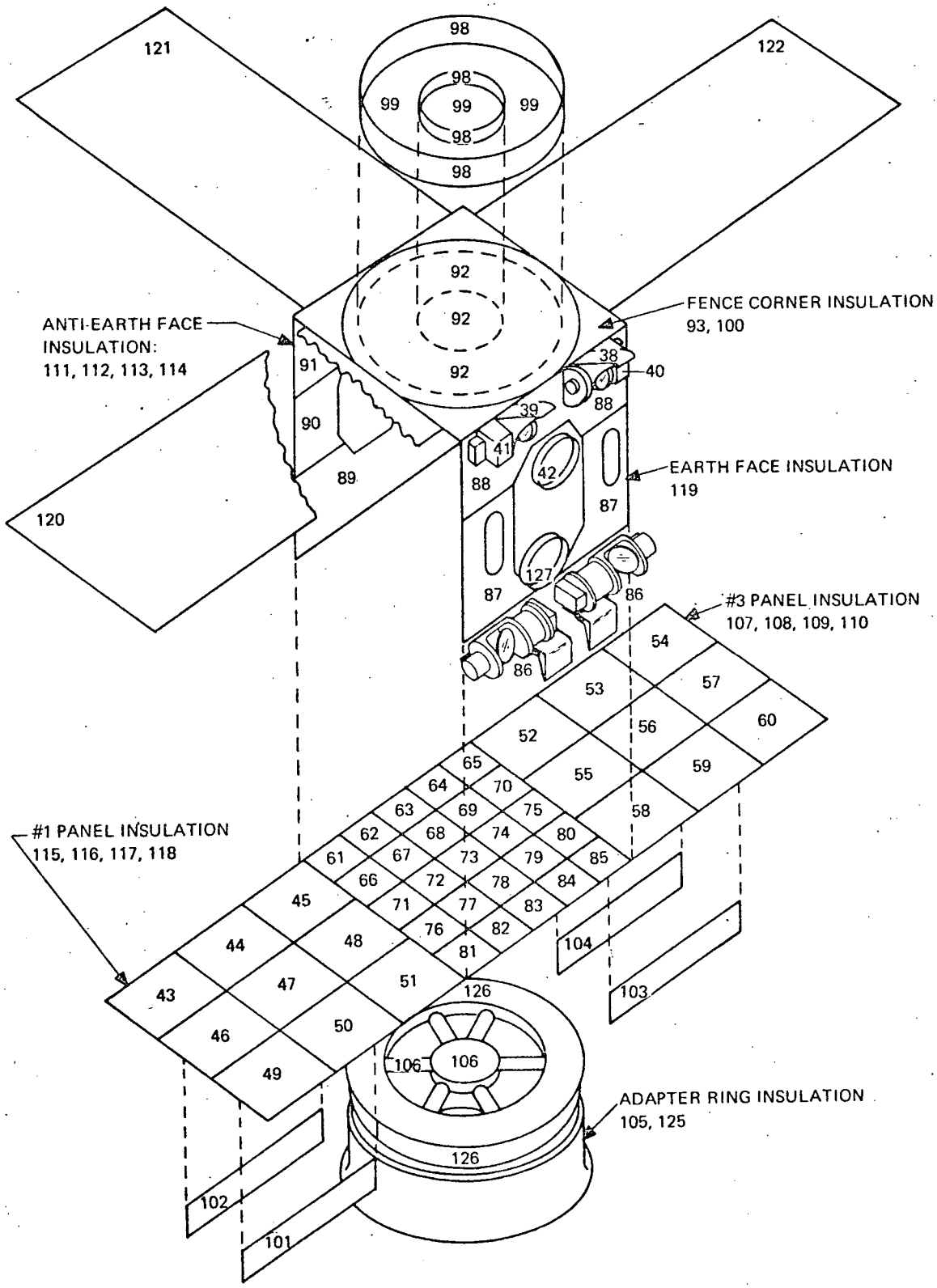

Figure III-5. Nodal Definitions for Analytical Thermal Model (Sheet 2 of 2)

TABLE III-3. ITOS D AND E OPERATIONAL AND ACQUISITION FLIGHT TEMPERATURE PREDICTIONS (Sheet 1 of 5)**

Node	Operational 30° Sun Angle (max pwr)	45° Acquisition*
1	37 °C	6 °C
2	33	6
3	27	6
4	43	9
5	31	7
6	26	5
7	26	6
8	26	3
9	26	2
10	25	4
11	25	4
12	22	6
13	27	5
14	24	4
15	37	9
16	-30	-24
17	29	7
18	28	6
19	28	5
20	35	10
21	23	6
22	21	3
23	23	6
24	26	12
25	25	5
26	30 °C	7 °C

* Panels Deployed

**These analyses were performed with a VHRR which had an electronics unit, located on the baseplate, dissipating 15 watts.

TABLE III-3. ITOS D AND E OPERATIONAL AND ACQUISITION FLIGHT TEMPERATURE PREDICTIONS (Sheet 2 of 5) **

Node	Operational 30° Sun Angle (max pwr)	45° Acquisition *
27	25 °C	13 °C
28	23	6
29	19	4
30	25	10
31	20	7
32	38	7
33	26	5
34	23	12
35	11	3
36	34	13
37	29	13
38	47	24
39	47	24
40	21	4
41	20	4
42	25	9
43	23	9
44	17	3
45	22	4
46	21	6
47	19	3
48	22	6
49	19	5
50	16	2
51	21	4
52	24 °C	4 °C

*Panels Deployed.
**These analyses were performed with a VHRR which had an electronics unit, located on the baseplate, dissipating 15 watts.

TABLE III-3. ITOS D AND E OPERATIONAL AND ACQUISITION FLIGHT TEMPERATURE PREDICTIONS (Sheet 3 of 5) **

Node	Operational 30° Sun Angle (max pwr)	45° Acquisition*
53	18 °C	4 °C
54	23	9
55	30	6
56	17	3
57	19	7
58	25	4
59	13	2
60	22	11
61	31	7
62	27	5
63	26	5
64.	28	5
65	32	7
66	25	4
67	22	2
68	24	3
69	22	0
70	26	3
71	23	4
72	26	4
73	26	4
74	25	1
75	26	2
76	24	4
77	27	5
78	29 °C	5 °C

*Panels Deployed.

**These analyses were performed with a VHRR which had an electronics unit, located on the baseplate, dissipating 15 watts.

TABLE III-3. ITOS D AND E OPERATIONAL AND ACQUISITION FLIGHT TEMPERATURE PREDICTIONS (Sheet 4 of 5) **

Node	Operational 30° Sun Angle (max pwr)	45° Acquisition*
79	40 °C	8 °C
80	32	5
81	25	5
82	27	5
83	29	5
84	34	6
85	29	5
86	30	10
87	28	6
88	25	8
89	26	6
90	25	8
91	28	13
92	42	31
93	25	11
94	21	4
95	20	4
96	24	4
97	25	4
98	50	41
99	33	9
100	126	88
101	-7	-1
102	4	0
103	-13	0
104	- 1 °C	0 °C

*Panels Deployed.

**These analyses were performed with a VHRR which had an electronics unit, located on the baseplate, dissipating 15 watts.

TABLE III-3. ITOS D AND E OPERATIONAL AND ACQUISITION FLIGHT TEMPERATURE PREDICTIONS (Sheet 5 of 5) **

Node	Operational 30° Sun Angle (max pwr)	45° Acquisition*
105	-64 °C	-78 °C
106	-53	-66
107	-16	-26
108	-33	-33
109	-50	-36
110	-51	-30
111	-24	-28
112	-43	-39
113	-59	-41
114	-61	-30
115	-16	-26
116	-33	-33
117	-48	-36
118	-52	-30
119	4	-16
120	46	-21
121	45	21
122	46	21
123	21	4
124	24	4
125	-115	-123
126	- 42	- 52
127	24 °C	8 °C

*Panels Deployed.

**These analyses were performed with a VHRR which had an electronics unit, located on the baseplate, dissipating 15 watts.

SECTION IV
VEHICLE DYNAMICS

SECTION IV
VEHICLE DYNAMICS

A. SUBSYSTEM DESCRIPTION

The design of the attitude control system is largely dictated by the pointing and stability requirements of the multiple environmental sensor system and by the rates of satellite and orbital plane motion. The optimum orientation for the multiple sensor/platform is continuous earth orientation. The coupling of a despun platform, through a bearing, to a spinning flywheel is the simplest method of meeting the sensor requirements while maintaining all the desirable dynamics of a spin-stabilized spacecraft.

The vehicle dynamics subsystem enables the satellite to align and maintain the roll, yaw, and pitch axes with a rotating set of coordinates consisting of the local horizontal, local vertical, and orbit normal. The subsystem will:

- Gyroscopically stabilize the despun platform (equipment module),
- Damp the nutation of the satellite to a half-cone angle of less than 0.3 degree,
- Precess the spacecraft until the momentum vector is nominally aligned with the orbit normal,
- Adjust the total momentum to within ±1.3 percent of the nominal design value of 212 inch-pound-seconds,
- Align and maintain the attitude about the pitch axis to ±1 degree about an earth reference, and
- Align and maintain the momentum vector to within ±1 degree about the orbit normal.

This vehicle dynamics subsystem is designed to operate continuously in the space environment for at least 1 year. The major functional elements of the subsystem are shown in Figure IV-1. The subsystem consists of a redundant pitch control loop, functionally redundant magnetic roll and yaw axes control (QOMAC and MBC) including sensors, redundant momentum control coils, redundant nutation dampers, and a digital solar aspect sensor.

In orbit, motion about the pitch axis is controlled by a flywheel and torque motor, utilizing error signals from one of two pitch horizon sensors, and the shaft encoder. The system is redundant, except for the flywheel. The horizon sensors derive their scanning from a mirror mounted on the flywheel. The pitch loop can be commanded to operate in the open-loop or closed-loop mode. In the open-loop mode, the flywheel rotates at one of two fixed speeds for

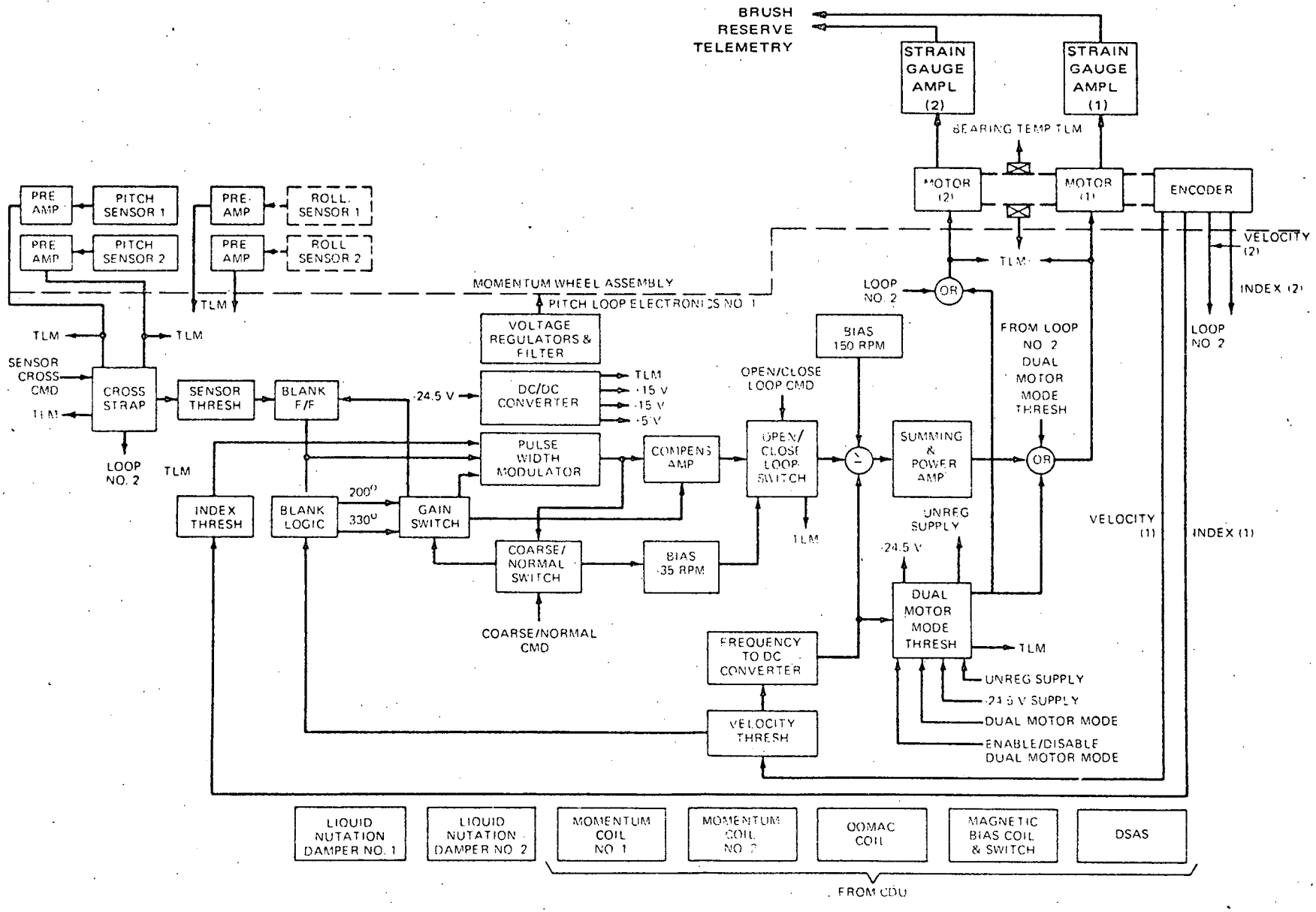

Figure IV-1. Vehicle Dynamics Subsystem, Block Diagram

dynamic stability; in this mode, the equipment module is not earth-oriented. In the closed-loop mode, the wheel rotates at a speed that causes the equipment module to despin to 1 revolution per orbit to establish its proper pitch orientation. The pitch control loop is capable of performing this orientation maneuver within approximately 6 minutes after the closed-loop command is received, assuming the spacecraft momentum and roll attitude are within specified design ranges.

If the momentum is not nominal, redundant magnetic coils can be activated to correct the pitch axis component. In addition to pitch axis control, the subsystem provides roll and yaw axis control by ground command. This is accomplished by utilizing the torques developed by the interaction of the earth's magnetic field with controlled dipole moments generated within the spacecraft. The controlled dipole moments are generated by the same type of magnetic coils flown successfully on the TOS spacecraft.

The magnetic bias control (MBC) coil, which is controlled by the magnetic bias switch, provides continuous torquing to offset in part the effect of the residual magnetic dipole along the pitch axis (i.e., flywheel spin axis) of the spacecraft. The level of current, and thus the dipole magnitude, is adjusted by groun command until the total dipole creates a torque that corrects for attitude changes due to orbital precession. The quarter orbit magnetic attitude control (QOMAC) coil, controlled by the command distribution unit (CDU), provides torquing to precess the spacecraft pitch axis about any vector lying in the orbit plane. By this means, "wheel mode" attitude (i.e., perpendicularity of the pitch axis with respect to the orbit plane) can be maintained. A constant level of current is applied to the QOMAC coil for a period determined by a ground-commanded program, with the direction of current reversed on a quarter-orbit basis. Three QOMAC modes of operation are provided. The high torque mode uses the combined maximum dipoles of MBC and QOMAC to provide a precession rate of about 10 degrees per orbit at nominal momentum. A lower precession rate (i.e., 1.2 degrees per orbit at nominal momentum), and therefore greater resolution, is obtained with only the QOMAC coil operating. Finally, in the unipolar mode, the continuous current-on-time is reduced and programmed to generate only undirectional dipoles at half orbit intervals to achieve precession about the line of nodes.

Spin axis nutation is controlled by liquid dampers similar to those flown on the TOS spacecraft. Nutation may result from the following disturbances: (1) second stage booster nutation, (2) operation of the separation equipment, (3) operation of the magnetic control components, (4) bombardment by micrometeorites, and (5) operation of payload components with uncompensated angular momentum.

The spacecraft is equipped with IR sensors to provide attitude information during each flywheel revolution. After the spacecraft is oriented in the wheel mode by the second stage booster, roll attitude information can be obtained throughout

the orbit with its availability restricted only by the location of the ground station. Pitch sensor scanning requires deployment of the solar panels to provide an unobstructed field of view. Additional attitude information, of particular value prior to pitch acquisition, can also be obtained from the digital solar aspect sensor (DSAS). The DSAS is similar to that flown on TOS and is mounted on the equipment module.

B. INITIAL ORIENTATION MANEUVER

1. Sequence

The initial orientation maneuver consists of the events required to alter the attitude and momentum of the spacecraft from second stage separation to three-axis earth-oriented control.

Subsequent to the yaw manevuer executed by the second stage, the spacecraft pitch axis is nominally perpendicular to the orbit plane. The following sequence of events occurs:

a. Booster propulsion will spin up the second stage and the spacecraft to 2.75 rpm ±10 percent.

b. Upon a signal from the second stage, the spacecraft will separate.

c. At the instant of separation, the separation switch will apply unregulated power to the pitch control electronics.

d. The pitch control loop, having been preselected for open loop operation in the coarse gain state, will accelerate the momentum wheel assembly to 115 rpm. The acceleration will require 50 seconds, maximum. Simultaneously, the equipment module spin rate will decrease to 0.66 rpm ±4.2 percent.

e. The transverse momentum induced by the second stage including the mismatch of the separation springs will result in a maximum tipoff and half-cone nutation angle of 12.3 degrees. This figure is based on the maximum transverse spacecraft rate of 3 degrees per second, defined by the cognizant NASA agency.

f. The spacecraft nutation will decay with a time constant of about one and one-quarter hours, due to the action of the liquid dampers.

g. Utilizing the roll sensor data telemetered over the 2.3-kHz subcarrier (Figure IV-2) and the DSAS, the following parameters will be determined during each ground station contact:

- Roll attitude, based on sensor earth time or fractional sky time history, sensor scan period, and spacecraft altitude,
- Equipment module spin rate, based on DSAS trigger sensor pulses,
- Momentum wheel spin rate based on time between successive index pulses,
- Nutation angle and instantaneous roll angle, based on minimum and maximum sensor earth time in one nutation period (30 seconds maximum).

h. If the maximum roll angle exceeds ±3 degrees, the QOMAC program will be utilized to bring the attitude within acceptable limits prior to step k.

i. If the equipment module spin rate is greater than 0.94 rpm or less than 0.39 rpm, with the momentum wheel rotating at 115 rpm, ground commanded commutation of the momentum coils may be utilized for adjustment prior to step k.

j. If the nutation half-cone angle exceeds 2 degrees, additional orbits of damping will be allowed to occur before initiating step k.

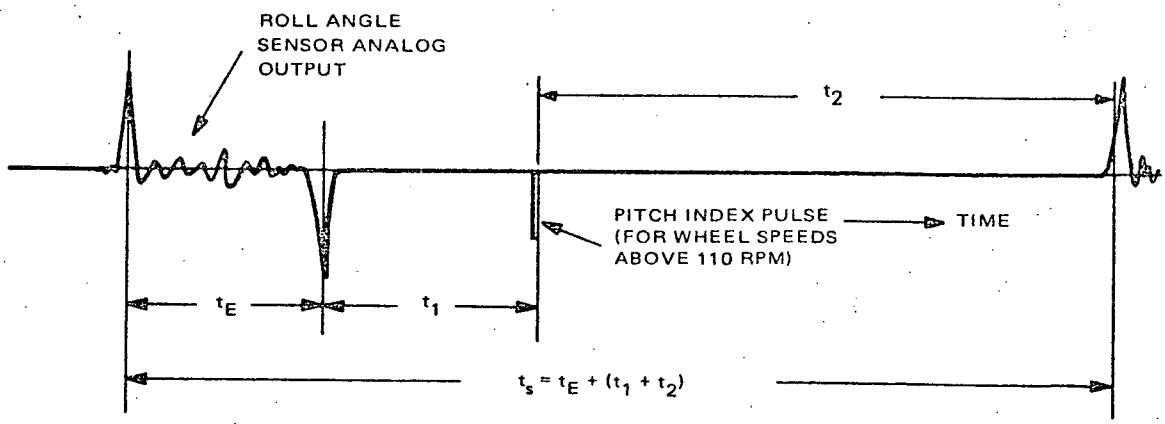

t_E ROLL SENSOR EARTH TIME

t_s SPIN PERIOD (WHEEL + EQUIPMENT MODULE)

t_1 TIME FROM ROLL SENSOR EARTH-SKY PULSE TO PITCH INDEX PULSE (CONSTANT AFTER PITCH LOCKON)

t_2 TIME FROM PITCH INDEX PULSE TO ROLL SENSOR SKY-EARTH PULSE

Figure IV-2. Typical Signals Telemetered on 2.3-kHz Subcarrier

k. During a ground station pass containing at least 10 minutes of contact time, the tachometer loop will be operated in the 150 rpm mode (normal gain setting). The equipment module spin rate will subsequently be between ±0.275 rpm. The transient will last no more than 1 minute and can be observed by measurements taken under step g above.

l. At a nominal wheel speed of 150 rpm, the solar panels are deployed by means of a ground command. The solar panel deployment will take a maximum of 170 seconds, and the equipment module spin rate will subsequently be between ±0.17 rpm.

m. After the completion of the solar panel deployment, earth lock-on (i.e., capture) will be commanded by selecting closed loop mode operation.

Capture can be verified by observing the magnitude and constant phase relationship of the output of the roll sensor and the pitch index pulse.

Subsequent to capture, the appropriate magnetic torquing coils will be utilized to maintain the pitch axis orthogonal to the orbit plane, and to support the level of system angular momentum at the nominal value of 212 inch-pound-seconds.

2. Biased Flywheel Operation

After separation from the second stage, it is necessary to establish a gyroscopically stable spacecraft configuration. Such stability can be achieved if the following equation is satisfied:*

$$\omega_3 (I_3 - I_1) + \omega_f I_f > 0 \qquad \text{(IV-1)}$$

where

ω_3 is the equipment module spin rate about the pitch axis,

ω_f is the flywheel spin rate relative to the equipment module,

I_3 is the spacecraft moment-of-inertia about the spin axis,

I_1 is the maximum spacecraft moment-of-inertia about a transverse axis, and

*Astro-Electronics Division of the RCA Corporation, Flywheel Stabilized Magnetically Torqued Attitude Control System for Meteorological Satellites Study Program, Final Report, Contract NAS5-3886, Princeton, N.J., December 4, 1964.

I_f is the flywheel moment-of-inertia.

This criterion is based on the following assumptions:

(1) Damper on despun body

(2) $H \cos \Theta = I_3 \omega_3 + I_f \omega_f$

(3) $H \sin \Theta = I_1 \omega_1$

(4) $2E = I_3 \omega_3^2 + I_1 \omega_1^2 + I_f \omega_f^2$

(5) ω_f = constant

where

H is the total momentum,

Θ is the half-cone nutation angle,

E is the total spacecraft rotational kinetic energy, and

ω_1 is the spacecraft spin rate about the transverse axis.

The maximum transverse moment-of-inertia for the ITOS D and E spacecraft was used to arrive at the conservative stability limits shown in Figure IV-3. Assumptions 1 through 4 above are definitions applicable to the system. Open loop operation of the flywheel satisfies assumption 5. A constant spacecraft spin rate can be maintained by momentum control through ground command.

C. NUTATION DAMPING

1. General

Nutation occurs when the angular momentum vector and spin vector (i.e., angular velocity vector) characterizing the spacecraft are not coincident. The spin vector then "cones" about the momentum vector at a rate determined by the inertia characteristics and the spin rates of the spacecraft and the flywheel. This motion must be kept to a minimum since it results in a pointing error of the primary sensors. Redundant dampers in the spacecraft provide an effective and simple method for reducing nutation angles to a small fraction of a degree.*

*A complete analysis of the dynamic action of these dampers is presented in the report referenced in Paragraph B.2.

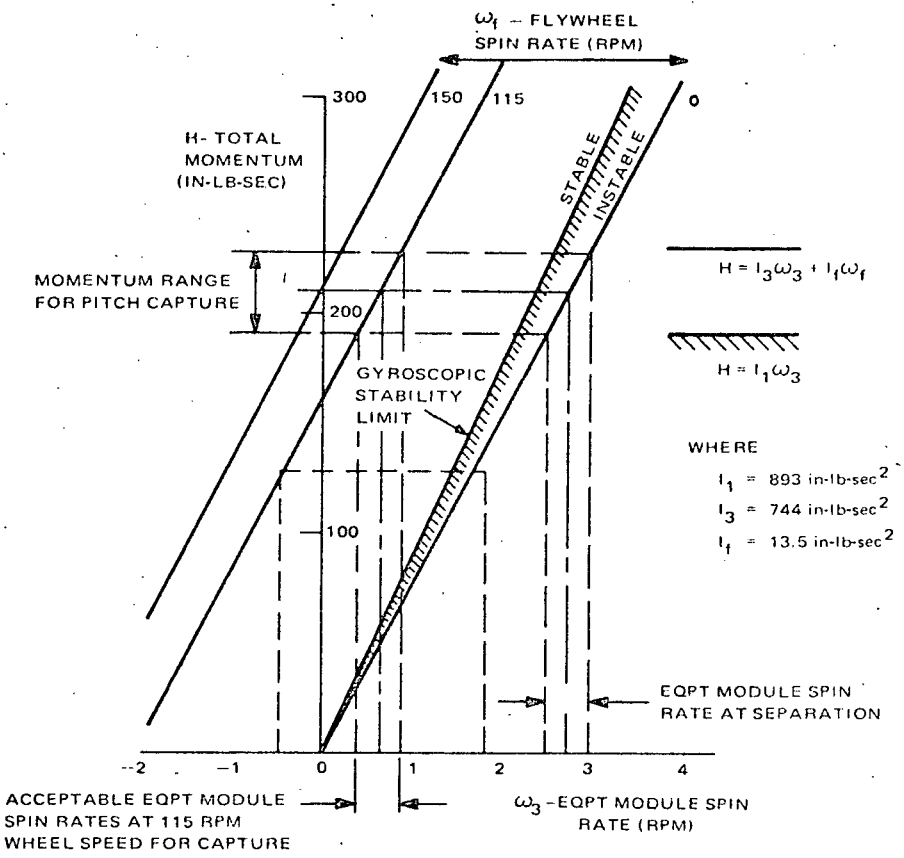

Figure IV-3. Equipment Module Momentum Versus Spin Rate

The optimum liquid damper configuration is a toroid completely filled with silicone oil and mounted with the plane of the toroid parallel to the spin axis. During nutation of the vehicle, transverse angular accelerations excite the oil, causing it to move relative to the toroid walls. The kinetic energy of rotation is expended as heat through the action of the viscous drag of the fluid. This loss of kinetic energy is manifest as a momentum transfer from the transverse axis to the spin axis of the spacecraft, thereby decreasing the nutation. This depletion of kinetic energy continues as long as the fluid maintains its Newtonian viscosity characteristics. Thus, with no external energy input to the spacecraft, the damper action continues driving the nutation cone angle towards null.

2. Basic Design

a. MATHEMATICAL ANALYSIS

A mathematical analysis of the dampers is presented in Volume III of Design Study Report for the Improved TOS (ITOS) System, Astro-Electronics Division of the RCA Corporation, Princeton, N.J., June 7, 1968, AED R-3308.

(Hereafter, this report will be referred to as the ITOS Design Study Report.) The analysis yields the following equation for computing the damper time constant:

$$\tau = \frac{I_t}{F I_d \dot{\phi}} \qquad \text{(IV-2)}$$

where

- τ is the damper time constant,
- I_t is the spacecraft moment of inertia with respect to that transverse axis about which the damper is mounted
- F is the coupling factor,
- I_d is the axial moment of inertia of the damper fluid, and
- $\dot{\phi}$ is the forcing frequency, the spacecraft nutation frequency when the vehicle is in earth-lock condition.

b. MECHANICAL CONFIGURATION

As shown in Figure IV-4, the nutation damper design is not the optimum toroid, assumed above. The dampers are mounted inside the spacecraft, on adjacent sides of the equipment module, with the plane of the dampers parallel to the spin axis. Each damper contains an accumulator-type expansion chamber to act as a void trap for gasses and to allow room for thermal expansion of the fluid. The fluid is a low viscosity silicone oil (Dow Corning type 200). The damper assemblies are fabricated from aluminum tubing, with an outside diameter of 1.0 inch and a wall thickness of 0.035 inch. The combined weight of the two nutation dampers is estimated at 10.9 pounds.

c. PRESSURIZATION

The damper performance as predicted by design calculations is based on the absence of vapor bubbles in the tube. These bubbles will form at temperatures below that prevailing during the filling process. For a spinning satellite such as the TOS series or a satellite launched with a rapidly spinning last stage, such bubbles will gather in the radial fill tube and thus have no essential effect on the damping process. However, for ITOS D and E, which is launched with a two-stage booster, such bubbles could form and remain in the main tube. In this situation the fluid inertial forces would not be able to overcome the surface tension for small angular excursions, thus resulting in a nutation angle threshold.

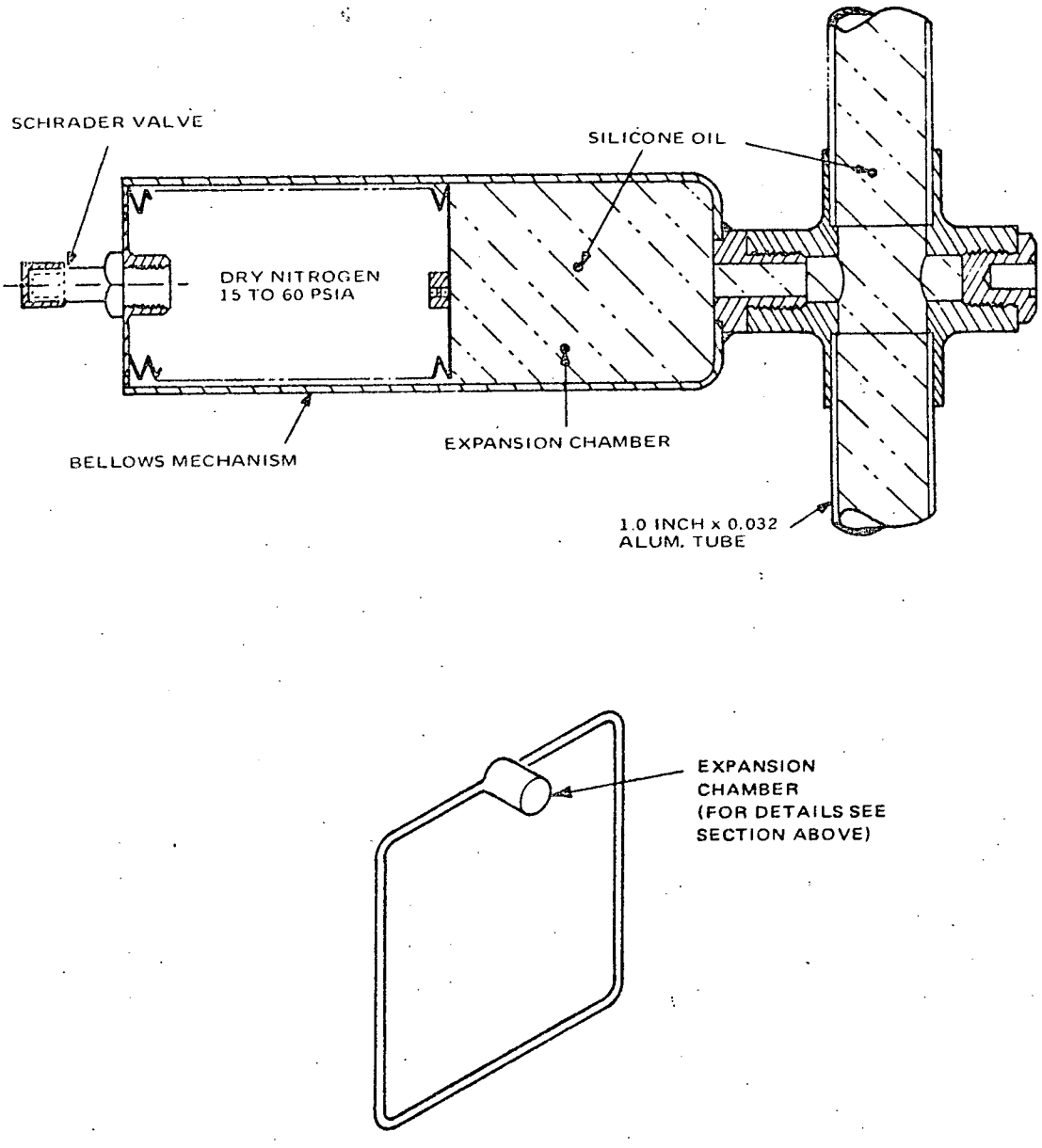

Figure IV-4. Liquid-Filled Nutation Damper

Therefore, the expansion chamber contains an accumulator which permits the fluid volume to vary with temperature, without the resultant formation of bubbles.

3. Damping Time Constant

For the damper configuration indicated above (i.e., dampers mounted about orthogonal transverse axes), the nominal damping time constant is given by:

$$\tau = \frac{(I_1 I_2)^{3/2}}{(I_1 + I_2)} \frac{1}{F I_d H} \qquad \text{(IV-3)}$$

consistent with Equation IV-2, where

I_1, I_2 are the transverse moments of inertia for the spacecraft,

H is the total system angular moment, and
the substitution $\phi = H/\sqrt{I_1 I_2}$ has been made.

Table IV-1 presents a summary of the spacecraft and nutation damper parameters during the principal dynamic modes.

D. ATTITUDE SENSING

1. General

The following sensors are used for determination of spacecraft attitude and spin rates:

- One digital solar aspect sensor (DSAS),
- Two pitch horizon sensors, and
- Two roll horizon sensors.

The digital solar aspect sensor can be utilized to measure the angle between the positive spacecraft pitch axis and the sun line and the spin rate of the equipment module. It derives its scanning from the rotation of the equipment module. Prior to pitch lock-on, such a measurement can be accomplished whenever ground station contact is established and the satellite is in daylight. Subsequent to pitch lock-on (i.e., when the equipment module, on which the DSAS is mounted, rotates once per orbit), sun angle readout is only possible once or

TABLE IV-1. DAMPING TIME CONSTANTS

Parameter	Dynamic Mode	
	Acquisition[1]	Mission[2]
Total Momentum, H (in-lb-sec.)	212	212
Transverse Inertias, I_1, (in-lb-sec.^{2}) I_2	893 893	1326 1134
Nutation Frequency, φ (radians/second)	0.237	0.171
Effective Damper Inertia, FI_d (in-lb-sec.^{2})	0.4166	0.4166
Time Constant, τ (minutes)	75	142

Notes:
1. Acquisition Mode - Solar panels folded
2. Mission Mode - Solar panels deployed

twice a day. Although the sun angle is of interest, particularly during the acquisition phase, its measurement by means of the DSAS is not essential to the mission.

Pitch and roll measurement is accomplished by means of pairs of redundant IR sensors, two for pitch and two for roll. Scanning is accomplished by means of the mirror assembly which is integral with the momentum wheel. The roll sensors can be utilized prior to solar panel deployment.

2. Digital Solar Aspect Sensor

The digital solar aspect sensor, DSAS, which has been space-proven on TOS flights, is used to determine the angle between the vehicle-sun line and the fly-wheel spin axis during the initial orientation maneuver (Figure IV-5). It is also useful for measuring equipment module spin rate prior to pitch sensor activation. The indicator has an entrance slit with a field of view of 128 degrees. As the spacecraft rotates, the 128 degree beam generates a solid angle of approximately 3.6π steradians about the satellite's spin axis. The sunlight that falls upon the entrance slit strikes a reticle that has a 7-bit Gray-coded pattern screen. Seven photocells are positioned behind the Gray-coded pattern, and, depending on the angle of incidence of the sun rays, all, some or none of the

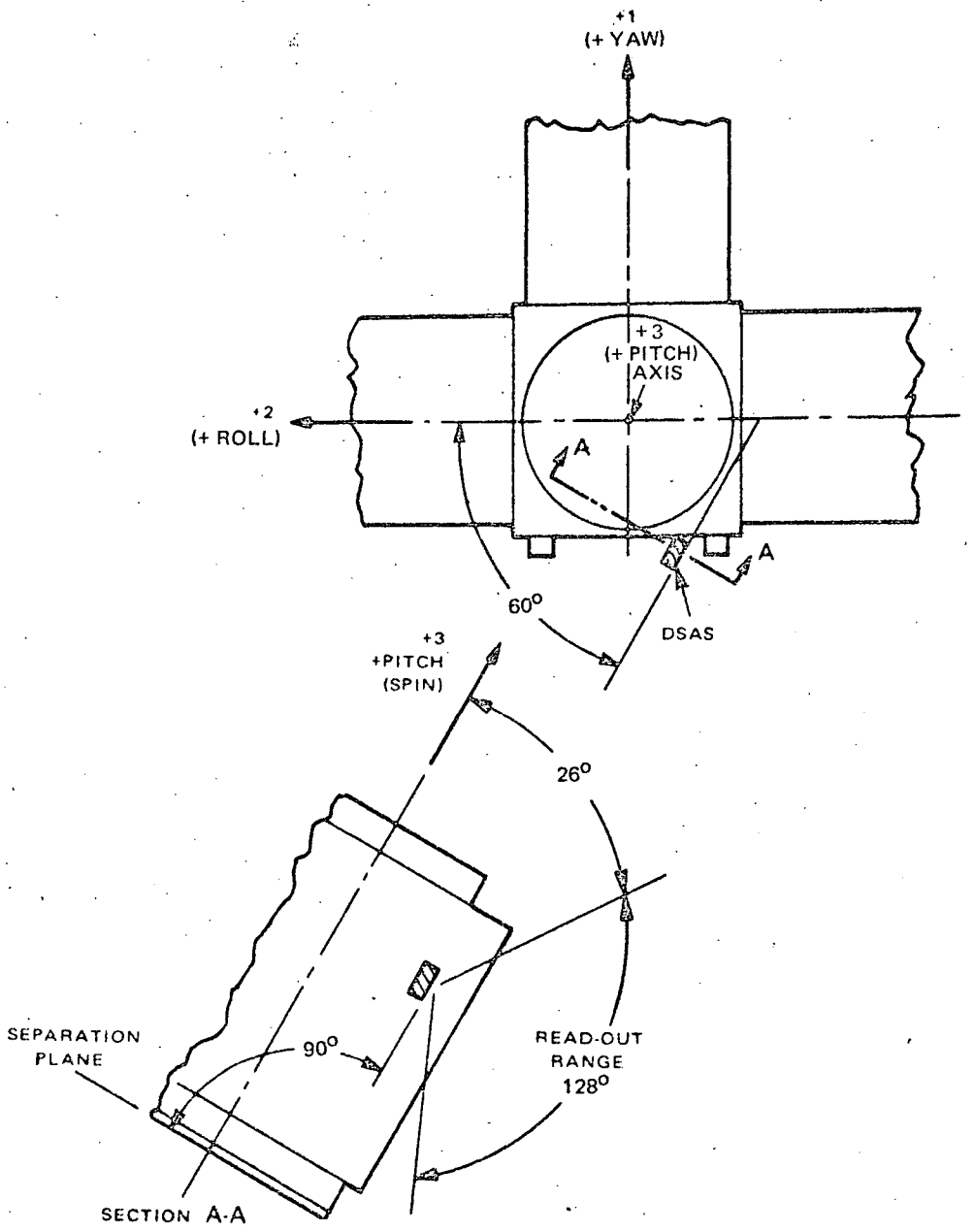

Figure IV-5. Digital Solar Aspect Sensor Alignment Angles Relative to Spacecraft Reference Axis

photocells are illuminated. The signal outputs of the seven cells are amplified, stored, and updated. When a trigger pulse is received from a command photocell, the stored data is read out serially. The DSAS has a resolution of 1.0 degree and an accuracy of ±0.5 degree.

3. Infrared Sensors

a. GENERAL

The pitch sensors and the roll sensors are identical in construction. They are distinguished by their orientation in the momentum wheel tee-plate and the geometry of their respective scanning mirrors. In the mission mode, the field of view of each sensor intersects the earth once per flywheel revolution. The bolometers respond to the radiance change between cold space and warm earth, thus producing the horizon-intercept data necessary for determining roll attitude and pitch reference. The scanning geometry is shown in Figure IV-6.

Each sensor comprises a 1-inch germanium lens system and a germanium-immersed bolometer. The bolometer contains an active thermistor which is exposed to incident radiation, and a compensating thermistor which is shielded from radiation and senses only the ambient temperature changes. The two thermistors form part of a bridge circuit across which a dc bias is applied. When the incident radiation is focused onto the active thermistor, its temperature rises. The change in temperature results in a change of thermistor resistance, which affects the bridge balance and results in a voltage output at the junction of the thermistors. This voltage has two components: (1) a dc component due to the mismatch of the resistance and (2) an ac component due to the change in radiation levels at the earth horizon crossover.

The resistance of each thermistor is approximately 1.40×10^5 ohms at 25°C. A change in resistance of less than 0.15 ohm generates a signal equal to the system noise level. Since the mismatch between the thermistors exceeds 1 percent of their resistance values, the dc signal may at times exceed the ac signal level by a factor of 10^4. Furthermore, the matching of thermistor resistances is not constant, but shifts with changes in ambient temperature. However, since only the ac signal is of interest, the bolometer output is capacitively coupled to the preamplifier, thereby differentiating the ac component while effectively blocking the dc component. Irradiation of the sensors by the sun, even through indirect exposure or reflection, during operation would significantly increase their recovery time. Since a long recovery time would interfere with the generation of horizon crossing signals, an 8-micron "cut-on" filter is provided in order to attenuate the off-axis solar radiation which might impinge upon the bolometer. This filter has previously been used in the TIROS and TOS programs.

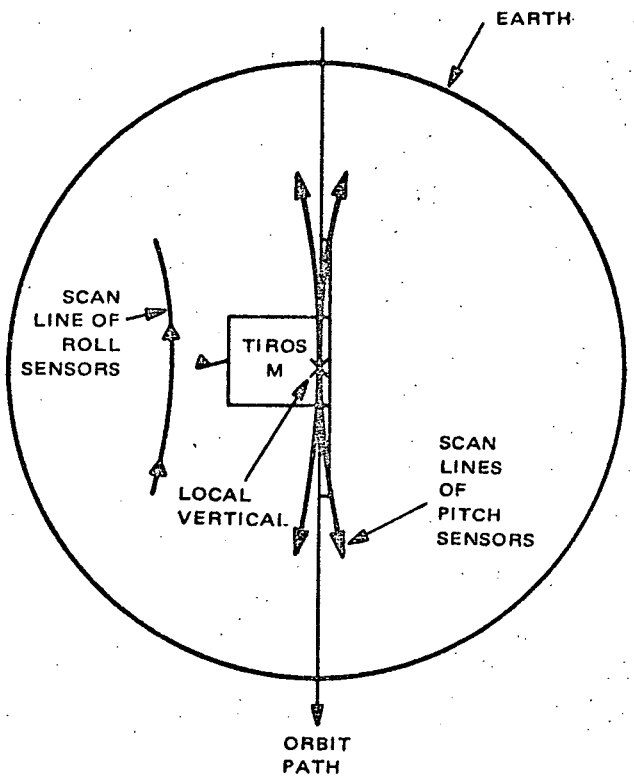

Figure IV-6. Scan Lines of Attitude Sensors

b. ELECTRONICS

The sensor electronics associated with the pitch and roll bolometers consist of a preamplifier, filter, regulator, and threshold amplifier (see Figure IV-7). The electronics are a flight-proven RCA design, modified to provide a bandwidth of approximately 15 to 160 Hz. The preamplifier and filter are located adjacent to the associated bolometers and are mounted on the same plate. The regulator and threshold amplifier are located in the pitch loop electronics package.

The preamplifier includes:

- A capacitor-coupled input and dc-coupled transistor stages throughout.
- A high-impedance, low-noise field effect transistor input stage,
- A dc bias loop that provides bias point stabilization, and
- Two separate negative feedback loops which maintain stable gain and dynamic characteristics.

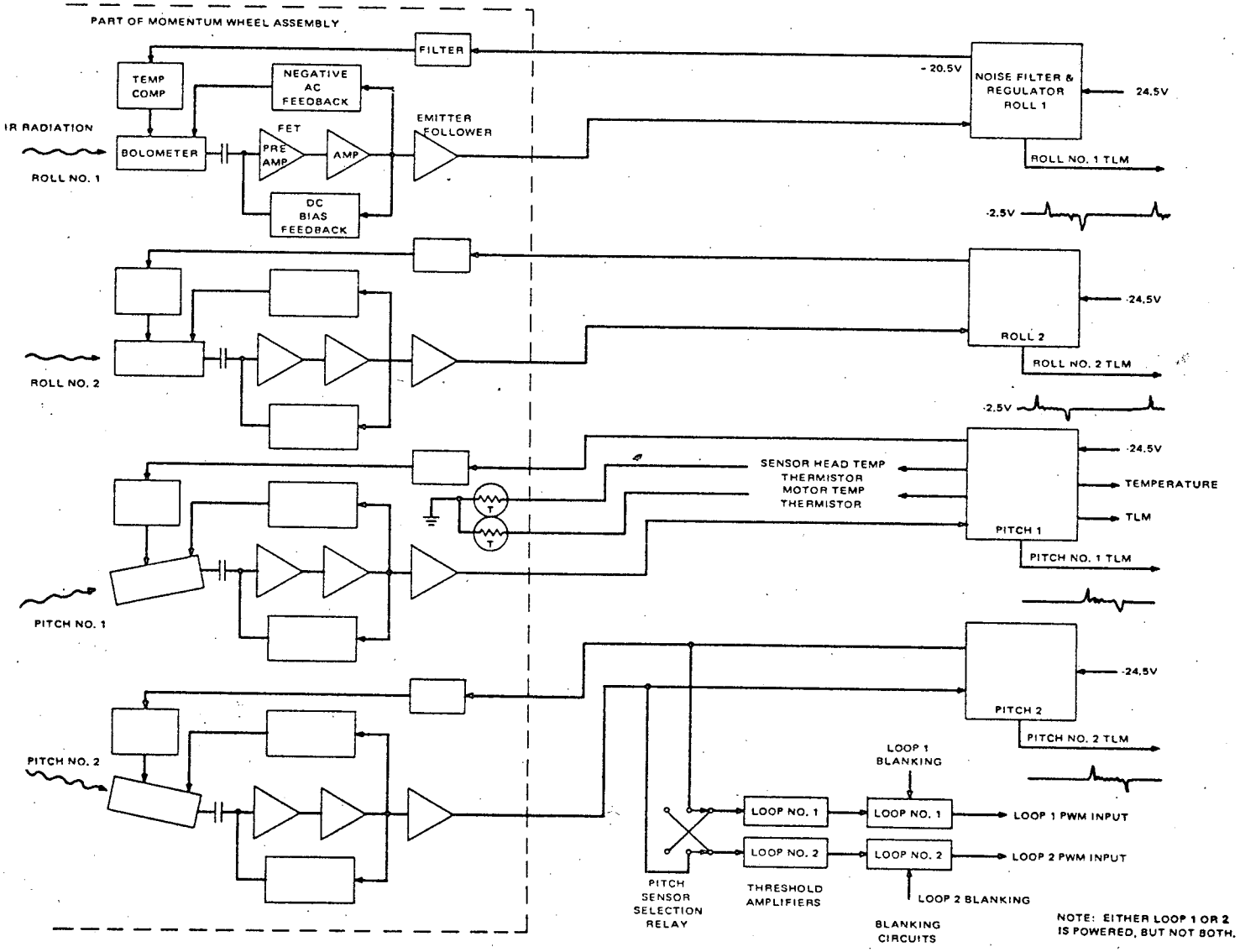

Figure IV-7. Pitch and Roll Sensor Electronics, Block Diagram

The primary function of the regulator is to act as an ultra-low-frequency rejection filter. The circuit is designed to reduce supply line ripple in the frequency range from 0.1 to 15 Hz. An active filter is included in the design to provide additional filtering for the bolometer bias supply throughout the bandpass of the amplifier.

4. Pitch and Roll Sensing

a. GENERAL

The pitch and roll sensors are germanium-immersed bolometers with a 1-inch diameter germanium lens system. As shown in Figure IV-8, the four bolometers are mounted in a fixed position in the momentum wheel tee-plate.

A mirror assembly, comprising two reflecting surfaces inclined with respect to the momentum wheel spin axis, is fixed to the wheel shaft. This assembly reflects the bolometer lines of sight. The two mirror surfaces, which are oriented 180 degrees apart, have an aluminized finish and are protected with a silicon monoxide coating.

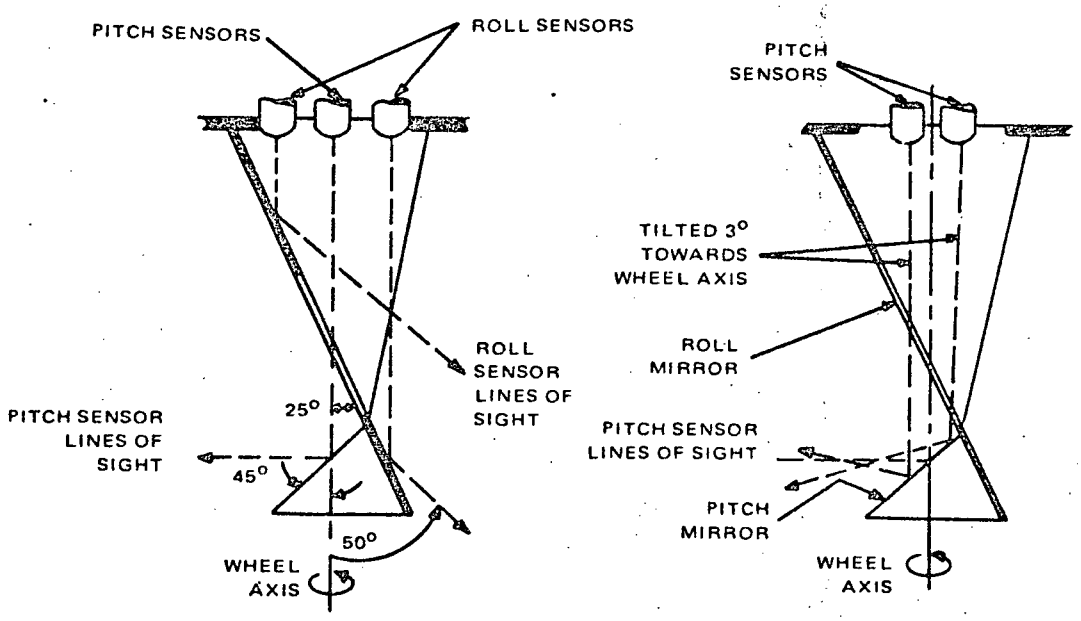

Figure IV-8. Attitude Sensor Configuration

The mirror reflecting surface for the roll sensors is inclined 25-degrees with respect to the flywheel spin axis. Accordingly, since the roll sensors are mounted such that their lines of sight are parallel to the spin axis, the scan angle (the angle between this axis and the sensor lines of sight) is 50 degrees. The pitch sensors, the reflecting surface for which is inclined 45 degrees with respect to the spin axis, are skew mounted such that their lines of sight are directed towards the spin axis at angles of 3 degrees. The effect of the skew mounting is manifest in the generation of a scan path which is asymmetric about the spin axis, being characterized by the sinusoidally varying scan angle shown in Figure IV-9.

By use of these two differently oriented scan paths and knowledge of the position of the moon, it is possible to avoid false input signals from the moon. Since the bolometers are heat detectors, they respond equally well to IR inputs from the moon or the earth. By virtue of the pitch sensor line of sight offset, limited field of view, and the blanking shown in Figure IV-9, the potentially misleading moon inputs occurring monthly can be avoided.

Depending upon the pitch servo gain state, either 200 degrees or 330 degrees of the pitch scan are blanked. The selection is made automatically by the servo loop as a function of the sensed pitch error. At operational momentum levels, once earth-lock has been established, 330 degrees of the scan are blanked. This limiting of the scan window minimizes the possibility of admitting spurious radiative inputs. In the presence of the large pitch errors commonly encountered during the search mode (i.e., prior to the establishment of earth lock), only 200 degrees of the pitch scan are blanked. However, in order to ensure unblanking of the scan prior to the initiation of the next flywheel rotation, the 330 degree deblanking pulse is retained in this mode as well.

b. PITCH SENSING

The pitch servo loop utilizes a horizon pulse generated within one of the pitch sensors at a space-earth transition, and an index pulse to derive an error signal which defines the pitch attitude of the equipment module with respect to the earth horizon.

The accuracy of the pitch attitude sensing depends primarily on the uncertainties of locating the infrared horizon. Since the earth-space transition is contaminated by noise from preceding earth and cloud temperature variations, only the space-earth transistion is used for pitch determination.

Variations in horizon temperature give rise to sensing uncertainties. The bolometer/preamplifier combination is calibrated for a nominal horizon temperature of 225^{o}K. As the horizon temperature deviates from the calibration level, the threshold amplifier trigger point varies from its nominal position in the scan rotation. Based on nominal bolometer and preamplifier characteristics (i.e., the response of the cascaded combination is characterized by a minimum

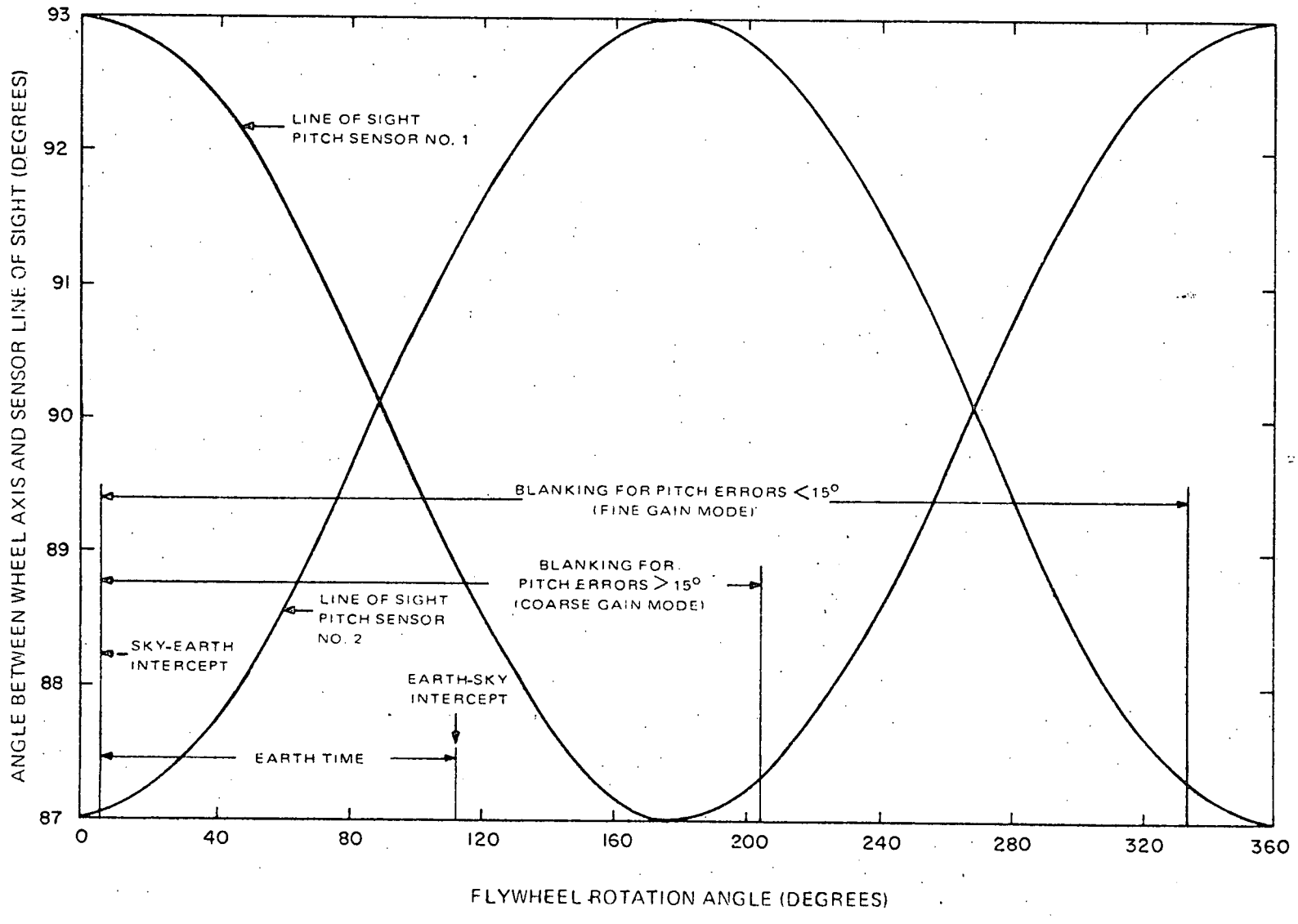

Figure IV-9. Pitch Sensor Scan Geometry

10 to 90 percent rise time of between 2.5 and 3.0 milliseconds and thresholding of the preamplifier output at the 160 millivolt level) this variation, expressed as a time displacement, approximates ±0.54 millisecond over the 200 to 280°K horizon temperature range as shown in Figure IV-10. The results displayed are predicated on a 150 rpm scan rate, a 1.3-degree, slightly rounded bolometer field-of-ivew, and a straight-edge target. The time-constant limited nature of the sensor response is immediately evident. Consistent with the assumed scan rate, the indicated time variation in threshold triggering corresponds to an angular position error of ±0.486 degree. Since the pitch servo provides time coincidence between the index pulse and the threshold amplifier horizon pulse, the angular position error attending horizon temperature variations is transformed directly into a pitch attitude offset. The relationships among the horizon temperatre, the time displacement of the threshold amplifier horizon pulse, and the resultant pitch attitude offset are portrayed in Figure IV-11.

The bolometer selected for use in the ITOS D and E system has a time constant of approximately 3.3 milliseconds. This selection was made in light of the following facts: (1) satisfactory experimental data when using peaking techniques, (2) previous experience in working with this bolometer, (3) bias source circuitry not available at time of implementation but necessary for a faster time constant bolometer, and (4) possibility of increased noise levels due to the added bias source.

Utilizing the space-earth transition as a reference for the local vertical assumes a circular orbit of known altitude. Variations in altitude, common to elliptical orbits, would induce an offset in pitch attitude, as indicated in Figure IV-12.

The effects of temperature changes in the mirror assembly upon the sensor accuracy were considered. The metallic mirror is thermally coupled to the flywheel and, therefore, can be expected to have a negligible temperature change during one rotation. The bolometers always view the surface of the mirror, but the mirror temperature and, consequently, the energy radiated from the mirror to the bolometer will be essentially constant during one spin period. The ac-coupled bolometer electronics will therefore see only changes in the radiant energy deriving from horizon crossings, with no noticeable signal due to mirror temperature changes.

c. ROLL SENSING

The horizon crossing data generated by either of the two roll sensors is telemetered to a CDA Station where it is processed to derive the required error-correction commands.

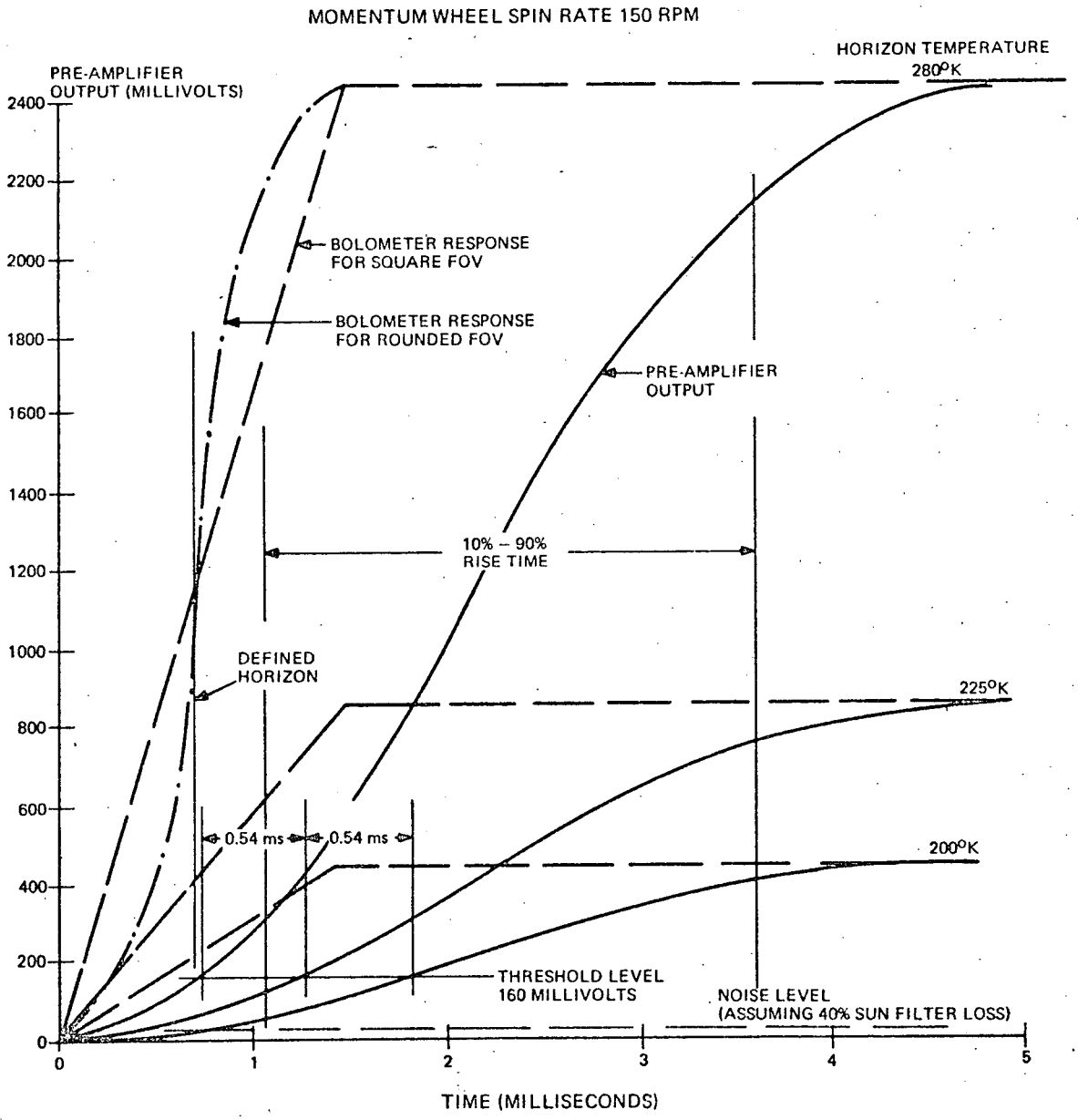

Figure IV-10. Horizon Sensor Pre-Amplifier Output

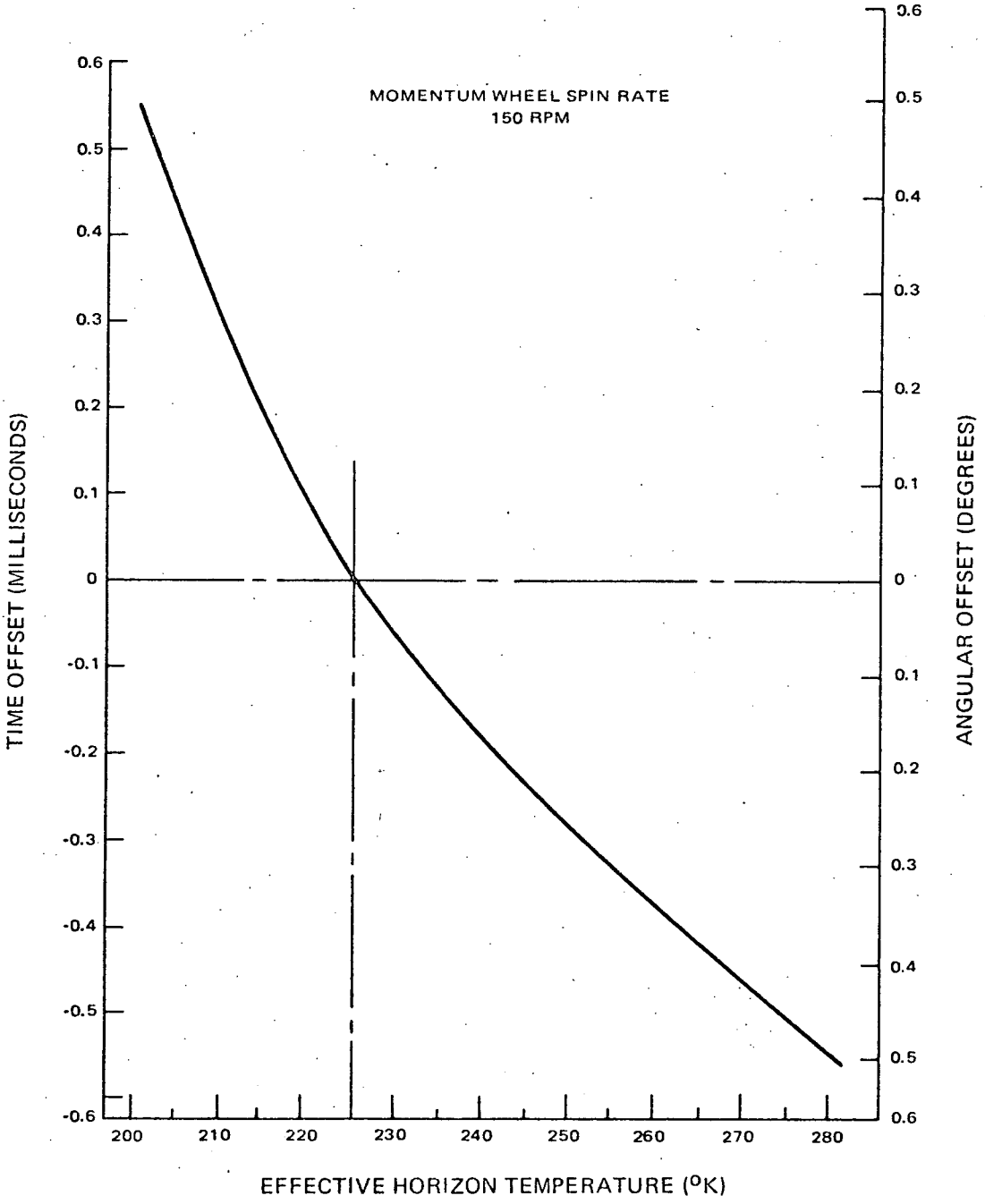

Figure IV-11. Pitch Horizon Pulse Offset as a Function of Horizon Temperature Variation

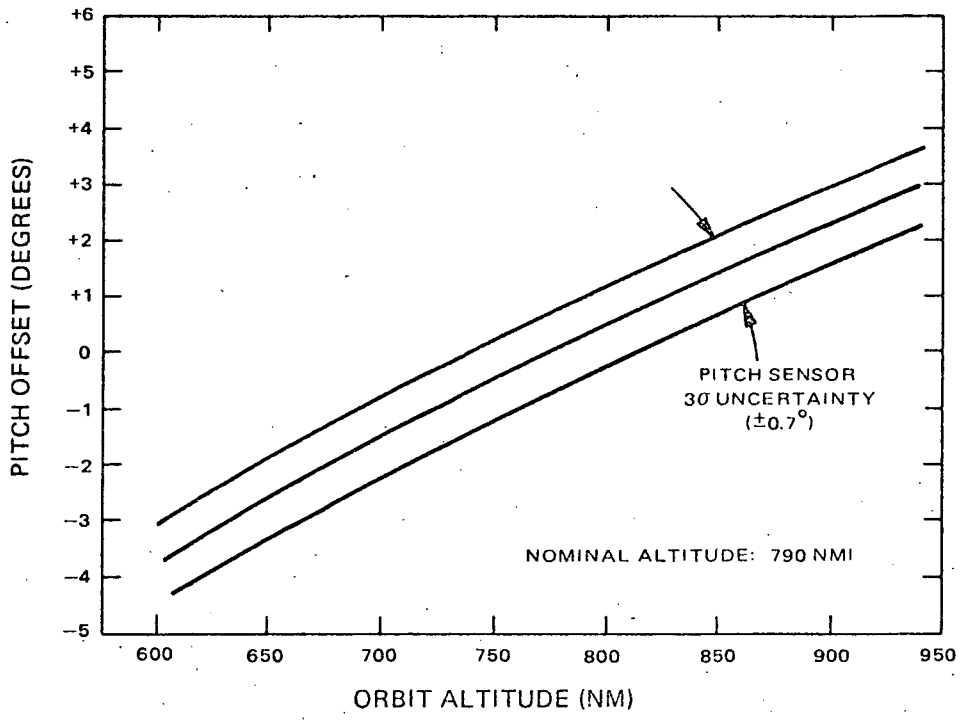

Figure IV-12. Pitch Offset Versus Orbit Altitude

In normal roll operation, the preamplifier provides an analog signal which produces a telemetry link peak-signal-to-rms-noise ratio of approximately 37 dB. This value is specified for a spin rate of 150 rpm, a horizon temperature of 280°K, and a grazing angle of 53.6 degrees. The telemetry data is subsequently processed to compute the error corrections required for maintaining proper attitude and spin control.

Since the geometry of the roll sensor scan is essentially a half-Vee scan, satellite ephemeris information is required for attitude determination. If a hybrid technique of combining half-Vee data with pitch data is employed, the ephemeris data is not required. A comparison of these techniques is presented in the ITOS Design Study Report, Volume III. The accuracy of roll determination depends on the method of data reduction at the ground station and the amount of data utilized. A 3σ-scatter in instantaneous roll measurement of about 0.56 degree random and a bias offset of less than 0.26 degree can be realized.

E. MAGNETIC ATTITUDE CONTROL AND MOMENTUM CONTROL

1. General

The magnetic attitude control and momentum control systems have two basic functions: (1) to keep the spacecraft momentum vector aligned with the orbit normal and (2) to control the total momentum of the satellite consistent with the dynamic range of the pitch control loop.

The magnetic attitude control system is identical to that used on TIROS M/ITOS-1. Roll control is maintained by quarter-orbit magnetic attitude control (QOMAC). Unipolar torquing precesses the satellite about the orbit line of nodes, with the primary purpose of counteracting the effects of solar torque. A magnetic bias control (MBC) coil nulls the residual magnetic dipole about the spacecraft pitch axis to a value which produces the required 1-degree-per-day precession rate for orbit motion compensation.

The magnetic momentum control system of the spacecraft is similar to the spin control system used on TOS spacecraft, utilizing control coils like the magnetic spin control (MASC) coils used previously. The basic change in the operation of the coils is that current commutation is not required after the spacecraft has achieved an earth locked condition. If momentum adjustments are desired prior to earth acquisition, coil current must be commutated at half spin intervals via ground command.

2. Coordinate System

To describe the spacecraft attitude and momentum control scheme, orbital geometry, magnetic fields, and related topics covered in this discussion, appropriate coordinate systems must be defined. A set of unit vectors, $\hat{\ell}$, $\hat{b}$, and $\hat{n}$, is used in desirbing roll control. A second set, $\hat{r}$, $\hat{t}$, and $\hat{n}$, is required for description of momentum control. As shown in Figure IV-13, $\hat{n}$ is directed along the positive orbit normal, $\hat{\ell}$ is directed along the line of nodes toward the ascending node, $\hat{b}$, is perpendicular to $\hat{n}$ and $\hat{\ell}$, $\hat{r}$ is directed along the radius vector from the center of the earth to the spacecraft, and $\hat{t}$ is directed along the spacecraft velocity vector. The $\hat{r}$, $\hat{t}$, and $\hat{n}$ set rotates with respect to the $\hat{\ell}$, $\hat{b}$, and $\hat{n}$ set once per orbit; the rotation angle, β, is the orbit anomaly angle measured from the ascending node.

The spacecraft coordinate system, $\hat{1}$, $\hat{2}$, and $\hat{3}$ and the attitude angles in the $\hat{r}$, $\hat{t}$, and $\hat{n}$ system are shown in Figure IV-14. The momentum vector of the spacecraft is along the $\hat{3}$ axis and should be directed along the orbit normal. Normally, the pitch axis is coincident with the $\hat{n}$ axis, the yaw axis with the $\hat{r}$ axis, and the roll axis with the $\hat{t}$ axis. The roll angle, ϕ, measured by the

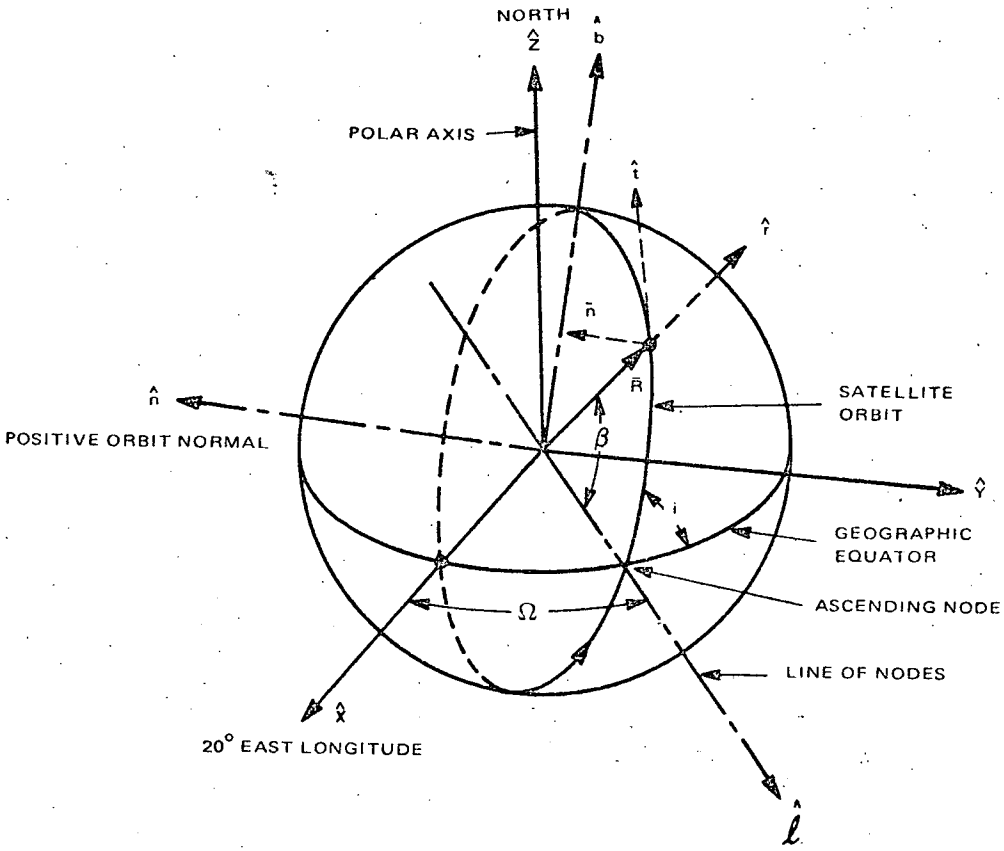

Figure IV-13. Orbital Coordinates

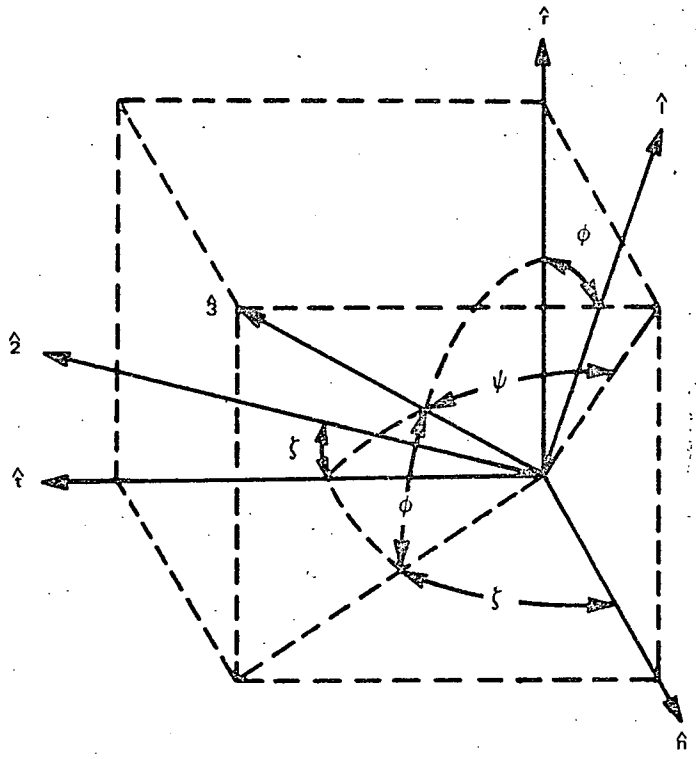

Figure IV-14. Spacecraft Coordinates and Attitude Angles

horizon sensors, is the angle between the pitch axis and the local horizontal plane. This angle is cyclic over an orbit due to the gyroscopic stiffness of the spacecraft. Attitude information is obtained from knowledge of the maximum roll angle, ϕ max, and its point of occurrence in the orbit.

3. Geomagnetic Field Equations

The earth's magnetic field equations have been derived and discussed on many earlier programs, including TOS. Expressed in the ($\hat{\ell}$, $\hat{b}$, $\hat{n}$) coordinate system, the field equations take the following form:

$$B_{\ell} = \frac{K}{R^3}\left[3/2\ (\cos i \sin i_m \cos \Omega - \sin i \cos i_m) \sin 2\beta + \frac{3}{2} \sin i_m \sin \Omega \cos 2\beta + 1/2 \sin i_m \sin \Omega\right], \quad \text{(IV-4)}$$

$$B_b = \frac{K}{R^3}\left[-3/2\ (\cos i \sin i_m \cos \Omega - \sin i \cos i_m) \cos 2\beta + 3/2 \sin i_m \sin \Omega \sin 2\beta + 1/2 \cos i \sin i_m \cos \Omega - \sin i \cos i_m\right], \text{ and} \quad \text{(IV-5)}$$

$$B_n = \frac{K}{R^3}\ (\cos i \cos i_m + \sin i \sin i_m \cos \Omega) \quad \text{(IV-6)}$$

The magnetic field model embodied in these equations is sufficiently accurate for computational and programming purposes.

In the preceding equations

- B_{ℓ}, B_b, and B_n are the earth's magnetic field components in the $\hat{\ell}$, $\hat{b}$, $\hat{n}$ coordinate system,
- K is the geomagnetic dipole moment constant,
- R is the orbit radius,
- i is the orbit inclination,
- i_m is the earth's magnetic dipole inclination, and
- Ω is an angle which defines the location of the orbit ascending node with respect to the intersection of the geographic and geomagnetic equators (see Figure IV-13).

For a three-axis stabilized spacecraft, the magnetic field equations are readily transformed into the $(\hat{r}, \hat{t}, \hat{n})$ system. This transformation is effected under a rotation of the $(\hat{\ell}, \hat{b}, \hat{n})$ system about $\hat{n}$ through the angle β. The resulting equations are:

$$B_r = \frac{2K}{R^3}\left[(\cos i \sin i_m \cos \Omega - \sin i \cos i_m) \sin \beta + \sin i_m \sin \Omega \cos \beta\right], \quad \text{(IV-7)}$$

$$B_t = \frac{K}{R^3}\left[-(\cos i \sin i_m \cos \Omega - \sin i \cos i_m) \cos \beta + \sin i_m \sin \Omega \sin \beta\right], \text{ and} \quad \text{(IV-8)}$$

$$B_n = \frac{K}{R^3}(\cos i \cos i_m + \sin i \sin i_m \cos \Omega). \quad \text{(IV-9)}$$

4. Quarter-Orbit Magnetic Attitude Control

The QOMAC coil is installed in the spacecraft with its dipole vector parallel to the pitch axis. The dipole moment, M_Q, of the QOMAC coil is taken to be positive when coincident with the system angular momentum vector, such that:

$$\overline{M}_Q = \pm M_Q \hat{3}. \quad \text{(IV-10)}$$

It has been shown that the precessional motion of the pitch axis at any instant will be directed oppositely to the earth's magnetic field vector at that instant.

Using the uncanted dipole model of the earth's magnetic field (i.e., $i_m = 0$ in the foregoing equations), the magnitude of the precession rate* (ω_{PQ}) averaged over one QOMAC torque cycle is given by:

$$\tilde{\omega}_{PQ} = \frac{3KM_Q}{R^3 H} \sin i, \quad \text{(IV-11)}$$

where H is the total spacecraft momentum.

*Astro-Electronics Division of the RCA Corporation, Design Report for the TIROS Operational Satellite (TOS) System, Contract NAS5-3173, Princeton, N.J., December 30, 1964.

In practice, the inclination of the earth's magnetic dipole can be neglected without significantly impairing the accuracy of the model. With a total of 212 inch-pound-seconds of angular momentum in the system and a low torque dipole moment of 4.2 Atm^2, the average precession rate if 0.545 degree per torque cycle or 1.09 degrees per orbit. Similarly, at nominal momentum, with a total high torque dipole of 38 Atm^2, the average precession rate of 5.0 degrees per torque cycle or 10.0 degrees per orbit.

5. Unipolar Torque

The normal QOMAC cycle consists of quarter-orbit reversals of current in the coil, initiated at a precise point in time measured from the ascending node crossing. For the nominal dipole moment (i.e., 4.2 ampere-turn-$meters^2$), a precession rate of 0.545 degree per torque cycle is obtained.

As shown in the disturbance analysis the maximum solar torques about the $\hat{b}$-axis can be as great as 0.6×10^{-4} pound-inch, on an orbit-average basis. This error could be corrected with normal QOMAC and would require a QOMAC cycle every fifth orbit. However, a unipolar torquing programmer has been added which will operate continuously to torque the satellite for approximately 5.6 minutes per half orbit. By this expedient, normal QOMAC will be required only once or twice a week to correct errors due to other disturbances as well as any possible accumulation of small errors from the unipolar torquing operations. This would also enhance the accuracy of attitude determination. The normal QOMAC operation will be accomplished with this programmer in the same manner as is employed on the TOS spacecraft.

The unipolar torquing programmer will command a positive dipole of a selected duration at two equally spaced intervals per orbit. The pertinent parameters, referenced to the standard QOMAC cycle, are defined in Figure IV-15. Torquing by this method can precess the satellite up to 3.8 degrees per day, with a resolution of 0.088 degree per day or 0.0035 degree per half orbit. This method requires the following programmer inputs:

- Delay time (as for normal QOMAC),
- Quarter orbit time (as for normal QOMAC), and
- Unipolar ON time.

The negative dipole is suppressed in this mode. Commandable delay times up to a maximum of 68.3 minutes can be realized with a resolution of 4 seconds. The range for the quarter orbit period is from 25.6 to 34.1 minutes with a nominal value of 28.5 minutes and a resolution of 4 seconds. Unipolar ON time can be varied from 16 seconds to 17.1 minutes, the maximum value being a function of the orbital period. The ON time resolution is 16 seconds.

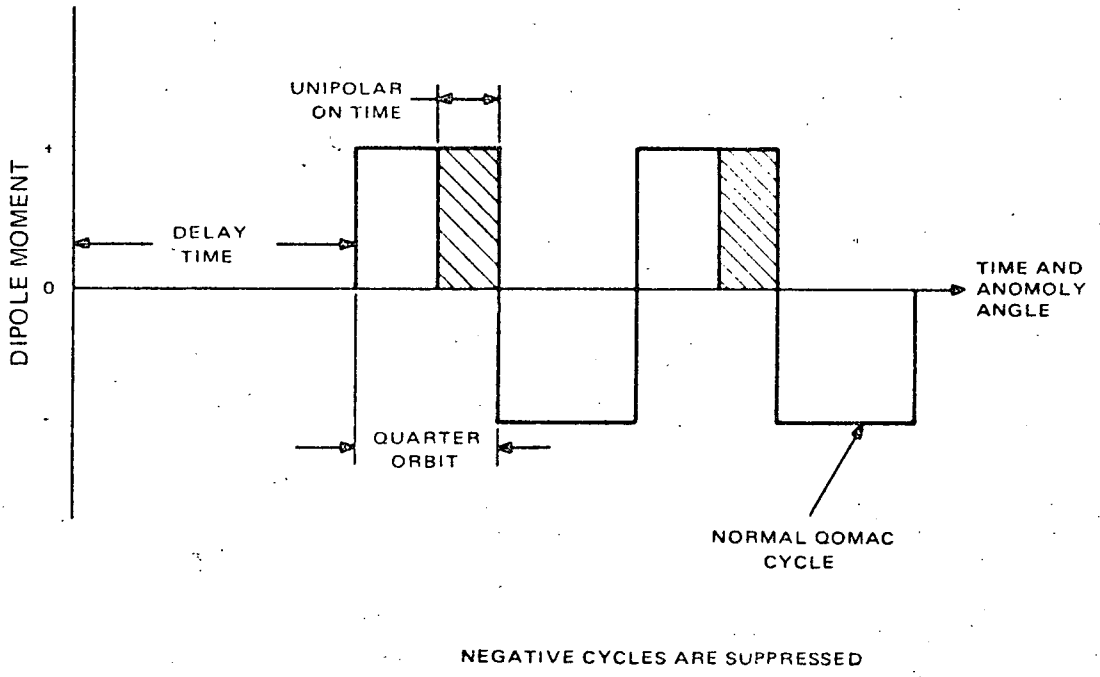

Figure IV-15. Unipolar Pulse Mode

Figure IV-16 shows the unipolar pulse superimposed on the orbit plane components of the earth's magnetic field. Generating a dipole pulse centered at a latitude of 33 degrees North during an ascending pass and at integer multiples of 180 degrees thereafter will cause the spacecraft to be precessed in the negative $\hat{b}$ direction, precession of the opposite sense can be obtained by programming a dipole centered about 33 degrees North latitude during a descending pass, and at integer multiples of 180 degrees thereafter. The average precession rate while torquing under this condition (i.e., for the unipolar pulse centered about the point where the $\hat{b}$ field component is zero) can be expressed as:

$$\left(\tilde{\omega}_{PUP} \right)_{\ell} = \frac{3\,KM \sin i}{R^3\, H\, a\pi} \sin 2\beta_i \sin \frac{a\pi}{2}, \qquad \text{(IV-12)}$$

where

K is the geomagnetic dipole constant,

R is the orbit radius,

i is the orbit inclination angle,

M is the coil dipole moment,

H is the total system momentum,

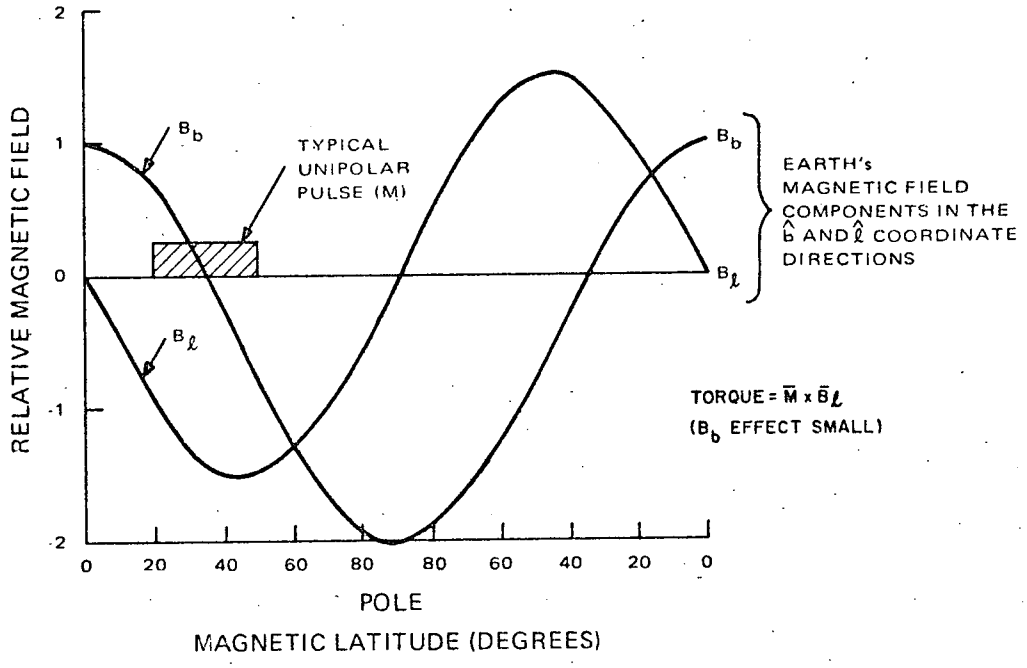

Figure IV-16. Unipolar Torque Correction for Solar Pressure Disturbance

β_i is the anomaly angle from the ascending node to the pulse center,

a is the ratio of ON time to quarter orbit period;

and an uncanted dipole model is assumed.

It follows, from the position of the dipole pulse indicated above, that $(\tilde{\omega}_{PUP})_b = 0$ per unipolar cycle. Once the attitude drift along the $\hat{b}$ axis has been ascertained, both unipolar ON time and delay time can be determined from graphs to be included in the Programming and Control Handbook for ITOS D and E.

Calibrations are also supplied to permit some generation of small precessions in the $\hat{b}$ direction by offsetting the unipolar pulse from the nominal position shown in Figure IV-16. The orbit-average precession vector due to solar torques is approximately aligned with the positive $\hat{\ell}$ axis. (See the ITOS Design Study Report.) Consequently the precession axis will be slightly displaced from the $\hat{\ell}$ axis with the sense of the displacement depending on the time of year.

By selecting the proper delay time for the unipolar torquing, satisfactory solar torque cancellation can be achieved during any season. The shift in the desired position of the dipole with respect to the earth's field varies very slowly over the year and can be plotted against time. Every few weeks a new delay time can be programmed. In this manner, the effects of solar torque can be removed with minimum effort at the ground station.

There are a total of eleven discrete switch positions on the magnetic bias switch, in addition to an off position. The dipole moment granularity between successive switch positions is 0.10 Atm^2. This granularity results in a worst-case drift rate of 0.09 degree per day. The range of dipole moments can produce a controlled attitude change from -1.7 to +1.7 degrees per day.

The switching arrangement for the MBC coil is essentially the same as is employed on the TOS spacecraft, except that the coil current polarity is reversed through a DPDT relay rather than with a center-tapped coil; this change was made to reduce the weight of the coil by a factor of two. In the low torque QOMAC mode, the MBC coil polarity is controlled from the CDU, and the power is routed through the switch resistors. In the high torque QOMAC mode, the MBC polarity is controlled by a set of QOMAC programmer drivers, and the power is applied from the -24.5-volt source on position 11 of the magnetic bias switch. When the QOMAC coil is enabled, the CDU connects the MBC coil directly across the regulated 24.5-volt potential; this results in the maximum coil dipole of 33.8 Atm^2. In this CDU state, the QOMAC and MBC coils are operated in parallel, producing an effective dipole of 4.2 + 33.8 or 38 Atm^2. When the QOMAC coil is disabled, the MBC coil remains connected to the QOMAC programmer with an 820-ohm resistor inserted in series, producing a QOMAC backup mode dipole of 4.8 Atm^2.

6. Magnetic Bias Switch

The magnetic bias switch consists of a rotary solenoid switch mechanism which controls the current levels, and thus the dipole magnitudes, of the MBC coil. The switch, shown schematically in Figure IV-17, is stepped by ground command. A second wafer on the switch provides means for telemetering the position.

7. Momentum Control After Pitch Lock

The total momentum of the spacecraft must be controlled between specified limits around the nominal design point consistent with the dynamic range of the pitch control loop. Magnetic momentum control entails the generation of a torque about the spacecraft pitch axis. Implementation of this control technique requires that the orientation of the plane of the coil be parallel to the pitch axis. Two momentum coils are mounted in this manner in the ITOS spacecraft. Any spacecraft momentum change will be transformed directly to a change in spin rate of the flywheel through the action of the pitch control loop.

The unipolar torquing approach for cancellation of attitude drift due to solar pressure torques was selected by RCA because of its inherent design simplicity and demonstrated satisfactory performance.

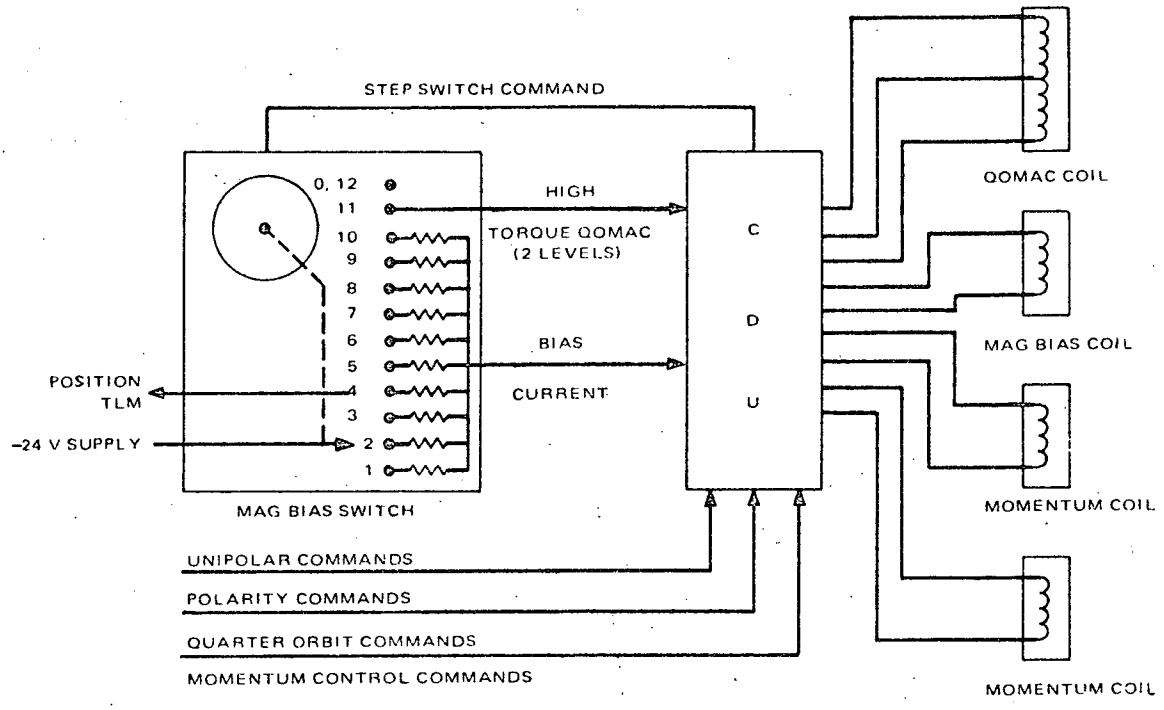

Figure IV-17. Magnetic Momentum Vector Control, Simplified Block Diagram

8. Magnetic Bias Control (MBC)

The MBC coil provides a continuous dipole to offset any undersirable shift in the residual magnetic dipole of the spacecraft along the pitch axis, the preferred value for which is 0.573 Atm^2. Coil current is selected through the magnetic bias switch by ground command to generate a torque that corrects attitude changes due to orbital precession which proceeds at a rate of approximately 1-degree-per-day. The MBC coil is wound on the same structure as the QOMAC coil; its dipole moment, M_{MB}, is aligned with the QOMAC coil dipole, such that:

$$\overline{M}_{MB} = M_{MB}\hat{3}. \qquad \text{(IV-13)}$$

The magnitude of the magnetic bias induced precession rate, ω_{PMB}, can be approximated as:

$$\omega_{PMB} \cong \frac{K M_{MB}}{2 R^3_H} \qquad \text{(IV-14)}$$

For a coil oriented such that its dipole moment, M_{MM}, lies in the $\hat{1}$, $\hat{2}$ plane displaced from the $\hat{1}$ axis by an angle of γ degrees, the following vector definition applies:

$$\overline{M}_{MM} = M_{MM} (\cos \gamma \, \hat{1} + \sin \gamma \, \hat{2}). \qquad \text{(IV-15)}$$

The interaction of this moment with the earth's magnetic field produces two torques: one, T_{SPIN}, changes the magnitude of the momentum and the other, T_{PREC}, has the undesirable effect of changing the direction of the momentum vector. From Equation IV-15, it follows that these torques are given by:

$$\overline{T}_{SPIN} = M_{MM} (B_2 \cos \gamma - B_1 \sin \gamma) \hat{3}, \text{ and}$$

$$\overline{T}_{PREC} = M_{MM} (B_3 \sin \gamma \, \hat{1} - B_3 \cos \gamma \, \hat{2}). \qquad \text{(IV-16)}$$

where B_1, B_2 and B_3 are the earth's magnetic field components in the $(\hat{1}, \hat{2}, \hat{3})$ coordinate system.

The $(\hat{1}, \hat{2}, \hat{3})$ coordinate axes are nominally aligned with the $(\hat{r}, \hat{t}, \hat{n})$ axes. Consequently, for small attitude error angles:

$$B_1 \cong B_r,$$

$$B_2 \cong B_t, \text{ and}$$

$$B_3 \cong B_n.$$

Referring to Equations IV-7 and IV-8, it can be seen that over some torquing interval, $\Delta\beta$, the average magnitude of B_r is twice that of B_t. In order to exploit this advantage, the angle betwen the momentum coil dipole moment and the $\hat{1}$ axis is made 90 degrres (i.e., the positive dipole moment lies along the $\hat{2}$ axis, or nominally along the spacecraft velocity vector $\hat{t}$). Equations IV-16 then take the form:

$$\overline{T}_{SPIN} = -M_{MM} B_1 \hat{3}, \text{ and}$$

$$\overline{T}_{PREC} = M_{MM} B_3 \hat{1}. \qquad \text{(IV-17)}$$

a. SPIN MOMENTUM CHANGE (T_{SPIN})

The torque about the pitch axis, T_{SPIN}, will change the magnitude of the total spacecraft momentum. Equations IV-9 and IV-17 yield a zero orbit-average value. Therefore, momentum control must be applied only over some fraction of an orbit; specifically that fraction during which real-time contact is established between the spacecraft and the ground stations. The average torque, T_{SPIN}, over some interval β_s to β_f, may be expressed as follows:

$$\tilde{T}_{SPIN} = \frac{-2M_{MM}K}{(\beta_f - \beta_s)R^3} \left[-(\cos i \sin i_m \cos \Omega - \sin i \cos i_m)(\cos \beta_f - \cos \beta_s) \right.$$

$$\left. + \sin i_m \sin \Omega (\sin \beta_f - \sin \beta_s) \right] . \qquad \text{(IV-18)}$$

When the pitch servo is in the closed-loop mode, a momentum change will be directly reflected as a change in the flywheel spin rate as follows:

$$\tilde{T}_{SPIN} = \frac{d}{dt} H = I_f \frac{d}{dt} \omega_f . \qquad \text{(IV-19)}$$

where I_f is the flywheel moment-of-inertia and ω_f is the flywheel spin rate. Thus, the average spin torque acting over an interval Δt changes the flywheel spin rate in accordance with:

$$\Delta\omega_f = \frac{\Delta t}{I_f} \tilde{T}_{SPIN} . \qquad \text{(IV-20)}$$

The momentum coil produces a dipole moment of 10.4 Atm^2.

Polarity reversals of momentum coil current are made through a DPDT relay as for the MBC oil. The relationship between the spin rate change derived from the operation of a single coil and the torquing period is implicitly defined in Figure IV-18 where the torquing period is given by $t_\tau = \tau\Delta\beta/360$ and τ is the orbital period. As indicated, a nominal orbital altitude of 790 nautical miles is assumed. A spin rate change is determined by computing the difference between the final and initial values of ω_f defined at the boundaries of the torquing period. The most efficient area of operation is near the north pole ($\beta \cong 90$ degrees). As an example, for a torquing interval from 60 to 107.05 degrees (corresponding to a 15-minute pass) and a 200-degree East longitude ascending node; the spin rate change would be 1.76 rpm. If both momentum coils were used, the change would be twice this amount. Using Figure IV-18, a torquing interval of predetermined length, initiated at some point during the period of ground station contact, can be utilizied to produce any required momentum change within the specified limits.

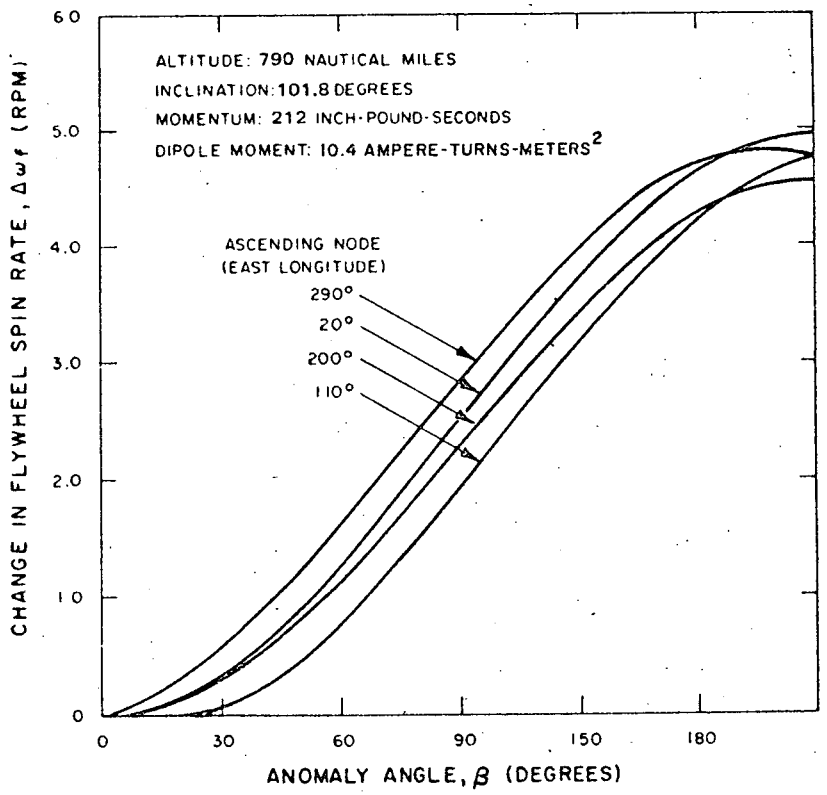

Figure IV-18. Momentum Change Versus Torquing Period (single coil)

b. PRECESSION DUE TO MOMENTUM CORRECTION (T_{PREC})

The torque along the $\hat{1}$ axis, T_{PREC}, is an undesired torque which will change the direction of the momentum vector by precessing the spacecraft. The torque equation is given by:

$$T_{PREC} = M_{MM} B_3 = \frac{M_{MM} K}{R^3} \left(\cos i \cos i_m + \sin i \sin i_m \cos \Omega\right) \qquad \text{(IV-21)}$$

It is evident that, for a given value of Ω, the magnitude of the precession torque is constant. Hence, the attitude change induced in a linear function of the duration of the time period during which the momentum coil is turned on. It follows then that the precession vector is a constant directed along the $\hat{2}$ axis. But this axis is rotating in the orbit reference frame with the result that the precession torque expressed in the (ℓ, b, n) coordinate system takes the following form:

$$T_{PREC} = M_{MM} B_3 (\cos \beta \hat{\ell} + \sin \beta \hat{b}.) \qquad \text{(IV-22)}$$

Averaging Equation IV-22 over the torquing interval, β_s to β_f, yields:

$$\tilde{T}_{PREC} = \frac{M_{MM}{}^{K}}{(\beta_f - \beta_s)\, R^3} (\cos i \cos i_m + \sin i \sin i_m \cos \Omega)$$

$$\left[(\sin \beta_f - \sin \beta_s)\, \hat{\ell} - (\cos \beta_f - \cos \beta_s)\, \hat{b}\right] . \qquad \text{(IV-23)}$$

The magnitude of the angular change, $\Delta\phi$, produced during the torquing time, Δt, is given by:

$$\left|\Delta\phi\right| \simeq \left|\tilde{T}_{PREC}\right| \frac{\Delta t}{H} . \qquad \text{(IV-24)}$$

The relationship between this angular change and the torquing period is implicitly defined in Figure IV-19 whereas for Figure IV-18 the torquing period is given by $t_T = \tau\Delta\beta/360$. The attitude error generated is the difference in value between the final and initial $\Delta\phi$ angles defined at the boundaries of the torquing interval. For the example cited earlier wherein a 200-degree East longitude ascending node and a torquing interval of from 60 to 107.5 degrees were postulated, the attitude error induced would be 0.11 degree. For a 20-degree East longitude ascending node, no attitude change would be produced regardless of the torquing period. Thus, by a judicious choice of the orbit during which momentum changes will be made the effects of attitude error can be kept to a minimum.

If both momentum coils are used for momentum corrections, the attitude change will be twice that shown in Figure IV-19 for the same torquing interval. Obviously, to produce the same momentum change, both coils need be operated for only half the time required for one coil.

9. Momentum Control Prior to Pitch Lock

Should the specified ±10 percent tolerances on spacecraft spin rate at separation be exceeded, ground commanded commutation of the momentum coils may be required to accomplish momentum adjustment prior to the initial pitch lock-on. Figure IV-20 shows the pertinent geometric relationships for this operation. The coils and the stator pitch index pickoff are body-bound to the equipment module. The roll sensor line-of-sight and the rotor pitch index pickoff rotate with the momentum wheel. Therefore, the position of the coils and consequently the resultant dipole is uniquely defined by the relationship between sensor horizon crossing and pitch index pulse occurrence.

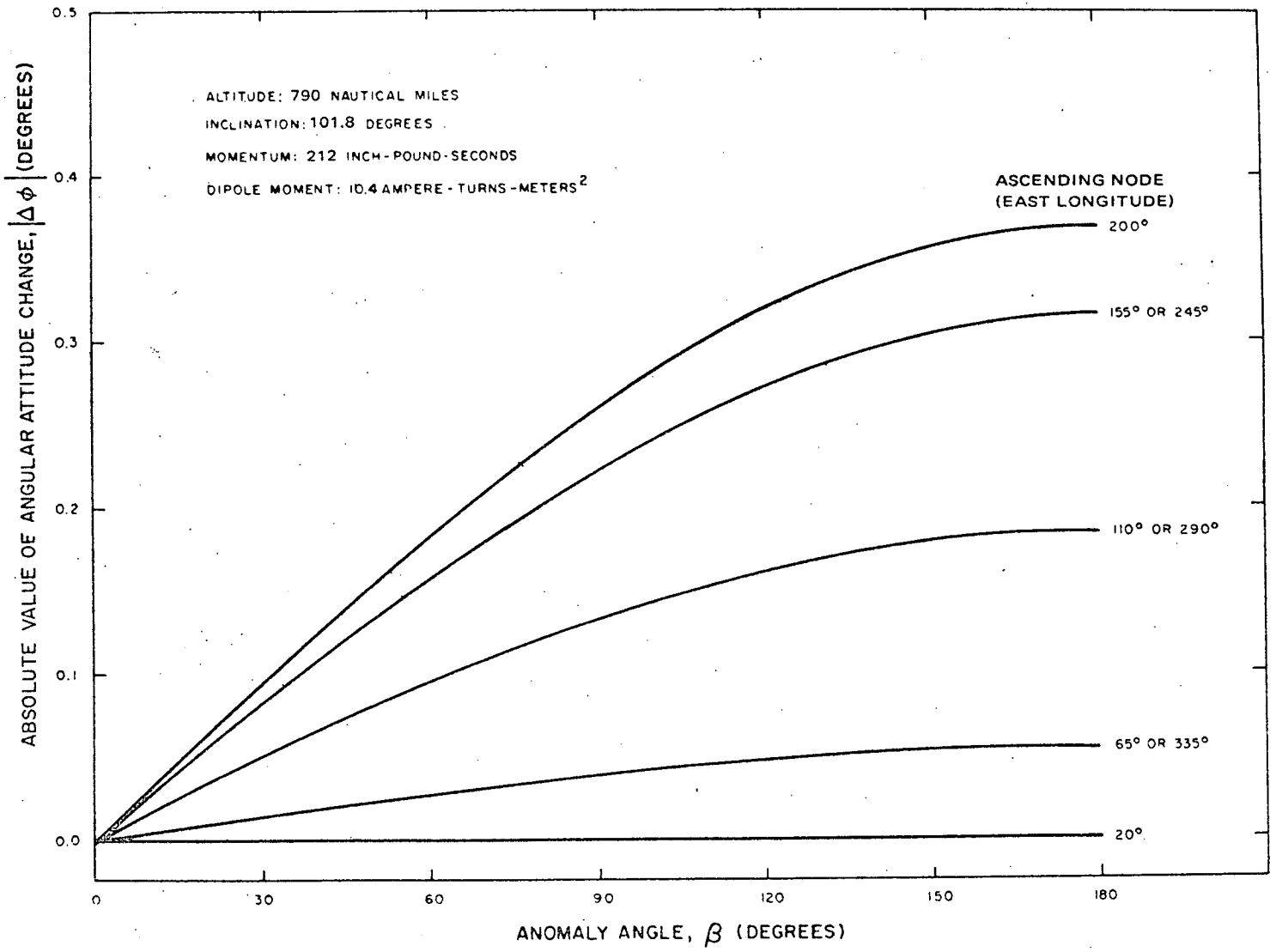

Figure IV-19. Attitude Change Versus Torquing Period (single coil)

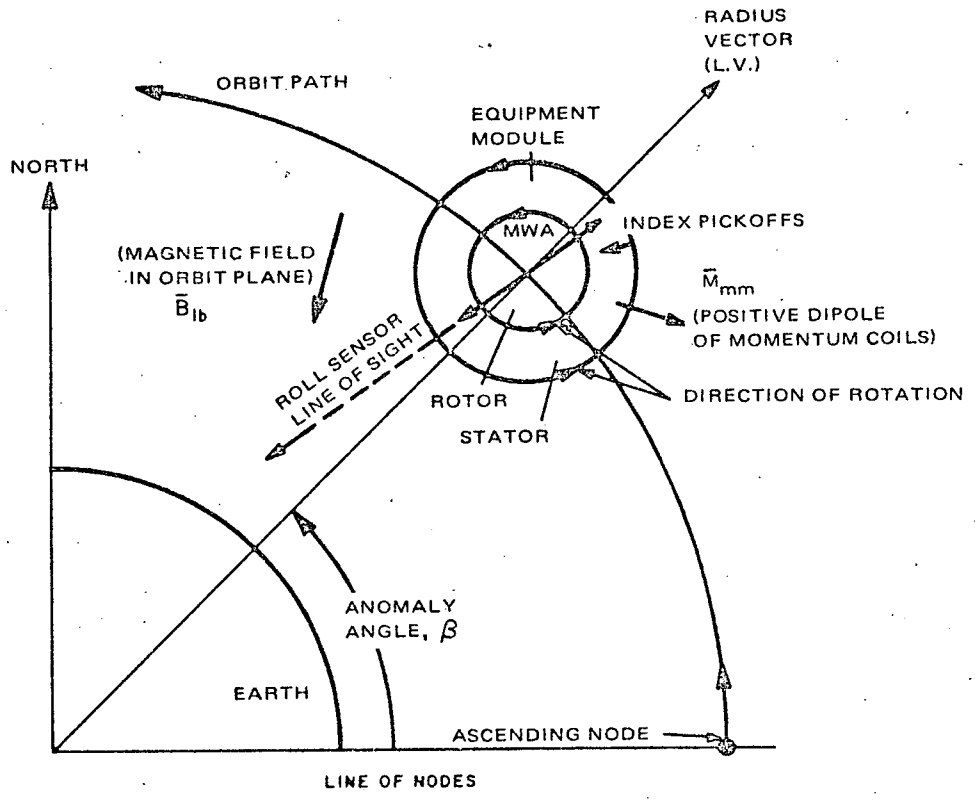

Figure IV-20. Geometry for Momentum Control Prior to Pitch Lock

As shown in Figure IV-21, the commutation of the coils must be precisely phased between the roll sensor sky-earth transition and the index pulse location. These signals are telemetered on the 2.3 kHz subcarrier for monitoring of the space-carft pitch axis offset in the operational mode. The signals also provide the phasing reference during the initial momentum adjustment.

Ideally, commutation should take place when the coil dipole is coincident with the earth's magnetic field vector in the orbit plane. With reference to Figure IV-21, it can be seen that this field vector is displaced with respect to the $\hat{\ell}$-axis by the angle β_{lb}, the definition for which is given by (refer to Equations IV-4 and IV-5):

$$\beta_{lb} = \tan^{-1}\left(B_b / B_L\right)$$

$$= \tan^{-1}\left\{\frac{(1/2)\sin i \cos i_m (3\cos 2\beta - 1) + \sin i_m \left[(1/2)\cos i \cos \Omega - (3/2)\sin i \cos i_m \sin 2\beta + \sin i_m \left[(1/2)\sin \Omega + (3/4)(\cos i + 1)\sin(2\beta + \Omega) + (3/4)(\cos i - 1)\sin(2\beta - \Omega)\right]\right.}{-(3/4)(\cos i + 1)\cos(2\beta + \Omega) - (3/4)(\cos i - 1)\cos(2\beta - \Omega)]}\right\} \quad \text{(IV-25)}$$

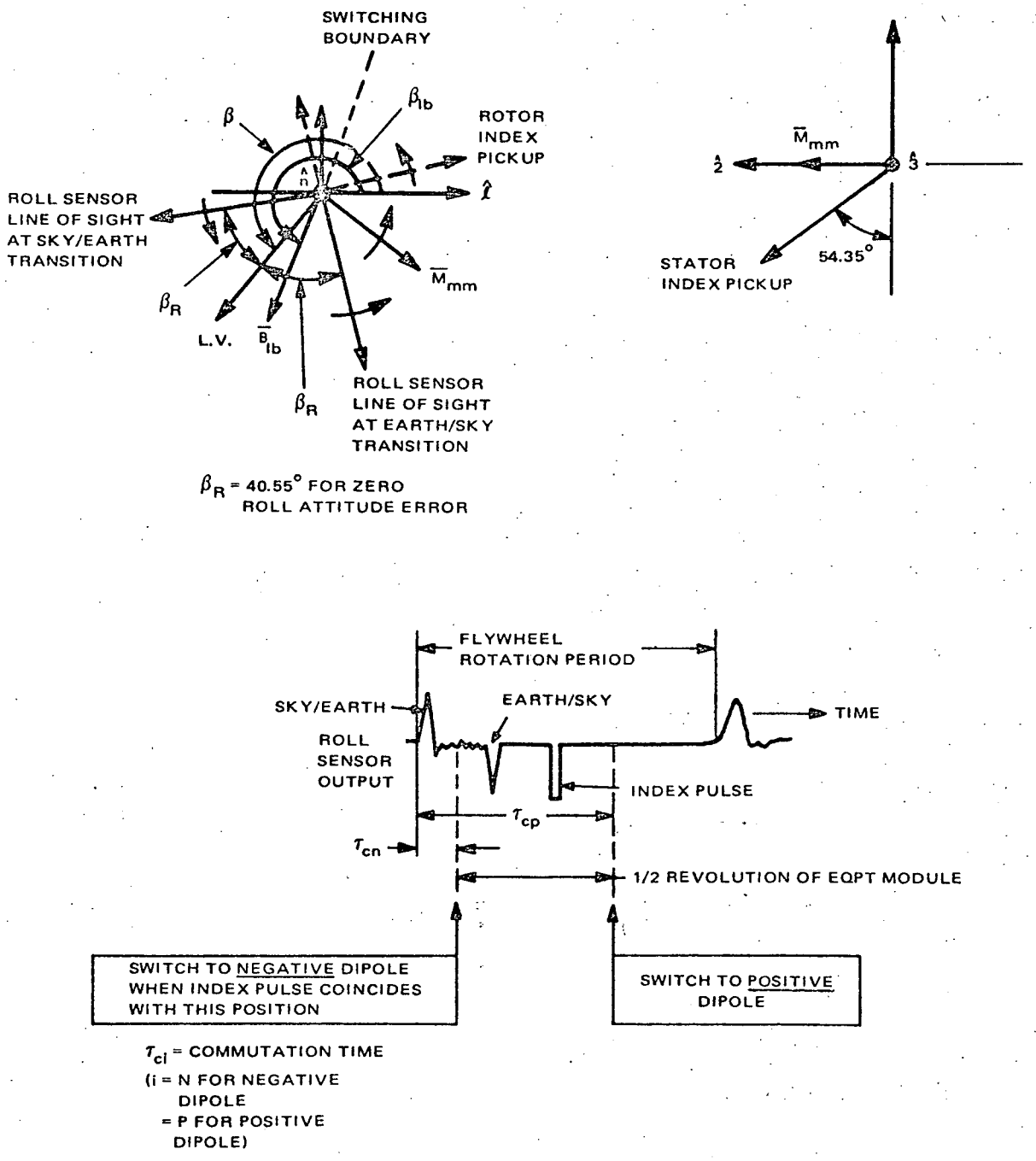

Figure IV-21. Dipole Definition and Phasing for Momentum Control Prior to Pitch Lock

where:

- i is the orbit inclination angle,
- i_m is the earth's magnetic dipole inclination angle,
- β is the satellite anomaly angle, and
- Ω is the angle of the orbit intersection of the geographic and geomagnetic equators with respect to the ascending node connoting displacement in the direction of orbital motion.

By invoking the uncanted dipole model (i.e., $i_m = 0$) for the earth's field, as utilized previously, Equation IV-25 reduces to the following form:

$$\beta_{lb} = \tan^{-1}\left(\frac{3\cos 2\beta - 1}{-3\sin 2\beta}\right) \qquad \text{(IV-26)}$$

This expedient has the effect of suppressing the influence of the angle Ω upon the commutation time without significantly impairing the accuracy of the results. The calibration curve of Figure IV-22 can then be used to establish the phasing between the horizon crossing and the index pulses suitable for commutation. The ordinate values of Figure IV-22 are related to the parameters of Figure IV-21 in the following manner:

$$\frac{\tau CP}{\tau_f} = \frac{76.2^o + (\beta_{lb} - \beta)}{360^o}$$

$$\frac{\tau CN}{\tau_f} = \left(\frac{\tau CP}{\tau_f}\right) \pm 0.5 \qquad \text{(IV-27)}$$

where τ_f is the flywheel rotation period.

For open-loop mode operation with the flywheel rotating at a fixed rate of 150 rpm, the phasing indicated in Figure IV-22 will decrease system momentum in case of excessive spacecraft spinup or increase momentum in case of insufficient spinup. Synchronization of the display scope at the ground station to the sky-earth transition facilitates the use of a simple slide-rule-type phasing indicator as a command aid. The frequency of the commutating ground commands is a function of the equipment module spin rate, as shown in Figure IV-23.

The efficiency of the magnetic torquing depends on the accuracy of the dipole phasing. Figure IV-24 illustrates that an error of 1 or 2 seconds at comparatively large equipment module spin rates results in only minor performance penalties. Similarly, minor deviations from zero roll attitude are not of great significance. However, it is recommended that the momentum adjustment not be made in the presence of roll angles in excess of 10 degrees.

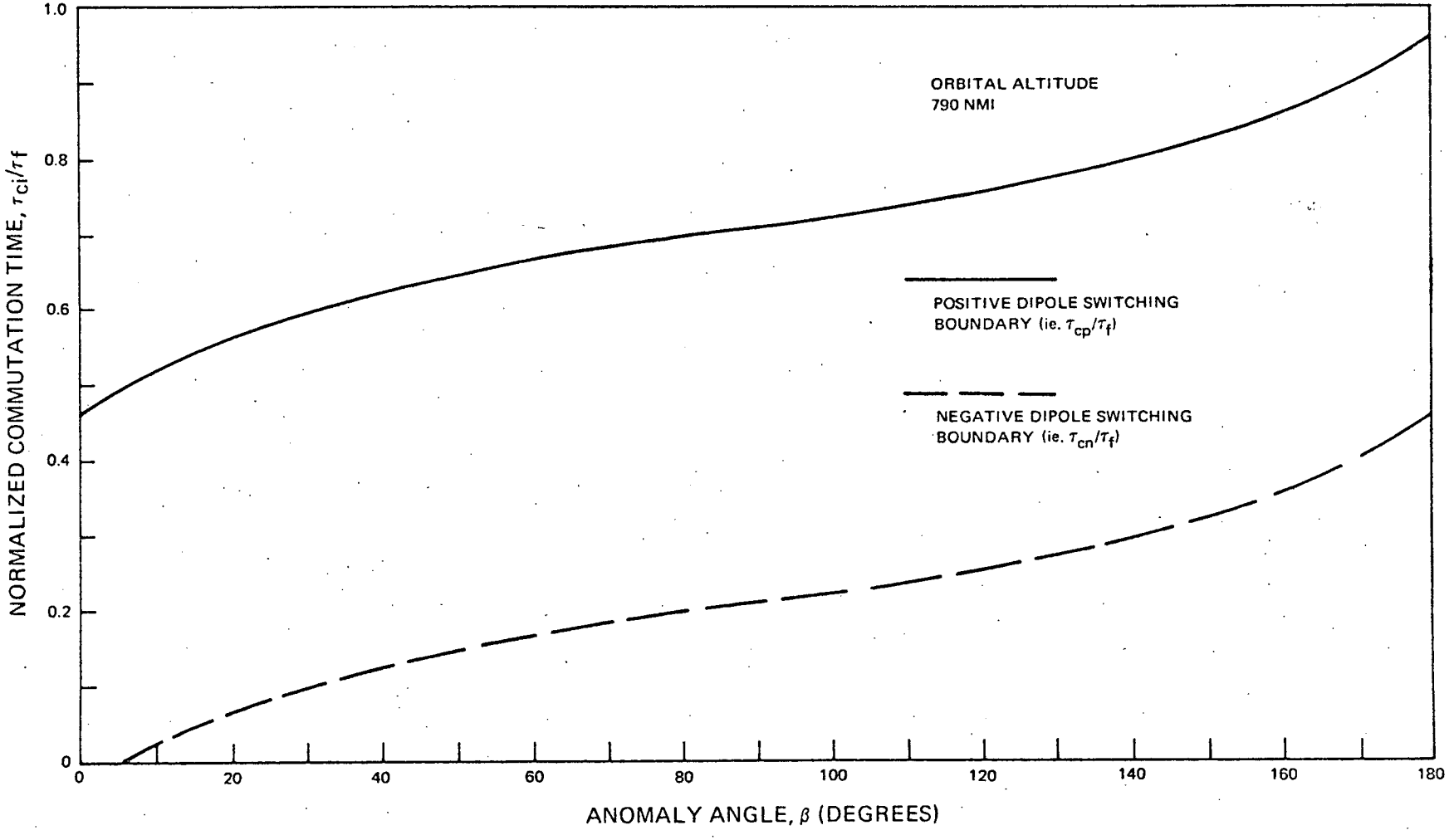

Figure IV-22. Commutation Time Versus Anomaly Angle

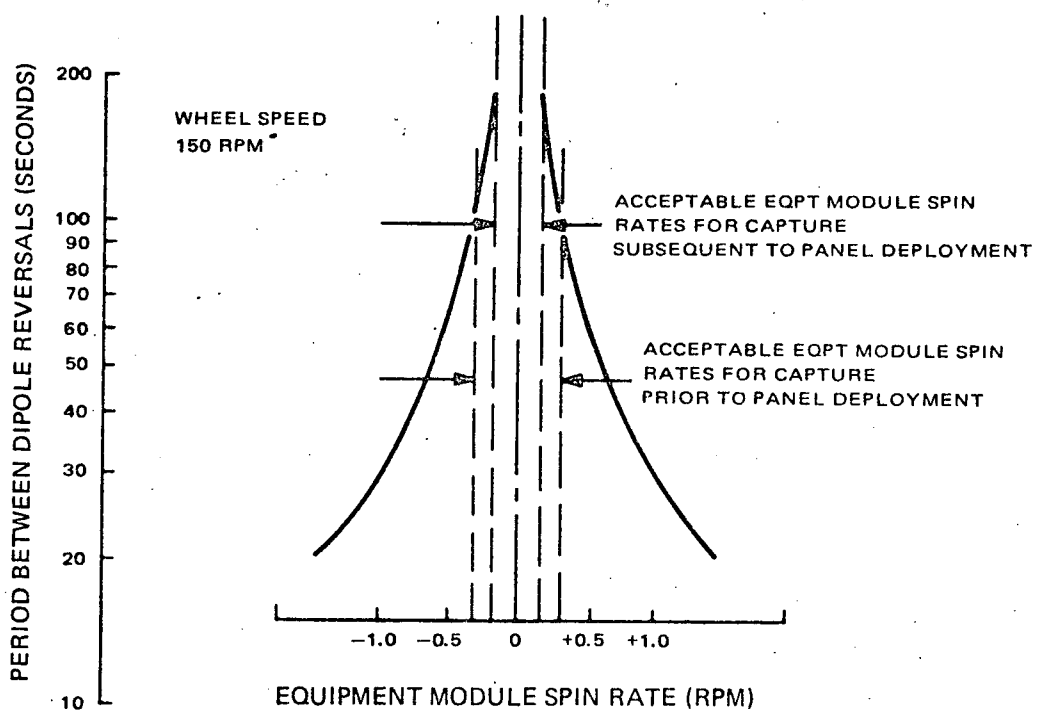

Figure IV-23. Time Between Required Momentum Coil Dipole Reversals Prior to Pitch Lock

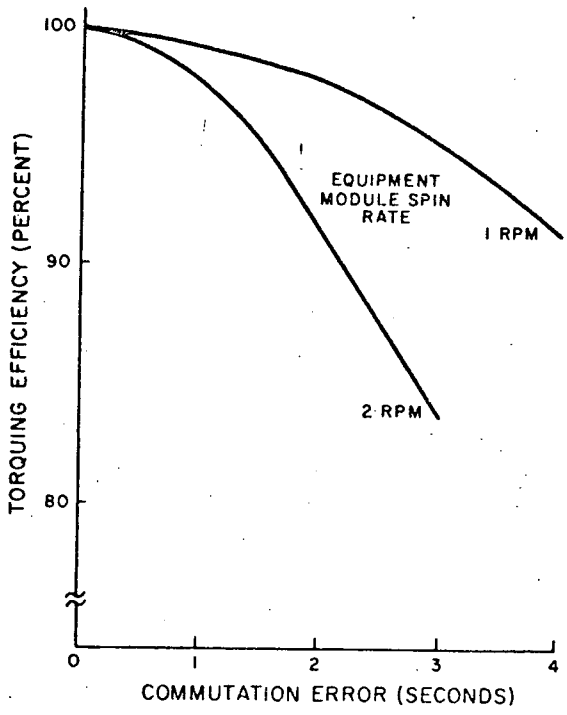

Figure IV-24. Commutation Error Effect on Torquing Efficiency

Except in the immediate vicinity of the magnetic equator, utilization of both coils (with an effective total dipole moment of 20.6 Atm^2) will change system momentum at a rate of approximately 0.2 inch-pound-second per minute. For an available total contact time of about 180 minutes per day from Gilmore and Wallops, a maximum adjustment of 28.8 inch-pound-seconds per day can be obtained. This figure is based on an 80-percent commutation efficiency while operating in the nominal orbit. If the momentum imparted at separation is within ±10 percent of the nominal value (i.e., 212 inch-pound-seconds), adjustment prior to pitch lock will not be required.

F. PITCH CONTROL

1. General

The Pitch Control Subsystem (PCS) maintains the equipment module in the desired orientation about the pitch axis with respect to an earth reference. In the absence of roll errors, this consists of aligning the yaw axis with the local vertical throughout the orbit. The PCS is commanded into operation after solar panel deployment.

The satellite motion about the pitch axis is controlled by momentum transfer between the flywheel and the body. Momentum is transferred by means of a dc torque motor which couples the flywheel to the body. The torque motor is controlled by an error voltage developed when a sky-earth horizon pulse is compared with a reference index pulse produced by a shaft encoder. Normally the pitch horizon sensor generates an output pulse for each rotation of the flywheel at the sky-earth transition. The index pulse is produced by a variable reluctance pickoff passing a body-fixed reference point. For the prescribed orbit altitude, this reference point is geometrically positioned so that the horizon pulse and the index pulse are time coincident for a zero pitch error. An operational block diagram of the pitch axis control loop is shown in Figure IV-25.

Two redundant pitch axis control loops are provided. One of the two torque motors with its corresponding electronic channel will be selected by ground command. Either of the redundant pitch sensors can be used with each of these channels.

The position error detector, which detects deviation of the body axis from the nominal local vertical, uses pulse width modulation (PWM) to measure the time displacement of the horizon pulse and the index pulse. A bipolar error signal of constant amplitude and variable pulse width is produced; the width of the error pulse is proportional to the magnitude of the sensed angular error and the polarity is a function of its direction. The signal is transformed into an amplitude-modulated voltage by filtering through a smoothing circuit. Subsequently, this voltage is compensated by frequency sensitive networks within the compensation amplifier and applied to the motor speed control loop. The voltages of the

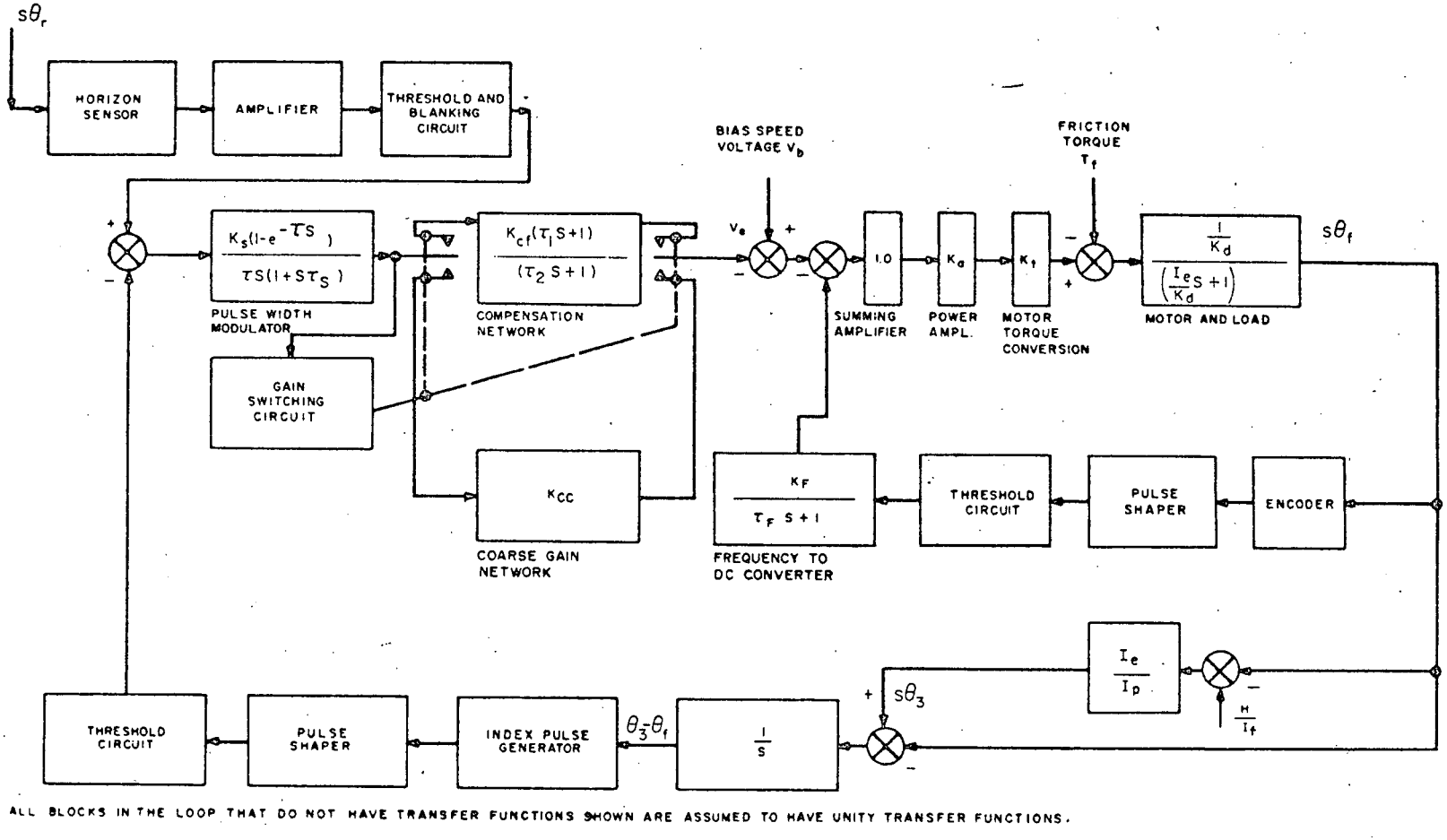

Figure IV-25. Pitch Axis Control Loop, Operational Block Diagram

fixed-speed bias and the compensated-position error circuits are compared with a rate signal proportional to the relative angular velocity of the flywheel and body in a summing amplifier. The rate signal is generated by a magnetic pulse encoder mounted integrally with the drive motor and generating 360 equally spaced pulses per revolution. The pulses are converted to a dc voltage by a frequency-to-dc converter and smoothed by processing through a simple lag circuit. The sum of the bias, position error, and rate signals is applied through a power amplifier to the armature of the dc torque motor. Finally motor action effects a continuing momentum transfer between the flywheel and the body until the pitch position error is nulled.

During initial pitch acquisition, the pitch error may be large enough to saturate the amplifiers. Under these conditions the effective loop gain would be reduced and the tachometer loop time constant would be increased, introducing the possibility of control instability. To eliminate this condition, a two-mode control system is utilized. The compensation amplifier gain is reduced when the position error exceeds a value that would normally cause the unstable condition. By definition, the system is in the coarse gain control mode when operating with reduced loop gain. Ensuring stability by loop gain reduction under all expected conditions, however, will also result in larger pointing errors for momentum deviations from the nominal level of 212 inch-pound-seconds. When the sensed pitch error is reduced to a value of 15 degrees, the system is automatically switched to the fine (i.e., high) gain control mode. For stability reasons, the compensation provided by the frequency sensitive network of the compensation amplifier is not utilized in the coarse-gain mode (i.e., in the presence of the large position errors possible during the initial pitch acquisition). A ground commanded override can place the loop in the coarse gain mode if desired.

2. Pitch Sensing

The pitch control error detector requires input pulses from a pitch horizon sensor and an index reference generator. Any deviation of the two pulses from coincidence generates an error signal which adjusts the speed of the torque motor. To obtain horizon information, one of two sensors selected by ground control is used.

The sky-earth pulse derived from the pitch horizon sensor is phase-compared to a magnetically generated index pulse derived from the encoder. Figure IV-26 illustrates the applicable geometry for the pitch horizon sensor and the encoder index pulse. The lines of sight of the sensors (VHRR, VTPR, and SR) are offset from the horizon by the half-earth angle, as defined by the orbit altitude at the instant of index pulse occurrence. Before launching, the encoder stator is positioned such that the magnetic index pulse will coincide with the sky-earth transition sensed by the horizon sensor when the equipment module is earth

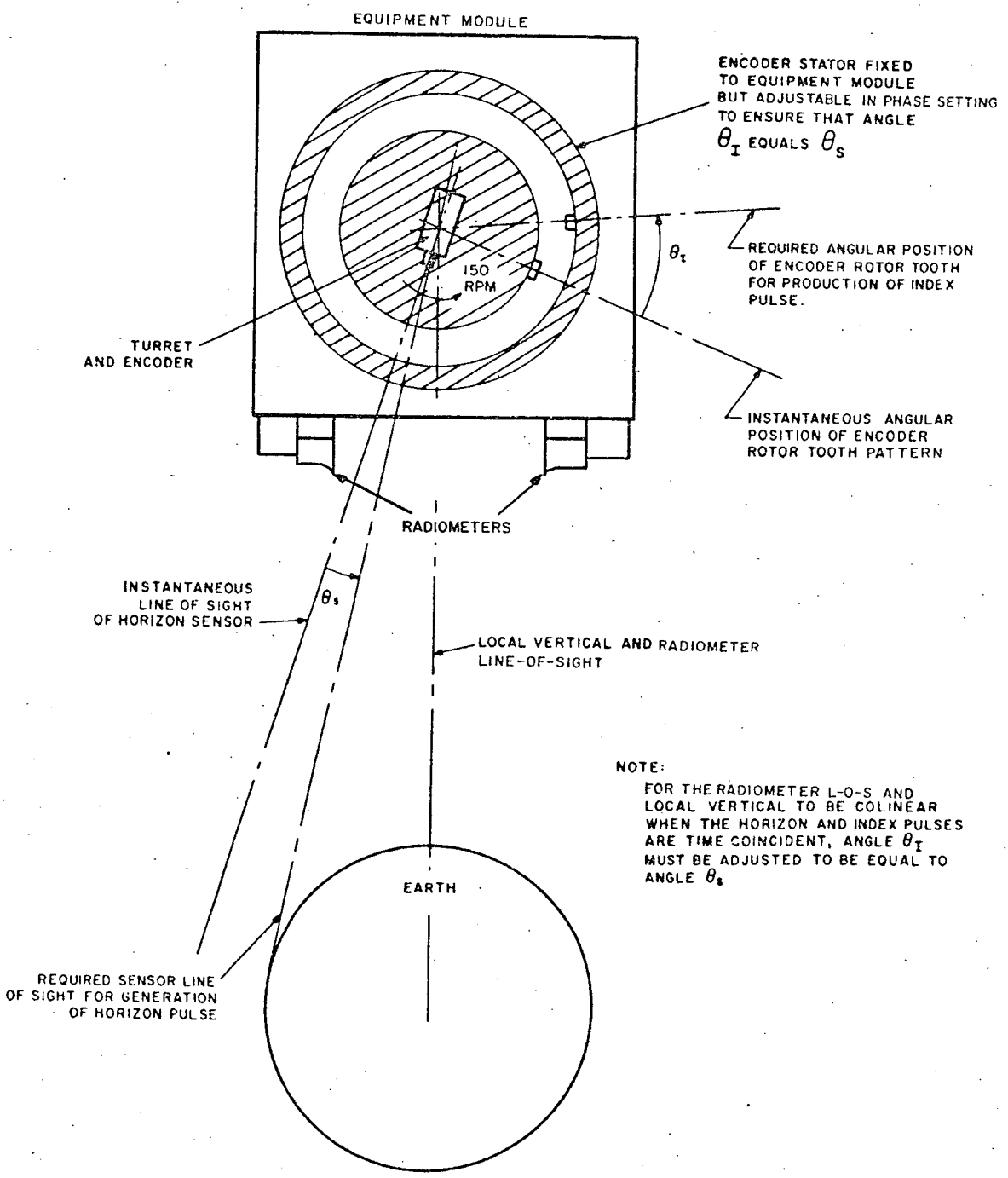

Figure IV-26. Geometry of Horizon Pulse and Reference Index Pulse

oriented. This orientation is achieved by properly aligning the entire electro-mechanical assembly relative to the equipment module.

3. Servo Design

The fine-gain-mode, open-loop transfer function for the single axis pitch control loop shown in Figure IV-25 is given by:

$$G(S) = \frac{(1 - e^{-\tau S})}{S\tau(1 + S\tau_s)} \left(\frac{K_s K_{cf}}{S}\right)\left(\frac{1 + \tau_1 S}{1 + \tau_2 S}\right)\left(\frac{I_f}{I_f + I_p}\right)\left(\frac{K_t K_a}{K_d + K_a K_f K_t}\right)$$

$$\left(\frac{1 + \tau_f S}{1 + \frac{I_e S}{K_d + K_a K_f K_t} + \frac{\tau_f I_e S^2}{K_d + K_f K_a K_t}}\right) \qquad \text{(IV-28)}$$

where:

S is the Laplacian operator,

τ is the sampling period (0.4 second at 150 rpm wheel speed),

K_s is the modulator dc gain (0.98 volt per radian),

K_{cf} is the compensation amplifier fine gain (45.2 volts per volt),

τ_1 is the fine gain compensation amplifier lead time constant (22.3 seconds),

τ_2 is the fine gain compensation amplifier lag time constant (417 seconds),

I_f is the flywheel axial moment-of-inertia (13.5 inch-pound-seconds^2),

I_p is the equipment module (i.e., spacecraft less flywheel) moment-of-inertia about the pitch axis (1177.5 inch-pound-seconds^2),

I_e is the effective flywheel moment of inertia about the pitch axis computed as $\frac{I_f I_p}{I_f + I_p}$ ($\simeq$13.35 inch-pound-seconds^2),

K_t is the motor torque constant (3.3 ounce-inches per volt),

K_a is the gain of the cascaded summing and power amplifiers (118 volts per volt),

K_f is the tachometer feedback gain (0.281 volt per radian per second),

K_d is the motor damping, including viscous friction and back emf (2.42 ounce-inches per radian per second),

τ_f is the encoder smoothing lag (0.05 second), and

τ_s is the PWM smoothing lag (0.8 second).

The nominal value for the compensation amplifier gain in the coarse gain state, K_{cc}, is 2.42 volts per volt.

The PWM error detector transfer function, derived as an approximation from sampled data theory, is given by:

$$G(S)_{PWM} = \frac{1 - e^{-TS}}{ST} \qquad \text{(IV-29)}$$

For sinusoidal analysis purposes, this transfer function can be expressed as follows:

$$G(j\omega)_{PWM} = \frac{\sin\frac{\omega T}{2}\, e^{\frac{-j\omega T}{2}}}{\frac{\omega T}{2}} . \qquad \text{(IV-30)}$$

Further, since the sampling period T will always be small compared with ω, Equation (IV-30) reduces to the following form:

$$G(j\omega)_{PWM} = e^{\frac{-j\omega T}{2}} . \qquad \text{(IV-31)}$$

The nominal level of momentum stored within the flywheel is specified as 212 inch-pound-seconds. For the 17.25-inch radius of gyration achievable within the envelope limits of the attach fitting, and the nominal spin rate of 150 rpm, the numerical ratio of the spacecraft pitch moment of inertia (i.e., $I_p + I_f$) to the flywheel axial moment of inertia approximates 88.2. The selected nominal

wheel speed is not only conducive to low brush wear and good commutation but also compatible with the attitude sensing scanning requirements and reasonable sampling rates. Within the above constraints, it is desirable to minimize the pitch position offset for this Class I servo loop resulting from momentum deviations. For the parameter values indicated above, the pitch servo velocity error coefficient in the fine gain mode is given by:

$$K_{V_f} = \left(\frac{K_s K_{c_f} K_t K_a}{K_d + K_a K_t K_f}\right)\left(\frac{I_f}{I_f + I_p}\right) = 1.78 \text{ sec.}^{-1} \qquad \text{(IV-32)}$$

The significance of this value is that a sizable momentum deviation of 5 percent from the nominal level will induce an offset in pitch attitude of no more than 0.29 degrees.

Figures IV-27 and IV-28 are Bode plots of the open-loop, single-axis, pitch servo response for fine- and coarse-gain mode operation, respectively. The figures indicate the need for the coarse-gain region. Although the system is adequately stable in its linear range, the phase margin of the fine gain curve would suffer severely if the loop gain were to decrease due to amplifier saturation.

It should be observed that the crossover frequency occurs at about 0.1 radian per second in both fine- and coarse-gain mode operation, or about two orders of magnitude below the nominal sampling frequency of 15.7 radians per second. It follows then that the PWM can be represented in the simplified model indicated above, and further that a PWM smoothing network with a time constant in the vicinity of the sampling frequency has little effect on the system stability. A Bode plot of the tachometer loop response is shown in Figure IV-29.

The gain switching circuit reduces the position loop gain and removes the lag-lead compensation network in the presence of the large pitch errors expected during the initial pitch acquisition and attendant recovery from unexpectedly large disturbances. Without such switching, amplifier saturations would result in a highly under-damped system.

4. Three-Axis Considerations

The previous discussion concerned the pitch servo design in terms of a single axis loop. Since deployment of the panels (i.e., solar arrays) introduces a substantial misalignment between the principal and control axes of the spacecraft, sizeable products of inertia characterize the flight configuration, These products, in combination with the roll sensitivity of the pitch sensor, significantly modify the dynamic characteristics of the single axis pitch loop in the vicinity of the nutation frequency. To ensure stability over the specified momentum range, a study utilizing a computer implemented linear servo analysis technique has been made to assess the suitability of the TIROS M/ITOS-1

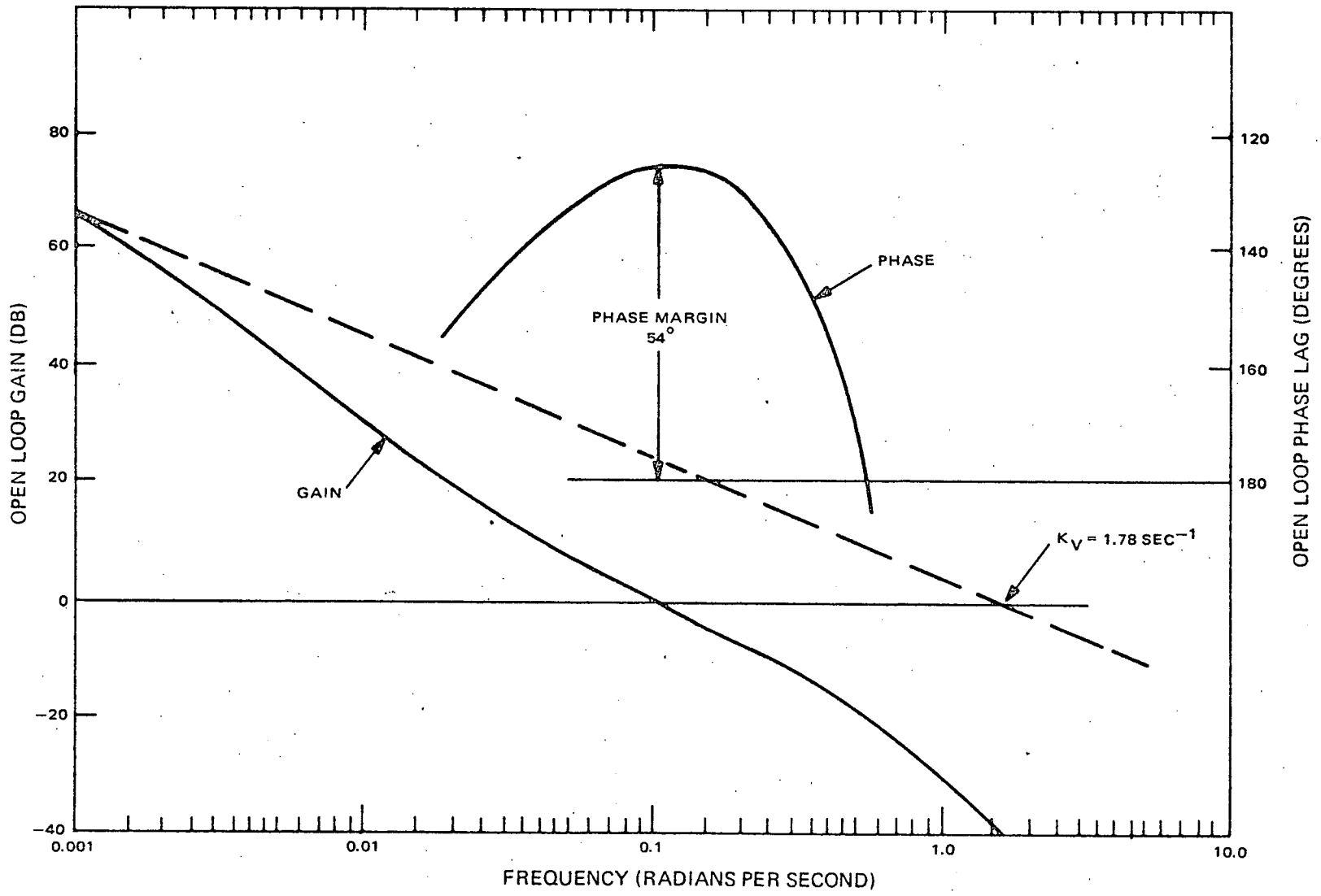

Figure IV-27. Open Loop Fine Gain Frequency Response of Single Axis Pitch Servo

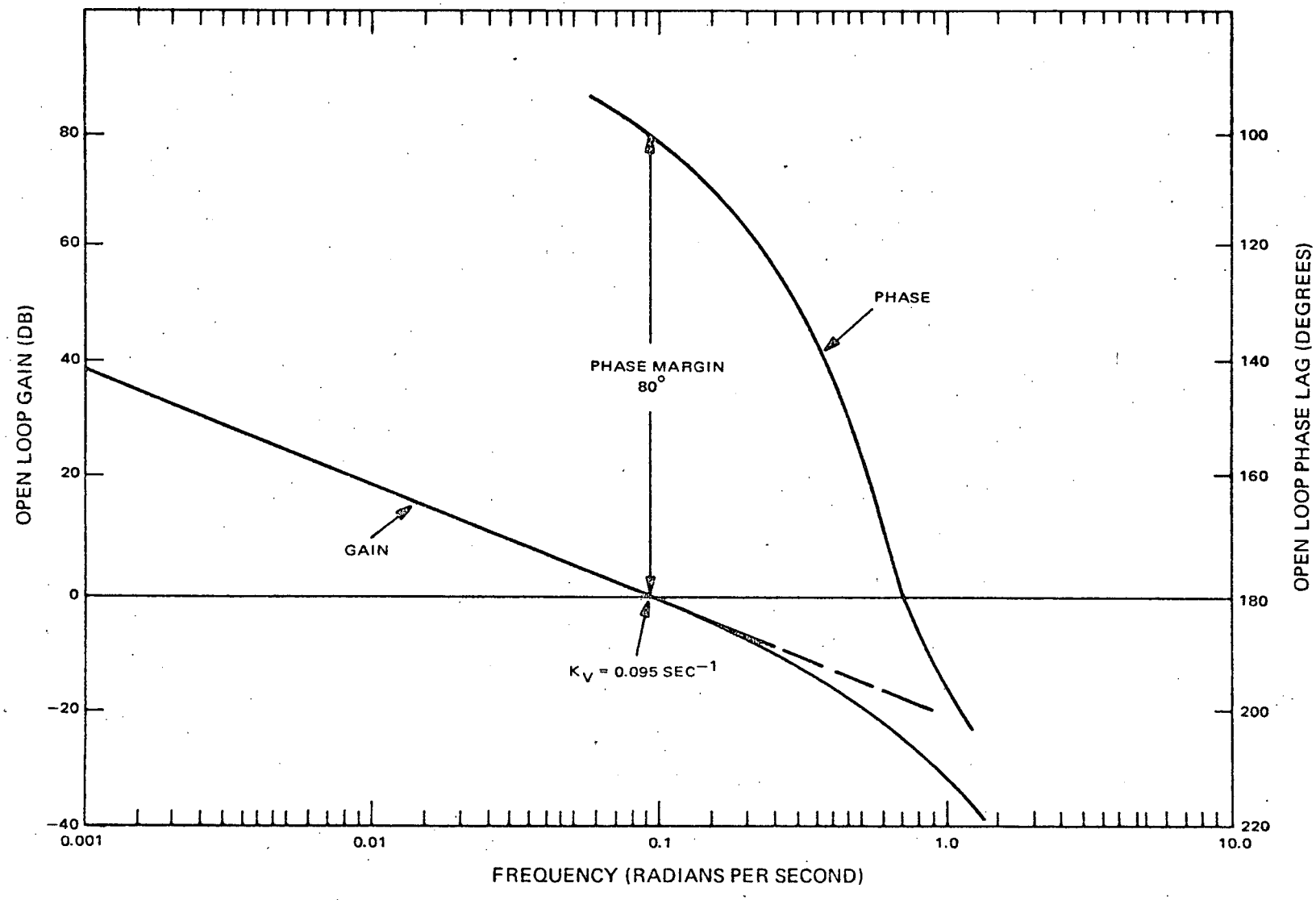

Figure IV-28. Open Loop Coarse Gain Frequency Response of Single Axis Pitch Servo

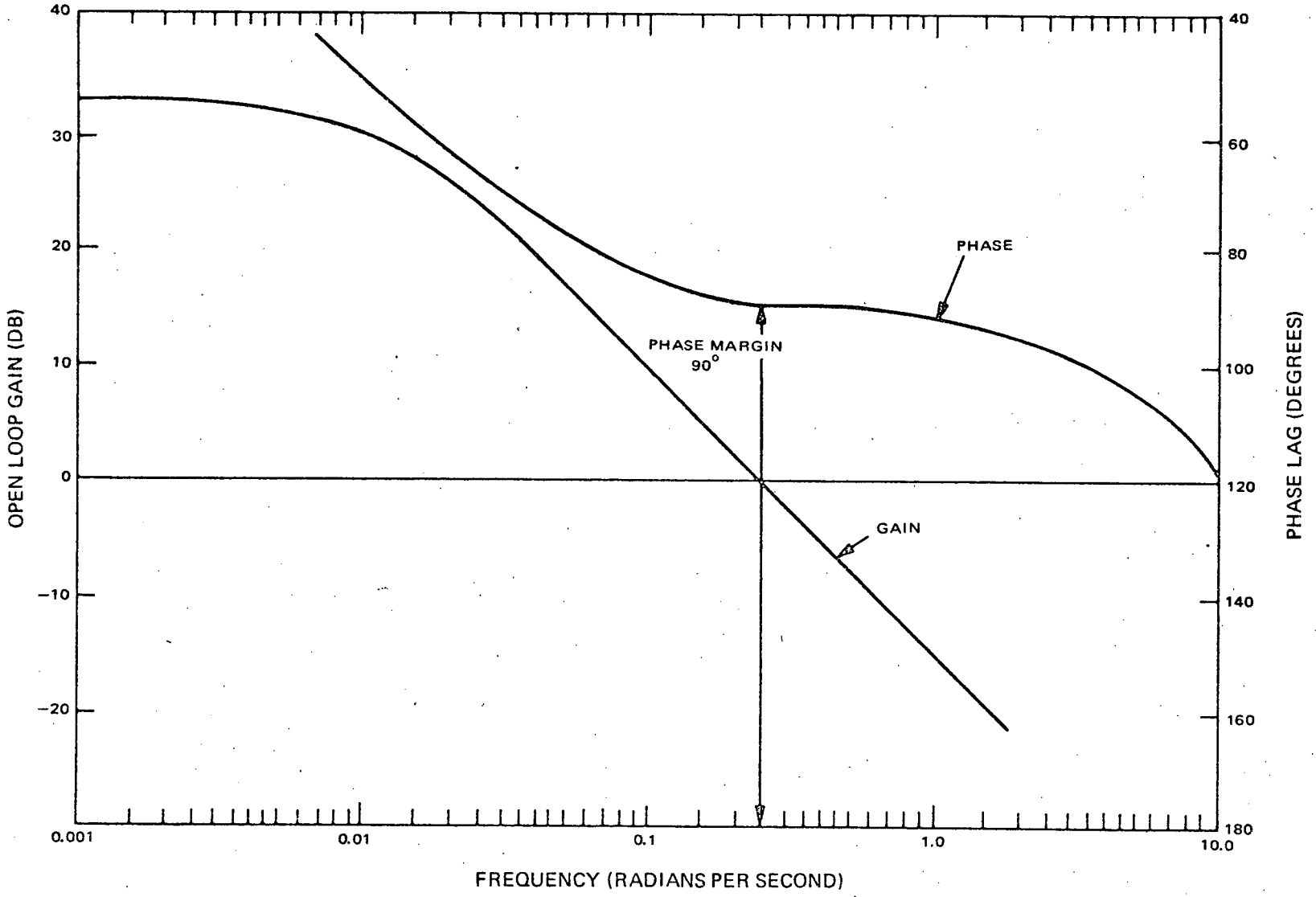

Figure IV-29. Open Loop Frequency Response of Tachometer Loop

PCS for the ITOS D and E spacecraft. The mechanism of cross-coupling whereby loop instability may arise has the following pathology: the torque motor induces a small roll error by the transfer of momentum into the equipment module, which in turn produces a sensed pseudo-pitch error which causes the control electronics to demand further corrective torque and thereby induces even a greater roll error.

The manner in which the pitch loop is reduced for computational purposes is shown in Figure IV-30. The spacecraft dynamics and sensor cross-coupling are represented by the relationship of the sensed pitch error θ_E to the torque delivered by the servo, T_D and the pitch control loop by the inverse function (i.e., the relationship of T_D to θ_E).

The results of this study indicate that satisfactory performance is realizable for the following conditions.

Momentum Range	Roll Angle Range	Mode
191 to 233 inch-pound-seconds	-3 to +3 degrees	Operational

Examining the pertinent analytical expressions will clarify this important cross-coupling mode. In the absence of amplifier saturation the pitch loop transfer function relating the torque delivered T_D to the sensed pitch error θ_E can, subject to linearization, be expressed as:

$$\frac{T_D(S)}{\theta_E(S)} = \left(\frac{K_a K_t K_s K_{cf}}{K_d + K_a K_t K_f}\right)\left(\frac{\tau_1 S + 1}{\tau_2 S + 1}\right)\left(\frac{1 + \tau_f S}{1 + \tau_s S}\right)$$

$$\left(\frac{I_e S}{\frac{\tau_f I_e S^2}{K_d + K_a K_t K_f} + \frac{I_e S^2}{K_d + K_a K_t K_f} + 1}\right). \qquad \text{(IV-32)}$$

This transfer function defines the torque response of the pitch loop to a pitch position error. Similarly, the transfer function defining the spacecraft dynamics and sensor cross coupling (i.e., that relating the sensed pitch error θ_E developed to the torque delivered T_D) can be linearized, for small angular excursions, to the form (refer to Equation IV-33 on page IV-55).

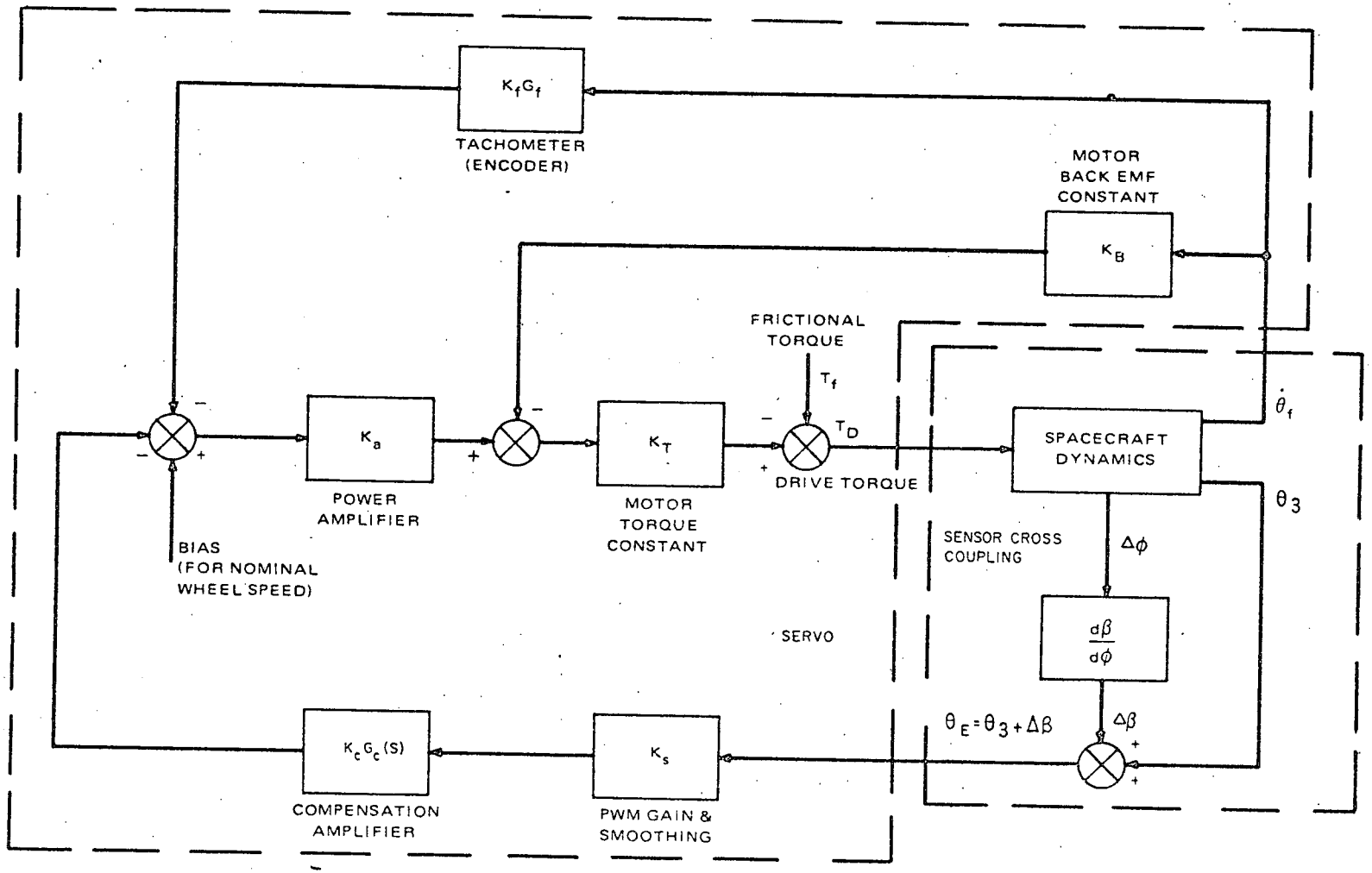

θ_3 : ANGLE BETWEEN SATELLITE YAW AXIS AND PLANE FORMED BY THE NOMINAL LOCAL VERTICAL AND THE PITCH AXIS.

$\Delta\beta$: FALSE ERROR CAUSED BY THE ROLL ANGLE DEVIATION AND THE EARTH'S CURVATURE.

Figure IV-30. Digital Computer Simulation of Pitch Loop System

Page intentionally left blank

Without product of inertia terms (i.e., in the absence of misalignment between the principal and control axes), Equation IV-33 reduces to:

$$\frac{\theta E^{(S)}}{T_D^{(S)}} = \frac{-1}{S^2 (I_{33} - I_f)} \qquad \text{(IV-34)}$$

The product of Equations IV-32 and IV-34 corresponds to the single axis open loop transfer function treated in the previous section. The cross-coupling term represented by Equation IV-33 shows the double integration relating torque to pitch error modified by the ratio of two quadratic expressions. Because of the very low damping inherent in both the numerator and denominator of this ratio, the gain-phase responses for the term are within 1 dB and 5 degrees of null, respectively, for all frequencies greater or less than ±5 percent of the nutation frequency. However, within this ±5 percent band about the nutation frequency, radical changes in gain and phase are manifest. Examination of this narrow frequency range by digital computer techniques permits rapid stability determination for any arbitrary combination of system parameters. Since the transfer functions utilized were derived subject to certain linearizing assumptions, including the existence of small pitch/roll attitude errors and the absence of amplifier saturation, it will be necessary to initiate additional analytical studies employing the time-domain, three-axis computer simulation incorporating in precise detail all the nonlinearities inherent in the system to obtain final stability verification. Such studies are mandatory if the capture characteristics of the system are to be examined.

Shown qualitatively in Figure IV-31a, in a gain-phase format, are representative frequency responses for the function:

$$G(S) = -\frac{1}{I_p S^2} \frac{T_D^{(S)}}{\theta_E^{(S)}}$$

$$= -K_{v_f} \left(\frac{\tau_1 S+1}{\tau_2 S+1}\right) \left(\frac{\tau_f S+1}{\tau_s S+1}\right) \left(\frac{I_e S}{\frac{\tau_f I_e S^2}{K_d + K_a K_t K_f} + \frac{I_e S}{K_d + K_a K_t K_f} + 1}\right) \qquad \text{(IV-35)}$$

where, as previously,

$$K_{v_f} = \frac{K_a K_t K_s K_{c_p}}{K_d + K_a K_t K_f}\left(\frac{I_f}{I_{33}}\right) \text{ and } I_e = \frac{(I_{33} - I_f)}{I_{33}} I_f ;$$

and the function,

$$F(s) = -I_p s^2 \frac{\theta_E(s)}{T_D(s)} . \qquad \text{(IV-36)}$$

Because the investigation of cross-coupled pitch loop stability can be confined to a narrow range of frequencies centered about the nutation frequency, ω_n, throughout which the frequency response of G(s) undergoes virtually no change, superimposing the response locus of F(s) on that of G(s) at the gain-phase coordinates corresponding to ω_n, as shown in Figure IV-31b, defines an approximation of the cross-coupled, open loop transfer function M(s) = F(s) G(s) sufficiently precise for preliminary analytical purposes. The evaluation of pitch loop stability can be further expedited by displacing the origin of the gain-phase plot such that it coincides with the G(s) response locus at the nutation frequency after the manner of Figure IV-31c. The 0 dB/180 degree point then appears as point S located at the coordinates G_n, ϕn. The pitch loop phase margin, an indicator of absolute system stability, can then be approximated to a high degree of accuracy as ϕ_m or ϕ'_m depending upon the sign of the pitch sensor roll-coupling coefficient. Should the point S be encircled by either locus, the pitch loop would, by definition, exhibit unstable performance for the class of operating conditions postulated.

Worst-case conditions were contrived for evaluation of the functions, G(s) and F(s). In general, the combinations of values chosen for the spacecraft moments and products of inertia, system angular momentum, and spacecraft roll angle, were such as to define the cross-coupling term coefficients that would produce minimum separation between the $+d\beta/d\phi$ and $-d\beta/d\phi$ loci of Figure IV-31. These worst-case combinations are summarized in Table IV-2 with the tolerances utilized. In the case of the spacecraft mass properties, the tolerances quoted represent 6σ values. The pitch sensor scan angles and the liquid damper parameters are characteristic of the TIROS M/ITOS-1 design. The limiting values indicated for spacecraft roll angle are consistent with the recommendation made for operation of the TIROS M/ITOS-1 PCS. The absolute value assigned the roll-coupling coefficient, while suitable for the combinations of α and ϕ tabulated, is predicated upon insertion of the spacecraft into a circular orbit of 846 nautical miles altitude, the equivalent of a 6σ- upper bound in terms of the tolerances prescribed for launch vehicle performance. The tolerances imposed on system angular momentum represent conservative

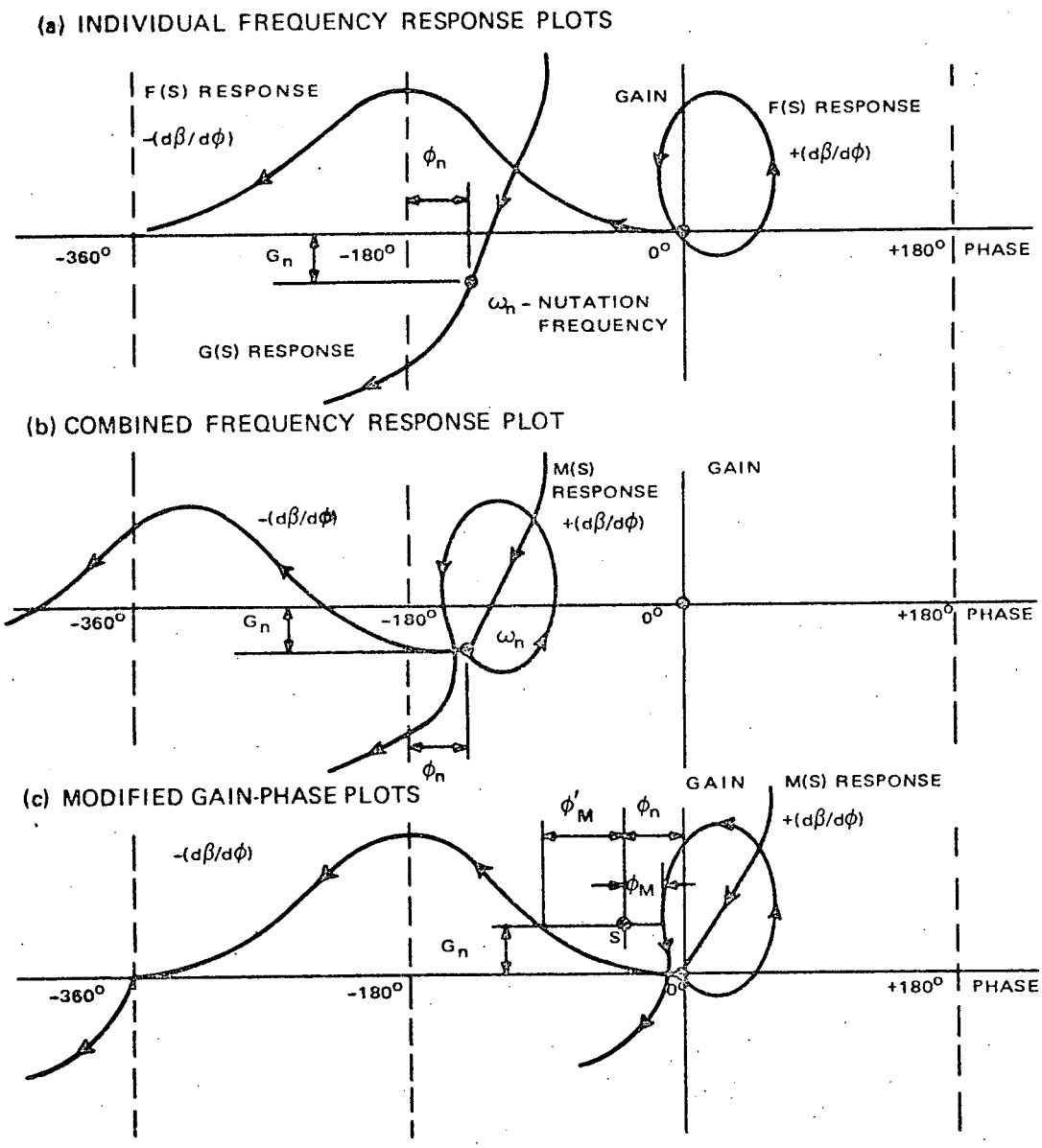

Figure IV-31. Typical Gain-Phase Presentations for G(s), F(s), and M(s)

TABLE IV-2. CROSS-COUPLING PARAMETERS WORST-CASE COMBINATIONS

Parameter	Nominal Value	Tolerance	$+(d\beta/d\Phi)^*$	$-(d\beta/d\Phi)^*$	Units
I_{11} - Yaw Moment of Inertia	1326.1	±28.6	1297.5	1354.7	inch-pound-seconds^2
I_{22} - Roll Moment of Inertia	1133.8	±28.2	1105.6	1162.0	inch-pound-seconds^2
I_{33} - Pitch Moment of Inertia	1190.7	±33.1	1157.6	1223.8	inch-pound-seconds^2
I_{12} - Yaw-Roll Product of Inertia	6.0	±12.6	-6.6	18.6	inch-pound-seconds^2
I_{23} - Roll-Pitch Product of Inertia	-8.0	±4.2	-12.2	-3.8	inch-pound-seconds^2
I_{31} - Pitch-Yaw Product of Inertia	71.6	±7.2	64.4	78.8	inch-pound-seconds^2
I_f - Flywheel Axial Moment of Inertia	13.5	None	13.5	13.5	inch-pound-seconds^2
I_d - Damper Axial Moment of Inertia	3.3	None	3.3	3.3	inch-pound-seconds^2
γ - Liquid Damper Viscous Coefficient	0.5716	None	0.5716	0.5716	$\frac{\text{inch-pound}}{\text{radian/second}}$
θ_p - Pitch Angular Offset**	0.0 / 0.0	±10.7 / ±0.3	10.7 / 0.3	-10.7 / 0.3	degrees
Φ - Spacecraft Roll Angle	0.0	±3.0	-3.0	+3.0	degrees
H_3 - System Angular Momentum	212	±21.2	233.2	190.8	inch-pound-seconds

* $d\beta/d\Phi$ values assigned consistent with 87 and 93 degree pitch sensor scan angles, ±3.0 degree roll angles, and assumed 846 nautical mile orbital altitude.

** Pitch angular offset according to servo mode; i.e., coarse gain offset/fine gain offset.

expectations for the performance of the accelerometer-controlled, closed-loop spin-up system planned for the launch vehicle of the ITOS D and E spacecraft.

Table IV-3 is a matrix of transfer function parameters suitable for testing the limits of the pitch servo response in order to establish boundaries for the motion of point S in Figure IV-31 under worst-case operating conditions. Parameters representative of both of the available servo gain states (i.e., coarse and fine) are tabulated for beginning-of-life (BOL) and end-of-life (EOL) conditions. For the BOL and EOL cases, combinations of non-nominal parameters which produce a servo response characterized by four distinct, min-max/gain-phase relationships are shown. The values prescribed for the velocity error coefficient, K_V, are predicated on the pitch moment entries of Table IV-2 consistent with the definition of Equation IV-35.

TABLE IV-3. PITCH SERVO PARAMETERS MATRIX

Parameter (Unit)	Coarse Gain State									Fine Gain State								
	BOL				Nom	EOL				BOL				Nom	EOL			
	Max ϕ[2] Min G	Min G Max ϕ	Min ϕ Max G	Max G Min ϕ		Max ϕ Min G	Min G Max ϕ	Min ϕ Max G	Max G Min ϕ	Max ϕ Min G	Min G Max ϕ	Min ϕ Max G	Max G Min ϕ		Max ϕ[3] Min G	Min G Max ϕ	Min ϕ Max G	Max G[3] Min ϕ
K_v - Velocity Error Coeff (sec^{-1})	0.0972	0.0902	0.0934	0.1003	0.0953	0.0965	0.0832	0.0946	0.1098	1.814	1.685	1.745	1.871	1.780	1.801	1.555	1.767	2.051
τ_s - PWM Smoothing Time Constant (sec)	0.85	0.85	0.75	0.75	0.80	0.92	0.92	0.68	0.68	0.85	0.85	0.75	0.75	0.80	0.92	0.92	0.68	0.68
τ_1 - Comp Amp Lead Time Constant (sec)	1×10^{-6}	1×10^{-6}	1×10^{-6}	1×10^{-6}	1×10^{-6}	1×10^{-6}	1×10^{-6}	1×10^{-6}	1×10^{-6}	21.0	21.0	23.6	23.6	22.3	19.0	19.0	25.6	25.6
τ_2 - Comp Amp Lag Time Constant (sec)	1×10^{-6}	1×10^{-6}	1×10^{-6}	1×10^{-6}	1×10^{-6}	1×10^{-6}	1×10^{-6}	1×10^{-6}	1×10^{-6}	392.0	392.0	442.0	442.0	417.0	355.0	355.0	479.0	479.0
τ_f - Encoder Filter Time Constant (sec)	0.047	0.047	0.053	0.053	0.050	0.0425	0.0425	0.0575	0.0575	0.047	0.047	0.053	0.053	0.050	0.0425	0.0425	0.0575	0.0575
τ_ω - Tach Loop[1] Time Constant (sec)	2.50	2.33	1.365	1.465	1.94	3.02	2.60	1.38	1.68	2.50	2.33	1.365	1.465	1.94	3.02	2.60	1.38	1.60

Notes:

1. $\tau_\omega = I_c/(K_d + K_a K_t K_f)$
2. The ordering of the gain-phase requirements (i.e., $\frac{\text{superior}}{\text{inferior}}$) indicates the priorities observed in parameter tolerance selection.
3. See text for explanation.

In the coarse gain state, the compensation amplifier is adequately represented by a simple gain devoid of dynamics. The stipulation of small but finite lead-lag time constants for the amplifier in this gain state is an artifice invoked to comply with the format of the digital program devised to evaluate the G(s) function, computation of the pitch servo response was undertaken for frequencies approximating those characterizing spacecraft nutation. Specification of these frequencies can be made by reference to the entries of Table IV-2. From the fully expanded form of Equation IV-36, the spacecraft nutation frequency can be approximated as:

$$\omega_n \simeq H_3/\sqrt{I_{11}I_{22}} \qquad \text{(IV-37)}$$

consistent with the definition of $\dot{\phi}$ in Paragraph C.3.

Of the combinations of pitch servo parameters shown in Table IV-3, those which yielded the most significant excursions of the stability point from its nominal position are noted[3]. The boundary positions defining the extent of these excursions are plotted in Figure IV-32. Shown also are those portions of the cross-coupling term with frequency response loci proximate to these boundary points. It is apparent that stable pitch loop performance is attainable for the worst-case operating conditions. The conditions for which minimum phase margin is realized are the fine gain mode operations at EOL where servo parameter variations capable of producing the maximum possible phase shift, in the presence of minimum gain, exits.

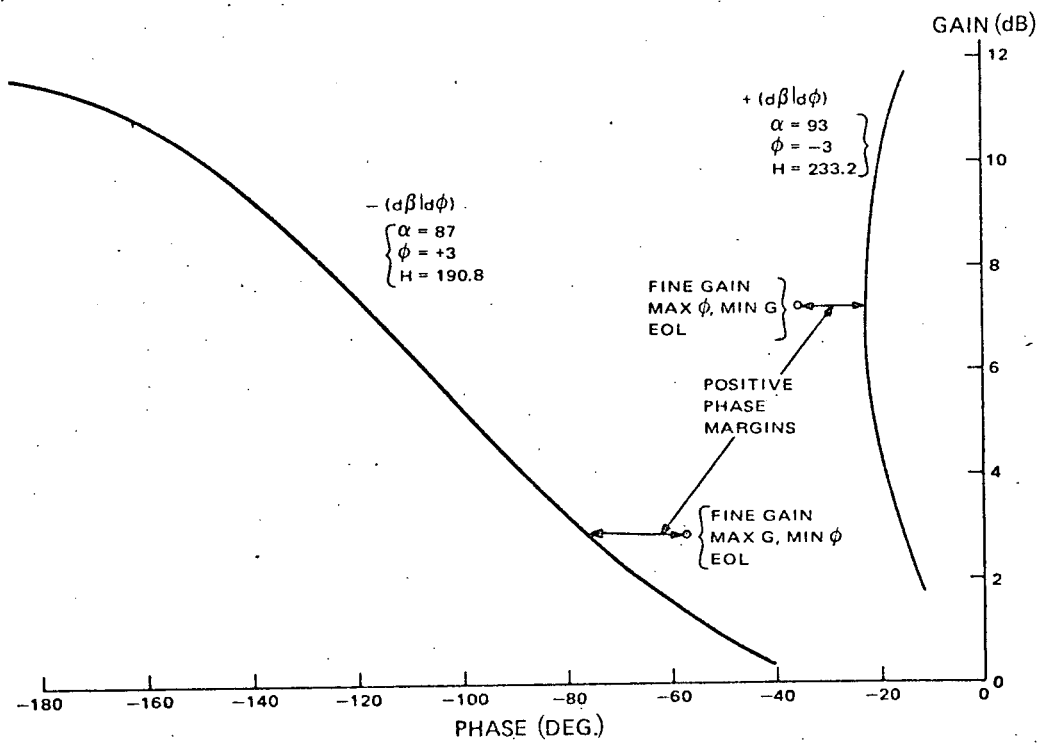

Figure IV-32. Stability Study Worst-Case Results (Preliminary)

5. Component Description

a. GENERAL

The P C S is comprised of the following components:

- pulse width modulator (PWM)
- compensation amplifier
- gain switching circuit
- summing amplifier
- power amplifier
- torque motor
- encoder
- encoder electronics
- frequency-to-dc converter
- dc-to-dc converter
- roll and pitch sensors
- sensor threshold amplifiers
- blanking circuits
- telemetry
- wheel speed threshold circuit
- electronics box

The sensors and sensor amplifiers are discussed earlier in this section. A general functional description of the remaining components follows. The entire P C S is shown in Figure IV-1 and Table IV-4 lists the component electronic specifications.

TABLE IV-4. PCS ELECTRONIC SPECIFICATIONS (Sheet 1 of 2)

Component	Characteristic	Specification
Pulse Width Modulator	Index pulse	30^{+1}_{-5} volts, negative
	Horizon sensor pulse	14 ±2 volts, negative
	Input pulse duration	>100 microseconds
	Input impedance (horizon)	10 kilohms ±20 percent
	Input impedance (index)	20 kilohms ±20 percent
	Output impedance (loop)	12.15 kilohms ±5 percent
	Output impedance (gain switch)	9.09 kilohms ±5 percent
	Gain	0.98 volt per radian ±5 percent*
	Smoothing time constant	0.8 second ±15 percent*
	Supply voltages	-24.5, -15, and +15 volts
Compensation Amplifier	Coarse gain	2.42 volts per volt ±4 percent*
	Fine gain	45.2 volts per volt ±4 percent*
	Input impedance	42.2 kilohms ±1 percent
	Output impedance	≤ 100 ohms
	Supply voltages	+15 and -15 volts
Gain Switching Circuit	Input impedance	>150 kilohms
	Threshold	±0.26 volt ±0.04-volt error (15 degrees)
	Supply voltages	-24.5, -15, and +15 volts
Summing Amplifier	Gain	19.6 volts per volt ±4 percent*
	Input impedance	51.1 kilohms ±1 percent
	Output impedance	< 500 ohms
	Supply voltages	-15 and +15 volts

*Denotes End-of-Life (EOL) tolerances.

TABLE IV-4. PCS ELECTRONIC SPECIFICATIONS (Sheet 2 of 2)

Component	Characteristic	Specification
Power Amplifier	Gain	6.1 volts per volt $^{+5 \text{ percent}}_{-20 \text{ percent}}$
	Input impedance	≥100 kilohms
	Output impedance	≤2 ohms
	Supply voltage	-26 to -36 volts
Encoder Electronics	Input impedance	>100 kilohms
	Input signal level	0 to 230 millivolts p-p
	Output impedance	<1000 ohms
	Output signal level	30 $^{+1}_{-5}$ volts p-p
	Supply voltages	+15 and -15 volts
Frequency-to-dc Converter	Sensitivity	0.281 volt per radian per second
	Smoothing time constant	0.05 second
	Ripple	≤100 millivolts p-p, at 900 Hz
	Input impedance	>100 kilohms
	Output impedance	10 kilohms ±0.5 percent
	Supply voltage	-24.5, -15 and +15 volts
	Static offset	≤ ±20 millivolts
Dc-to-dc Converter	Output voltages	+15, +5, and -15 volts
	Efficiency	65 percent at rated load
	Supply voltage	-24.5 volts ±1 percent
Blanking Circuits	Blanking angles for pitch scan	200 degrees coarse mode, or 330 degrees fine mode
	Supply voltages	-15, +5, and +15 volts

b. PULSE WIDTH MODULATOR (PWM) ERROR DETECTOR

The function of the PWM error detector is to generate an error pulse whose width is proportional to the time difference between the horizon sensor sky-earth pulse and the encoder index pulse. The polarity of the error pulse is determined by the order of occurrence of the pulses, a leading index pulse corresponding to a positive pitch error and a leading horizon pulse to a negative error. The error pulse is smoothed in an RC lag network to provide an average dc level.

Operationally, the leading edges of the input pulses set the respective control binaries whose outputs feed a difference amplifier. The difference amplifier provides a bipolar output error pulse which is processed by the RC lag network.

After both binaries are set, resetting of the AND gate is initiated upon receipt of the next positive tachometer pulse, after which the binaries are ready to accept the next set of input pulses. Should the binaries fail to reset, a second reset pulse derived from the 200 degree blanking pulse is OR'ed into the reset circuit of the PWM; however, this redundancy exists only in the fine-gain mode. The error measurement characteristics are shown in Figure IV-33. As the analog error decreases, the pulse width error decreases correspondingly. The equivalent dc level after smoothing is a satisfactory linearization of the analog error.

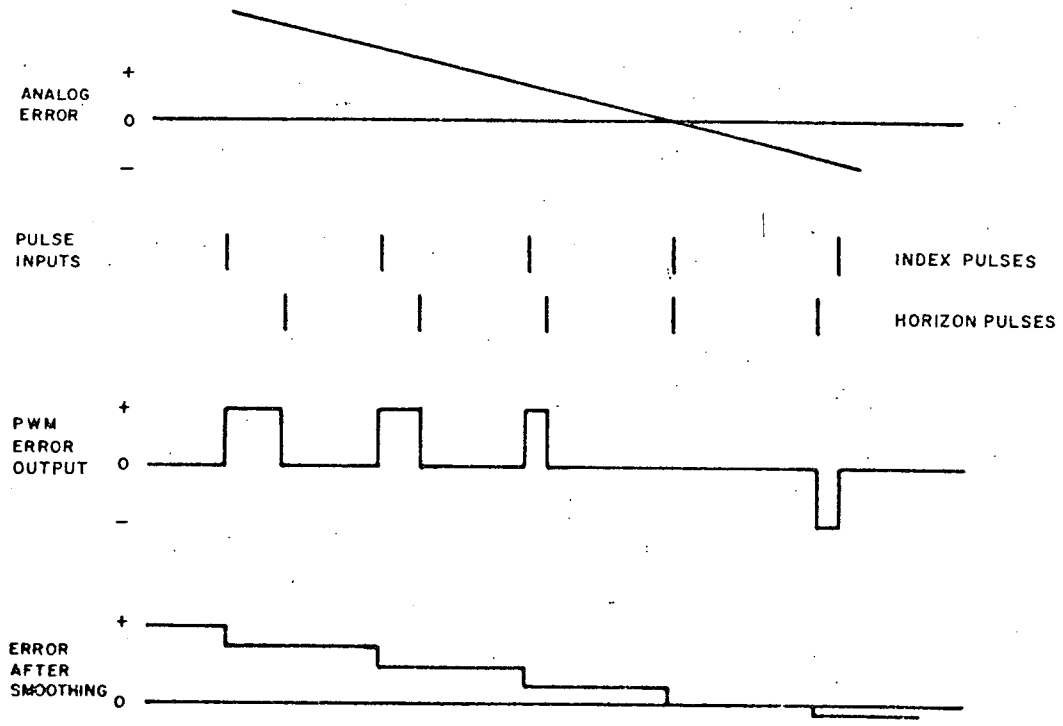

Figure IV-33. Error Detection

c. COMPENSATION AMPLIFIER

The compensation amplifier is a high-gain dc operational amplifier used to generate specific transfer characteristics. The inverting operational amplifier is shown in Figure IV-34.

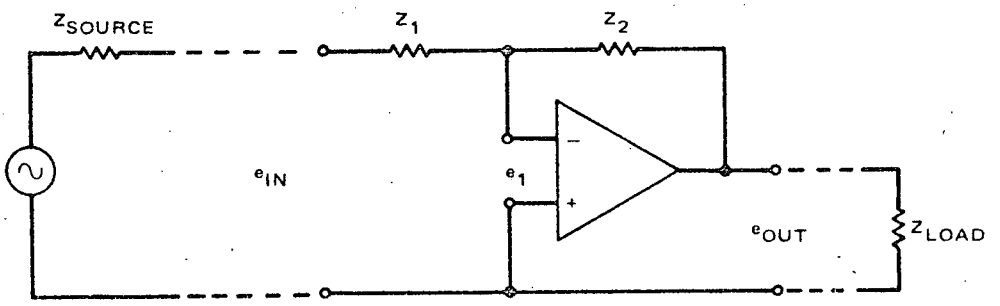

Figure IV-34. Operational Amplifier, Simplified Schematic Diagram

Assuming zero source impedance, very large load impedance, infinite gain, and infinite input impedance, the transfer characteristic of the compensation amplifier can be expressed as follows:

$$\frac{E_{out}}{E_{in}} = \frac{Z_2}{Z_1}, \qquad \text{(IV-38)}$$

By adjusting Z_2, the required signal gain and phase compensation are provided.

d. GAIN SWITCHING CIRCUIT

A block diagram of the gain switching circuit is shown in Figure IV-35. This circuit consists of a differential amplifier from which the absolute value of the smoothed error signal is derived, a filter, a threshold circuit, and a relay driver. When the error signal exceeds a preset level, the relay driver is activated and the feedback network in the compensation amplifier is automatically reselected.

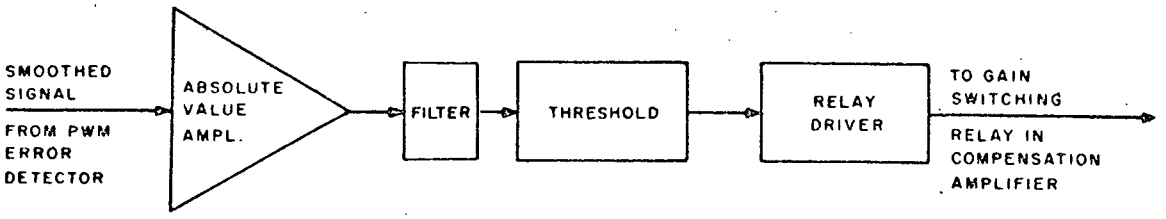

Figure IV-35. Gain Switching Circuit, Block Diagram

e. SUMMING AMPLIFIER

The summing amplifier, shown schematically in Figure IV-36, is a high-gain dc operational amplifier which sums the motor bias voltage, the frequency-to-dc converter output, and the compensated position error signal. In the open loop mode, the compensated position error signal is removed and the motor bias voltage level is determined by the position of the coarse/normal relay. The motor speed is 150 rpm in NORMAL mode operation and 115 rpm in COARSE mode operation. A clamping circuit precludes the motor speed falling below 115 rpm by limiting the minimum net input voltage to the summing amplifier.

f. POWER AMPLIFIER

The power amplifier extends the dynamic range of the summing amplifier to the full capacity of the unregulated power supply, and serves as an efficient power interface between the summing amplifier and the torque motor.

g. TORQUE MOTOR

The following criteria were applied in the selection of a torque motor for the P C S.

- The inside diameter of the motor must properly support and accommodate installation of the pitch and roll horizon sensors to permit the use of mirror-scanning horizon sensors and eliminate the need for sensor slip rings.
- The motor must operate from the available -26- to -36-volt unregulated power supply to avoid the inefficiencies associated with dc-to-dc power conversions.

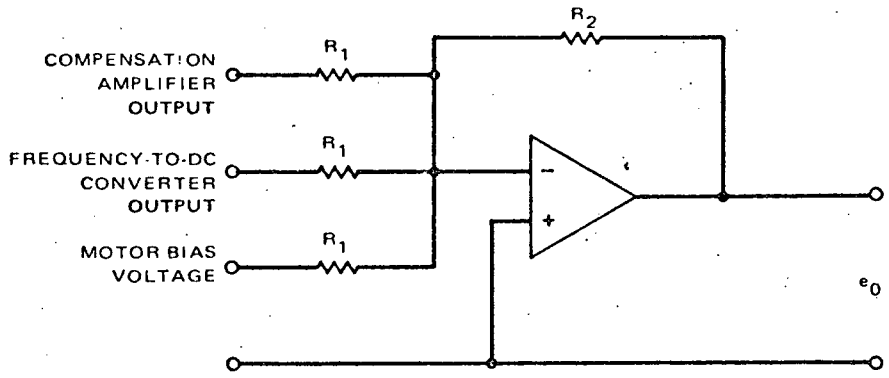

Figure IV-36. Summing Amplifier, Simplified Schematic Diagram

- The motor must supply a steady-state load torque of 20 ounce-inches deriving from bearing friction, brush friction, and magnetic drag, and must have adequate reserve capacity to accomplish capture in the presence of a ± 15-percent deviation from nominal in system angular momentum.

- The motor must be a direct drive, pancake type to eliminate any gearing requirements.

The Inland Model T-4437A dc torquer or its equivalent was selected for the redundant configuration. For the minimum available voltage, 24 volts allowing 2 volts for power amplifier drop, the torque-speed characteristics shown in Figure IV-37 satisfy criteria 2 and 3. The motor, exclusive of the power amplifier, draws 3.44 watts of power at the design point.

Before the brush-type torque motor was selected, special attention was given the problem of ensuring suitably reliable operation of the armature brushes throughout the life of the mission. Testing by RCA, under thermal-vacuum conditions with 50/50 silver-graphite brushes, demonstrated the required performance reliability. Both bearing and brushes operate in an oil vapor atmosphere derived from a low vapor pressure synthetic lubricant stored within the momentum wheel assembly. It is of interest to note that the motor manufacturer

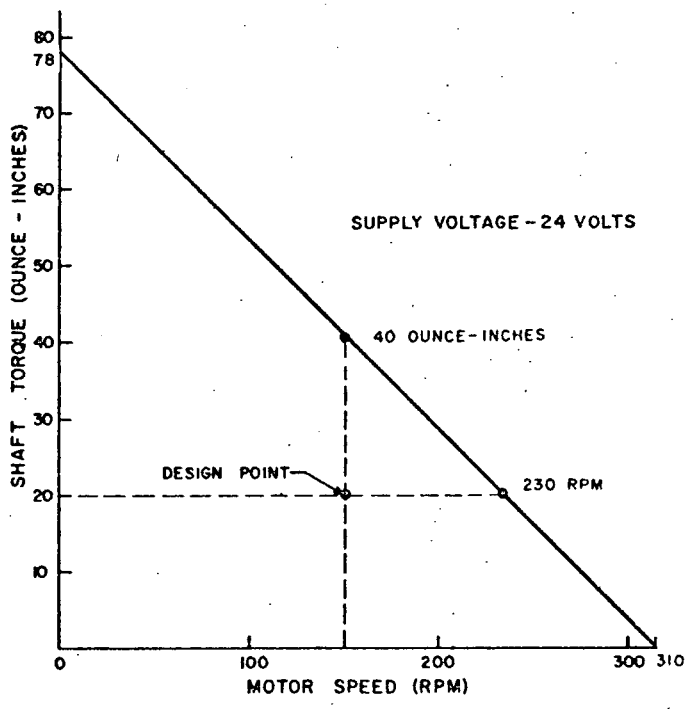

Figure IV-37. Torque and Speed Characteristics for Inland Torque Motor Model T-4437A

experienced significantly higher wear rates for silver-graphite brushes under standard atmospheric conditions. Accordingly, it is inferred that, from the standpoint of brush wear, the lubrication provided in vacuum conditions was superior to that present under standard atmospheric conditions.

Difficulties encountered during life testing of the motor precipitated an intensive study of the dynamics of motor brush wear and of preventative methods for brush wear suppression. The brush wear study suggested the substitution of diethyl hexyl sebacate for the dioctyl adipate originally used as a lubricant. In addition, design changes were introduced to reduce the thermal coupling of the motor, thereby making the unit more isothermal in operation. During testing, a strain gage assembly and amplifier were used to monitor brush reserve. These items were incorporated in the motor design to provide continuous monitoring of brush reserve suitable for telemetry during operation in orbit.

h. ENCODER

The encoder is a two-track, variable-reluctance, magnetic transducer with redundant windings for each output and a pair of outputs for each control loop. Full-periphery sensors minimize the effects of shaft misalignment and mounting eccentricities. One of the tracks, the velocity track, provides a 360-pulse per revolution rate signal (i.e., tachometric) for feedback around the motor. The other track, the index track, produces the desired pitch index pulse once per revolution. The outputs from the encoder are low level signals which require amplification and processing prior to utilization in the pitch control loop.

i. ENCODER ELECTRONICS

The two encoder output signals utilized in the PCS loops, the velocity track pulse train and the index pulses, are amplified by a threshold amplifier, provided for each signal. The velocity signal is thresholded very nearly at the zero crossings to produce sharp pulses. The index signal is thresholded at a level corresponding to a flywheel speed of approximately 110 rpm.

j. DC-TO-DC CONVERTER

The PCS dc-to-dc converter uses the same type of circuit as is utilized in the other dc-to-dc converters in the spacecraft. The input voltage to the converter is -24.5 volts dc ± 1 percent; the nominal output voltages are +15, +5, and -15 volts dc. A 3-percent tolerance is maintained on output voltages for load current levels of 20 to 100 milliamperes inclusive with a minimum overall conversion efficiency of 65 percent.

k. PITCH SENSOR THRESHOLD AMPLIFIERS

The sensor threshold level is 10 times the zero-to-peak noise which corresponds to a level of 160 millivolts. The threshold amplifier driven by the horizon sensor is a biased dc operational amplifier, set to switch at the 160-millivolt input. For the lowest expected horizon temperatures, the input is sufficiently high to exceed this threshold. The threshold networks are connected to the outputs of each of the pitch horizon sensors by switches commandable from the ground. This arangement accommodates ground commanded cross-strapping of the pitch horizon sensors with the redundant pitch control loops.

l. EARTH BLANKING

As the horizon sensors scan the earth, the varying temperatures of the earth cause fluctuations in the bolometer output. From previous experience, it is reasonable to assume that during the earth scan time certain pulses produced will trigger the threshold circuit. For proper performance of the pitch control electronics these earth pulses must be suppressed. Consequently, earth blanking of the sensor outputs is included.

A 9-bit shift register with a 511-pulse capacity is used to count the encoder velocity track pulses. Since 360 pulses are generated per revolution, each pulse corresponds to 1 degree of rotation.

The shift register is reset upon receipt of the 360th velocity track pulse or a pitch sensor sky-earth horizon pulse, whichever occurs first.

Signal outputs are derived from the register at elapsed pulse counts of 200 and 330, corresponding to 200 and 330 degrees of scan, respectively. These signals are used in the blanking.

In the fine gain mode, all horizon sensor threshold amplifier outputs are blanked between 0 and 330 degrees of flywheel rotation. The region from 0 to 200 degrees is blanked in the coarse gain mode to permit rapid horizon acquisition in the presence of large pitch errors. The 330-degree fine gain mode deblanking pulse is retained for backup purposes.

m. ELECTRONICS BOX

This box consists of three parts: top cover, wrapper and base. The top cover houses five connectors; two for test point connection, one for command and telemetry, and two for interface with the momentum wheel assembly. The wrapper encloses seven circuit boards which are mounted in Birtcher slides and plug into board connectors on the harness board. The harness board provides the electrical tie between the individual circuit boards

and the interface between the boards and the outside connectors. The base houses two dc-to-dc converters, the two power resistors used in the wheel speed threshold circuits and the two power transistors used in the power amplifier.

6. MWA Mechanical Design

The momentum wheel assembly is a single electromechanical unit consisting of an outer fixed housing and an inner rotating turntable, each shaped to accommodate and retain the following essential parts: (1) an encoder with redundant coils, (2) labyrinth seals, (3) redundant torque motors, (4) oil reservoirs (5) a flywheel, (6) a mirror assembly, and (7) bolometers and bolometer electronics. The turntable assembly is supported by the external housing through a single bearing.

The assembly incorporates a single bearing rather than two spaced bearings for support of a rotating shaft for the following reasons:

- The single bearing has less friction than two bearings.
- The single bearing allows visual inspection of motor concentricity during assembly. Two bearings would require sufficent axial spacing to give a reasonable base, necessitating a motor mounting between bearings. With the attendant buildup of assembly tolerances, such an arrangement would introduce greater errors in motor concentricity.
- The single bearing assembly permits a shorter design length thus saving weight.
- The single bearing meets all of the system performance requirements satisfactorily.

The Conrad four-point contact, ball bearing utilized is the Kaydon Type KD45XP with a selected diametral clearance between 0.0008 and 0.0012 inch and a maximum angular tilt of 0.00045 radians.

The allowable bearing loads based on standard usable Brinell values are:

- Radial load: 12,400 pounds,
- Thrust load: 30,800 pounds, and
- Moment: 31,000 pound inches.

It has been demonstrated that an inverse temperature difference between the bearing races (i.e., inner race warmer than outer race) of 13°C would cause constriction of the diametral clearance by as much as 0.0008 inch, the minimum value provided by the design, with possible bearing seizure. It was established that for a temperature safety factor of 2.0 an outer-to-inner race differential in excess of 6°C is unacceptable. Significantly, the results of the MWA thermal analyses indicated that, even during an emergency power overload, the steady-state bearing race temperature differential is unlikely to exceed 1°C. Further, it was determined that, under all likely conditions the temperature of the inner race will never be more than 6°C below that of the outer race. Moreover, the most probable value for the maximum inner- to outer-race temperature difference was found to approximate 2°C. Should the maximum diametral clearance (i.e., 0.0012 inch) be realized in assembly, an inner-to-outer-race temperature differential of 10°C can be accommodated before the encoder gap, a critical performance parameter, becomes intolerably large due to the shaft wobble deriving from thermally induced expansion and contraction during operation.

The bearing races and balls are SAE 52100 steel which shows excellent oxidation resistance up to 250°F. This intrinsic resistance in addition to the lubricating oil film precludes corrosion of the bearing during storage.

Each motor consists of three separate parts: a two-segment brush assembly, an armature, and a stator. Radial self-locking screws align the stator to the rotational center of the bearing.

The encoder is installed at the top of the assembly. Both the rotating part and the fixed part of this magnetic transducer are mounted through adaptors which provide the flexibility necessary to accommodate the exact dimensions of the encoder.

60 grams of lubricant are stored within three Nylasint oil reservoirs which utilize about one third the available volume. Lubrication is achieved by low pressure vaporization of the oil in the closed housing. The vapor lubricates the motor brushes and the bearing. The synthetic lubricant is diethyl hexyl sebacate, a dibasic acid ester. Selection of this lubricant is based on its successful performance during thermal-vacuum testing.

A labyrinth-type sealing system is utilized in the assembly. The leak rate of this labyrinth determines the functional lifetime of the lubrication system. The labyrinth seals are constructed of stacks of magnesium sheets of the proper diameter. The thickness is chosen so that the rotating sheets have a nominal 0.02-inch clearance and thus no rubbing contact (i.e., no associated friction). Experience has shown this construction to be satisfactory.

The theoretical lubricant loss rate through the two labyrinth seals for the applicable free molecular flow region is given by:

$$W = \left[0.0583\ P\left(\frac{M}{T}\right)^{1/2}\ A\right]^{*} f \qquad \text{(VI-39)}$$

where

W is the oil loss rate (grams per second),

P is the vapor pressure (mm Hg),

M is the molecular weight of the oil,

T is the oil temperature (°K),

A is the aperture area (cm^2), and

f is the transmission probability of molecular flow.

The transmission probability is a function of the length-to-clearance ratio of the seal and the number of directional changes from the inner cavity to the surrounding environment. Each of the two labyrinth seals consists of 14 consecutive L-shaped segments. The diethyl hexyl sebacate, with a molecular weight of 426, loss rate is illustrated in Figure IV-38.

Four bolometers are mounted on a support tee which extends through the hub of the rotating assembly to a structural mounting point. Electronics which provide preamplification for the bolometer signals are mounted on the support tee adjacent to the bolometers. The optical axes of the bolometers are aligned by a shimming technique.

A spoked flywheel having a continuous rim is attached to the rotating hub. The outside diameter of the flywheel is selected to provide minimum clearance between the wheel and the inside of the Marman clamp projecting below the baseplate section of the satellite. When the four separation-spring-operated, mushroom-shaped, pushoff pads are removed from the adapter, the fully integrated momentum wheel assembly is inserted and attached to the baseplate.

Attached to the flywheel hub is the sensor mirror assembly. This assembly includes the large roll mirror and the smaller pitch mirror. The pitch mirror reflects incident radiation to the pitch bolometers through a hole in the

---

*W.A. Salmon and C.M. Apt, "A Lubrication System for Space Vehicles", Automotive Engineering Congress Paper 632E, January 1963, and D. Santeler, "Vacuum Technology", International Science and Technology, No. 13, January 1963, pp. 46-54.

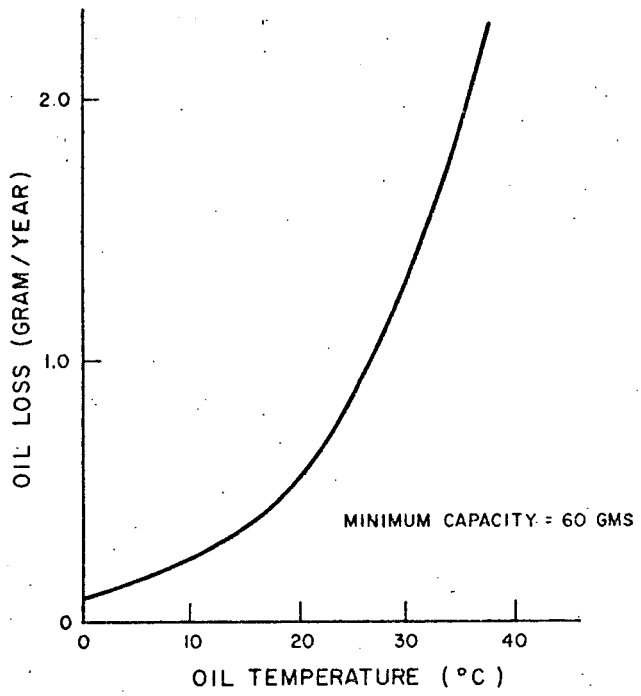

Figure IV-38. Molecular Flow Loss of MWA Lubricant P-10 (Diethyl-hexyl Sebacate)

roll mirror. The roll mirror reflects incident radiation to both of the roll bolometers. The composition of both mirrors is 6061-T3 aluminum alloy which serves as a structural base. A pure aluminum surface finish is vacuum deposited on the aluminum alloy base and overcoated with silicon monoxide. Prior to the final finish, nickel electroplating and physical surfacing is performed as required.

The lower end of the roll mirror is a flat plate cantilever. The centrifugal force deriving from rotation at 150 rpm will cause deflection of the mirror. Local changes in the mirror angle of approximately 2 minutes of arc at the outermost tip and 1 minute of arc at 0.6 inch from the tip, a position corresponding to the line of sight intercept for roll bolometer No. 2, are likely. Although reflections compound these deviations, such changes are insignificant.

G. SYSTEMS INTERFACES

1. Power

The power for this subsystem will be drawn from the -26 to -36-volt unregulated bus and the -24.5-volt regulated spacecraft power supply. Other voltages used in the P C S will be derived from a dc-to-dc converter operating off the -24.5-volt supply. Table IV-5 summarizes the power requirements for the operational mode.

2. Command and Control

All required switching will be routed through the command distribution unit (CDU).

3. Telemetry

All telemetry data will be routed to the signal conditioner. All PCS telemetry points will be conditioned to assure compatibility with voltage and impedance requirements of the spacecraft telemetry subsystem.

TABLE IV-5. OPERATIONAL POWER REQUIREMENTS

Item	Power at -24.5 Volts (watts)	Operation Time	Equivalent Continuous Drain (watts)
Pitch Axis Control Loop*	8.4	Continuous	8.6
Magnetic Bias Coil	0.013 to 0.13	Continuous	0.013 to 0.13
Momentum Coil	1.8 per coil	**	**
QOMAC Coil	0.78	1/5 orbit/orbit (23 minutes)	0.16
Total (continuous maximum)			8.89

*Power from both regulated (-24.5 volts) and unregulated (-26 volts) supplies.

**As required for adjustment.

H. DISTURBANCE ANALYSIS

A summary of all significant disturbances with a brief description of dynamic effect on the spacecraft is given in Table IV-6. The following constitutes an outline of the material which led to the tabulated predictions.

1. Residual Magnetic Dipoles

The MBC (magnetic bias coil) nulls the residual dipole along the spacecraft pitch axis, $\hat{3}$,* to the value required for sun synchronous precession (i.e., 0.573 Atm^2). On a spinning spacecraft such as TOS, the effects of residual dipoles along the transverse axes ($\hat{1}$ and $\hat{2}$) cancel over each spin. However, for the three-axis stabilized ITOS spacecraft, transverse residual dipoles cause both an attitude precession and a momentum change. Although cancelling over a complete orbit, these effects will contribute to the instantaneous roll/yaw and pitch attitude errors.

With the spacecraft in an earth-locked condition, the residual dipoles along the three control axes, interacting with the earth's magnetic field, induce the following disturbance torque:

$$\overline{T} = \overline{M} \times \overline{B} = \hat{1}\,(M_2 B_n - M_3 B_t) + \hat{2}\,(M_3 B_r - M_1 B_n) + \hat{3}\,(M_1 B_t - M_2 B_r) \quad \text{(IV-40)}$$

where (B_r, B_t, B_n) are the components of the earth's field resolved in the local vertical/horizontal orbital reference frame described in Paragraph E. The torque acting on a body with stored angular momentum, $\overline{H} = H\,\hat{3}$, is given by

$$\overline{T} = \left(\frac{d}{dt} H\right)\hat{3} + H\left(\frac{d}{dt}\,\hat{3}\right) \quad \text{(IV-41)}$$

The change in the unit vector $\hat{3}$ entails redirection only, implying rotation about an axis normal to $\hat{3}$ which is expressible in vector notation as:

$$\frac{d}{dt}(\hat{3}) = \overline{\omega}_P \times \hat{3} \quad \text{(IV-42)}$$

where $\overline{\omega}_P$ is defined as the directed precession rate of the spacecraft with respect to which the orbital rate (1 rev/orbit) is negligibly small by comparison.

*All notations and coordinate systems are based on the material presented in Section E.

TABLE IV-6. SUMMARY OF DISTURBANCES AND EFFECTS (Sheet 1 of 3)

Source of Disturbance	Axis of Torque	Effect of Disturbance of Spacecraft
1. Residual magnetic dipole		
a. 1 Atm^2 along yaw axis	Pitch	Sinusoidal modulation of momentum, ±0.15 percent peak change in momentum; ±0.0085-degree peak pitch error, zero average over an orbit.
	Roll	Slow precession of pitch axis around a cone, one complete cycle per orbit; maximum excursion of 0.034 degree.
b. 1 Atm^2 along roll axis	Pitch	Sinusoidal modulation of momentum, ±0.3 percent peak change in momentum; ±0.017-degree peak pitch error, zero average over an orbit.
	Yaw	Slow precession of pitch axis around a cone, one complete cycle per orbit; maximum excursion of 0.034 degree.
c. 0.05 Atm^2 along pitch axis (resolution of mag bias coil)	Nodal	Net drift of ±0.086 degree per day about the $\hat{b}$ axis.
2. Solar pressure (Disturbance torque, 10^{-4} inch-pounds)	In Orbit Plane	Slow precession of momentum vector in response to torque, which is normal to a plane defined by the spacecraft pitch axis and the sun line; magnitude and direction is function of orbit sun angle and season.

TABLE IV-6. SUMMARY OF DISTURBANCES AND EFFECTS (Sheet 2 of 3)

<table>
<tr><th>Source of Disturbance</th><th>Axis of Torque</th><th>Effect of Disturbance on Spacecraft</th></tr>
<tr><td rowspan="2">2. Solar pressure (con't)</td><td>In orbit plane</td><td>Disturbance Torque (10^{-4} inch-pounds)
<table><tr><th>Time of Year</th><th colspan="3">Orbit Sun Angle (degrees)</th></tr><tr><th></th><th>30</th><th>45</th><th>60</th></tr><tr><td>Summer Solstice</td><td>+0.40 $\hat{\ell}$
-0.49 $\hat{b}$</td><td>+0.32 $\hat{\ell}$
-0.38 $\hat{b}$</td><td>+0.23 $\hat{\ell}$
-0.27 $\hat{b}$</td></tr><tr><td>Winter Solstice</td><td>-0.25 $\hat{\ell}$
-0.58 $\hat{b}$</td><td>-0.20 $\hat{\ell}$
-0.46 $\hat{b}$</td><td>-0.15 $\hat{\ell}$
-0.33 $\hat{b}$</td></tr></table>Maximum potential $\hat{\ell}$ precession of 1.35 degrees per day is corrected by unipolar torquing. Maximum potential $\hat{b}$ precession of +.93 degree per day is corrected by mag bias torquing.</td></tr>
<tr><td>In orbit plane</td><td>Sinusoidal modulation of attitude angles, magnitude is function of orbit sun angle.
<table><tr><th>Orbit Sun Angle (degrees)</th><th>Roll/Yaw Peak-to-Peak Attitude Perturbation (degrees)</th></tr><tr><td>30</td><td>0.027</td></tr><tr><td>45</td><td>0.018</td></tr><tr><td>60</td><td>0.009</td></tr></table></td></tr>
</table>

TABLE IV-6. SUMMARY OF DISTURBANCES AND EFFECTS (Sheet 3 of 3)

Source of Disturbance	Axis of Torque	Effect of Disturbance on Spacecraft
2. Solar pressure (con't)	Pitch	Sinusoidal modulation of momentum, zero average over an orbit; peak change is function of orbit sun angle. Orbit Sun Angle (degrees) / Momentum Change (max percent) 30 / 0.037 45 / 0.020 60 / 0.027
3. Magnetic hysteresis and eddy-current losses	Pitch	Slow decay of momentum; 1 percent per week, maximum
4. Gravity gradient	Roll	Sinusoidal precession at orbital frequency, zero average over an orbit; peak change in attitude is 0.105 degree.
	Pitch	Slow decay of momentum; 4.2 percent per week, nominal. Occasional momentum control is required for compensation.
5. Internal rotating components (uncompensated transverse momentum)	-	Steady state effect due to continuously operating components is a negative yaw error of 0.063 degree.

Thus, the kinetic reaction excited by the disturbance torque due to residual dipoles is given by:

$$\overline{M} \times \overline{B} = \left(\frac{d}{dt} H\right)\hat{3} + H\left(\overline{\omega}_P \times \hat{3}\right) \qquad \text{(IV-43)}$$

Suppressing the small residual dipole directed along the pitch axis deriving from the resolution of the MBC dipole. Equations (IV-40 and IV-43) yield

$$(M_2 B_n)\ \hat{1} - (M_1 B_n)\ \hat{2} = H\ (\overline{\omega}_P \times \hat{3}) \qquad \text{(IV-44)}$$

with the result that the precession rate of the spacecraft can be defined as

$$\omega_P = \frac{M_{12} B_n}{H} \qquad \text{(IV-45)}$$

where $M_{12} = \sqrt{M_1^2 + M_2^2}$, the total transverse residual dipole.

The maximum angular excursion due to this precession occurs after half an orbit has elapsed and is given by:

$$\theta_P = \tilde{\omega}_P t = \frac{M_{12} B_n \tau}{\pi H} \text{ orbit} \qquad \text{(IV-46)}$$

where τ is the orbital period and $\tilde{\omega}_P = 2\ \omega_P / \pi$, the half-orbit average precession rate.

Because the transverse residual dipoles are body-bound, rotating with the spacecraft as it traverses its orbit, the disturbance induced torque excites nutation. As a consequence, the spacecraft pitch axis deviates from the orbit normal, precessing in a coning motion such that spatial coincidence is reestablished at the completion of an orbit. For the nominal orbit (i.e., circular, 790 nautical miles altitude), in mission-mode attitude, at nominal momentum (i.e., 212-inch-pound-seconds^2), the maximum excursion per transverse residual dipole-Atm^2 is 0.034 degree.

For the residual dipole along the pitch axis, Equations (IV-40 and IV-43) yield:

$$-(M_3 B_t)\,\hat{1} + (M_3 B_r)\,\hat{2} = H\ (\bar{\omega}_P \times \hat{3}) \qquad \text{(IV-47)}$$

From this result, it can be inferred that the orbit-average precession of the spacecraft is directed about the $\hat{b}$-axis at a rate consistent with:

$$\tilde{\omega}_P = \frac{M_3 \tilde{B}_{rt}}{H} = \frac{M_3 B_o}{H} \qquad \text{(IV-48)}$$

where B_o is the secular fraction of the in-plane component of the earth's magnetic field and the disturbance torque is directed about the $\hat{\ell}$ -axis.

For the residual dipole about the pitch axis, Equations (IV-40 and IV-43) yield:

$$\frac{d}{dt} H = (M_1 B_t - M_2 B_r) \qquad \text{(IV-49)}$$

such that

$$\Delta H \simeq (M_1 B_t - M_2 B_r)\,\Delta t \qquad \text{(IV-50)}$$

Since, in mission-mode operation, the total transverse residual dipole rotates once per orbit relative to the average in-plane component of the earth's magnetic field, there is no net change in momentum over an orbital period. A 1 atm^2 residual dipole directed along the roll axis induces a maximum momentum deviation of approximately 0.3% in a half orbit's time. Postulating a pitch servo velocity error coefficient of 1.78 sec^{-1} and a spacecraft to flywheel inertia ratio about the pitch axis of 88.2, it can be demonstrated that this momentum modulation induces a maximum pitch offset of 0.017 degree.

The modulation effect of a 1 atm^2 residual dipole directed along the yaw axis is approximately half that for the roll axis dipole.

2. Solar Torques

In the ITOS D and E design, the solar arrays are hinged at the thermal fence end of the spacecraft so in mission attitude with arrays deployed, the equipment module structure does not shadow the photosensitive cells. This physical arrangement results in a large offset between the spacecraft

center-of-gravity and its center of pressure (i.e., the point at which the total force deriving from incident solar radiation can be considered to act), resulting in a solar radiation induced disturbance torque having both cyclical and secular components. This disturbance torque alters both the magnitude and direction of the spacecraft momentum vector.

In general, any surface may absorb a fraction, α, of the incident radiant energy, specularly reflect a fraction, ρ_s, and diffusely reflect a fraction, ρ_d. Since the total energy impinging on the surface must equal the sum of these fractional constituents, it follows that:

$$\alpha + \rho_s + \rho_d = 1 \cdot \tag{IV-51}$$

It has been demonstrated that the force exerted on an elementary surface area dA due to impinging photons can be expressed as:

$$\overline{dF} = P_o \, dA \left[\alpha (\hat{S} \cdot \hat{N}) \hat{S} + 2 \rho_s (\hat{S} \cdot \hat{N})^2 \hat{N} + \rho_d (\hat{S} \cdot \hat{N}) (\hat{S} + \frac{2}{3} \hat{N}) \right] \tag{IV-52}$$

where

$\hat{S}$ is a unit vector directed along the sunline in the sense of the incident radiation (i.e., toward the surface),

$\hat{N}$ is a unit vector, normal to the surface and positive inward, and

P_o is the solar radiation pressure.

The resultant torque acting on the body of which the irradiated surface area dA is a part is given by

$$d\overline{T} = (\overline{r} - \overline{r_o}) \times \overline{dF} \tag{IV-53}$$

where

$\overline{r}$ is a displacement vector from any convenient origin to the area dA, and

$\overline{r_o}$ is a displacement from the same origin to the center of rotation about which torques are to be taken; in the present instance, the spacecraft center of gravity.

Areal integration of Equation (IV-54) over the irradiated portion of the spacecraft surface including the three solar panels, the fence end and the earth facing side yields, after some manipulation, the following secular disturbance torque, directed along an axis perpendicular to the plane defined by the spacecraft pitch axis and the sun vector:

$$\bar{T} = \Bigg\{ +3\,(L - r_o)\,A_\rho\,(\alpha_\rho + \rho_{d\rho})\cos\sigma + (L - r_o)\,A_e\,(\alpha_e + \rho_{de})\cos\sigma$$

$$+ \frac{1}{2\pi}\left(\frac{a+2}{4}\right) A_s\,(\alpha_s + \rho_{ds})\,a\cos\sigma$$

$$+ \frac{1}{\pi\sqrt{2}}\; A_s\,(\alpha_s + \rho_{ds})\left(\frac{L}{2} - r_o\right)\sin\sigma$$

$$+ \frac{5}{3\pi\sqrt{2}}\; A_s\left(\frac{L}{2} - r_o\right)\; \rho_{ss}\sin\sigma$$

$$+ \frac{1}{3\pi}\left(\frac{\pi+2}{4}\right) A_s\,\rho_{ds}\left(\frac{L}{2} - r_o\right)\Bigg\} P_o \sin\sigma\left[\sin\lambda'\,\hat{\ell} - \cos\lambda'\,\hat{b}\right] \qquad \text{(IV-54)}$$

where

a is half the width of the spacecraft structure measured normal to the pitch axis,

L is the length of the spacecraft structure measured along the pitch axis,

r_o is the displacement between the spacecraft coordinate origin and the center of rotation about which torques are considered to act, the spacecraft center of gravity,

A_ρ is the area of one panel,

A_s is the area of earth facing side,

A_e is the area of the fence end,

α_B, ρ_d, and ρ_d are the absorption and reflection coefficients defined above,

σ is the orbit sun angle measured from the sun line to the orbit normal, and

λ' is the anomaly of the projection of the sun line in the orbit plane.

The subscript's' indicates the earth facing side, p, the solar panels and e, the fence end.

For a 3 pm ascending node orbit, the angle λ' varies from + 38.9 to -23.4 degrees during one year. The resulting disturbance torques, averaged over one orbit, are tabulated below.

SOLAR RADIATION INDUCED DISTURBANCE TORQUES (INCH-POUNDS)

Time of Year	Orbit Sun Angle (degrees)		
	30	45	60
Percent sun-time	100	80.5	74
Summer solstice	$+0.40 \times 10^{-4}\hat{\ell}$	$+0.32 \times 10^{-4}\hat{\ell}$	$+0.23 \times 10^{-4}\hat{\ell}$
	$-0.49 \times 10^{-4}\hat{b}$	$-0.38 \times 10^{-4}\hat{b}$	$-0.27 \times 10^{-4}\hat{b}$
Winter solstice	$-0.25 \times 10^{-4}\hat{\ell}$	$-0.20 \times 10^{-4}\hat{\ell}$	$-0.15 \times 10^{-4}\hat{\ell}$
	$-0.58 \times 10^{-4}\hat{b}$	$-0.46 \times 10^{-4}\hat{b}$	$-0.38 \times 10^{-4}\hat{b}$

The torques at 45- and 60-degree orbit sun angles are considerably reduced due to the partially eclipsed orbits. The torque about the negative $\hat{b}$ axis induces gyroscopic precession of the spacecraft about the positive $\hat{\ell}$ axis. This disturbance is counteracted by utilizing $\hat{b}$ axis precession deriving from unipolar torquing for a few minutes per half orbit in a programmed mode. The gyroscopically induced torque about the $\pm\hat{\ell}$ axis is corrected by the MBC (magnetic bias coil) dipole.

The orbit-average torque of $+3.2 \times 10^{-5}$ inch-pound occurring at summer solstice for a 45-degree orbit sun angle, requires an MBC dipole of -0.43 Atm^2 for compensation. At the winter solstice, a 30-degree orbit sun angle will result in a disturbance torque of -2.5×10^{-5} inch-pounds necessitating an MBC dipole of +0.34 Atm^2 for compensation. The range of the MBC dipole is ±1.0 Atm^2 about the nominal 0.573 Atm^2 value provided by a permanent magnet, for sun synchronous precession of the spacecraft.

For a 30-degree orbit sun angle in which condition the spacecraft is illuminated for the entire orbit, the torque resulting from the radiation force normal to the anti-earth solar panel produces a 0.027-degree peak to peak cyclical perturbation of spacecraft roll/yaw attitude. However, for a partially eclipsed orbit this force produces a compensating torque which reduces the secular disturbance in the orbit plane approximately 15 percent.

3. Magnetic Losses

a. HYSTERESIS

Momentum loss due to hysteresis is a function of the presence and distribution of magnetic material in the spacecraft. Based on previous experience in the TOS/ESSA spacecraft series and a program emphasizing the minimization of μ-metal usage in the ITOS spacecraft, a maximum momentum decay of 1 percent per week due to hysteresis effects is predicted.

b. EDDY CURRENT

The eddy current losses are very small since the major portion of the spacecraft makes only one revolution per orbit. Even the spinning flywheel should not result in any significant losses, because the wheel spokes are electrically nonconducting.

4. Gravity Gradient

The disturbance torque exerted on the spacecraft due to the non-uniformity of the earth's gravity field arises from the fact that the earth oriented spacecraft axis is not a principal axis. This misalignment is primarily attributable to the deployment of the solar arrays and manifests itself in the presence of finite inertia products. In general the gravity gradient disturbance torque, acting about the mass center of a spacecraft of arbitrary configuration, can be expressed as

$$\overline{T}_{gg} = -3\,\omega_o^2\,(\hat{\rho} \times \overline{\overline{\phi}} \cdot \hat{\rho}) \qquad \text{(IV-55)}$$

where

ω_o is the orbital rate (i.e., 1 revolution per orbit)

$\hat{\rho}$ is a unit vector directed from orbit focus to the spacecraft mass center, and

$\overline{\overline{\phi}}$ is a dyadic formed of the open product $\Sigma_n\, m_n\, (\overline{r_n}\ \overline{r_n})$ with m_n, $\overline{r_n}$ representing, respectively, the mass of the n^{th} particle within the spacecraft and its directed displacement relative to the spacecraft mass center.

For ITOS, the $\hat{1}$, $\hat{2}$, $\hat{3}$ axes comprising the spacecraft reference frame are respectively aligned with the local vertical, the orbital velocity vector, and the orbit normal. For this orientation the gravity gradient disturbance torque of Equation (VI-55) reduces to the following form:

$$\overline{T}_{gg} = -3\omega_o^2(-I_{13}\hat{2} + I_{12}\hat{3}) \qquad \text{(IV-56)}$$

where, as indicated previously, I_{31} is the spacecraft pitch-yaw product of inertia and I_{12} the yaw-roll product.

The roll component of this disturbance torque rotates with the spacecraft once per orbit and induces a nutation, as did the transverse residual dipole. The maximum angular excursion due to this torque occurs after half an orbit has elapsed and equals 0.105 degrees. The pitch torque component produces a nominal momentum decay of 1.28 inch-pound-second per day which is equivalent to a nominal 4.2 percent decay per week in wheel spin rate. Occasional momentum control torquing can compensate for this loss.

5. Internal Rotating Components

All rotating components interior to the spacecraft are mounted such that their axes of rotation are parallel to the roll axis. Consequently, when a rotating component is in operation, the spacecraft angular momentum vector no longer lies along the spin axis of the flywheel. As a result, the spin axis will precess in a coning motion about the total momentum vector, the half-cone angle for which is a function of the magnitude of the momentum inherent in the rotating components and the time at which their operation is initiated.

Figure IV-39 is a stereographic display which presents the loci traced out by the spin axis as it cones about the momentum vector. The angle γ_o is the initial nutation half-cone angle. With the generation of transverse momentum in one or more of the rotating components, the total momentum vector shifts from point O to point P. The spin axis now moves about the cone bounded by the angles $\theta_{1\,max}$ and $\theta_{2\,max}$. These angles are functions of the location of the spin axis on the cone at the moment operation of the rotating components is initiated. The worst-case situation arises when operation commenses as the spin axis reaches its maximum displacement from P as shown. When the rotating components are turned off, the momentum vector returns to point O, and the spin axis cones about that point. Again, the cone angle depends on the location of the spin axis on the cone at the time the operation of the rotating components is terminated. The worst-case situation occurs for a spin axis located at point Q. For different phasing, the nutation angle is reduced.

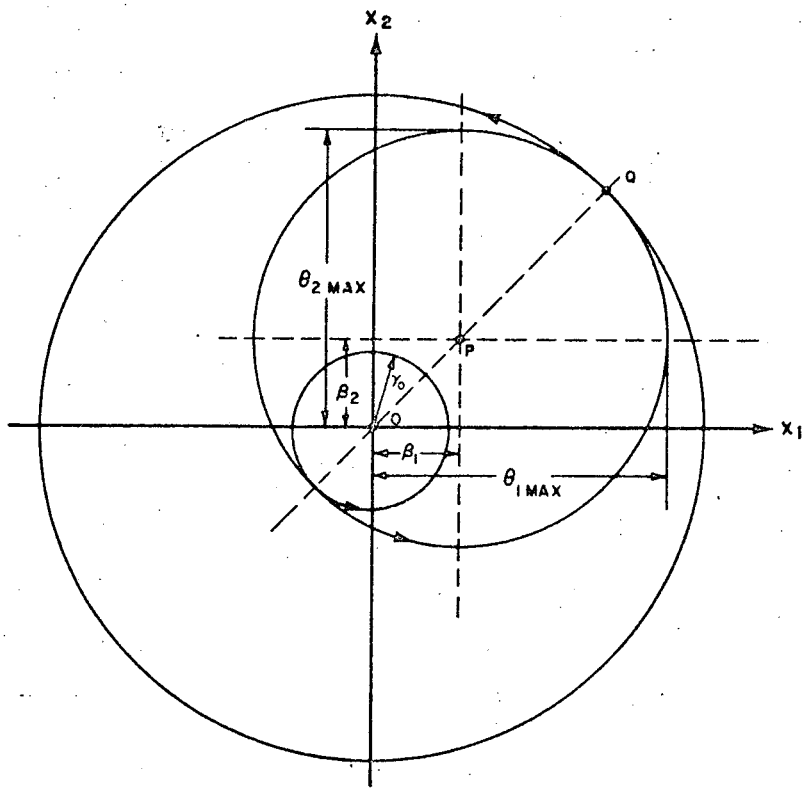

Figure IV-39. Nutation Cone Angles Due To Transverse Momentum

The expressions for $\theta_{1\ max}$ and $\theta_{2\ max}$ are given by:

$$\theta_{1\ max} = \sqrt{\frac{\lambda_1}{\lambda_2}}\,\gamma_o + \beta_1 + \sqrt{\frac{\lambda_1}{\lambda_2}}\,\sqrt{\beta_2^{\,2} + \frac{\lambda_2}{\lambda_1}\,\beta_1^{\,2}}\,,$$

(IV-57)

and $$\theta_{2\ max} = \gamma_o + \beta_2 + \sqrt{\beta_2^{\,2} + \frac{\lambda_2}{\lambda_1}\,\beta_1^{\,2}}\,,$$

for which

$$\lambda_1 = \left(\frac{I_{33} - I_{11}}{I_{11}}\right)\omega_o + \frac{h_f}{I_{33}}\,,$$

$$\lambda_2 = \left(\frac{I_{33} - I_{22}}{I_{22}}\right)\omega_o + \frac{h_f}{I_{33}}\,,$$

and

$$\beta_1 = \frac{h_1}{I_{11}\,\lambda_1},$$

$$\beta_2 = \frac{h_2}{I_{22}\,\lambda_2},$$

where

I_{11} is the spacecraft yaw moment of inertia (1326 inch-pound-seconds^2)

I_{22} is the spacecraft roll moment of inertia (1134 inch-pound-seconds^2)

I_{33} is the spacecraft pitch moment of inertia (1191 inch-pound-seconds^2)

ω_o is the orbital rate (0.91×10^{-3} radians/second)

h_1, h_2 are respectively the roll and yaw transverse angular momenta excited by rotating components, and

h_f is the flywheel angular momentum (212 inch-pound-seconds).

Since, as indicated above, all rotating components are located with their axes of rotation parallel to the roll axis, $h_1 = \beta_1 = O$. Also $\lambda_1 = \lambda_2 = 0.178$, since $\frac{hf}{i_{33}}$ is the dominant term. Accordingly Equation IV-57 reduces to the following form:

$$\theta_1 \max = \gamma_o + \beta_2,$$

$$\theta_2 \max = \gamma_o + 2\beta_2. \qquad \text{(IV-58)}$$

The rotating components on board the ITOS D and E spacecraft include:

- Two scanning radiometers (SR),
- Three scanning radiometer recorders, (SRR)
- Two very-high resolution radiometers (VHRR),
- One very-high resolution radiometer recorder (VHRRR), and
- Two vertical temperature profile radiometers (VTPR).

In the normal mission sequence, both VHRR's, one VTPR and one SR are operating continuously. Additionally, an SR recorder is recording continuously. The uncompensated momenta attending operation of the individual components are summarized in Table IV-7.

TABLE IV-7. ROTATING COMPONENT DISTURBANCES

Component	Uncompensated Angular Momentum (inch-pound-second)
Scanning radiometers	0.07/each
Scanning radiometer recorders	0.0025/each (record) 0.04/each (playback)
Very high resolution radiometers	0.0625/each
Very high resolution radiometer recorder	0.02
Vertical temperature profile radiometers	0.0625/each

The angular dimensions of the nutation induced in the course of the normal operational sequence specified above are given by

$$\theta_{1\ \max} = 0.063°$$

$$\theta_{2\ \max} = 0.126°$$

where the initial half-cone angle, γ_o, has been suppressed. Since the disturbances are time-invariant and body-bound (i.e., rotating with the spacecraft), the induced nutation will ultimately be transformed into an angular displacement of the spacecraft pitch axis relative to the orbit normal, under the action of the liquid dampers. The offset will appear as a negative error in the local-yaw attitude of the spacecraft (i.e., the pitch axis will be displaced from the orbit normal toward the spacecraft velocity vector in the local-horizontal plane approximately 0.063 degrees).

SECTION V

POWER SUPPLY

SECTION V

POWER SUPPLY

A. INTRODUCTION

The ITOS D and E power supply subsystem is a solar-cell, rechargeable battery subsystem which delivers a regulated output voltage of -24.5 ±0.25 volts and an unregulated output of -26.0 to 36.2 volts. It consists of a three-panel solar cell array, redundant series voltage regulator, a shunt dissipator with redundant control amplifiers, two nickel-cadmium battery packs each with its own charge controller, and associated telemetry circuits. The power supply subsystem is identical to that used on TIROS M except for a change in battery size. The heavier electrical load defined for the ITOS D and E spacecraft requires a change from 4.0 ampere-hour to 6.0 ampere-hour batteries in order to maintain the maximum depth of discharge to less than 25 percent and the end of night battery voltage above the minimum requirement of 26.5 volts at the end of life. The battery size change also requires changes in charge control circuitry and charge current telemetry to adjust the charge rates and telemetry range.

The significant loading during each orbit is defined by the following spacecraft operational programming:

(1) Scanning radiometer (SR) data recorded and transmitted in real time during the full orbit;

(2) Vertical temperature profile radiometer (VTPR) data recorded over the full orbit.

(3) Very high resolution radiometer (VHRR) data transmitted in real time over the full orbit and an approximate nine-minute remote recording; and

(4) A 12-minute spacecraft interrogation and readout of radiometer recorders via S-band data link.

Both nominal and worst-case expected energy balance analyses have been performed for the operational loads. Both analyses show energy balance deficits at 60° sun angles and six-months life in orbit for spacecraft operation as described above. When solar array output decreases (due to charged particle radiation degradation and/or high sun angles) to a value insufficient to fully recharge the batteries, the beacon transmitter and telemetry system may be turned off.

When the array output decreases further, the very high resolution radiometer, VHRR processor, and S-band transmitter and vhf transmitter may be programmed or turned off to permit full battery recharge.

B. FUNCTIONAL DESCRIPTION

1. General

A block diagram of the ITOS D and E power supply subsystem is shown in Figure V-1. The subsystem consists of a solar array, a shunt limiter, batteries, charge controllers, and series voltage regulators. The solar array converts incident energy from the sun to electrical energy. The shunt limiter prevents the array bus voltage from exceeding prescribed limits by shunting solar array current which is in excess of that required to recharge the batteries and supply the spacecraft load. The shunt limiter consists of three shunt dissipators, mounted on the solar panels, and two control amplifiers, located in the power supply electronics. The batteries supply power to the spacecraft during eclipse periods and also supply peak loads during satellite day. The charge controllers provide protection for the batteries by limiting charge currents to proper levels during charge and overcharge periods. The redundant series voltage regulators maintain the regulated bus within limits during variations in load current and input voltage. Only one regulator at a time can be connected into the system. The regulators are selected by ground command.

Certain loads which contain their own regulation system or which do not require precision regulation are powered from the unregulated bus. The magnetic bias bus and the two squib load buses (one from each battery) are powered directly from the batteries with special buses. An enable plug is provided to enable external battery charging through the external power input with all loads disconnected. When the plug is removed, all spacecraft load power is interrupted.

A ground plate next to the power supply electronics unit on the spacecraft baseplate is the main spacecraft grounding point. Subsidiary ground plates are provided on the equipment panels, connected to the main ground plate by cables. The main ground plate is the only point on the spacecraft which is electrically connected to the spacecraft frame, for all units except the rf equipments.

The operation of the ITOS D and E power supply subsystem is the same as for the TIROS M subsystem. Table V-1 presents a summary of the ITOS D and E power supply subsystem design features.

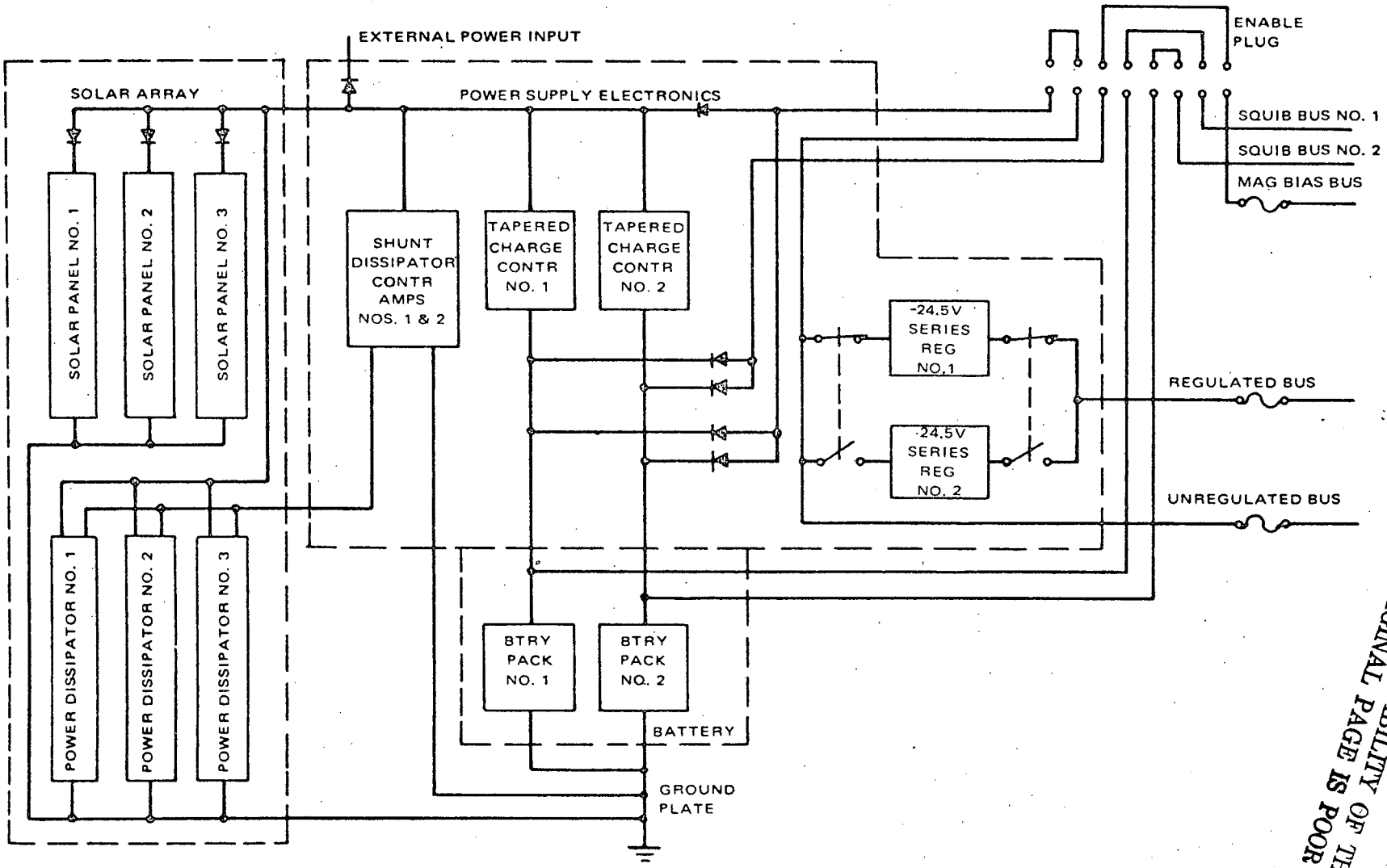

Figure V-1. ITOS D and E Power Supply Subsystem, Block Diagram

TABLE V-1. SUMMARY OF ITOS D AND E POWER SUPPLY SUBSYSTEM PARAMETERS

Parameter	Value
POWER SUPPLY ELECTRONICS	
Units per spacecraft	1
Minimum input voltage from battery	-26.5 volts
Regulated bus output with maximum steady-state 6-ampere load	-24.5 volts ± 0.25 volt
Unregulated output voltage	-26 to -36.2 volts
Regulated bus output with a 10-ampere transient load, less than 1 millisecond in duration, and rise and fall time to less than 200 microseconds, in addition to steady-state load	-24.5 volts - 0.25, to +0.49 volt
Charge current limit to each battery	1.45 ± 0.12 amperes
Maximum battery voltage limit at battery temperature:	
10°C	34.43 volts
25°C	33.25 volts
Battery trickle charge by ground command	0.225 ± 0.075 ampere per battery
Weight	12.5 pounds (max)
SOLAR ARRAY	
Panels per spacecraft	3
Dimensions, each of three identical panels	65.15 by 36.38 inches along the chord
Panel shape	Curved with 75.6 radius
Solar cell area	2 by 2 cm each
Base resistivity	1 to 3 ohm/cm

TABLE V-1. SUMMARY OF ITOS D AND E POWER SUPPLY SUBSYSTEM PARAMETERS (Continued)

Parameter	Value
SOLAR ARRAY (Continued)	
Cover glass thickness (microsheet)	0.006 inch
Air-mass-zero efficiency (with cover glass)	10.3 to 11.6 percent
Solar cell (with cover glass)	
Short-circuit current (I_{sc})	121.1 mA at 28°C (10.3 percent efficiency)
Open-circuit voltage (V_{oc})	0.586 volt at 28°C
Maximum-power-point current (I_{mp})	109.0 mA at 28°C (10.3 percent efficiency)
Maximum-power-point voltage (V_{mp})	0.475 (10.3 percent efficiency)
Circuits per panel	5
Strings per circuit	9 (equal to 9 parallel cells)
Strings per panel	45
Strings per array	135
Series cells per string	76
Array diode type	JAN1N1206
Panel weight (with shunt dissipator)	20.5 pounds (max)*
Array weight	61.5 pounds (max)*

*Does not include weight of: deployment mechanism, locking mechanism, hinges, bumpers, or snubbers.

TABLE V-1. SUMMARY OF ITOS D AND E POWER SUPPLY SUBSYSTEM PARAMETERS (Continued)

Parameter	Value
BATTERY (NICKEL CADMIUM)	
Batteries per spacecraft	2
Cells per battery	23 in series
Storage capacity	6 ampere-hours per cell (min)
Weight	20.0 pounds each (max)
Charge control method	Taper charging with voltage and temperature control
Operating temperature (cells)	10° to 35°C
Charge rate	1.45 ±0.120 amperes per battery (normal maximum), taper charge rate determined by battery voltage and temperature
Maximum depth of discharge	24 percent (readout during day at 30-degree sun angle)

2. Solar-Cell Array

a. GENERAL

The primary purpose of the solar cell array is to provide power for the spacecraft loads by converting solar energy into electrical energy. The ITOS D and E solar array design is identical to the TIROS M solar array including provisions for mounting shunt dissipator components on the substrate ribs.

The solar-cell array consists of three panels connected electrically in parallel to provide power to operate the spacecraft.

b. COMPONENTS

(1) SOLAR CELLS

The solar cells are boron-doped N on P silicon wafers 0.012 ±0.002-inch thick and 0.788 ±0.005-inch thick on a side. Base resistivity of the wafers

is 1 to 3 ohm-cm. Solar cells for the ITOS D and E programs are identical to the cells used on TIROS M. The temperature coefficient for voltage of the cells is 2.2 mV/°C at beginning of life (BOL). The temperature coefficient for short-circuit current is 60 microamp/°C at BOL.

(2) SOLAR CELL COVER GLASS

Each cell has a cover-glass filter bonded to the active surface. The cover glass has an anti-reflective coating applied to the exposed surface to enhance transmission of energy to the solar cell in the region of peak spectral response and a coating applied to the opposite surface to provide ultraviolet rejection in the region between 300 and 370 millimicrons. The cover glass base material is 0.006-inch thick microsheet 0.748 x 0.788 inch in dimension. The cover glass dimensions are equivalent to the nominal dimensions of the solar cell area excluding the negative cell contact. The cover glass used for ITOS D and E are identical to those used on the TIROS M spacecraft.

(3) SOLAR CELL COVER GLASS ADHESIVE

The Sylgard 182 cover glass bonding adhesive used on the TIROS M/ITOS spacecraft will be used for ITOS D and E. Sylgard 182 adhesive retains its resiliency throughout the temperature range anticipated. Degradation of optical characteristics in a radiation environment appears to be less for Sylgard 182 than for other adhesives used for this application.

(4) SOLAR CELL BONDING ADHESIVE

Each solar cell is individually bonded to the substrate with a pedestal of silicone rubber approximately 5/8 inch in diameter. The adhesive is a mixture of RTV 560 and RTV 580 blended to provide the consistency required to control the pedestal diameter. The RTV 560/580 adhesive retains its resiliency throughout the temperature excursion encountered in orbit.

(5) SOLAR CELL INTERCONNECTION

Solar cells on ITOS D and E are interconnected utilizing the same design used on TIROS M. Expanded silver mesh 0.002-inch thick is formed to provide stress relief in the series direction between cells. Stress relief between cells, connected electrically in parallel, is provided by orientation of the silver mesh and limitation of the size and location of the solder joint to the solar cell positive surface.

(6) SUBSTRATE

The TIROS M substrate design will be used for ITOS D and E. The substrate consists of aluminum honeycomb sandwiched between two sheets of aluminum. The array bonding surface is insulated with a polyvinyl-fluoride material which is applied to the aluminum skin prior to bonding to the honeycomb. Insulation material thickness is 0.002 inch.

c. CHARACTERISTICS

The solar cells are electrically connected in series in the same configuration as they were for the TIROS M spacecrafts. Five solar cell circuits, electrically connected in parallel, are bonded to each panel. Each circuit consists of nine parallel rows of 76 series-connected cells for a total of 3420 cells per panel. Each solar cell circuit is isolated from the other panel circuits by redundant diodes.

(1) DIMENSIONS

Each of the solar cell panels is 65.15 inches long by 36.38 inches wide along the chord. Panel array bonding width across the panel curvature is 36.64 inches. Each panel has a nominal radius curvature of 75.6 inches. Three of the ribs provide thermal mass for the three shunt dissipator sections located on each panel, in addition to providing support to the panel.

(2) WEIGHT

Each solar cell panel, including shunt dissipator components and array, but excluding antennas, snubbers, etc. shall weigh no more than 20.5 pounds.

d. FUNCTIONAL DESCRIPTION

(1) DESIGN PARAMETERS

The solar-cell array will meet the mission spacecraft electrical requirements after allowances are made for the following parameters:

- Angle to the sun vector
- Variation of solar illumination incidence angle on the curved panel surface versus time in orbit.

- Blocking diode drop
- Telemetry resistor drop
- Variation of temperature over the curved panel surface versus time in orbit.
- The product of the following assumed current degradations:

Solar constant	0.967
Power Prediction	0.97
UV Damage	1.00
Curved Panel Model	0.995

- Voltage Degradation
- Wiring loss 0.98

The initial power output will not exceed the limits set by the shunt dissipator components.

(2) SOLAR CELL I-V CHARACTERISTICS

The maximum and minimum current-voltage solar cell characteristics for a single cell are shown in Figure V-2. The lower curve in Figure V-2 represents the minimum solar cell characteristics after six months radiation degradation for the 1968 flux data without solar flare allowance.

e. SECONDARY DESIGN PARAMETERS

The solar panels are designed to withstand orbital temperature extremes of +42°C to -88°C with local warm spots ranging up to 87°C if launched in a 30-degree sun angle orbit. The warm spots will occur directly over the shunt dissipator components. When array output limiting occurs through localized heating, the shunt drive current is reduced, thereby reducing the local heating effect. The result is a self-leveling situation between the spacecraft loads, the solar panel output, and the panel temperature. This array limiting situation occurs only when excess energy is diverted to the shunt dissipator.

f. SHUNT DISSIPATOR

Since the solar array is a constant current source (i.e., high impedance source), the array bus voltage will increase as the spacecraft loads are removed.

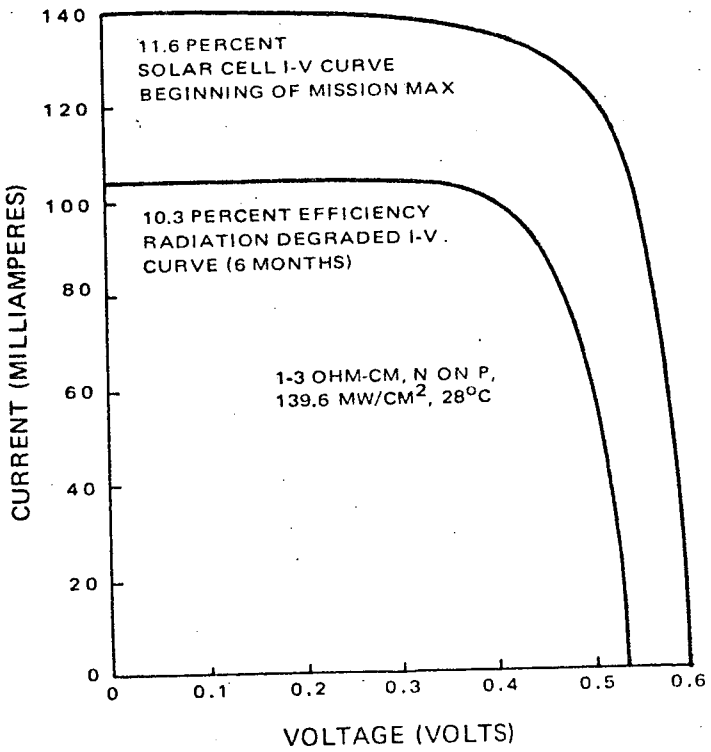

Figure V-2. Solar Cell I-V Characteristics

Current, therefore, must be shunted through the shunt dissipator sections to maintain the solar array bus voltage below an upper limit of -36.8 volts.

Each of the nine shunt dissipator sections is designed to dissipate one-eighth of the total 490-watt shunt dissipator requirement. This means that only eight sections are required to handle worst-case conditions. Figure V-3 shows the amount of power each component per shunt section may dissipate. At the maximum power levels, the solar panel provides sufficient thermal paths to limit the upper temperature extremes of the components within their design limits.

Mechanical packaging of the nine shunt dissipator sections is accomplished by locating one section on each of the panel support ribs. At each point where the shunt transistors are attached to the panel ribs, an additional amount of thermal mass is attached to limit the lower temperature extreme of the transistors.

Temperature extremes approaching -55° C are expected on the dissipator components as the spacecraft emerges from the earth eclipse in a 60-degree sun angle orbit at end of life (EOL). In a 75-degree sun angle orbit, the transistors are expected to cool to a temperature below the recommended lower limit of -55° C.

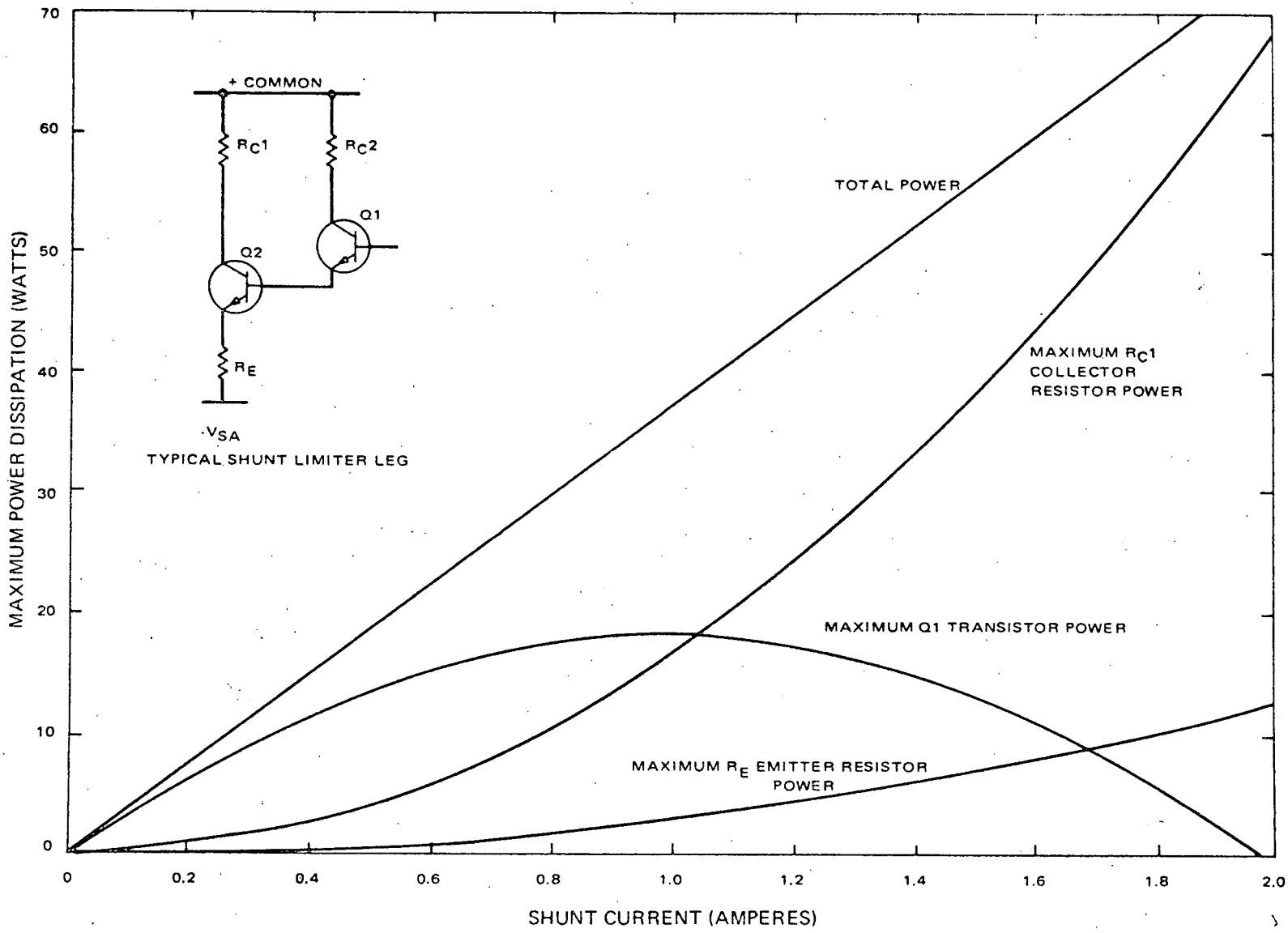

Figure V-3. Power Dissipation Versus Shunt Current (per Shunt Dissipator)

3. Batteries

a. GENERAL

The electrical power subsystem of the ITOS D and E spacecraft contains two nickel-cadmium batteries. These batteries store part of the electrical energy generated by the solar array during periods of sunlight and supply electrical energy to the various spacecraft subsystems during periods of eclipse or during periods when the spacecraft power requirements exceed the solar array capability. The two batteries are not redundant; both are necessary to fulfill the design requirements of the power subsystem.

b. MECHANICAL DESIGN

Each battery is an assembly of 23 series-connected, hermetically sealed, nickel-cadmium cells having a nominal capacity rating of 6 ampere-hours. The cells are rectangular and encased in stainless steel, with the positive terminal insulated by means of a ceramic-to-metal seal. The negative terminal is electrically common with the cell case.

In the battery assembly, the cells are electrically insulated from one another and from the supporting aluminum chassis. The cells are mounted in two parallel rows of 12 cells each, except that the end cell of one row is a dummy cell. Each cell is held in place by holddown clips. Two of the cells contain thermistors, which provide temperature signals for charge control and telemetry circuits, mounted on the cell covers. The power leads, individual cell sensing and temperature sensing leads terminate in a 50-pin connector which provides the electrical interface between each battery and the other units of the power subsystem. A clear plastic cover is installed over the battery assembly to protect the top of the battery and electrical connections.

The maximum battery weight is 20.0 pounds with dimensions approximately 11.8 by 5.8 by 5.2 inches. A baseplate approximately 11.6 by 5.5 inches is the mechanical interface between each battery and the spacecraft. Except for the cell size, this battery design is identical to that used on the TIROS M spacecraft.

c. ELECTRICAL DESIGN

A schematic diagram of the battery pack is shown in Figure V-4. All interconnections between cells are redundant, using two 18-gauge wires. The connections between the end cell terminals and the positive and negative bus bars use three 18-gauge wires. All of the cell voltage sensing wires and the thermistor wiring are 26-gauge wire. All connections between the bus bars and the 50-pin connector are of 20-gauge wire with a minimum of two wires in each power circuit path.

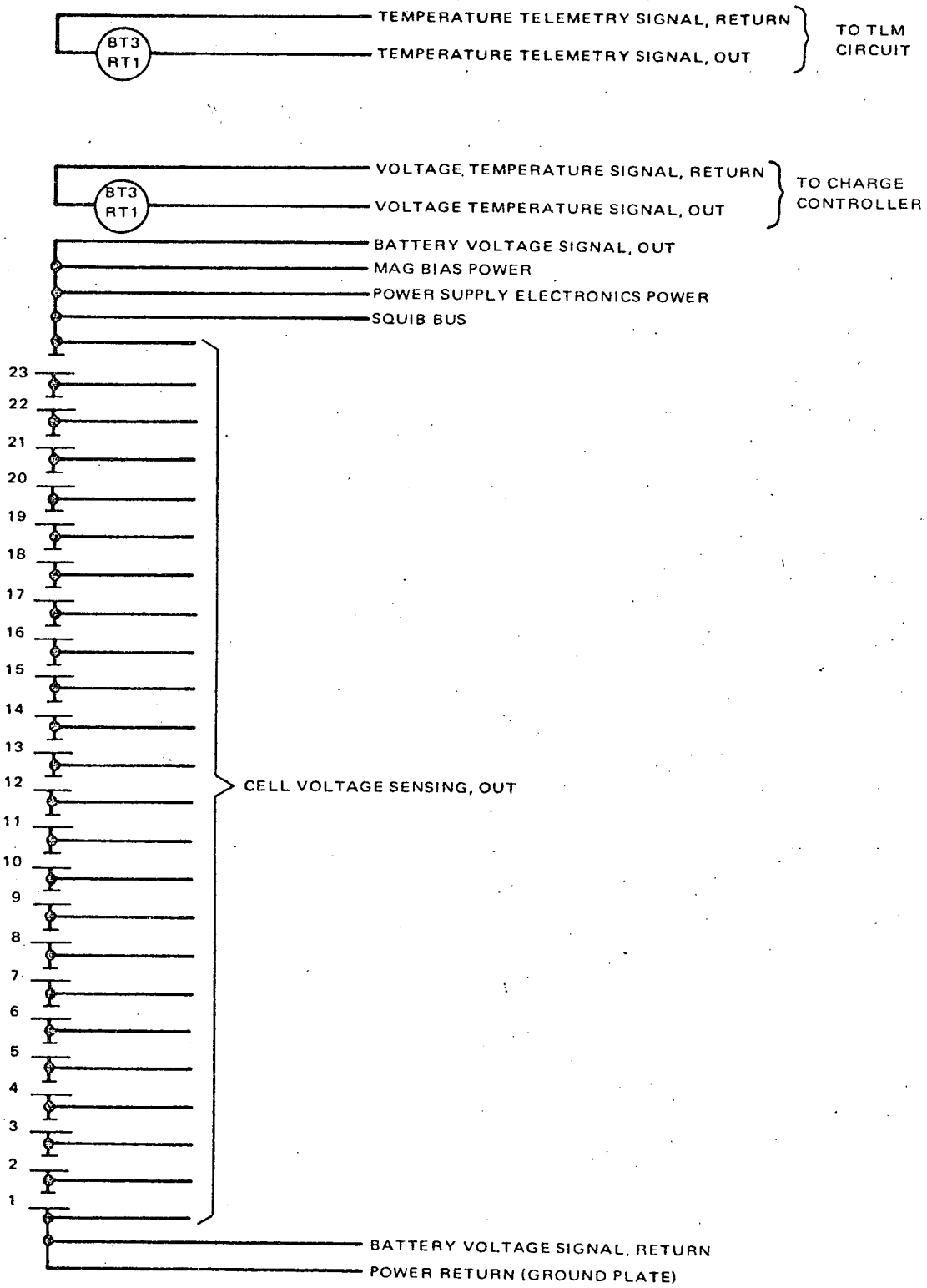

Figure V-4. Battery Pack, Schematic Diagram

Operating in a spacecraft environment, the PSE performs four major functions:

- Power distribution and voltage regulation. During satellite day, this unit accepts solar array and/or battery power at voltage levels varying between -26.5 and -36.8 volts and distributes conditioned power to spacecraft loads. During the satellite night, the PSE accepts battery power at voltage levels varying between approximately -26.5 and 31.5 volts and distributes conditioned power to spacecraft loads. One of two redundant voltage regulators provides a voltage of -24.5 volts to loads requiring total steady-state currents up to 6 amperes and short-term transient currents of 10 amperes. An unregulated voltage in the range of -26.0 to -36.2 volts is available for unregulated loads.
- Battery charge control. When solar power is available, circuits within the PSE control the recharging of the power subsystem battery modules at a maximum rate of approximately 1.425 amperes by sensing battery voltage and temperature. Separate control circuits are provided for each battery module.
- Ground control commands and analog telemetry signals. The PSE provides a means for switching voltage regulators and shunt limiter amplifiers and reducing the battery charge current when signaled by ground command signals. Telemetry circuits are included to provide output analog signals of key power subsystem performance parameters.
- Shunt limiter control. The PSE contains two redundant shunt limiter control amplifiers to sense the solar array bus voltage and provide a signal to control nine remote shunt dissipator sections. The shunt dissipator sections, located on the solar array panels, act as a shunt load on the solar array to maintain the solar array bus voltage below an upper limit of -36.8 volts.

There are two automatic switching circuits, one for each control amplifier, which act to remove a shorted control amplifier.

b. FUNCTIONAL OPERATION

(1) VOLTAGE REGULATOR

Two identical voltage regulators are incorporated in the ITOS D and E spacecraft. Each regulator is capable of providing a -24.5 ± 0.25-volt regulated bus to the spacecraft systems over a load current range of 0.40 to 6 amperes. One regulator supplies the total -24.5-volt bus load and the second is

in a power off mode, ready to be switched "on line" via ground command, in the event of a failure in the "on line" regulator. Only one regulator can be commanded "on line" at any time.

The -24.5-volt regulator is shown in block diagram form in Figure V-5. A differential amplifier compares voltage variations across the load with a voltage reference zener diode. The output of the differential amplifier is directly coupled to a second differential amplifier connected in complementary symmetry. A stage of current gain provides the necessary drive to the series-pass transistors to support the required load current.

(2) SHUNT LIMITER

The shunt limiter is designed to limit the voltage on the solar array bus to a safe upper limit and is identical to the TIROS M shunt limiter.

Power to the ITOS D and E spacecraft loads is furnished by the solar array. In a normal mode, the solar array is operating in the constant current area of its I-V characteristic. When the spacecraft load is below the solar array current output, the shunt limiter is used to control the maximum solar array bus voltage by functioning as a shunt voltage regulator at the cut-in voltage level. Control of the maximum solar array bus voltage is achieved by shunting current through the shunt dissipator sections when the control amplifier(s) sense an increase in solar array voltage above a cut-in level. The shunt limiter consists of nine shunt dissipator power sections on the solar array panels and two control amplifiers in the power supply electronics unit.

Sensing of the solar array bus voltage is done by both control amplifiers. Each control amplifier compares the solar bus voltage to a voltage reference and provides an output current which is proportional to the difference (error signal). The control amplifier output current is fed through isolation diodes to a common bus and then through isolation networks to each of the shunt dissipators.

The shunt dissipator amplifies the control current, causing some of the solar array current to become shunt limiter current, which, in turn, decreases the solar bus voltage to a level where the control amplifier error signal is minimized. The net effect is a closed-loop, negative-feedback, control system which provides voltage limiting.

Either, or both, of the control amplifier outputs are connected or disconnected by two relays which may be actuated by either ground command or by an automatic failure (short circuit) detection control. Both amplifiers cannot be simultaneously commanded off.

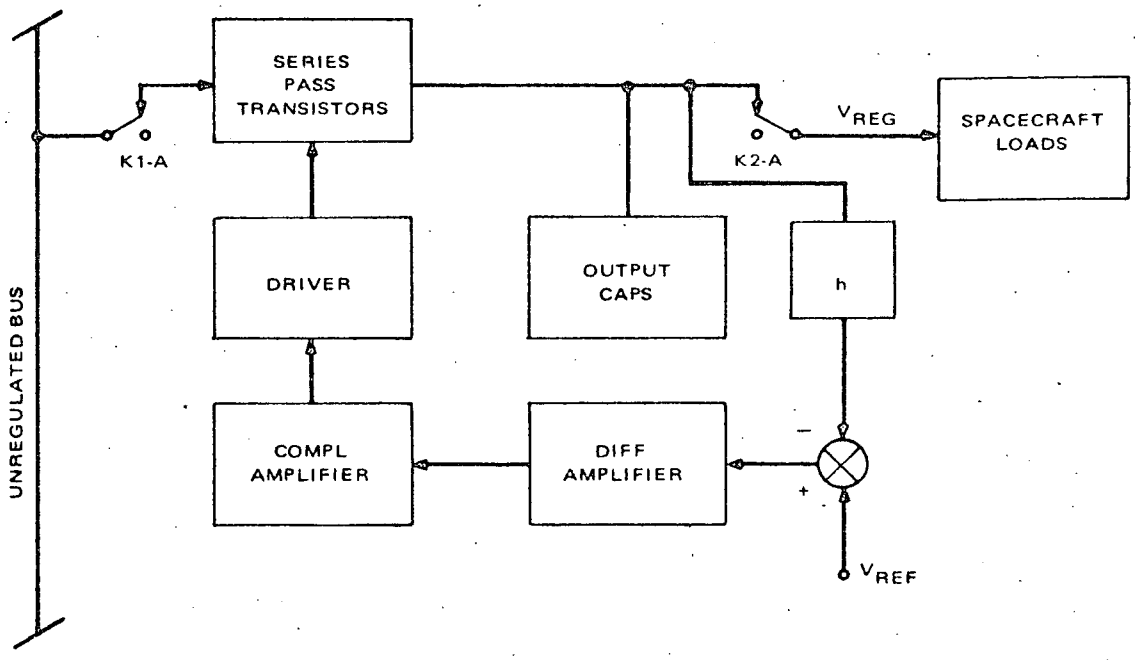

Figure V-5. Voltage (-24.5V) Regulator, Block Diagram

The threshold, or cut-in, voltage of each of the two control amplifiers is 36.25 volts, when the total shunt dissipator current is 0.1 ampere. Temperature and aging effects may cause the threshold voltage to vary by no more than ± 0.25 volt at the end of 1 year including all environmental effects. The solar array bus voltage may increase by 0.3 volt, maximum, when the shunt dissipator current increases from 0.1 to 15.3 amperes. (The 15.3-ampere current figure is the nine-leg dissipator capacity as compared to a beginning-of-life array current, at $\gamma = 30°$, of 13.2 amperes.)

The control amplifier failure detection control protects the spacecraft against any failure in a control amplifier which causes the shunt dissipators to be turned on in error. This is done by detecting a simultaneous condition of solar array voltage less than -29 volts and the presence of control amplifier output current. Each of the two redundant control amplifiers is provided with an independent failure detection control. The functional diagram of this control is shown in Figure V-6.

(3) CHARGE CONTROLLERS

Battery charging is controlled by two taper charge circuits, one for each battery. Both of these circuits are in the power supply electronics. The charge current to the battery is limited to a maximum value when the battery

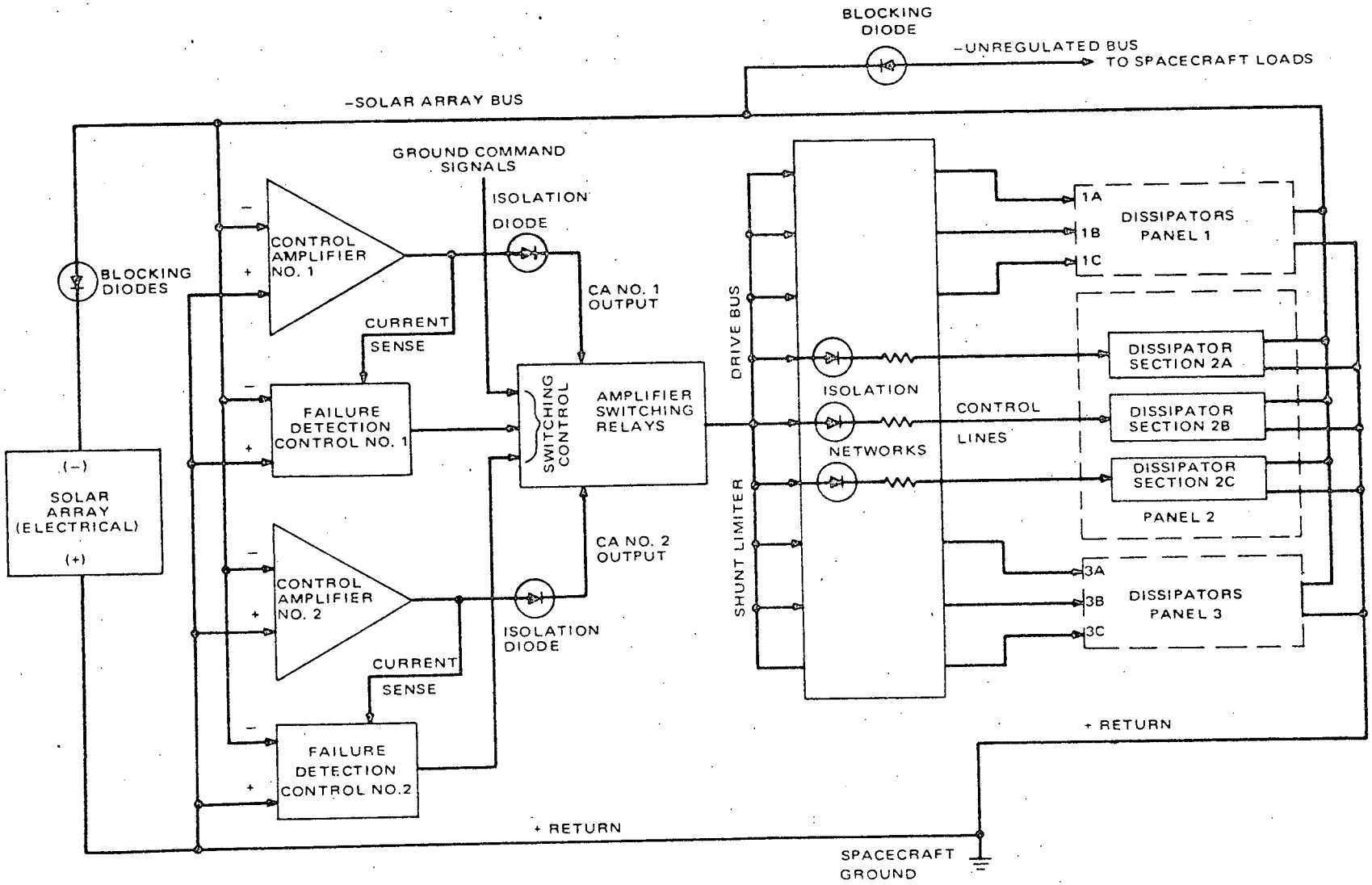

Figure V-6. Shunt Limiter, Functional Block Diagram

voltage is below the limit prescribed for the battery temperature. When the battery voltage reaches the voltage limit, the charge controller reduces the charge current to hold the battery voltage at the prescribed limit. The voltage limit corresponds closely to the point where the battery has been returned to a fully charged state. The battery will continue to charge at progressively decreasing rates as the voltage limit is held and as the battery state of charge increases. The minimum charge current taper level is equal to the trickle charge rate described below.

The voltage limit thus ensures that the charge current will be reduced to a safe overcharge rate for the battery. Some overcharging of the battery is required in order to sustain satisfactory charge-discharge cycling performance during the entire mission.

The ITOS D and E normal charge rate is 1.425 ± 0.120 or C/4 (where C is nominal battery capacity in ampere-hours). The charge current can be reduced to the trickle charge rate (150 ± 50 milliamperes per battery) upon command from a ground station. Although the voltage limit ensures that a fully charged battery will be charged at a reduced rate, the trickle charge feature further reduces the heat dissipation in the battery, during 100-percent suntime operation, by further reducing the charge current. This mode of operation should be used when telemetry indicates that the battery temperature exceeds 35°C and suntime is 100 percent.

The charge controller block diagram is shown in Figure V-7. The charge controller battery voltage limit as a function of temperature is shown in Figure V-8.

(4) TELEMETRY

(a) General Description

Various subsystem functions are telemetered to provide a means of analyzing the performance of the subsystem in meeting the spacecraft power requirements and to provide information in the event of power subsystem or spacecraft failure. These telemetry functions are useful during the spacecraft test phases as well as during orbital flight. A summary of the characteristics of the telemetry circuits is shown in Table V-2.

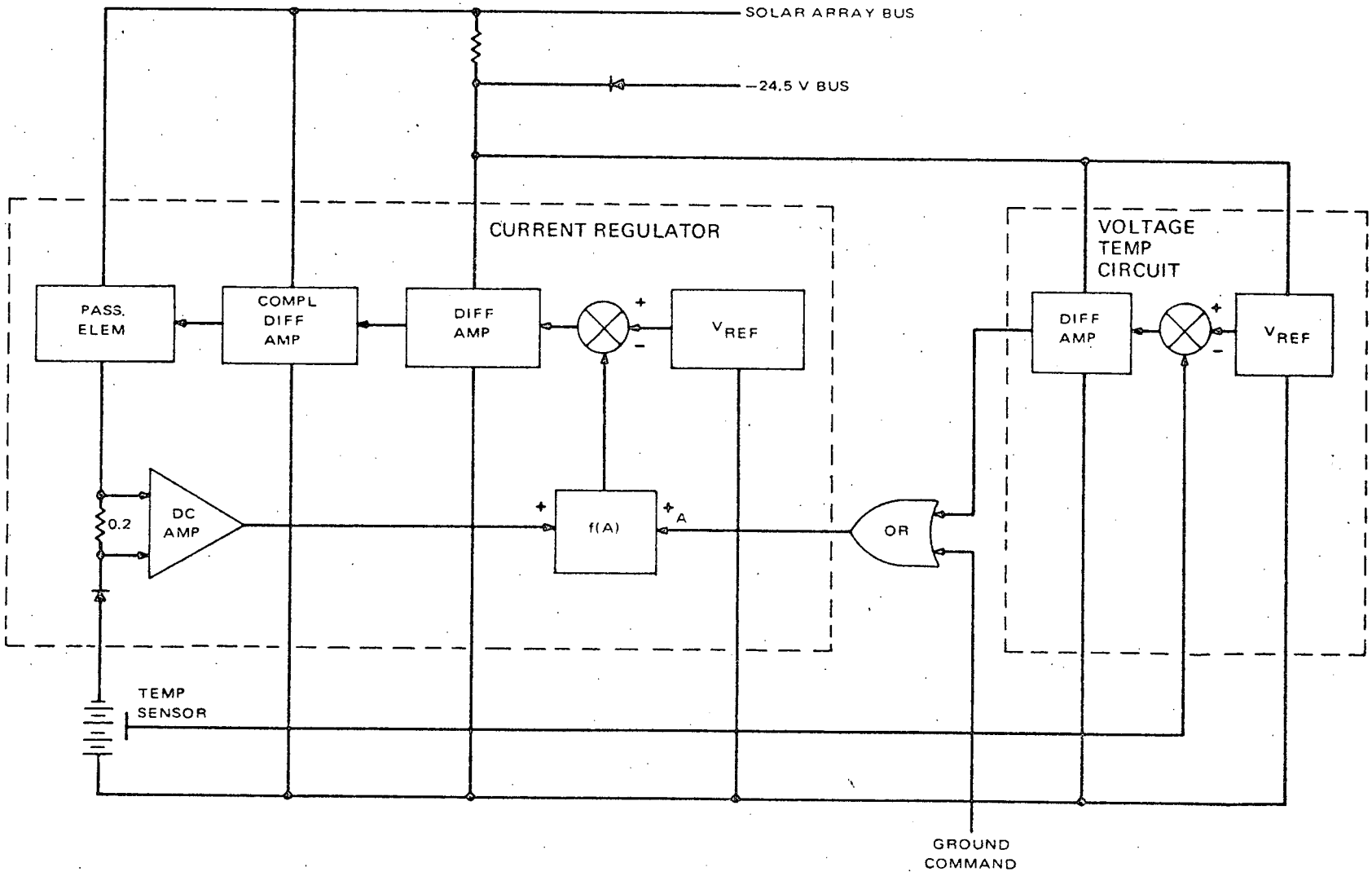

Figure V-7. Battery Charge Controller, Functional Block Diagram

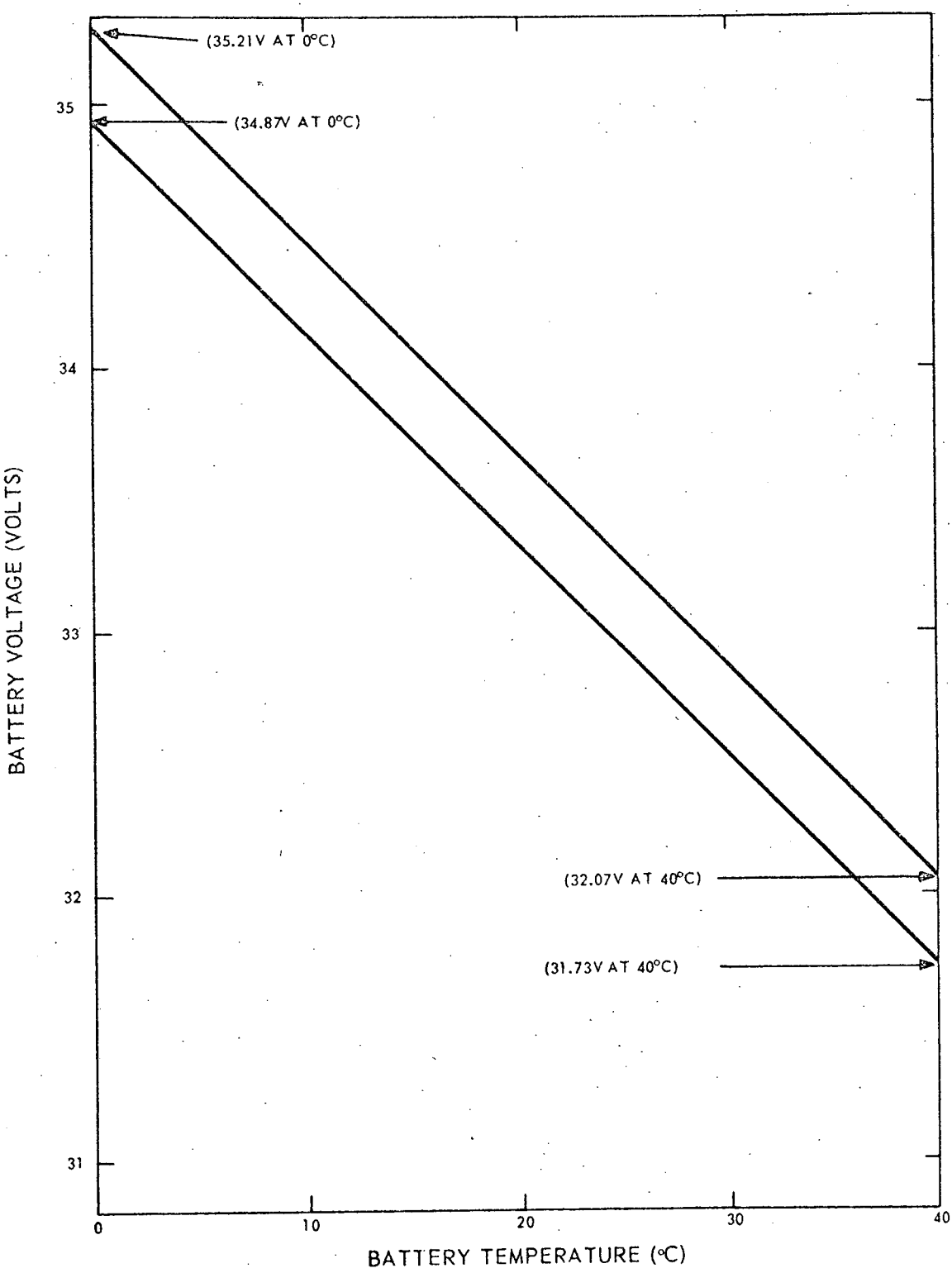

Figure V-8. Specified Voltage Limit Versus Temperature

TABLE V-2. SUMMARY OF TELEMETRY CHARACTERISTICS

Symbol	Telemetry Type	Nominal Input Range	Nominal Output Range (volts)	Open Circuit Accuracy[1]	Source Impedance[7] (in kilohms)	Max Shunt Loss (mA)	
						ON	OFF
V_1	Solar Array Voltage	-22 to -40V	-0.5 to -4.5	1%[2]	5.3 ±5%	2.6	1.2
V_2 V_3	Battery Voltage	-22 to -40V	-0.5 to -4.5	1%[2]	5.3 ±5%	2.6	1.2 (ea)
V_4	Unreg Bus Voltage	-22 to -40V	-0.5 to -4.5	1%[2]	5.3 ±5%	2.6	1.2
V_5	Reg Bus Voltage	-15 to 35V	-0.5 to -4.5	1%[3]	5.3 ±5%	3.0	0.97
T_1 T_2	Battery Temperature	-10° to +50°C	-1.0 to -4.5	2°C[4]	2.65 ±12%	1.6	0 (ea)
T_3 T_4 T_5	Shunt Lim Temperature	-65° to +100°C	-0.1 to -4.5	8.8°C[4]	2.70 ±12%	1.6	0 (ea)
T_6	PSE Temperature	-10° to +85°C	-1.0 to -4.5	4.5°C[4]	2.70 ±12%	1.6	0
T_7 T_8 T_9	Solar Array Temperature	-100° to +60°C	-0.1 to -4.5	8.7°C[4]	2.75 ±12%	1.6	0
I_{1a} I_{1b} I_{1c}	Solar Array Current	0 to 5.2 A	-0.5 to -4.5	3%[5]	4.35 ±3%	6.3	0.72 (ea)
I_2	Shunt Lim Current	0 to 15.3 A	-0.5 to -4.5	6%[2]	2.48 ±2%	0.2	0
I_3 I_4	Battery Charge Current	0 to 1.5 A	-0.5 to -4.5	3%[5]	4.35 ±3%	6.6	0.73
		Condition					
V_6	Shunt Lim Control Ampl Selector	Control Ampl 1 ON Only	-1.8	5%[6]	2.70 ±7%	1.5	1.5
		Control Ampl 2 ON Only	-4.49				
		Both Control Ampl ON	-2.7 -3.73				
V_7	Regulator and Charge Current Mode Selector	Reg 1 ON-Trickle Chrg ON	-2.85	8%[6]	2.475 ±18%	3.27	3.27
		Reg 1 ON-Chrg Cur Norm	-1.80				
		Reg 2 ON-Trickle Chrg ON	-4.40				
		Reg 2 ON-Chrg Cur Norm	-3.70				

[1]Calibrated, worst-case, full scale accuracy. This represents the maximum, full scale deviation from a calibration curve for an end-of-life period of 1 year.

[2]Calibration at 25°C and V_R midrange.

[3]Calibration at 25°C and V_u midrange.

[4]Calibration at V_R midrange.

[5]Calibration at three temperatures and regulated and unregulated voltage midrange.

[6]Without calibration curve.

[7]< 30 kilohms (specification).

(b) Voltage Telemetry

ITOS D and E uses zero suppressed, expanded scale voltage telemetry, identical to that used on TIROS M. There are two voltage sensing circuits, but they are functionally identical. The main difference between the two circuits is in the voltage ranges telemetered.

(c) On-Off Telemetry Operation

The shunt limiter control amplifier selector telemetry provides four distinct voltage levels, depending on the states of the control amplifiers switching relay. The four levels are required so that each of the four relay state combinations is known. The circuit operates as a simple resistor voltage divider with selected resistors shorted out to produce the desired voltage levels.

The combination regulator selector and charge current mode selector on-off telemetry circuit also provides four distinct voltage levels to define the various states of the two circuits simultaneously.

A zener diode is used to establish a relatively constant voltage for the regulator selector section represented by the unregulated bus. The remainder of the circuit operates as a simple resistor voltage divider with resistance values selected to produce the desired voltage levels for each of the combined on-off conditions.

(d) Temperature Telemetry Operation

All temperature telemetry circuits consist of resistor-thermistor voltage dividers designed to produce the most linear telemetry characteristics over the temperature ranges desired. Thermistors are located on the batteries, the PSE baseplate, the solar array, and near the warmest transistor of the shunt limiter. Any change in temperature causes a change in thermistor resistance, and, in turn, a change in the current flowing through the output resistor. A capacitor across each output reduces any high frequency noise which might appear.

(e) Current Telemetry

The battery charge current and the solar panel current telemetry circuits are functionally identical. A voltage drop is created across the sensing resistors by the current telemetered. This drop is then converted to a usable analog telemetry signal.

The shunt dissipator current telemetry consists of a simple resistor voltage divider connected across the collector resistor of the shunt dissipator through which the main portion of the shunt dissipator current flows.

5. System Protection

All system loads are fused with Littlefuse high reliability subminiature picofuses. This type fuse requires no encapsulation and is available in ratings from 0.125 to 5.0 amperes. A 3-to-1 safety margin was used in selecting fuse ratings. The largest fuse rating used on the regulated bus is 5 amperes.

An evaluation of the operating characteristics of the regulator and the current versus blow time characteristics of the fuses has indicated that no damage can be done to the -24.5-volt regulators if they are required to blow any of the fuses on the bus. The evaluation considered the available power to the regulator, and then described the excursions of the regulator operating point when the regulator is required to supply the additional current to blow the fuse. The limiting characteristic in all conditions is the maximum junction temperature reached in the three parallel pass transistors of the regulator. Under no conditions can this temperature reach the maximum allowable operating temperature, even under worst-case circuit degradation characteristics and worst-case thermal environment for the power supply electronics.

C. SYSTEM ANALYSIS

1. Introduction

This section defines the permissible regions of operation for the nominal and expected worst-case conditions of the ITOS D and E power subsystem at an altitude of 790 nautical miles.

The system analysis evaluates power subsystem performance for sun angles from 30 to 60 degrees and an orbit altitude of 790 nmi. The analysis is in two parts: (1) predicting nominal or expected performance based on typical component parameters, and (2) predicting for conditions at worst-case extremes to assist in the hot and cold thermal analyses. The latter part of the power analysis indicates what the power subsystem performance would be if all parameters were at the worst case extremes. The analysis results in predictions of state-of-energy balance and the power subsystem component dissipations. Parametric variables for these analyses are spacecraft operating modes which include the acquisition, preoperational, and operational modes.

2. Load Requirements

The load profile for the acquisition and minimum pre-operational load is identical to the TIROS M spacecraft load except that higher battery charge currents exist due to the increased battery size. The load profiles shown in Figure V-9 show only the loads on the power subsystem and do not show battery charge current or shunt limiter current. The acquisition mode is the period after launch when the spacecraft is slowly rotating with the pitch axis aligned with the orbit normal and the solar panels deployed. The pre-operational mode is the same as the acquisition mode but after earth lock and before operational loads are turned on.

The load profile for the operational mode is shown in Figure V-10. The VHRR recorder can be programmed to record for approximately nine minutes at anytime in the orbit. For energy balance purposes, record was selected to occur during the first nine minutes of satellite night.

The spacecraft interrogation and readout period was established as 12 minutes, which allows nine minutes to playback the recorders and three minutes for ground command and telemetry. The 12-minute interrogation and readout interval was programmed to occur in satellite day near the end of the orbit.

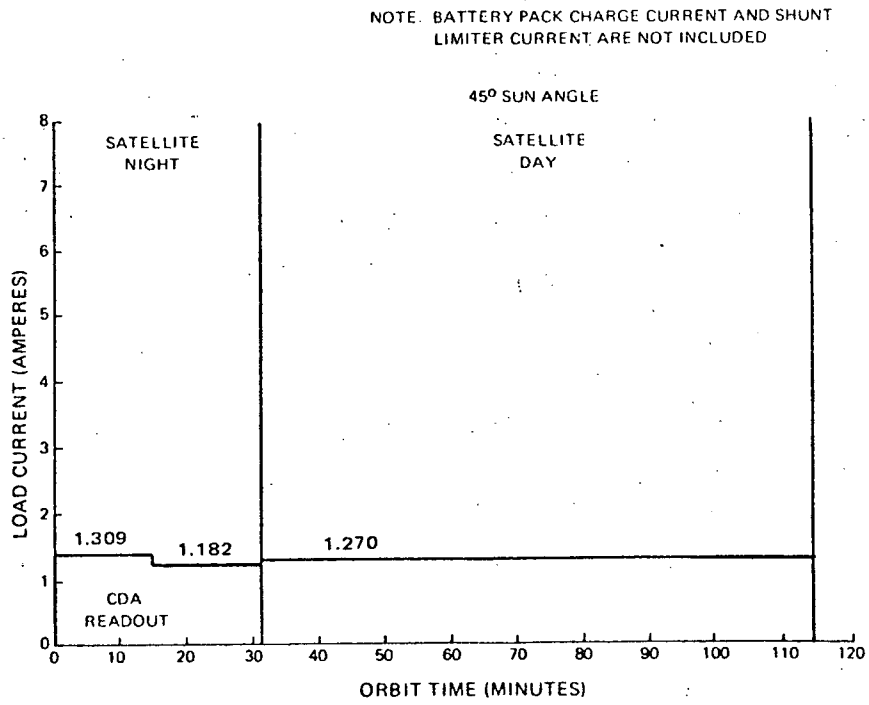

Figure V-9. ITOS D and E Acquisition and Pre-operational Load Current Profile

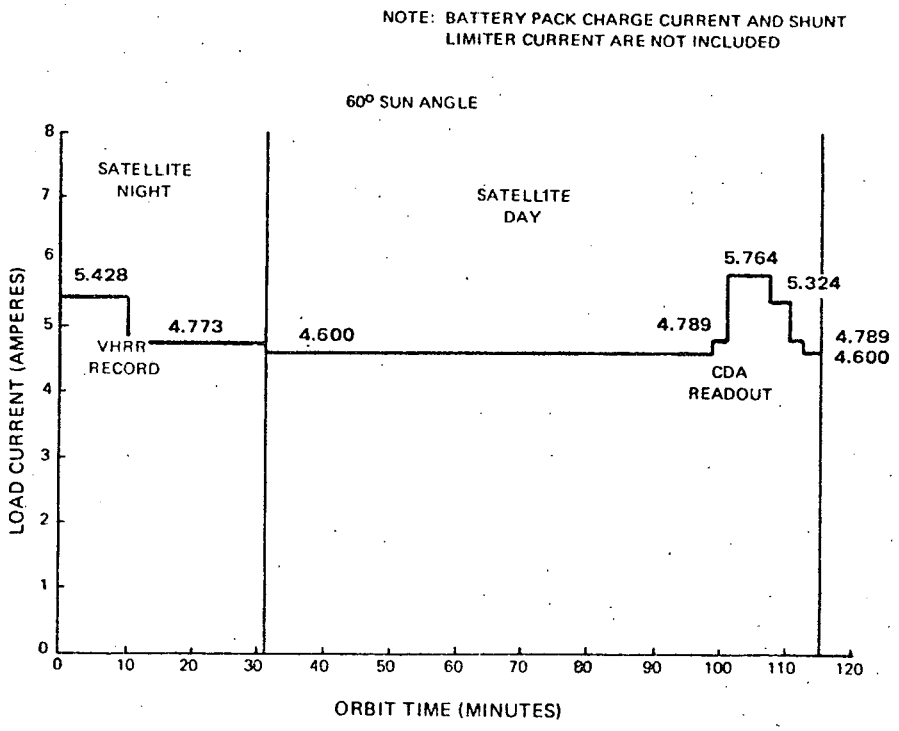

Figure V-10. ITOS D and E Operational Load Current Profile

Various power requirements, such as DSAS readout, QOMAC operation, momentum coil operation, and additional SR recorder readout time required after a blind orbit are not included in energy balance considerations because they are temporary load profile changes.

If, due to solar array degradation, energy balance is not obtained with full operation, operation of selected units must be curtailed to maintain balance.

3. Computer Energy Balance Parameters

The computer program solves for component voltages, currents, power dissipations, and the battery state of charge. Component parameters of the solar array, battery pack, power supply electronics, and the load profile are entered as required for the specific case being studied such as nominal or the respective worst case. Four parameter classifications were established with variation for 30°, 45°, and 60° sun angles within a classification. These classifications are:

- Beginning of Life (BOL), hot
- Beginning of Life (BOL), nominal

- End of Life (EOL), nominal
- End of Life (EOL), cool

Beginning of life, hot, defines a power subsystem which dissipates the maximum amount of power within the spacecraft.

End of life, cool, defines a power subsystem which dissipates the minimum amount of power within the spacecraft.

The array output at a 60° sun angle is minimum and this is the array output case chosen to evaluate performance with respect to energy balance.

Beginning of life, nominal, defines a power subsystem with typical nominal values. This classification approximates actual spacecraft conditions at launch.

End of life, nominal, defines a power subsystem with typical values for six months of operation.

Acquisition and pre-operational energy balance computations are made at the beginning of life, nominal classification only.

4. Power Dissipation

Energy balance analyses were made for; a 30° sun angle, beginning of life, hot, classification with the ITOS D and E operational load profile; and a 45° sun angle, beginning of life, nominal classification with the ITOS D and E acquisition and pre-operational loads. The thermal design section describes the effect of these modes on spacecraft component temperatures.

5. Energy Balance and Power Subsystem Capabilities

Nominal solar array current output versus sun angle for beginning of life, six months, and one year are shown in Figure V-11. Load lines are shown in Figure V-11 for: (1) full time operation of the VHRR, (2) 14 minutes of night inhibit, and (3) 28 minutes of night inhibit. The load-line intersections with the solar array output curve gives the approximate sun angle which can be supported for the orbital life represented by that solar array curve. The six months curve predicts energy balance to a maximum of 58° sun angle for a full-time, no inhibit, VHRR operation; it can be improved to a maximum of 60° sun angle by inhibiting the electronics VHRR processor, and S-band transmitter for 28 minutes at night.

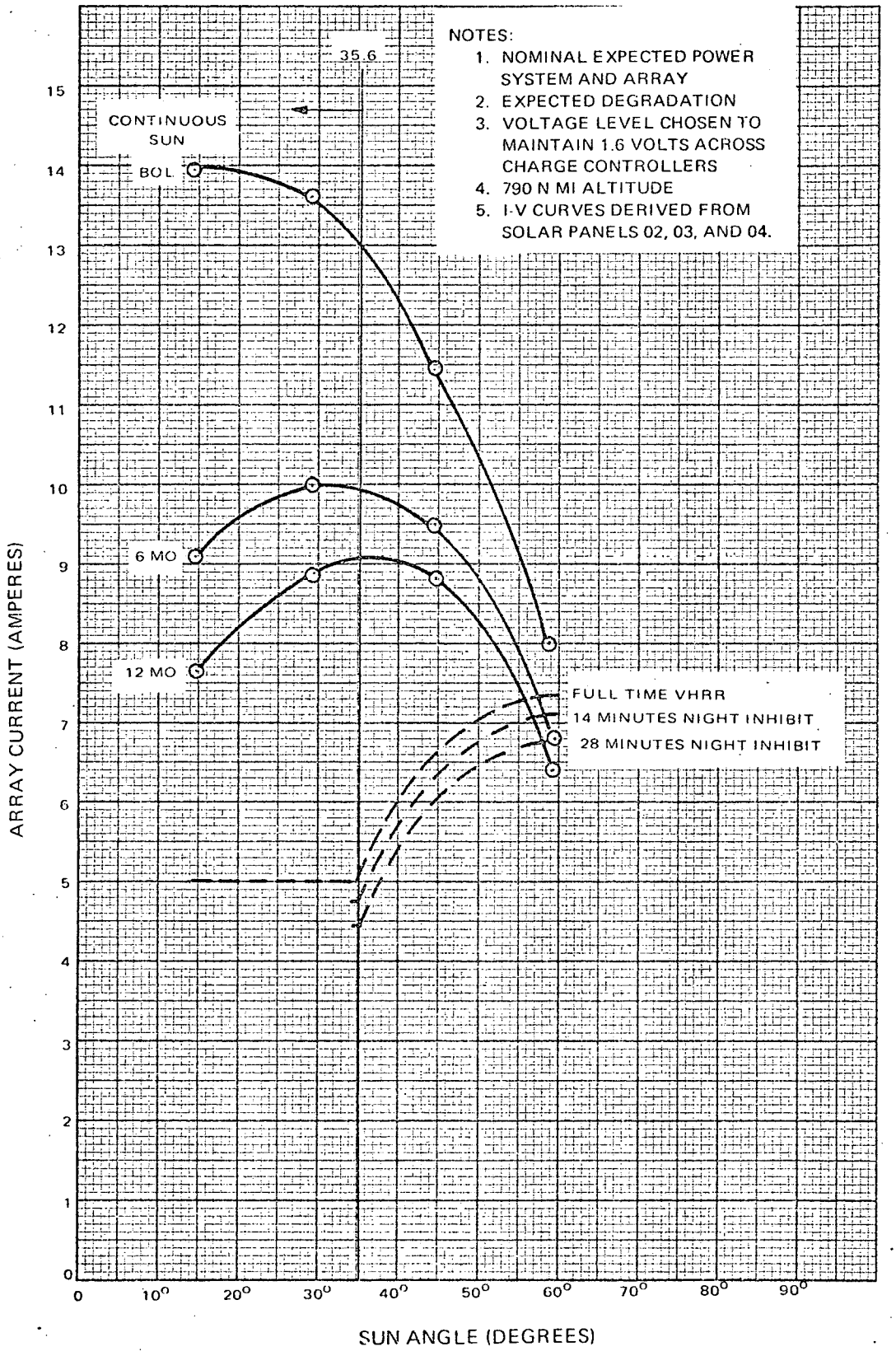

Figure V-11. Nominal Solar Array Output Versus Sun Angle

Worst expected solar array current output versus sun angle for beginning of life, six months, and one year are shown in Figure V-12. The load-line, solar array curve intersections show the largest sun angle which can be supported for the orbital life represented by that solar array curve. Energy balance is obtained at 47° sun angle for a full time, no inhibit, VHRR operation after six months of operation.

The worst expected solar array current output differs from the nominal in the following manner:

(1) A change from 135 to 132 solar cells in parallel to allow for random solar cell failures (10,260 solar cells are mounted on the three panels).

(2) A change from 100 percent to 96.7 percent solar intensity constant.

(3) A change from zero to -3 percent standard cell error.

(4) A change from 4 percent average albedo to zero albedo.

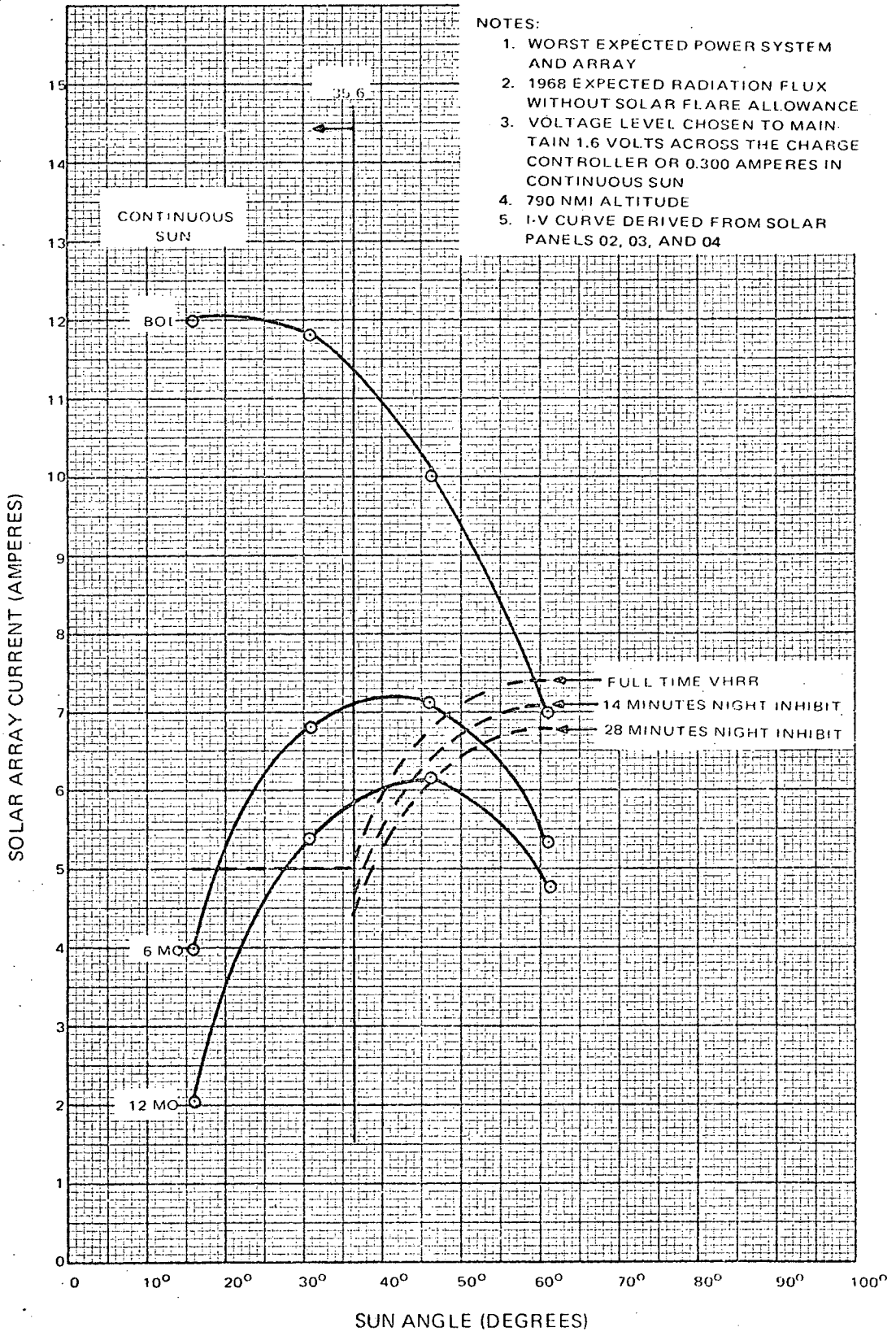

Figure V-12. Worst-Case Solar Array Output Versus Sun Angle

SECTION VI

ENVIRONMENTAL SENSORS

SECTION VI

ENVIRONMENTAL SENSORS

A. INTRODUCTION

The environmental sensing functions of the ITOS D and E spacecraft are performed by four sensor subsystems: the SR, VHRR, VTPR, and SPM. Full orbital coverage (both day and night) of earth cloud cover and temperature profile is recorded for playback to a CDA Station. In addition, real-time cloud cover is sensed in both the visible and infrared spectral regions and transmitted to the local user's ground stations, via VHF radio transmission for the SR data and via S-band radio transmission for the VHRR data. The sensors and associated equipment in each subsystem are as follows:

- A redundant scanning radiometer (SR) subsystem, each side of which is composed of a scanner and electronics, SR processor, a VHF transmitter, and two of three tape recorders with their associated electronics. The two SR processors are packaged as a single unit. The third tape recorder may be used in place of either of the other two, to give full redundancy. The SR processor also provides a modulated 2400-Hz carrier for transmission over the VHF real-time transmitter.

- The two very high resolution radiometers (VHRR) operating in a phased mirror mode, with a VHRR processor, supply real-time data via an S-band transmitter. A single non-redundant tape recorder and its electronics store a portion of the high-resolution data for later playback to a CDA Station. Two redundant VHRR processors are packaged into a single unit.

- Data from a redundant vertical temperature profile radiometer (VTPR) via a redundant digital data processor (DDP) unit is recorded on a track of an SR recorder.

- The solar proton monitor (SPM) measures the proton fluxes encountered in the spacecraft orbit and converts these measurements to a floating point binary code for recording and subsequent playback and transmission to ground stations.

Power and signal switching circuits, controlled by ground command, provide means for selecting one of the redundant sides of a sensor subsystem. For the SR and the VTPR, the switching arrangements are such that it is possible to select either radiometer for operation with any pair of SR recorders. When the first recorder of a selected pair is filled, the second will automatically begin recording.

The primary mode of operation for the VHRR is real-time transmission via the S-band link. However, approximately 9 minutes of data may also be recorded on the VHRR recorder. The start of record may be delayed up to 223 minutes in 54-second increments.

Both of the VHRR's are used simultaneously to provide a time-multiplexed visible and infrared composite signal in the normal mode of operation. If either VHRR fails, a back-up mode of operation is available where both the visible and infrared signal from one radiometer modulate separate subcarrier oscillators to give a frequency multiplexed signal. The signal-to-noise ratio for the back-up mode is lower than that of the normal mode.

The SR data, from the SR recorders, and the digital data from the VTPR and SPM are played back and transmitted to the ground upon command of a CDA Station. From here, these data are relayed over long lines to ESSA facilities for meteorological analysis.

The VHRR recorder is played back on command from the CDA Station. VHRR data also can be relayed over long lines to ESSA facilities for meteorological analysis. The time required to relay a 9-minute VHRR record sequence is 72 minutes.

The solar proton monitor (SPM) will be used, in conjunction with other satellite-borne and ground-based sensors, to provide warnings of solar proton storms. These warnings are currently used in several ways. High altitude users, such as supersonic transports and manned spacecraft, make provisions for the protection of personnel on the basis of this data. Solar proton storms affect radio frequency links (VLF through HF), and since satellite warnings often precede ionospheric disturbances, alternate radio paths or frequencies are often selected in advance.

B. SCANNING RADIOMETER

1. Subsystem Design

a. GENERAL

The scanning radiometer (SR) subsystem measures emitted radiation from the earth during day and night and measures reflected solar radiation from the earth during daytime. The data obtained is transmitted in real-time to local user stations, and is also recorded for later playback to the CDA stations.

The radiometer has two channels: a visible channel and an infrared (10.5- to 12.5-micron) channel. The visible channel provides coverage during the day, in the same spectral region used by the TIROS television cameras. The infrared (IR) channel operates in an atmospheric window region which has sufficiently

low reflected solar radiation so that day performance is comparable to night performance. This channel is calibrated for surface temperatures in the region of 180° to 315°K, thus permitting measurement of cloud top and surface temperatures.

The design of the radiometer permits a large variation in spacecraft operating parameters. The performance of the radiometer will not be compromised if the spacecraft altitude is varied over the range of 600 to 900 nautical miles, although the nominal design altitude of the radiometer is 790 nautical miles. Similarly, the radiometer is designed to operate satisfactorily in sun-synchronous orbits within 1 hour of the nominal 9 AM descending and 3 PM ascending node orbits. Major operating parameters of the SR subsystem are given in Table VI-1.

The SR subsystem comprises: (1) two scanning radiometers; (2) a dual SR processor; (3) three scanning radiometer recorders (SR recorders); and (4) two VHF transmitters. A block diagram of the subsystem is shown in Figure VI-1. Each radiometer and tape recorder can be turned on or off by command from a CDA Station. Each half of the SR processor is associated with one radiometer and is powered when that radiometer is powered. The VHF transmitters can be inhibited, by ground command, for n of 8 orbital segments. The radiometers are mounted on the spacecraft structure in a manner which permits solar illumination of the visible calibration target, and to permit a scan of approximately 150 degrees without obstruction.

As the spacecraft proceeds along its orbit, the radiometer scans the earth's surface from horizon to horizon, perpendicular to the orbital plane. The radiometer scans the earth by means of a continuously rotating mirror which is inclined 45 degrees to its axis of rotation (parallel to the satellite's velocity vector). The optical axis scans in a plane perpendicular to the satellite's velocity vector as shown in Figure VI-2.

Mirror rotation causes a transverse scan across the earth (shown in Figure VI-2 as scan n). In the time required for one complete mirror rotation, the satellite progresses approximately 4 miles along the orbit track. Another area is then scanned, shown as scan n + 1, and this is repeated throughout the orbit.

The SR output signals are routed to the SR processor, where time code data and SR telemetry data are combined with the infrared and visible radiation signals. The processed visible and infrared channel signals are sent, on separate outputs, from the SR processor to the fm modulator in the tape recorder and then to separate heads in the tape transport. The distance between the two heads is equal to the length of tape required to record one half of a scan line. The earth scan portion of both the visible and the infrared signals are recorded simultaneously. The second half of the earth scan line is inhibited so that the recorded signal is the infrared scan followed by the visible scan. The playback

TABLE VI-1. SCANNING RADIOMETER PARAMETERS

Parameter	Visible Channel	IR Channel
Resolution		
Angular	2.8 milliradians	5.3 milliradians
Ground at 790 nmi	2 nmi	4 nmi
Spectral Region	0.52 to 0.73 microns	10.5 to 12.5 microns
Sensitivity, Noise Equivalent Irradiance	7.5×10^{-10} w cm^{-2}	4.2×10^{-10} w cm^{-2}
Dynamic Range	20 to 10-k foot-lamberts (scene brightness)	180 to 315°K (scene temperature)
Detector	Silicon photovoltaic	Thermistor bolometer
Electrical Bandwidth	1200 Hz	600 Hz
Diameter of Optics	5 inches	
Scan Rate	48 rpm	
Size		
Scanner Unit (inches) not Including Sunshield	15.8 by 8.4 by 6.4	
Electronics Module (inches) not Including Mounting Flanges	6.0 by 6.0 by 6.5	
Weight		
Scanner Unit (lb)	12.1	
Electronics Module (lb)	6.2	
Sun Shield (lb)	0.9	
Power Requirement		
Maximum at -24.5 volts	7.4 watts	

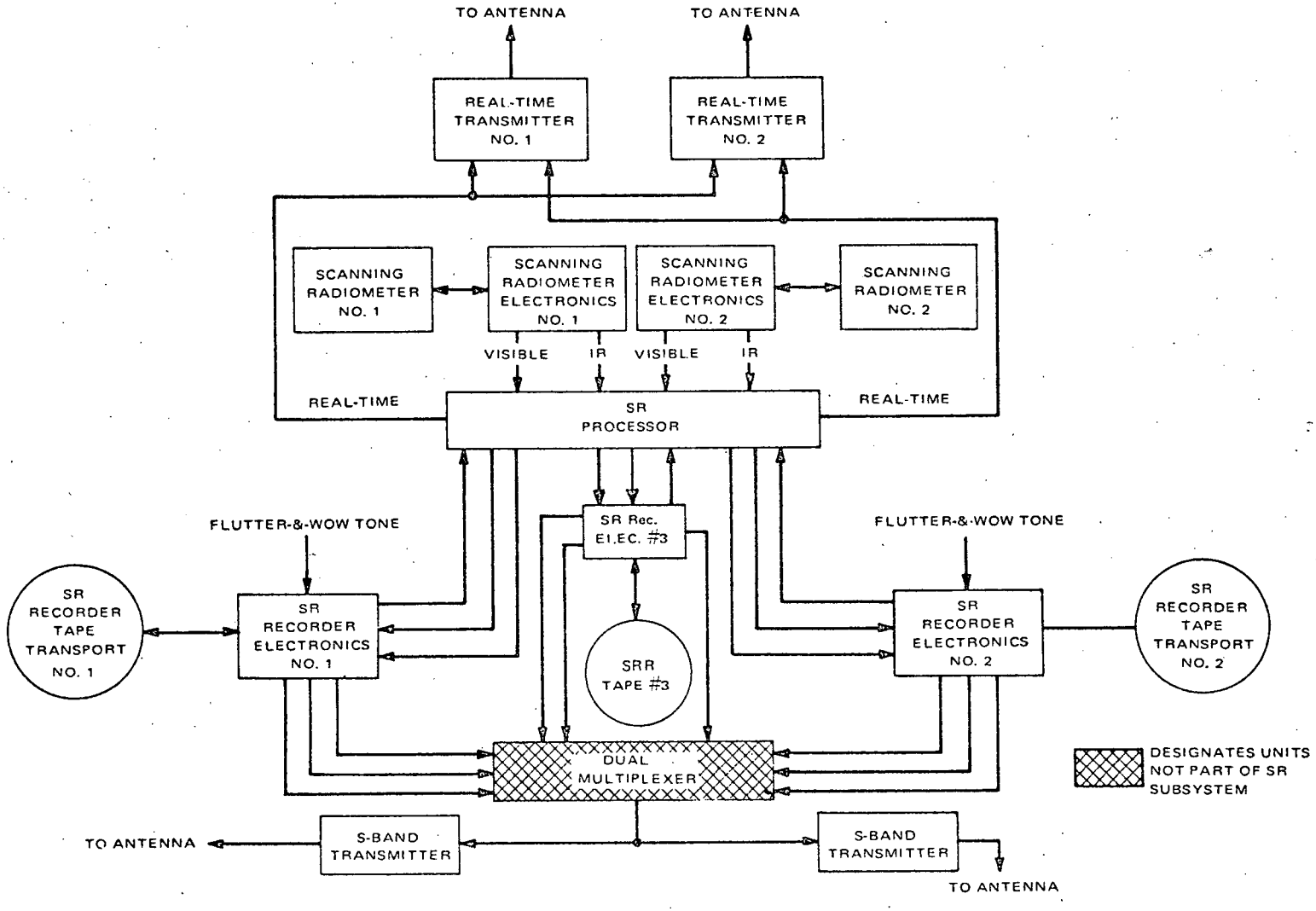

Figure VI-1. Scanning Radiometer Subsystem, Block Diagram

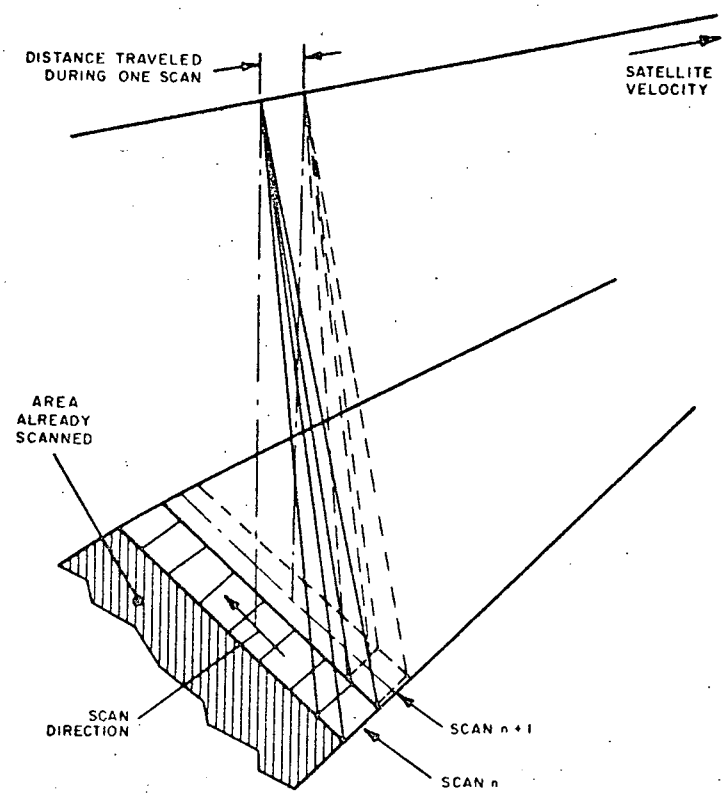

Figure VI-2. SR Scan Projection

head is operated during the record sequence, so that the recorded time multiplexed signal is also used as the real-time signal. A flutter and wow signal is recorded on another track for use during the recorder playback. Playback of the recorders can be commanded to occur either simultaneously or separately.

b. SYSTEM AND ELECTRICAL DESCRIPTION

The block diagram of Figure VI-3 shows the division of functions into two separate boxes which comprise the SR. The scanner unit is mounted on the earth-facing side of the spacecraft and the electronics module is located in the electronics bay of the spacecraft.

The scanner unit has an elliptically shaped flat scan mirror and primary optics which are common to both the IR and visible channels. The scan mirror is set at an angle of 45 degrees with the scan axis and rotates at 48 rpm. The two channels are optically separated by a dichroic beam splitter, after which the radiation in each channel is imaged onto the channel detector. The dichroic beam splitter also acts as a 10.5- to 12.5-micron bandpass filter, to limit the IR channel spectral response. Short wavelength, visible radiation is reflected

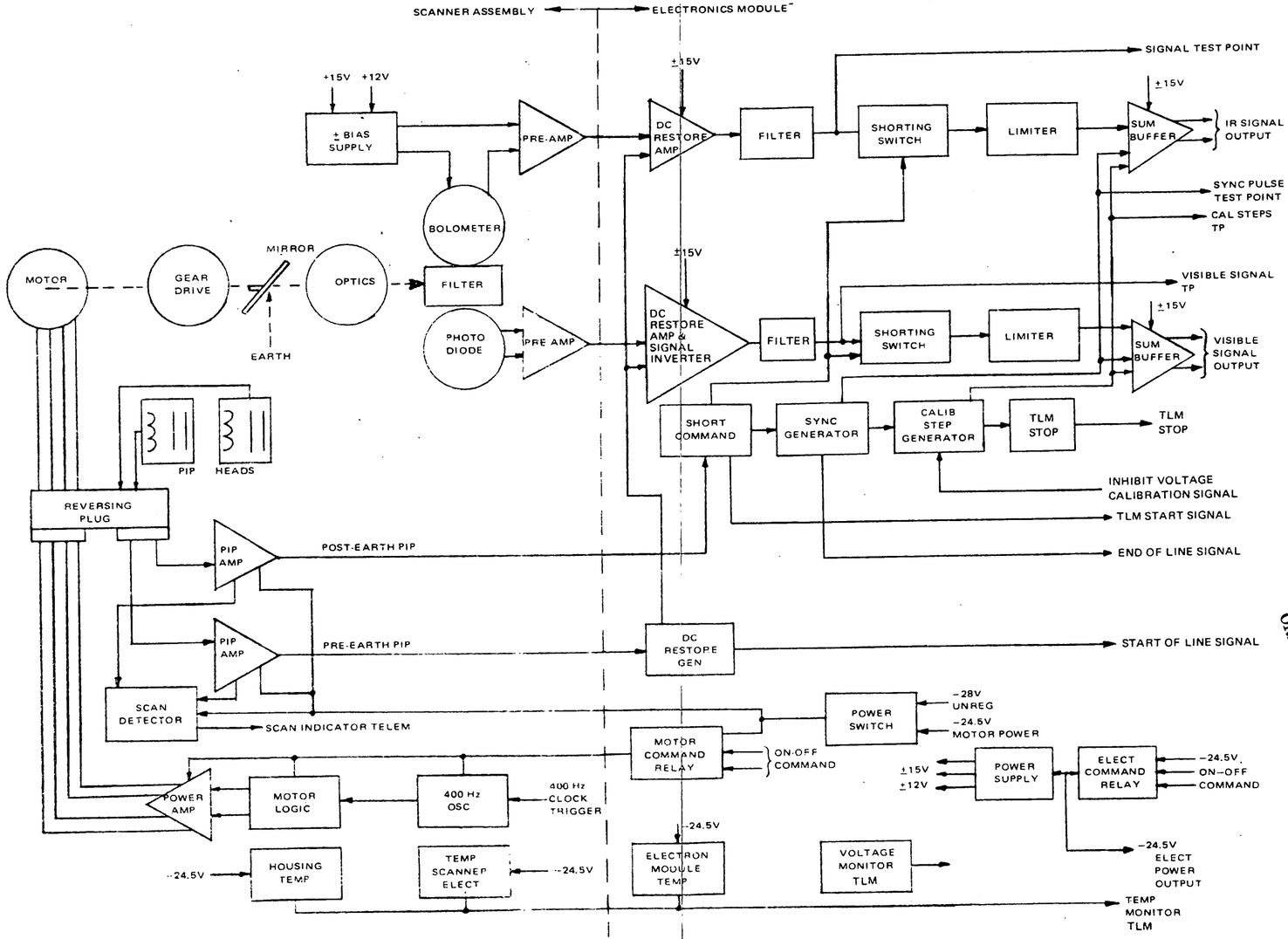

Figure VI-3. Scanning Radiometer, Block Diagram

FOLDOUT FRAME 1

REPRODUCIBILITY OF THE ORIGINAL PAGE IS POOR

FOLDOUT FRAME 2

REPRODUCIBILITY OF THE ORIGINAL PAGE IS POOR

from its front surface. Figure VI-3 illustrates how the visible and IR channels are optically separated and the manner in which the signals are processed.

The detected signals are amplified by the two channel preamplifiers. The IR detector (bolometer) requires a dc bias which is supplied by the bias power supply. This power supply contains a dc-to-dc converter whose voltage output is controlled by two temperature compensating circuits. The first circuit senses the temperature of the detector and varies the bias voltage to give a constant detector output signal for constant radiance input over the temperature range of -5 to +45° C. The second circuit, which also senses the bolometer temperature, sharply reduces the bias voltage at temperatures over +47° C to assure safe internal bolometer temperatures.

The Infrared (IR) channel preamplifier has two capacitor-coupled sections. The first section is a differential field effect transistor (FET) pair, followed by additional amplification using bipolar devices. A capacitor between the detector and first section is used to block the dc voltage variations that result from the two bolometer flakes not tracking accurately over the temperature range. The second section is made up of a differential FET pair followed by an integrated circuit operational amplifier. An RC network between the first and second sections permits "tuning out" the secondary time constant of the bolometer.

The preamplifier for the visible channel is a low noise operational amplifier having a FET differential input. It is connected in the current mode, causing the photovoltaic diode to operate into very nearly a short circuit. This preamplifier is dc-coupled (the Infrared channel preamplifier is capacitor-coupled).

The dc restore amplifier (both channels) consists of a main amplifier with provisions to select gain, a feedback/error amplifier, and an FET switch. In the amplifying mode, the main amplifier passes the signal, the FET switch is open, and the error amplifier does not function. In the IR channel, an RC feedback network provides a boost of 6 dB per octave over the range of about 150 to 450 Hz in order to compensate for bolometer rolloff, which approximates a single pole at 150 Hz. When a "dc restore" signal from the logic is applied to the switch, the FET conducts with a low on resistance. This connects the error amplifier output to the main amplifier input, driving the main amplifier output to -0.25 volt in the IR channel, and -6.00 volts in the visible channel. The signal is inverted by the visible channel's dc restore amplifier.

The band limiting filters which follow the dc restore amplifier limit the high frequencies of each channel. The filter in the IR channel is a Gaussian type three-pole filter with a break frequency at 600 Hz. The visible channel filter is a two-pole Gaussian type with a break frequency at 1200 Hz. The filter characteristics are selected to minimize the settling time for the signal to go from 10% to 98% of its final amplitude. Overshoot is controlled to less than 3% of the final amplitude.

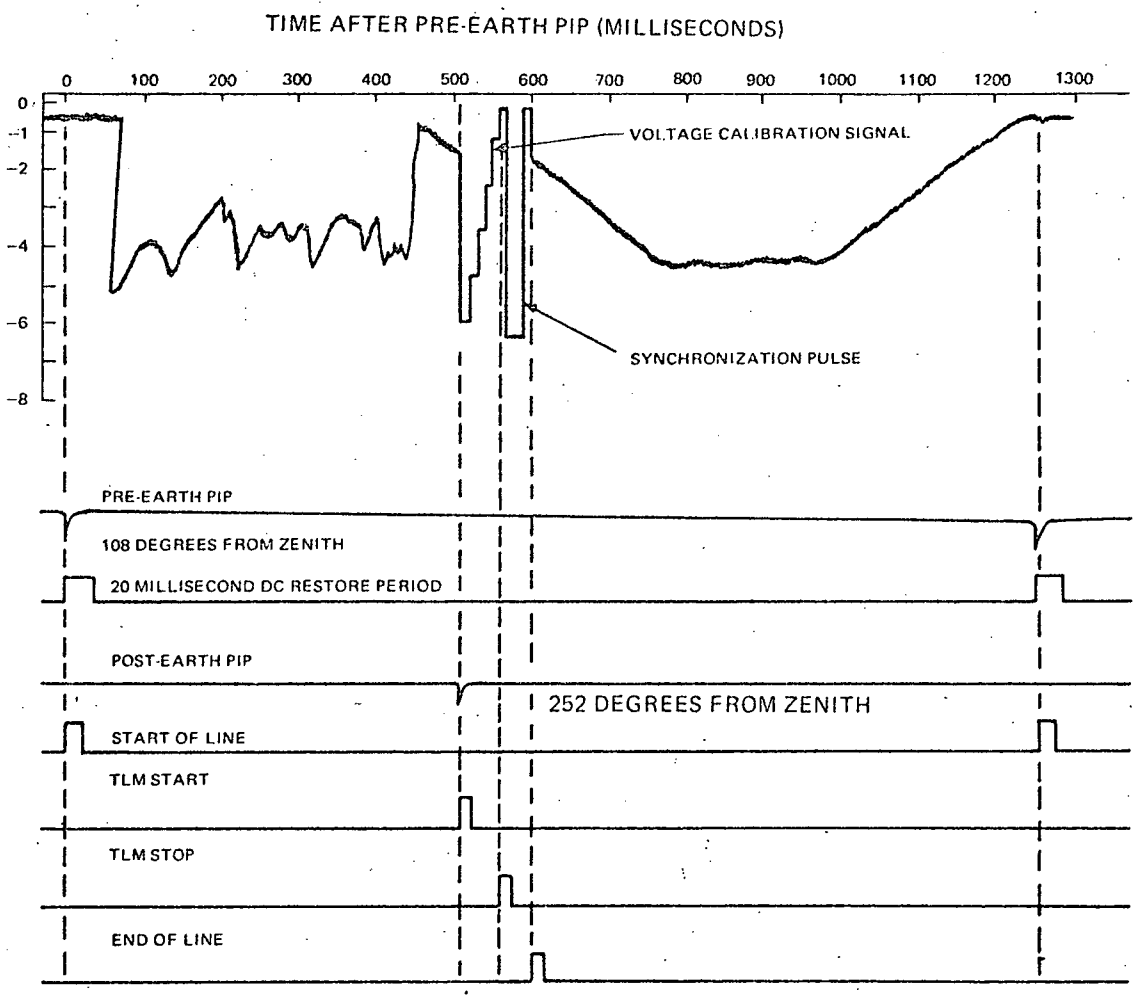

Figure VI-4. SR Subsystem Timing

The end of the voltage calibration signal initiates two more signals, the synchronization signal and the "TLM stop" signal. The synchronization signal consists of three sections: a sync pulse which has an amplitude of -6.66 volts and a duration of 30 milliseconds, and porches at 0-volt level which precede and follow the sync pulse. (These porches have time durations of 10 milliseconds.) The "TLM stop" signal times the operation of the SR processor. At the completion of the synchronization signal, a fourth timing signal ("end of line") is initiated.

When the SR processor changes the voltage level from 0 to 5 volts on the voltage calibration inhibit input to the SR, the voltage calibration signal is inhibited and not placed in the composite video signal. The timing logic continues to count in order to delay the start of the synchronization signal for 50 milliseconds after the post-earth pip.

Telemetry is provided for several radiometer functions to establish calibration of the instrument and to monitor its operating status. Four temperature sensors are located in the portion of the housing viewed during back scan. Two of the four provide more reading accuracy over a reduced temperature range. These are used to establish an in-flight calibration of the Infrared channel. Another temperature sensor monitors the case temperature of the bolometer, while two more monitor the temperature of the electronics in the scanner unit and in the electronics module. A telemetry signal is provided to indicate the presence of -24.5-volt power at the radiometer electronics. Another telemetry signal monitors the rotation of the scan mirror; this signal operates from either the -24.5-volt supply or the -28-volt supply any time the scan motor is commanded on.

Five test point locations are monitored in the electronics, and their signals are brought to a connector on the electronics module; thus internal points in the electronic circuits can be monitored without opening up the modules.

c. OPTICAL DESIGN

The optical system consists of a scan mirror, a primary mirror, a secondary mirror, and a dichroic beam splitter which divides the energy into two channels (see Figure VI-5). The 2.8-milliradian visible channel detects energy in the 0.52- to 0.73- micron band and consists of a visible filter, a field stop, and a silicon photovoltaic detector. The visible filter defines the spectral bandwidth of the visible channel. The 5.3-milliradian infrared channel detects energy in the 10.5- to 12.5-micron band and consists of a bandpass filter (transmission portion of a dichroic), an Irtran II field lens (a relay lens) which also serves as a long-wavelength blocking filter, a folding mirror, and the germanium immersed thermistor bolometer. The combination dichroic filter beam splitter assembly defines the spectral bandwidth of the infrared channel. The design configuration of the radiometer is illustrated in Figure VI-6, which is an optical schematic showing the telescope and the filter detector module.

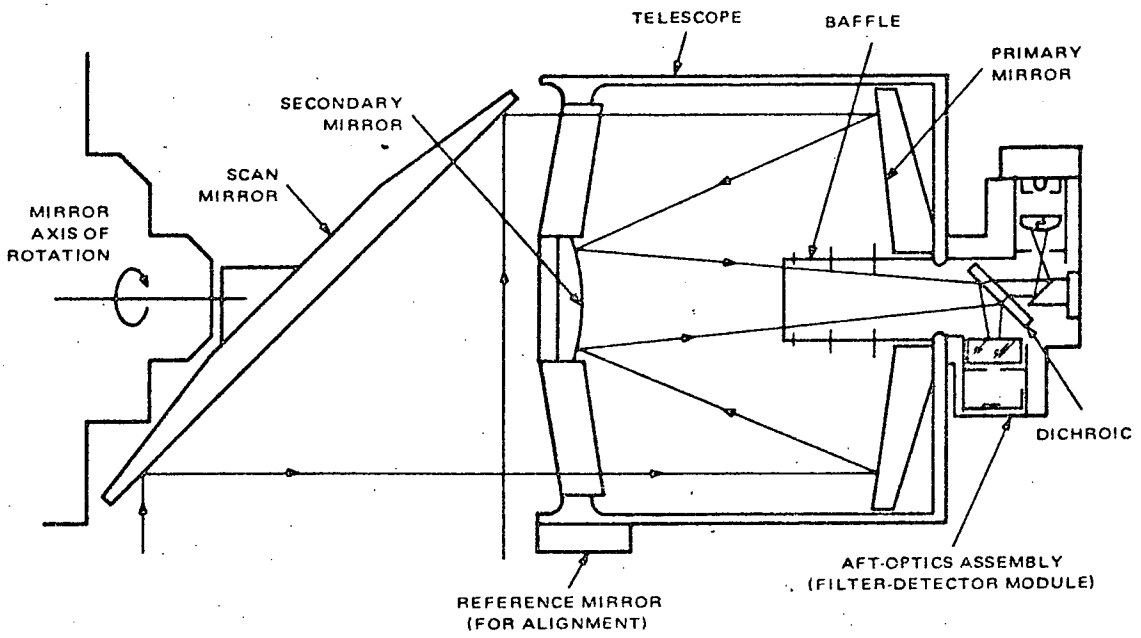

Figure VI-5. Scanning Radiometer, Optical Schematic

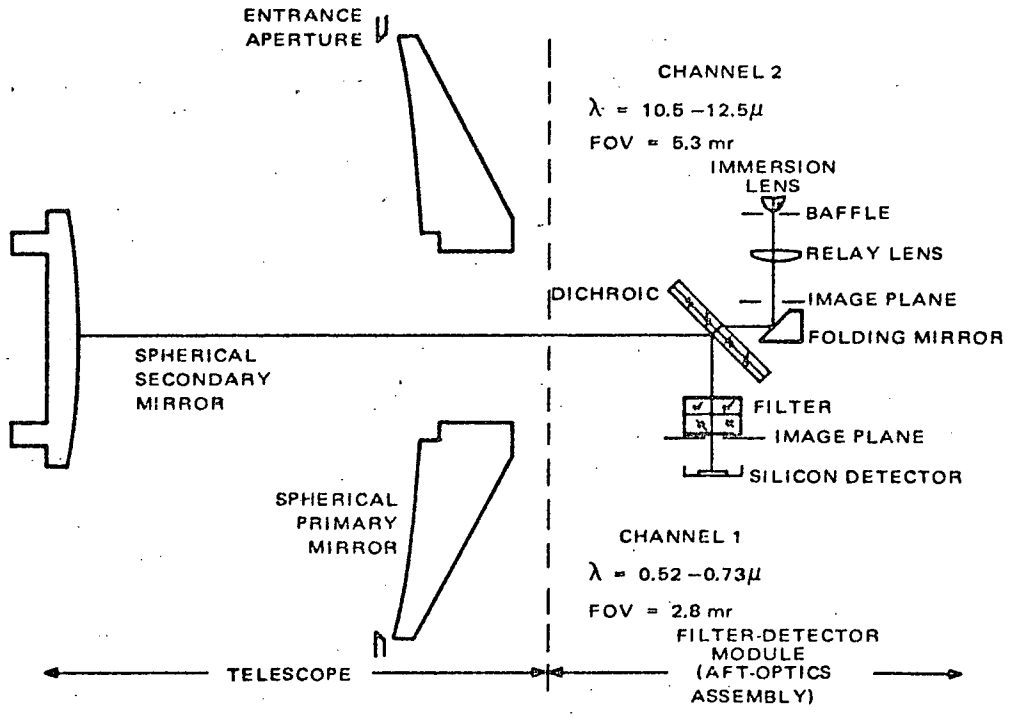

Figure VI-6. Scanning Radiometer, Detailed Optical Schematic

The "stop" at the primary mirror establishes the 5.0-inch diameter entrance aperture of the telescope. An area of 2.160 inches in diameter is obscured by the secondary mirror and its holder. A concomitant objective of the telescope design was to provide baffling which prevents rays (energy) from the object scene from directly reaching the radiometer field stops. The design of the telescope baffles prevents this object scene radiation from reaching the field stops along calculated paths with less than two reflections from optically black painted surfaces. The addition of a sunshade further reduces the number of optical paths which have a small number of "reflections". Radiation, which is diffusely reflected from the inside of the finned primary mirror baffle, reaches the radiometer field stops and detectors by reflection from the center of the secondary mirror and, also, directly into the field stops. Consequently, the sunshade minimizes the exposure of the finned primary mirror baffle (interior) to the sun's rays. The telescope baffling was designed to be compatible with the sunshade. The telescope tubular structure is grooved (for trapping stray radiation) and painted with 3M Velvet Black paint.

The telescope design provides a 101.7-cm^2 clear aperture area. While this is less than the 110-cm^2 design goal, the resulting loss in clear aperture area was offset by an increase in the energy obtained from the corners of the radiometer IFOV* in the infrared channel. Since the condensing optics (in the filter detector module) utilizes a relay optical system, it provides more energy in the corners of the IFOV.

The telescope optical design uses spherical primary and secondary mirrors. The all-spherical mirror provides a predicted image "spot size" of 1.5 milliradians within the 5.3-milliradian IFOV. The telescope focuses the image in the plane of the pseudo field stop. This image is relayed by an Irtran II lens onto the flake of the square thermistor bolometer, which is the actual field stop defining the IFOV of the infrared channel (see Figure VI-7). An oversized square "field stop-baffle" is located at the prime image to function as an additional baffle to reject stray radiation. If, however, the bolometer flake is slightly oversize, resulting in an out-of-tolerance IFOV, the field stop-baffle may be used as a "trimmer field stop" to accurately control the size of IFOV.

The nominal back focus distance setting of the telescope is accomplished by the adjustment of the secondary and primary mirror spacing, with the use of a shim at the rear of the secondary mirror. Fine focus adjustments of the filter detector module (aft optics section) to the telescope image location are accomplished by installing a shim between the telescope back reference surface and the mating surface of the filter-detector module.

*IFOV denotes "instantaneous field of view" as defined by the field stop in the visible channel, and defined by the bolometer flake in the infrared channel.

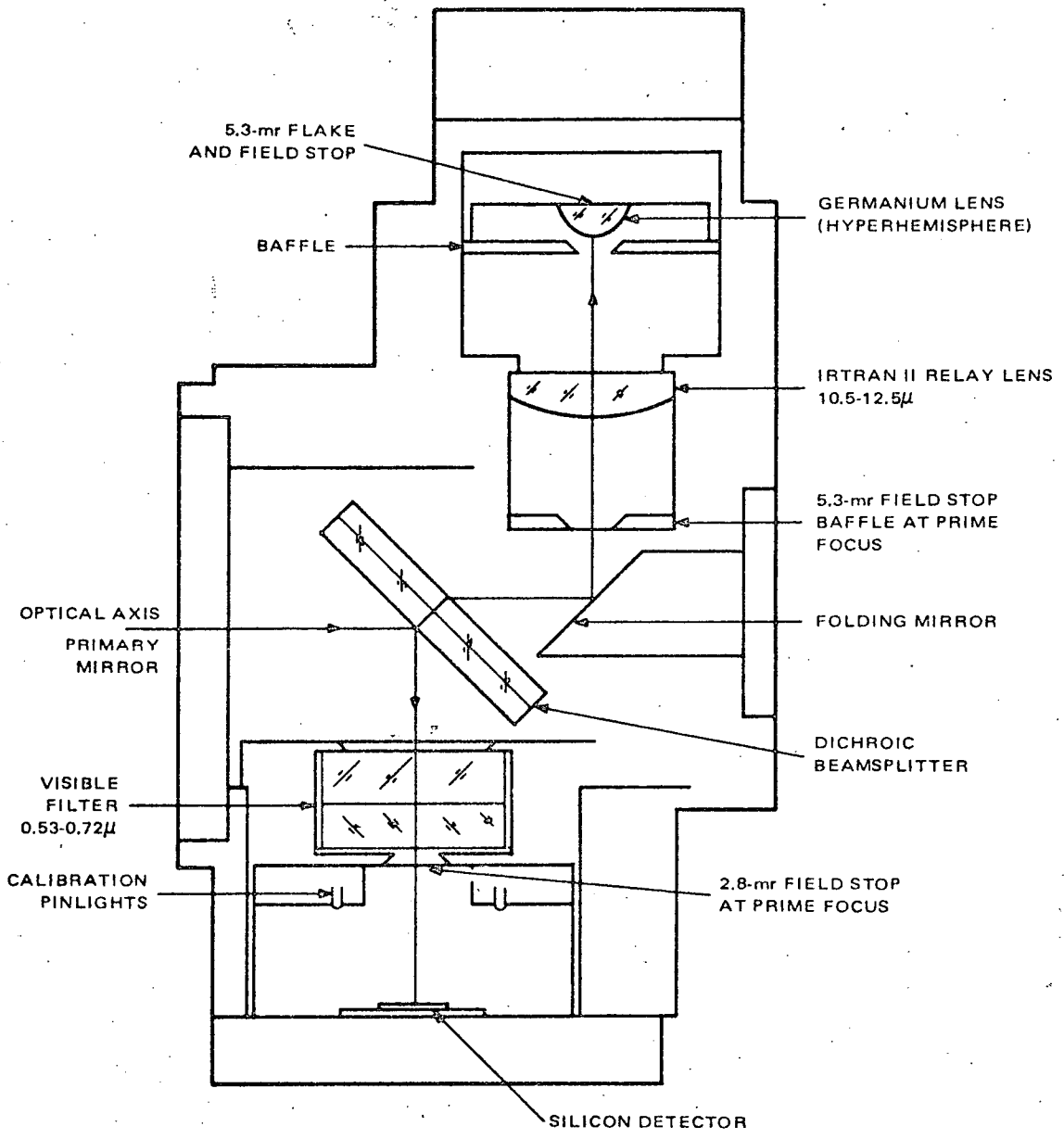

Figure VI-7. Aft Optics Assembly

The defocusing of the telescope over a ±25°C temperature range (caused by thermal expansion of the telescope tube and by mirror radii changes) was calculated to be ±0.008-inch net change in back focus distance. The ±0.008-inch shift from the nominal image plane is well within the "depth of focus" for a 0.026-inch diameter blur circle formed by an f/3.4 optical system. This conclusion was confirmed by data taken on a similar telescope design used in the NASA/GSFC Two-Channel Radiometer.

The active optical axis of the telescope is defined by the center of the IFOV of the infrared channel. The alignment of the telescope to the three reference mirrors mounted on the radiometer scanner housing is determined only after the assembly of the telescope and the filter detector module (aft optics). Only two of these mirrors are used to align the radiometer on the spacecraft but three are required so that the radiometers may be mounted in two orientations. The filter detector module is assembled and aligned to provide a nominal channel-to-channel alignment at the subassembly level. Final channel-to-channel alignment does not require any changes in the telescope since the final alignment adjustments are provided in the filter detector module at the visible channel subassembly mounting.

Two types of condensing optical designs (in the filter detector module) were investigated during the design study: (1) aperture imaging on the bolometer flake and (2) field imaging on the bolometer flake. The "field imaging" approach was chosen for the scanning radiometer design.

The entrance aperture of the telescope is imaged on the immersed bolometer flake. The IFOV is defined at the field stop immediately in front of the germanium immersion lens. The simplicity of this optical configuration is desirable; however, the effectiveness of this approach depends upon the fixed optical parameters built into the immersed bolometer. In addition, the corners of the IFOV are almost entirely lost due to internal reflections of rays incident at angles exceeding the "critical" angle at the rear surface of the immersion lens.

Tests performed with aperture imaging condenser designs have indicated narrower measured IFOV's than predicted by the nominal optical design. In addition, the immersed bolometer optical tolerances have not always been held by the detector manufacturer. Consequently, the condenser optical design study was conducted to determine the IFOV-degrading effects of all combinations of optical tolerances in the immersed bolometer. The lowest reported value of the index of refraction of the modified selenium glass layer (2.45) was used because it sets the tightest limits on the bolometer internal acceptance angle. (The selenium glass layer, 0.0005-inch thick, is the optical immersion medium between the bolometer flake and the germanium immersion lens.)

Concurrent with a tolerance analysis of the aperture imaging condenser system, other condenser optical design configurations were evaluated. The basic approach to an improved condenser design was to distribute the optical

tolerances among a greater number of optical surfaces and to provide degrees of freedom for corrective adjustments. The design goal was to use the same flake size as that used in the initially proposed aperture imaging condensing design (maintaining the needed optical gain of the system) but with "less critical" optical tolerances.

The bolometer flake size achieved for the optics using the field imaging condenser design is nearly identical to that originally calculated for the nominal aperture imaging design. In addition, the energy at the corners of the IFOV is collected on the bolometer flake.

A more detailed diagram of the filter detector module is shown in Figure VI-7. Note the location of the visible calibration test lamp.

Figure VI-8 shows the distribution of energy across the field of view. The overall spectral response of each channel is given in Figures VI-9 and VI-10. These curves, which are typical for all ITOS scanning radiometers, were measured on the P-1 radiometer.

The dichroic filter/beam spliter underwent a major improvement during the development of this radiometer for TIROS M. The earliest model had a marked variation

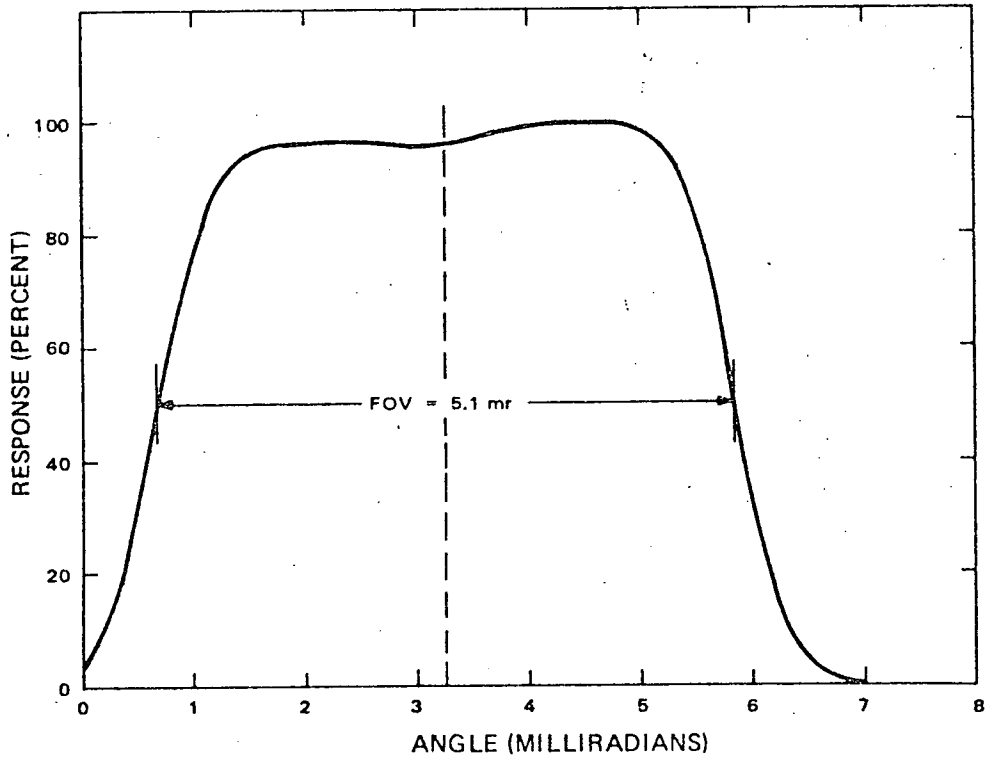

Figure VI-8. IR Response versus Displacement Angle

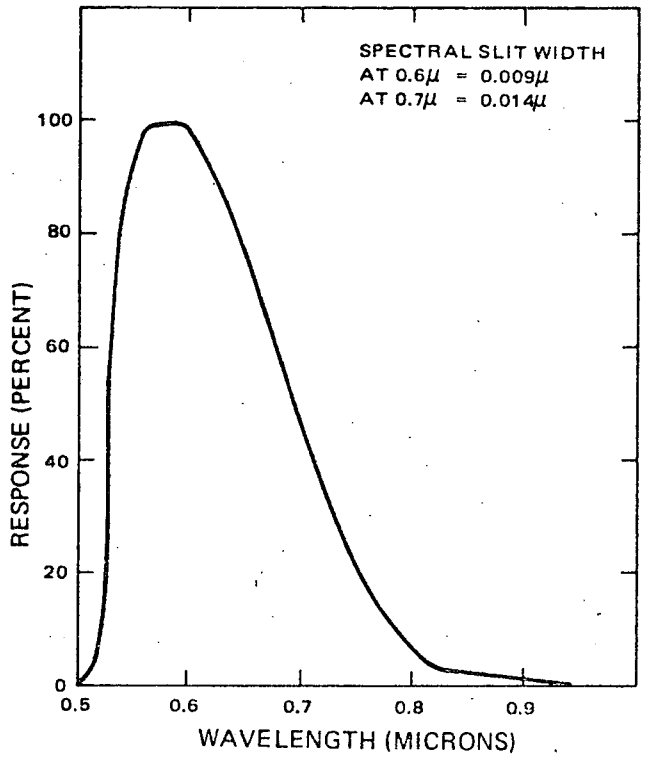

Figure VI-9. Visible Channel, Relative Spectral Response

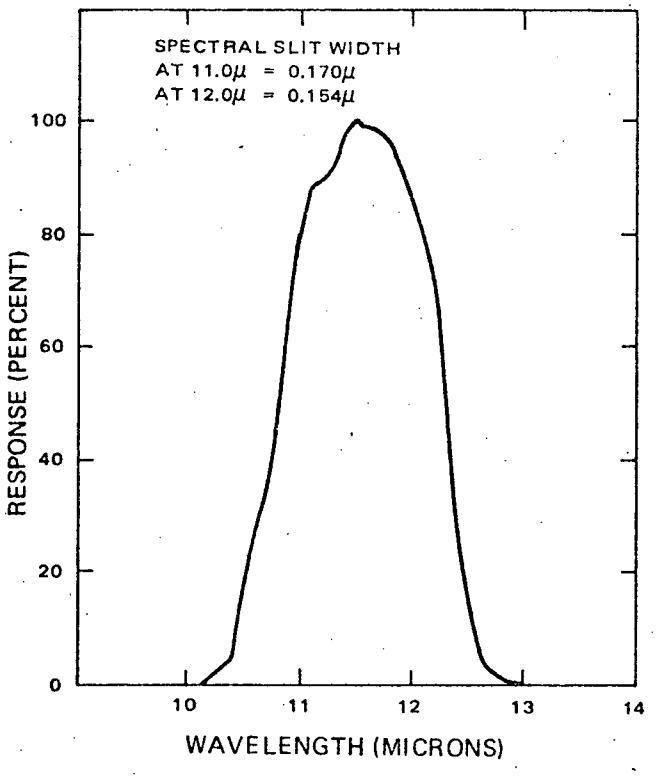

Figure VI-10. IR Channel, Relative Spectral Response

in reflectance over the spectral region sensed by the visible channel. This variation took the form of a cycle variation with six complete cycles in the interval of 0.50 to 0.86 micron. The minimum reflectance was as low as 4 percent, while the maximum was as high as 60 percent. Optical Coating Laboratories, Inc. was later able to produce dichroic filters/beam splitters with a reflectance characteristic which peaked near the center of the visible channel spectrum and gradually fell off at the two ends to a value of about 80 percent of the maximum transmission. This new filter proved to be durable and to have a high thermal channel transmission.

Three alignment mirrors are attached to the main housing casting. The mirror on the bottom of the scanner unit and one of the side mirrors are required to establish the coordinate system of the radiometer. During the assembly and alignment of the optics, the position of the scanned field of view is determined and related to the alignment mirror.

d. MECHANICAL DESIGN

The scanner unit, which is on the outer spacecraft structure, was designed with a low profile to keep it within the constraints established by the launch rocket fairing. This requirement made necessary a very narrow neck area (with beryllium reinforcement rods) connecting the telescope and the scan mirror drive. The length of the radiometer has also been held to a minimum to reduce the overall profile. The scanner unit consists of four subassemblies:

- Scanning housing,
- Scan mirror drive assembly,
- Telescope assembly, and
- Aft optics assembly.

Figure VI-11 identifies the subassemblies and their locations. In addition, it shows the alignment mirrors to indicate necessary "clear paths" required for radiometer installation. The main housing for the scanner is a cast magnesium tube (AZ91C alloy), open at the ends and locally along the wall to permit a scan mirror view of ±75 degrees. Four mounting pads (integrally cast) on C section legs extend from the tube, 180 degrees from the mirror view opening. To ensure structural integrity through the throat section, two cylinders, also integrally cast, run parallel to the main radiometer axis between the C section legs. A beryllium tube is held to withstand torsional loading but allowed to float axially to accommodate any expansion differential between the beryllium and magnesium.

A serrated surface is machined into the housing wall directly opposite the mirror view opening and coated with a high emissivity paint to serve as a blackbody calibrator for the thermal channel. The temperature of this surface is monitored

by four thermistors spaced on the surface. Alignment mirrors are located on the sides and bottom of the scanner to implement the spacecraft/radiometer alignment. The reference mirrors are Pyrex blanks with aluminum vacuum deposited on the surface, expoxied into the casting.

The scan mirror is driven by a 2000-rpm synchronous motor having an output torque of 0.12 oz-in. The ball retainers in the motor bearings are phenolic, vacuum impregnated with Pioneer P10 oil. A nylasint reservoir impregnated with P10 oil is also contained in the motor case. The motor has a labyrinth seal at the output shaft and is otherwise sealed from the environment.

A magnesium casting forms the outside housing of the scan mirror drive assembly. The register diameter is machined into the scan mirror drive housing to mate with the scanner housing. The mount flange and cover provide an external mounting surface for those subassemblies associated with the mirror drive and position readout; i.e., the magnetic head assemblies, the pip amplifier and a terminal board. Thus, the scan drive module allows head-to-magnet spacing, gear train run-in, and electrical checkout before assembly into the scanner housing.

A stainless steel (type 416) shell with grooves for O-ring seals is fitted into the magnesium casting to provide support for the bearings and the gear shafts. The advantages gained from this design are:

- Precision inline boring of the bearing supports;
- Similar thermal-expansion characteristics; i.e., stainless steel shell, bearings, shafts and gears; and
- Bearing preload adjustment and overall gear train inspection and checkout can be performed before assembly into the scan drive castings.

The gear train consists of two meshes with an overall reduction ratio of 40.67:1. The reduction from the motor to the mirror is in two steps, as follows:

- 2000:288 rpm, and
- 288:48 rpm.

The gears and pinions are made from 416 stainless steel to AGMA No. 14 quality, with contact surfaces electrolized to obtain maximum wear resistance.

Although antibacklash gears are used, the combined residual backlash and transmission error remaining in the system was calculated to be 0.00345 radian total. Test data indicates that the jitter resulting from backlash is less than 0.0005 radian.

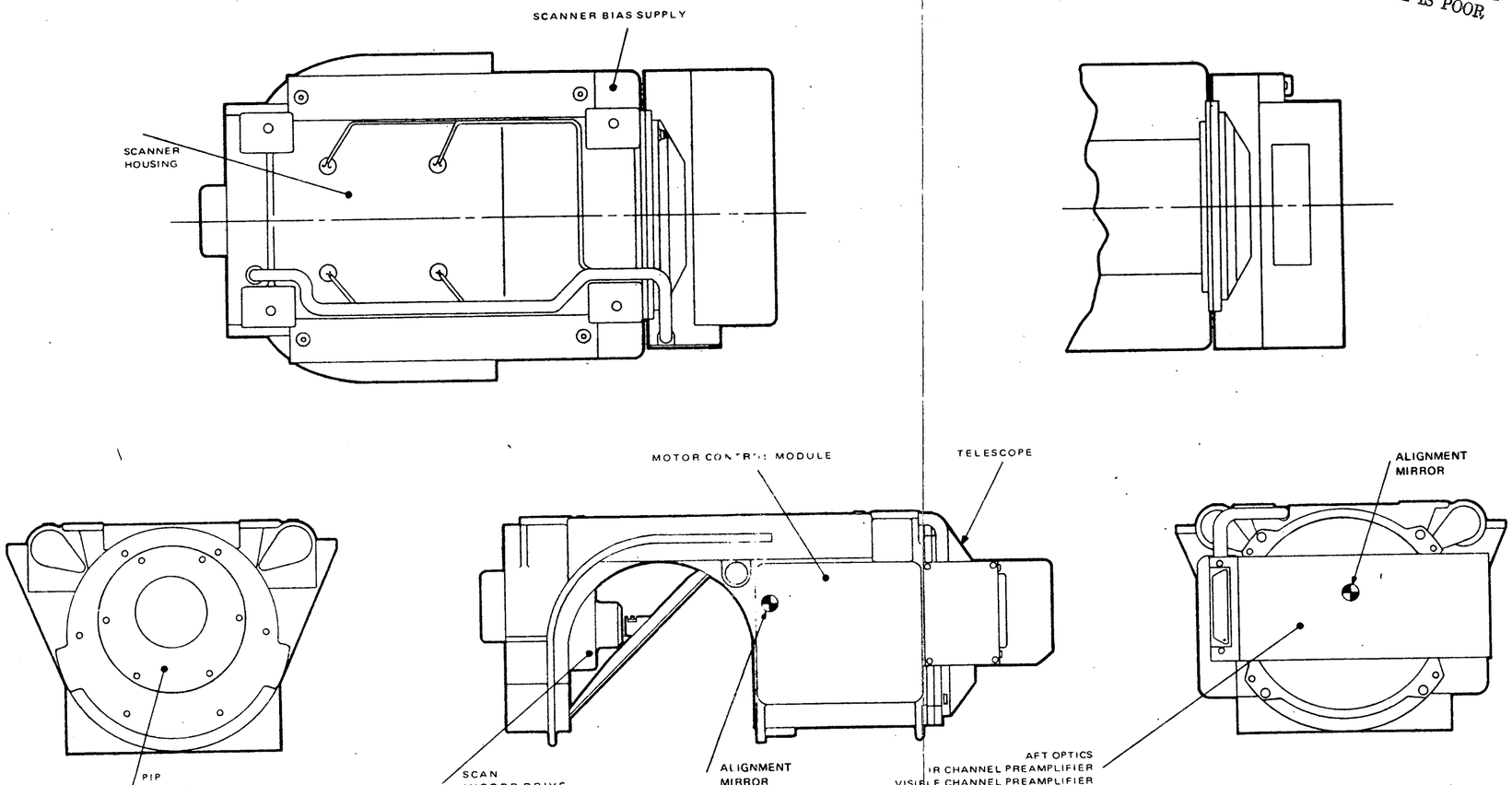

FOLDOUT FRAME 1

Figure VI-11. Scanner Housing Module, Outline Dimensions

FOLDOUT FRAME 2

The seal at the output shaft of the scan drive assembly is a modified labyrinth arrangement with a nominal 0.0006-inch clearance arond the shaft exposed to the space environment. A bypass arrangement encourages vapor flow around, rather than through the bearing immediately inboard of the labyrinth opening. Calculations show a flow rate of 1.05×10^{-4} grams per year, based on Pioneer P10 oil, through a 0.0006-inch clearance around a 0.375-inch diameter shaft. Tests over a 2-month period during the design and fabrication of TIROS M in thermal-vacuum indicate the oil contained in the scan drive would far exceed the 1-year requirement.

The telescope assembly is simply a tube closed at one end with a bracket. The bracket is common to the telescope and the aft optics housing; it is the support for the primary mirror on the forward side and provides registry and support for the aft optics on the back side.

The aft optics housing assembly consists of a rectangular block with the detectors and optical elements mounted in tubes which assemble into and register to the block. The dichroic mirror is inserted into one end of the block and is pinned for accurate alignment. The 45 degree folding mirror is inserted into the back side with a register diameter and pins for accurate alignment.

The scanner cavity from the mirror view opening through the detector preamplifiers is gasketed to minimize radio frequency interference. The gasketing consists of Metex strips bonded where necessary with space-qualified electrically conductive adhesive. It is impossible to effectively eliminate RFI through the scan mirror look opening. The scanner design is unchanged from TIROS M.

The electronics module contains five circuit boards. Four are mounted in conventional printed circuit board slides and these plug into a mother board which is keyed to prevent insertion of the wrong board. These boards may be removed by unscrewing a side cover. Though some of the board layouts have been changed for ITOS D and E, the basic module is the same as for TIROS M.

The power supply board is located in the machined-out base of the module. This location provides improved heat sinking for the power transistors and provides a metallic shield around the dc-to-dc converter. This circuit board is covered with a dust cover, which is flush with the mounting flanges. All joints between covers and the main machining of the module are fitted with Metex strip rf gaskets.

2. Modification of TIROS M Design for ITOS D and E

Three major changes have been made to the scanning radiometers for the ITOS D and E spacecraft. These changes are:

- The data format time period was reduced to permit time multiplexing of the visible channel and IR channel signals.
- Transient response of both visible and IR channels were modified.
- A solar illuminated target was added to give improved accuracy of the visible channel onboard calibration.

The first of these changes is entirely implemented by changes on the two logic boards in the electronics module. The timing of the voltage calibration signal was altered such that this signal occurs before the synchronization pulse rather than after it. The synchronization pulse and the voltage calibration signal are clocked by a timing signal generated in the radiometer. This clocking signal, which had a period of 20 milliseconds has been reduced to 10 milliseconds on the ITOS D and E radiometers.

A function has been added to the operation of the logic circuits, i.e., the inhibiting of the voltage calibration signal. During the period that an external signal level is present on the inhibit voltage calibration input, the voltage calibration stairstep waveform is not generated. Instead, the signal from the detector is placed in the composite signal during the time that the voltage calibration signal would normally be displayed. The detector signal during this time senses the radiance coming from the visible calibration target. To simplify the electronics, both channels are inhibited during this period although only the visible channel calibration is meaningful. To implement the time multiplexing function, the number of timing signals generated by the radiometer logic have been increased from two to four. These signals are "start SR line," "TLM start", "TLM stop," and "end of line."

Changes were made to both channel amplifiers to make the transient response more suitable for quantitive radiometric measurements. The transient response has been tailored to minimize the time to change from one radiance level and stabilize on the new level. (The TIROS M radiometer filter was selected to optimize the signal-to-noise ratio with a transient response that would be satisfactory for television picture use.) For ITOS D and E, the bandwidth has been increased in the radiometer to prevent the effect of cascading the break frequencies. The settling time has been taken as the prime objective.

The actual bandwidth is now selected by the user. By selecting a bandwidth, he may choose between improved spatial resolution or higher radiometric accuracy.

Settling time of the channel amplifiers is the time from the 10 percent response point to the point where the signal reaches and remains within 2% of the final signal level. Figure VI-12 illustrates this definition. On ITOS D and E, the settling time on the infrared channel is less than 1.5 milliseconds and less than 0.8 millisecond on the visible channel.

The solar illuminated target has been added to the SR on the ITOS D and E spacecraft, to provide accurate and stable calibration for the visible channel. It has been implemented by using a fused silica lenticular lens mounted as an integral part of the sunshield. Studies leading to this method of implementation were performed at both Santa Barbara Research Center and the Astro-Electronics Division of RCA. A summary report of these studies follows.

A solar illuminated target provides an accurate means of calibrating the visible channel because the level of illumination is accurately known. Though the solar illumination target would be difficult to calibrate accurately here on the earth's surface, the characteristics of the target can be accurately established in the laboratory and the final calibration delayed until the spacecraft is in orbit.

Two general types of targets were considered; one reflecting the radiation from its surface and the second transmitting the radiation. A reflecting target must have a diffusely reflecting surface to reduce the level of radiation to the range that

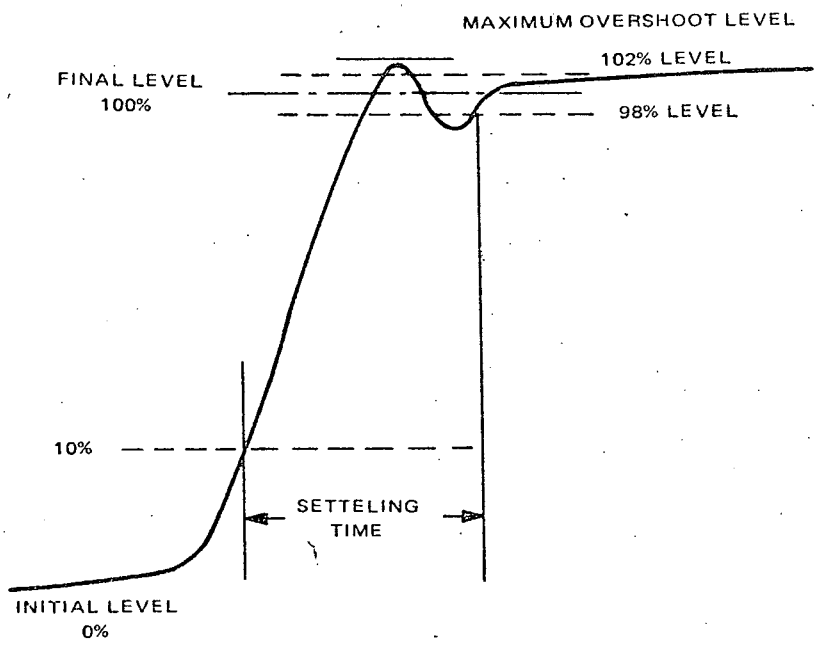

Figure VI-12. Settling Time of Channel Amplifiers

would be expected from the scene. The diffused surface also obviates moving the target to mirror the image of the sun. Two suitable surface materials were studied which would provide a surface which would not degrade due to space environment, especially the ultraviolet exposure. Because these two surfaces were close to a lambert-law diffuser and since the target could be mounted parallel to the earth's surface the illumination would be directly correlated with the scene illumination at the sub-satellite point.

The transmission targets were first assumed to be a diffusing material. However, if the diffusing properties are good, at least one-half of the energy would be diffused back into the hemisphere which contained the source. This would leave only one-half of the energy to be diffused in the direction of the radiometer optics. The result would be that the maximum obtainable signal from the diffused transmission target would be half the full amplitude signal. This reduction does not account for the transmission losses of the diffuser.

A second approach to the transmitting target would be to have a lens system that would increase the efficiency of gathering the radiation. Santa Barbara Research Center proposed a lenticular lens for this application. The transmitting materials are subject to solarization which will affect the long-term stability of calibration target. Fused quartz, however, is highly resistant to solarization and other forms of browning that are experienced in space.

The lenticular lens has the property of dispersing the incoming pencil of radiation into a fan shaped area, as shown in Figure VI-13. If the pencil is normal to the surface, the fan will be symmetrically distributed about the normal. The major dispersion is perpendicular to the ridge lines of lens elements with no significant dispersion in the other direction. The reciprocal case is true. If the energy were to come from anywhere within the fan, it would emerge approximately normal to the surface of the lens. This is the way a lens would be used in the solar target application. The sun would be in the area of the fan and the radiometer would view the lenticular lens nearly normal. The lens can be designed to cover a substantial area as shown by the transmission curve of a sample lens made at the Santa Barbara Research Center (Figure VI-14), or it may be designed to cover a more restricted range. By having the ridge lines on one surface of the base material run perpendicular to that on the other surface, a solid angle can be defined where the collecting power of the lens is high.

The spacecraft was studied to determine the location which would be suitable for the solar calibration target. Both the reflective and transmitting targets were considered. The reflective target could be mounted in the greatest number of locations and still be correctly illuminated. The transmission target has a much more limited range of locations as it must be located between the scanning optics and the sun. The location of the SR's on the earth-facing panel towards the thermal fence is an ideal location for obtaining solar calibration.

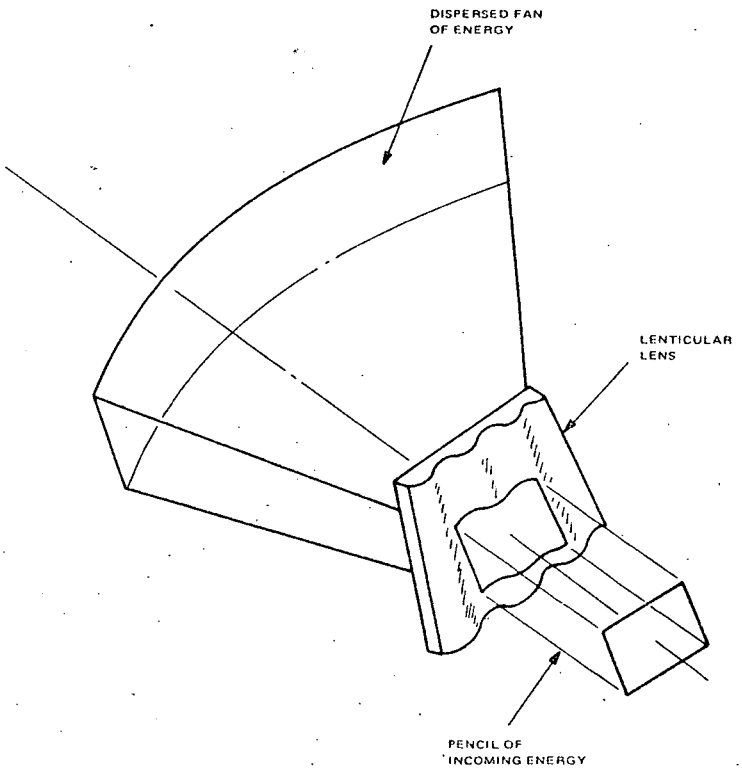

Figure VI-13. Lenticular Lens Dispersing Characteristics

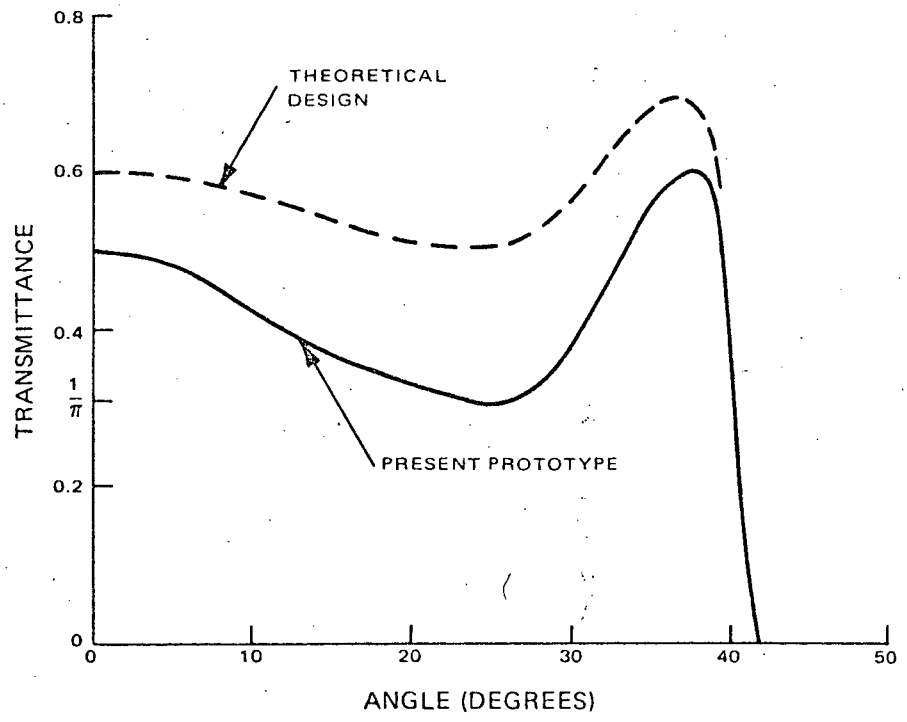

Figure VI-14. Sample Lens, Transmission Curve

The acceptable location for targets was limited by the field of view constraint of the other radiometers and the S band antennas. After considering all constraints, only one location was acceptable for each type of target, as shown in Figure VI-15.

The final selection of target type first considered the permanence and stability of the target. The reflective target is better in this respect. However, on further evaluation, three items influenced the selection transmission target.

- The uncertainty of illumination falling onto the reflective target.
- The effect of the thermal control system due to shadowing caused by the reflective target.
- The reduction in solar array power caused by the reflective target shadowing a portion of the solar panels.

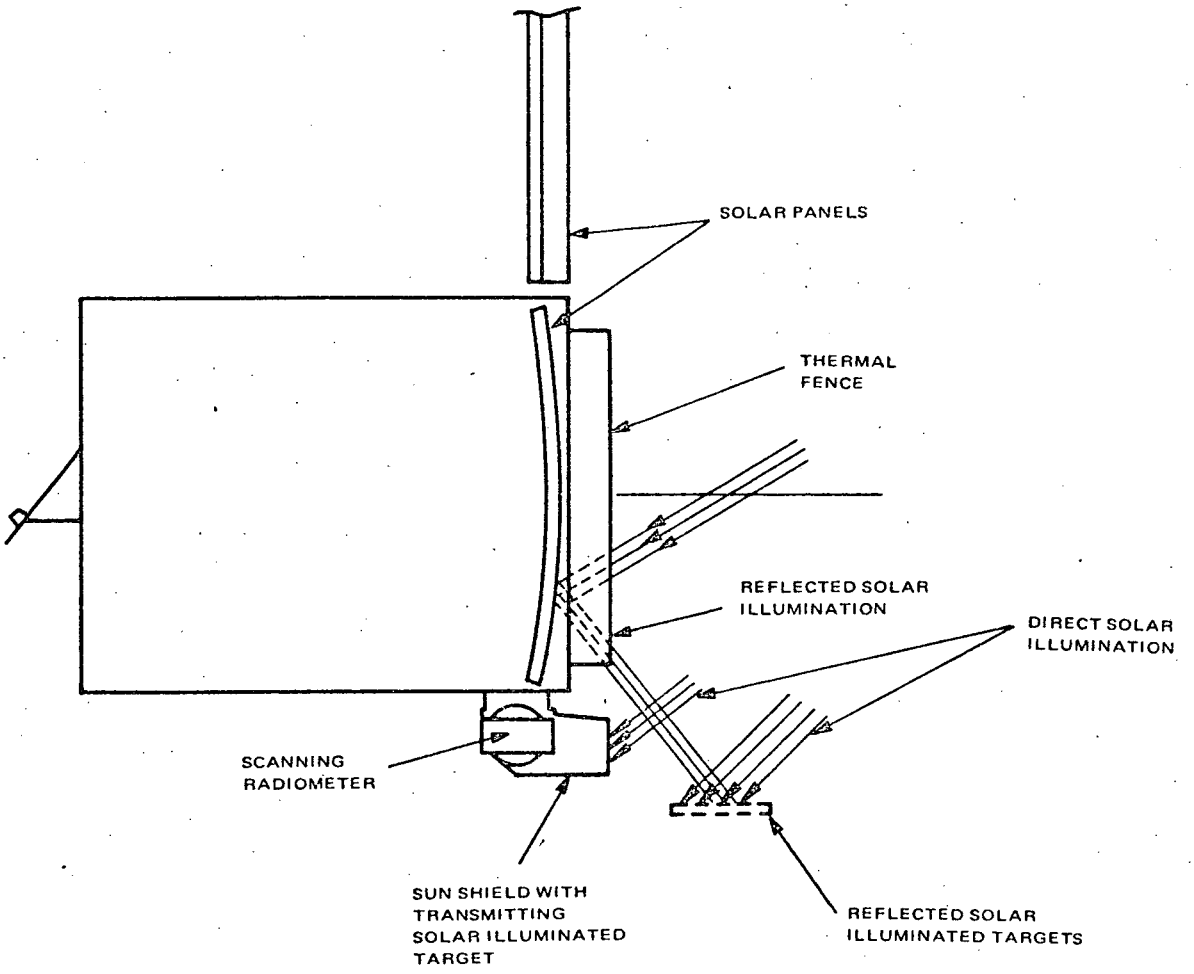

Figure VI-15. Scanning Radiometer Mounted on ITOS D and E Showing Locations of Transmitting and Reflecting Targets

The first item is illustrated in Figure VI-15. The illumination on the target is the combination of the direct solar illumination and the solar illumination reflected by the surface inside the solar fence. This area is highly reflective but is not optically flat. Therefore, the reflected illumination from this surface would not be known accurately enough to use for calibration. An attempt to locate the target to eliminate reflected radiation was unsuccessful. The direction from the radiometer to target required by the radiometer look angle keeps the target in reflected sun light at all distances except those so close that other instrument constraints cannot be met.

The second and third items affect the spacecraft if the target is mounted from 18 inches to beyond 48 inches from the spacecraft.

C. VERY HIGH RESOLUTION RADIOMETER

1. Introduction

The very high resolution radiometer (VHRR) is a cloud-mapping radiometer similar to the scanning radiometer, but with markedly improved resolution. The VHRR will give the local real-time user a cloud cover map with 0.5 mile resolution at the sub-satellite point. As with the scanning radiometer, the cloud cover is mapped by a side-to-side scan generated by a rotating mirror. The forward motion of the spacecraft provides the displacement of scan in the direction perpendicular to the mirror scan.

The VHRR will provide a visible channel operating in the limited spectral range of 600 to 700 nanometers. This will provide more contrast than the SR between the earth and the clouds by reducing the effect of haze. The second channel is sensitive in the 10.5- to 12.5-micron atmospheric window. The use of this spectral region permits radiance measurements twice daily of the earths' surface and cloud tops. Reflected solar radiation has no measurable effect on the data in this channel.

In the regular mode of operation, the visible and infrared data are time-multiplexed, so that the earth scan of the infrared channel is transmitted, followed by the earth scan portion of the visible channel. This process is repeated 400 times a minute, which is the scan rate of the VHRR. In the backup mode, when one of the VHRR's is inoperative, the scan data is transmitted on two separate subcarriers. In this mode, the earth scan of both visible and infrared channels occur simultaneously.

In addition to the real time readout of the VHRR approximately 9 minutes of data may be recorded on board the spacecraft and later retransmitted to one of the CDA stations.

A summary of the VHRR characteristics is given in Table VI-2.

TABLE VI-2. VHRR CHARACTERISTICS

Parameter	Visible Channel	IR Channel
Resolution:		
Angular	0.6 milliradians	0.6 milliradians
Ground (from 790 n mi orbit)	0.47 n mi	0.47 n mi
Spectral region	600 to 700 nanometers	10.5 to 12.5 microns
Sensitivity, noise equivalent irradiance	3.7×10^{-11} W/cm^{-2}	4.2×10^{-10} W/cm^{-2}
Dynamic range	65 to 10 KfL (scene brightness)	180°K to 315°K (scene temperature)
Detector	silicon photo-voltaic	mercury-cadmium telluride
Electrical bandwidth	35 kHz	35 kHz
Diameter of optics	5 inches	
Scan rate	400 rpm	
Size:		
Scanner unit (inches)	18.9 × 12.1 × 10.4	
Weight:		
Scanner unit	14.0 pounds	
Electronic unit	6.0 pounds	
Power Requirement:		
Maximum, from -24.5 volts regulated supply	210 milliamperes	

2. Radiometer

Within the radiometer, the radiance information is combined with synchronization signals and certain telemetry data to form a composite video signal. Using both radiometers together, a time-multiplexed signal is formed. Onboard calibration of both the visible and infrared channels is provided within the radiometer.

The composite video as formed in the radiometer for a single scan line is shown in Figure VI-16. The precursor, which appears to precede the line synchronization pulse, actually is a portion of the previous scan line. The function of the precursor is to identify whether the earth scan data which follows is from the visible data and a 18.75 kHz burst, the infrared data. The voltage amplitudes of the precursors are 50 percent of the synchronization pulse amplitude.

The leading edge of the line synchronization pulse is the initial time reference that is used throughout the composite video signal. This edge is in phase with a 300 kHz spacecraft generated signal which is used to time the subsync markers, the voltage calibrator, and the post-earth sync pulse. The line sync pulse occurs at approximately 27 degrees of scan angle (13 milliseconds) before the earth horizon. The actual angle is dependent on the roll attitude of the spacecraft. Two radiance signals are inserted in the space scan between the sync pulse and the location of the horizon. These radiance signals in the infrared channel are for the 240°K and 300°K calibration targets that occur during the back scan, which is blanked out. In the visible channel, there is only the solar calibration target radiance level. These two signals occur 4.2 and 8.3 milliseconds after the start of the synchronization signal.

Two subsync markers are placed in the composite video signal, 30 degrees before and after the nominal nadir. Each marker consists of one cycle of a square wave, first going black and then white. Each half of the marker cycle is 26.6 microseconds in width. The subsync markers start 21.7 and 46.7 milliseconds after the start of the synchronization pulse.

The voltage calibration signal is generated in the radiometer and added to the composite video approximately three degrees of scan angle after the earth-space horizon. The voltage calibration consists of seven voltage levels going from zero amplitude to full amplitude of the signal. This signal may be used to determine the linearity of the communication channel following the radiometer. It does not provide a check on the linearity or the gain stability of the radiometer itself. The zero volt level of the voltage calibration signal starts 58.4 milliseconds after the leading edge of the synchronization pulse.

The post-earth sync is used during the playback of the data from the onboard tape recorder. For this reason, both the leading edge and the trailing edge of

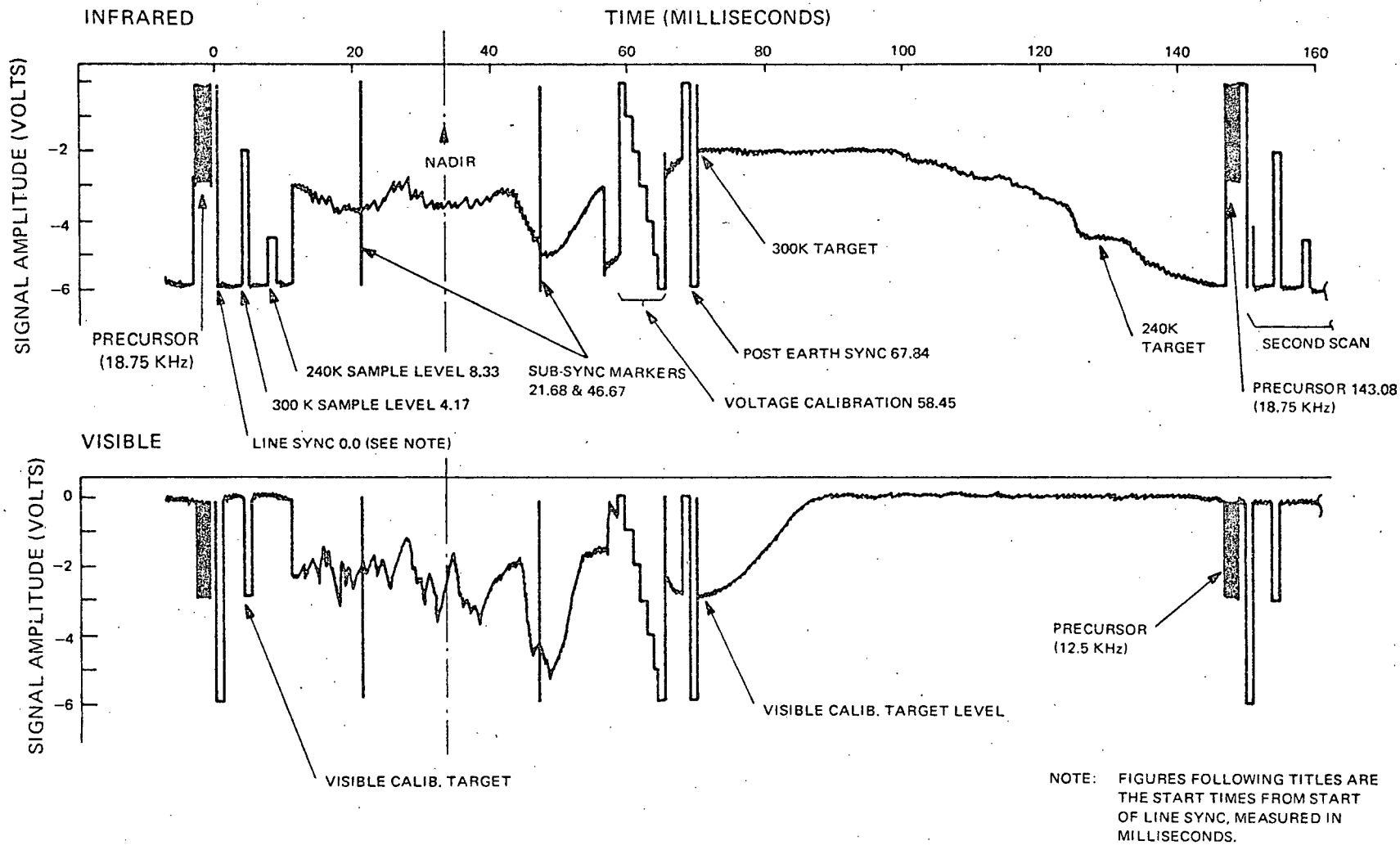

Figure VI-16. Typical Scan Line Showing Timing of Electrically Generated Functions

this signal are clocked from the line sync pulse. The time to the leading edge of the post-earth sync from the line sync signal is 67.8 milliseconds. This signal is a full amplitude pulse.

As stated earlier, the precursor is the last part of the composite video signal. It is clocked to start 147 milliseconds after the line sync signal.

Time multiplexing of the visible and infrared channels is provided by phasing the scan mirror in the two VHRR's 180 degrees apart. One, therefore, scans the earth, while the other looks away from it. When the first completes the earth scan, the second is in position to start it. The visible signal is taken from one radiometer, while the infrared signal is taken from the other. The composite signal of the two channels is shown in Figure VI-17. The radiometer from which the infrared channel data is taken generates a 180-degree index pulse, which is clocked by the 300 kHz spacecraft clock frequency in the same manner as the signals in the composite video. The radiometer producing the visible channel data is salved to this signal so that the line sync signal that it generates occurs at the same time as it receives the 180-degree index pulse from the other VHRR. If the two pulses do not occur simultaneously, the visible channel radiometer changes speed slightly until both pulses do occur simultaneously. When synchronization does occur, the radiometers run from the same spacecraft clock frequency.

The VHRR has an onboard radiance calibration system which may be used to verify or reestablish the calibration of both the visible and infrared channels. The infrared channel has a three point calibration scheme. Space viewed before starting the earth scan provides for a zero radiance point. The other two points, at approximately 240°K and 300°K, are provided by looking at portions of the radiometer housing. These portions of the housing are prepared to have an emissivity of very close to unity. Temperature sensors located in the same regions indicated the actual temperatures. The temperatures of these radiant target areas vary with the spacecraft temperature since they are not actively controlled.

The visible channel is calibrated using a two-point scheme. Zero radiance (black) is obtained by viewing space at the same time the infrared channel views space. A solar illuminated target is provided for the second point of the visible calibration. The intensity of the illumination on this target is calculated by knowing the angle between the sun direction and the normal to the orbit plane. The position of the spacecraft in the orbit at the time that the calibration is obtained is required for the calculation.

Since all the target data occurs in a portion of the scan that is deleted in order to multiplex the visible and infrared channels, it was necessary to electrically relocate this radiance data.

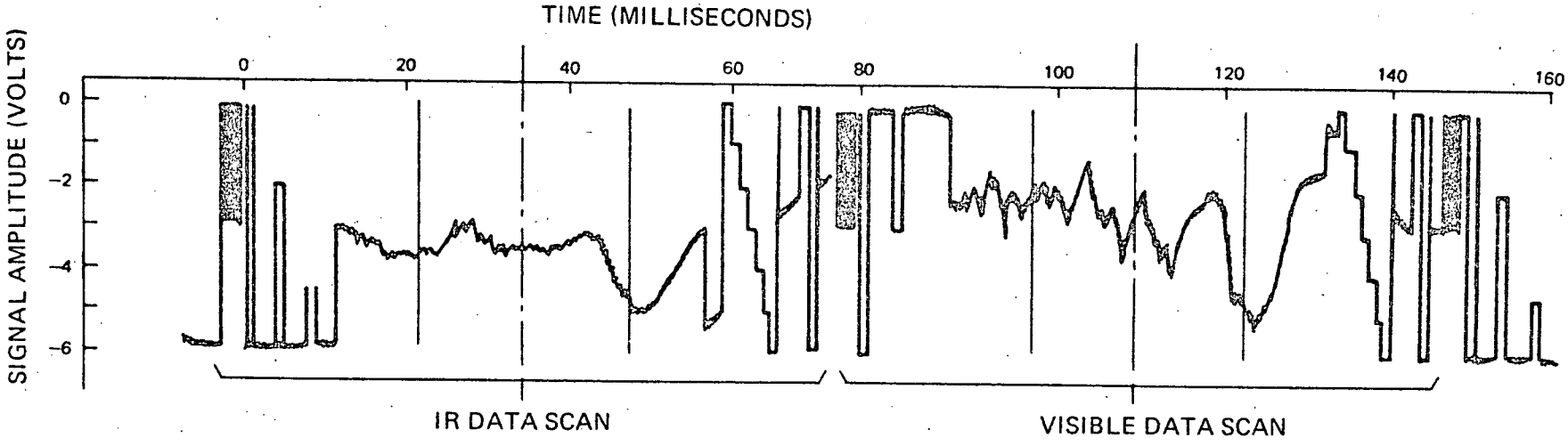

Figure VI-17. Composite Signal of Both IR and Visible Channel

3. Optics

The optical system of the VHRR is schematically depicted in Figure VI-18. The incoming beam of radiation is deflected from the 45-degree surface of the scan mirror to the primary telescope (collecting optics). A Dall-Kirkham optical system, consisting of an ellipsoidal primary mirror and a spherical secondary mirror, focuses the incoming radiation at a point behind the primary mirror. The visible detector is placed at the focus of the primary optics. The radiation reaching the silicon photodiode is limited by a bandpass filter. A dichroic beam splitter reflects approximately 80 percent of the IR radiation which then comes to a focus in the plane of the IR channel field stop. Relay optics are used to reimage the IR radiation on the mercury-cadmium-telluride detector. The relay optics function insures that only a small diameter pencil of collimated radiation is required to pass through a hole in the cooler. The prime objective of the IR bandpass filter is to define the spectral characteristic of the IR channel. In addition, this filter, cooled by its location, limits the radiation entering the cooler which would otherwise heat the detector cold plate. In each channel, the 0.6 milliradian field-of-view is defined by the size of the detector.

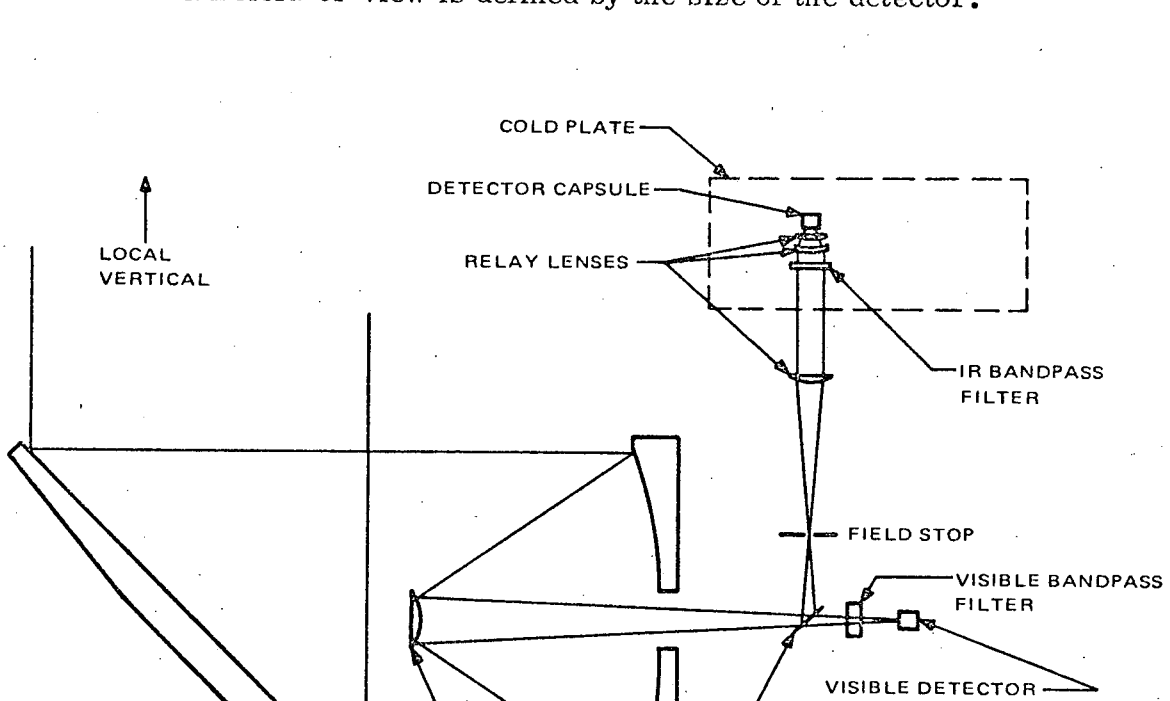

Figure VI-18. Very High Resolution Radiometer, Optics Schematic

The two detectors are fixed during the optical alignment procedure so that they are optically superimposed (i.e., they both "see" the same resolution element on the subsatellite track at any instant). However, since two different radiometers are used to provide the visible and infrared channel data, in the normal mode of operation, there is no attempt to provide registration of the data of the two channels.

Two filters are used in the visible channel to define the 600 to 700 nanometer transmission characteristics. Figure VI-19 shows the relative spectral response of the visible channel as it is calculated for the entire optical system.

The spectral response of the infrared channel is defined by a single infrared bandpass filter. An Irtran window on the detector blocks the long wavelength out-of-band infrared radiation. The calculated relative spectral response of the infrared channel is shown in Figure VI-20.

4. Thermal Design

The infrared detector is cooled to near-liquid nitrogen temperature by a two-stage radiant cooler. A relatively large cooling patch is used to give the

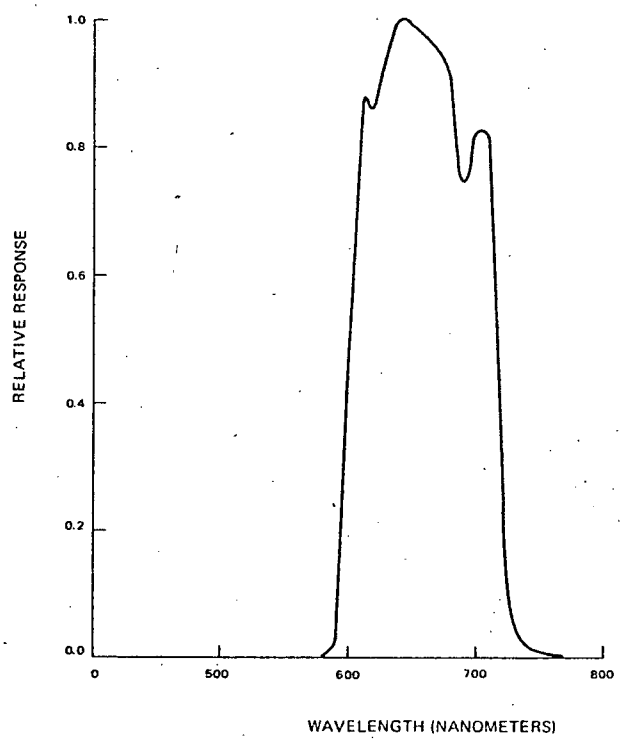

Figure VI-19. Relative Spectral Response of Visible Channel VHRR

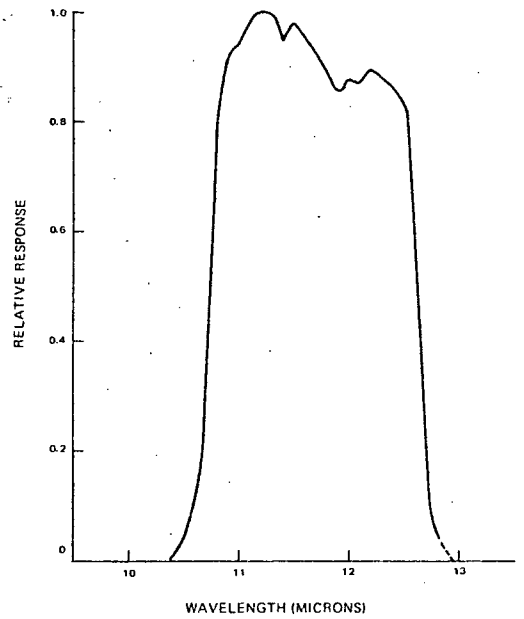

Figure VI-20. Relative Spectral Response of IR Channel of VHRR

high cooling capacity required to permit correct biasing of the detector for the optimum signal to noise ratio. The cooler design is optimized to give the maximum space view from the ITOS orbit.

The housing and portions of the first stage cooler limit the view of the detector cooling patch so that it only views space. The cooling patch is suspended on Kapton bands to minimize the heat conducted into it. Thermal blankets placed within the cooler assembly reduce the radiant coupling between the cooler housing and the patch. The ruggedization of the Kapton band suspension system is sufficient to enable the patch to withstand periods of vibration such as experienced during launch. A truss type construction of the Kapton bands holds the alignment to tight angular limits despite the vibration, and without the necessity to cog the cooling patch.

The thermal characteristics of the VHRR have been evaluated for the case with the scanner and all associated electronics mounted on the outside of the spacecraft. Under these conditions, which assume that the radiometer is covered with thermal blankets, the radiometer would stay with in an operating range of +5 to +45° C. However, further thermal analysis of the instrument is required and it must consider the actual thermal losses of the scan mirror cavity radiating to space.

5. Electronics

A block diagram of the VHRR electronics is shown in Figure VI-21. The input signal to the visible channel from the silicon photodiode is fed into a differential amplifier. The effective resistance that loads the detector is in the order of 10 megohms. The preamplifier feeds a second amplifier which has a treble boost to compensate for frequency roll off of the detector due to shunt capacitance. The dc level is restored each line by comparing the signal received during the space scan with a zero level reference signal. The voltage level needed to correct the space scan signal to zero is held throughout the remainder of the 150 millisecond scan line.

The visible signal with the dc level restored is fed to the visible channel time multiplexer where the synchronization signals and the voltage calibrator signals are added. During the time that these signals are present, the dc restor circuit blanks the radiance signal coming from the detector. Buffer amplifiers are used to isolate the multiplexer from the following 35-kHz low-pass filter. The output of the visible channel low-pass filter is buffered and fed to the second radiometer where it is time multiplexed with the IR signal from that radiometer.

The IR channel differs from the visible channel in two basic areas:

- The nominal impedance of the IR detector is only 10 to 100 ohms as compared to megohms for the visible detector.
- The IR channel is reversed in polarity (i.e., the zero radiance, or cold space, level is at -6 volts, and the output approaches ground or zero at the 330°K radiance level).

To match the low input impedance of the mercury-cadmium-telluride detector, the differential preamplifier is comprised of discrete components. The 2N5042 has an exceptionally low noise figure when operated with this low source impedance. The IC amplifier following the preamplifier has a high gain and also inverts the signal. In the IR channel, the DC restore correction is applied at the inverting input of the differential preamplifier. The space scan signal, however, is compare to a minus 6-volt reference voltage rather than the 0-volt level used in the visible channel.

A separate blanking circuit is used in conjunction with the first IR channel time multiplexer to blank out the detector signal. After sync and calibration voltage insertion, the composite IR signal is buffered and fed to the low-pass filter. The output of the 35-kHz low-pass filter is buffered in the same manner that was used in the visible channel.

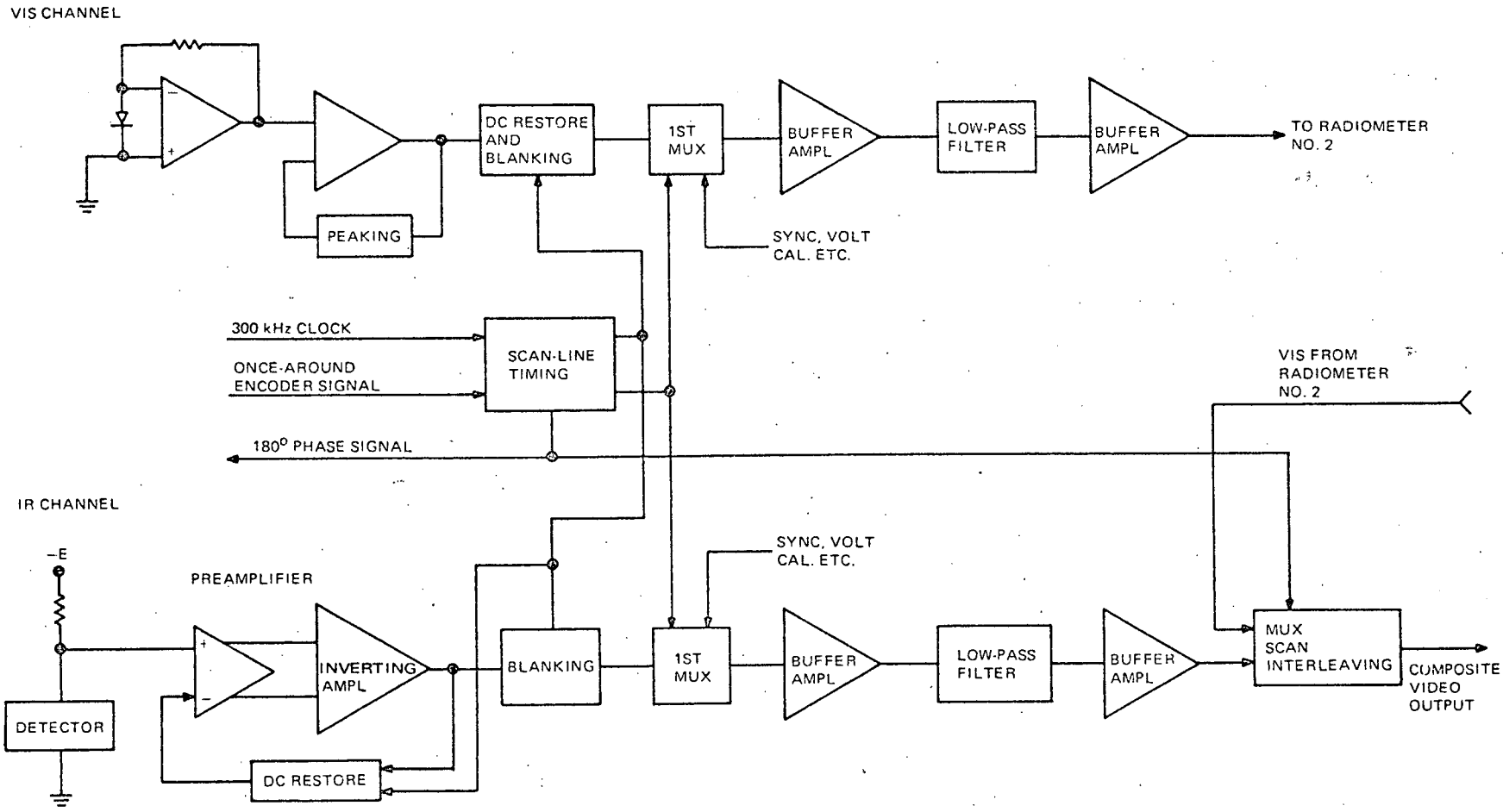

Figure VI-21. VHRR Electronics, Block Diagram

A second time-multiplexer, common to both radiometers, is ued to interleave the IR channel earth scan from radiometer no. 1 with the visible channel earth scan data coming from radiometer no. 2. This multiplexer is powered from a separate -24.5 volt regulated input. In the backup mode of operation, this multiplexer may be powered without having either the timing signals or the IR signal coming from radiometer no. 1. In this event, only the visible channel signal from radiometer no. 2 will be available at the output.

Timing of the various events that occur during a scan line, is initiated by a once around signal taken from an optical encoder. Although this is the same encoder that is used to control the speed of the dc torque motor, the once around signal is derived from a separate track of the encoder. Tests have shown that the once around signal has a revolution-to-revolution pulse jitter of less than 1 microsecond.

In order to locate all function accurately within the scan, timing is derived from a 300-kHz signal generated by the spacecraft clock. The once around signal from the encoder starts the counting sequence. The need to wait from the occurrence of the once around signal until the start of the next cycle of the 300-kHz signal gives rise to a line-to-line jitter of synchronizations signals of ±3.3 microseconds.

Four functions are generated directly by the synchronized pickup pulse:

- The "space" and "ground" pulses, which enable the sampling gates in the ACC circuits during the space scan.
- A pulse, which resets the 16-bit counter at time zero.
- A pulse, which is used as a time reference for phasing the two VHRR scan mirrors.

All other functions are based on a 16-bit digital counter operating from the 300-kHz spacecraft clock. The counter is reset by the synchronized pickup signal so that all counter times are measured with respect to this reset pulse.

Pulse positions for the various functions within the scan line are determined by ten 16-input digital decoders, operating on the primary counter. Table VI-3 shows the decoder functions and their respective time slots with respect to the line sync pulse.

The radiometer is calibrated in orbit by viewing two calibration targets. One of these targets is the 300°K used to calibrate both the visible and IR channels while the 240°K target is only used to calibrate the IR channel.

TABLE VI-3. DECODER FUNCTIONS

Function	Code Ones	Clock Time (MS)	Angle (°)
Line Sync	No Decoder	0	0
Read 300K Target and Nat. Source	11+ (8 - 6)	4.17	10
Read 240K Target	12+ (9 - 7) + 3	8.33	20
Sub-Sync #1	13+ 12+ 9+ 7+ 6+ 4	21.68	52.03 NADIR 82°
Sub-Sync #2	14+ 13+ 11+ 10+ 8+ 6+ 4	46.67	112
Step Calib.	15+ 11+ 8	58.45	140.28
Post Sync	15+ (12 - 8)	67.84	162.81
180° Index	15+ 13+ (11 - 6)+3	75.00	180
Sample 300°K & Nat. Source	15+ 14+ 10+ 8+ (5 - 3)	84.17	202
Sample 240° Target	16+ 13+ 12 + 7+ 5+ 3+ 2	129.99	311.98
Precursor	16+ 14+ 12+ 11+ 7+ 5+ 3	147.08	353

The 300°K target is made of a diffusing optical material which also provides a calibration for the visble channel.

Since the positions of these targets cause the signals to occur during the "black-scan" which is normally blanked to permit time multiplexing the IR and visible data, they are not normally available to the user. Therefore, these segments of the video signal are sampled by three separate sample and hold circuits, and reinserted into the transmitted portion of the video. The termperature of these targets is sensed and transmitted to the ground over the regular housekeeping telemetry system.

Two pulses from the decoders are used to sample the video at the proper locations. (Only two pulses are required since the 300°K and natural source are in

the same position.) The voltage levels are then held until two other decoder pulses at 10° and 20° cause these to be multiplexed into the video output.

A voltage calibration signal is generated to provide a means of calibrating the readout device and to check the linearity of the communication.

This voltage calibration signal consists of six steps one volt apart. It is inserted in the video signal following the earth scan period.

This signal is generated by digital logic in the following manner. Refer to the timing diagram, Figure VI-22. A pulse from the decoder triggers a gating flip flop whose output enables a NAND gate, allowing a 1.17 kHz signal from the primary counter to be fed to a 3 bit counter. The outputs of the three flip flops are fed through offset elimination gates which transform the imprecise logic levels to exact zero or five volt levels. These outputs are then added using a 1-2-4 weighted resistor network. The gating flip-flop is reset at the completion of a full count. The result is the step signal shown in Figure VI-22. The gating flip-flop output is also used to enable the multiplex circuits, so the seventh step never appears in the output.

These pulses are generated by circuits such as shown in Figure VI-23. A pulse triggered flip-flop is turned off by the appropriate decoder pulse. The flip-flop remains in this state through a full cycle of the input clock signal at which time it is reset by the negative transition of the clock. The NOT output is used to gate the clock signal, resulting in a single pulse equal to one half cycle of the clock. This pulse in turn gates six volts into the multiplex circuits. Hence when the true output from the flip-flop gates this level into the video signal a dual, zero to -6 volt, pulse results. The clock inputs are derived from the primary counter: 1.17 kHz for the post sync pulse, and 18.75 kHz for the sub-sync pulses.

The final signal in each scan line is the precursor which "alerts" the ground station that a new line is about to start. This precursor signal also identifies whether the following channel is visible or infrared data. The two frequencies used in the identification scheme are counted down from the 300 kHz clock and fall in the frequency range between 5 to 20 kHz. The frequencies are not harmonically related. The square wave outputs of these counters are fed to the channel multiplexers where they are gated into the video signal as a 2 millisecond burst of frequency, followed by a zero level for 1 millisecond, and then the line sync pulse.

All of the previously discussed functions come together at the 1st multiplexers. There is a separate MUX for each channel. A timing chart of multiplexed scan line is shown as Figure VI-24.

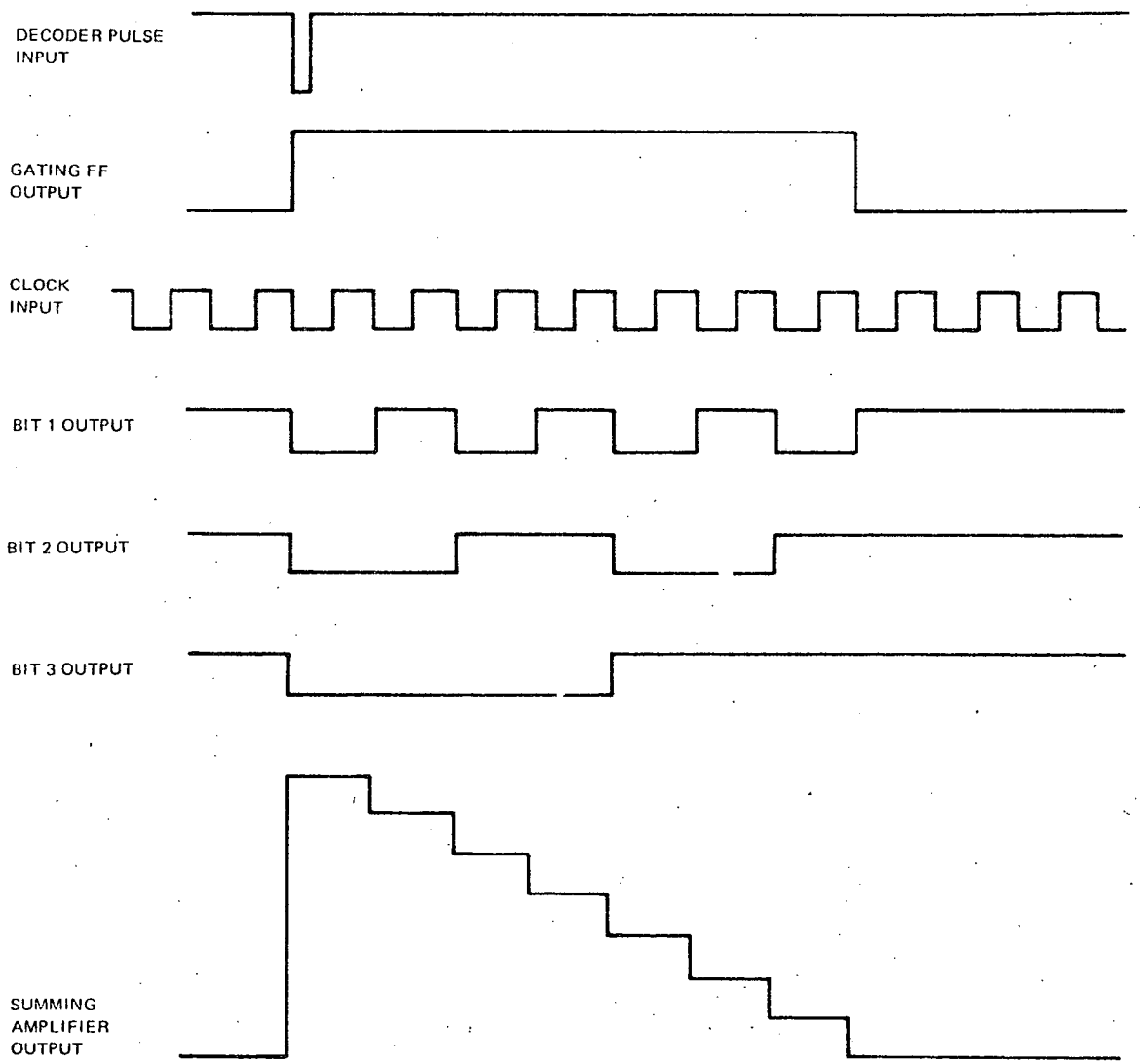

Figure VI-22. Calibration Step Voltage Timing Chart

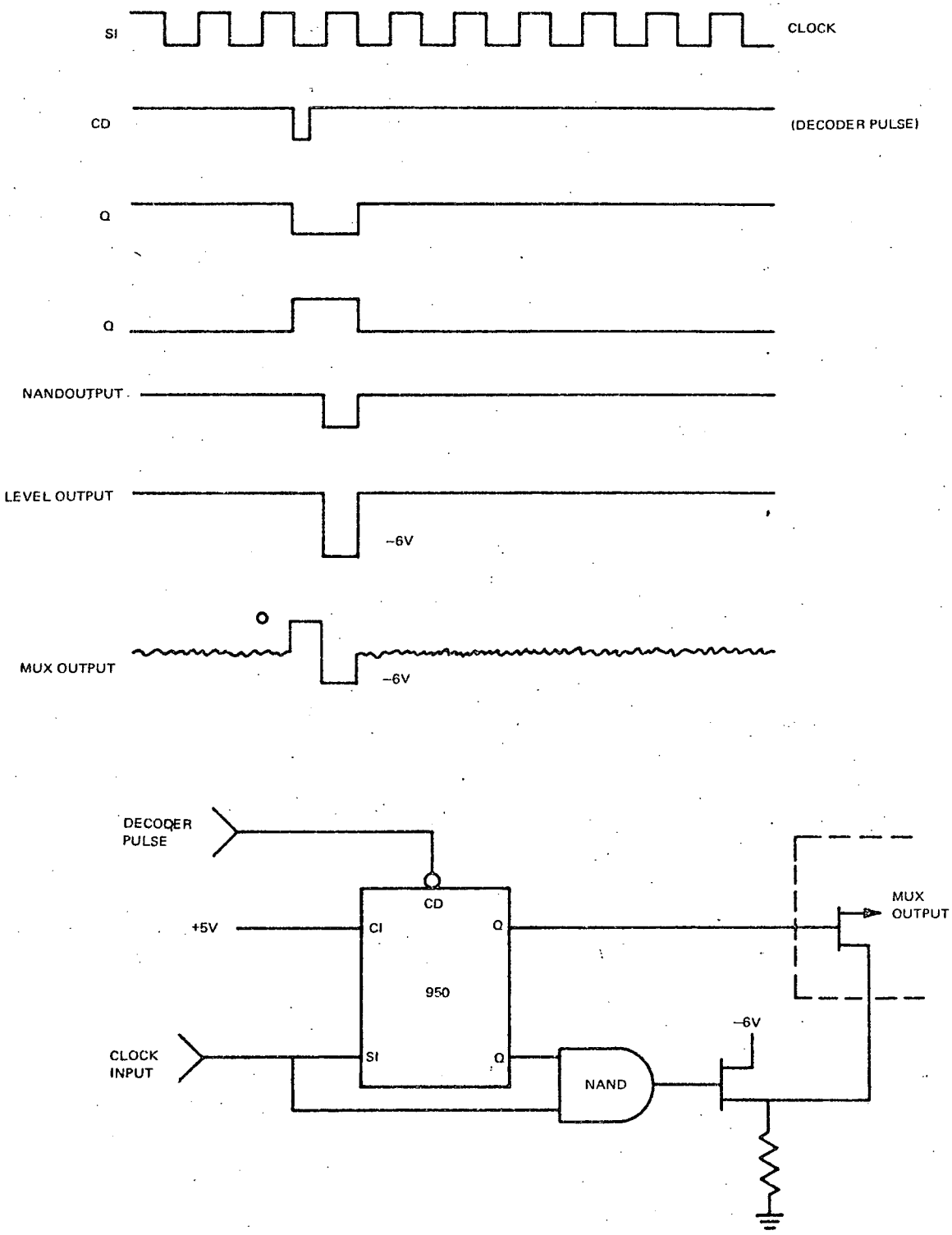

Figure VI-23. Timing Diagram-Dual Polarity Pulse Circuits

Figure VI-24. Typical IR Scan Line Timing Chart

In addition to the signal handling electronics the VHRR has electronics which are used to drive the scan mirror.

The brushless dc torque motor requires phased commutation of its six windings. This commutation is controlled by an optical encoder mounted on the motor shaft. A block diagram of the motor drive arrangement is shown in Figure VI-25.

The scanning radiometer operates at a constant speed of 400 rpm, maintained by a phase-lock loop (see Figure VI-26). A phase detector compares the reference oscillator signal with a velocity track signal generated by an optical encoder mounted to the motor shaft. The phase detector output is a signal whose pulse width is proportional to position error in the normal mode of operation. In slewing mode, the phase detector saturates, causing maximum motor torque. A compensation amplifier smoothes the phase detector output and provides phase shift to stabilize the loop against oscillation. The pulse width modulator adds the error signal to a constant frequency sawtooth signal, and then threshold detects the summed signal. The resulting signal is pulse-width modulated in proportion to the compensated position error signal and then applied to the motor through the logic and drivers.

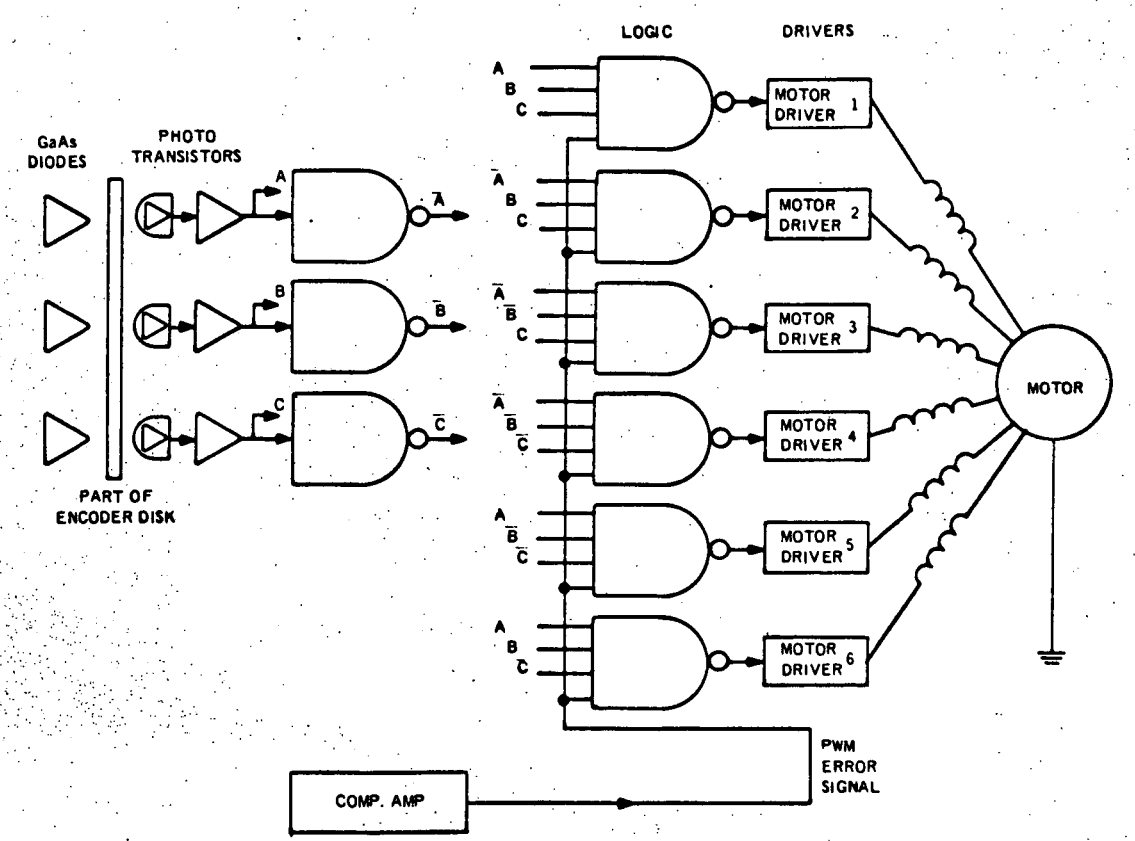

Figure VI-25. Motor Drive, Block Diagram

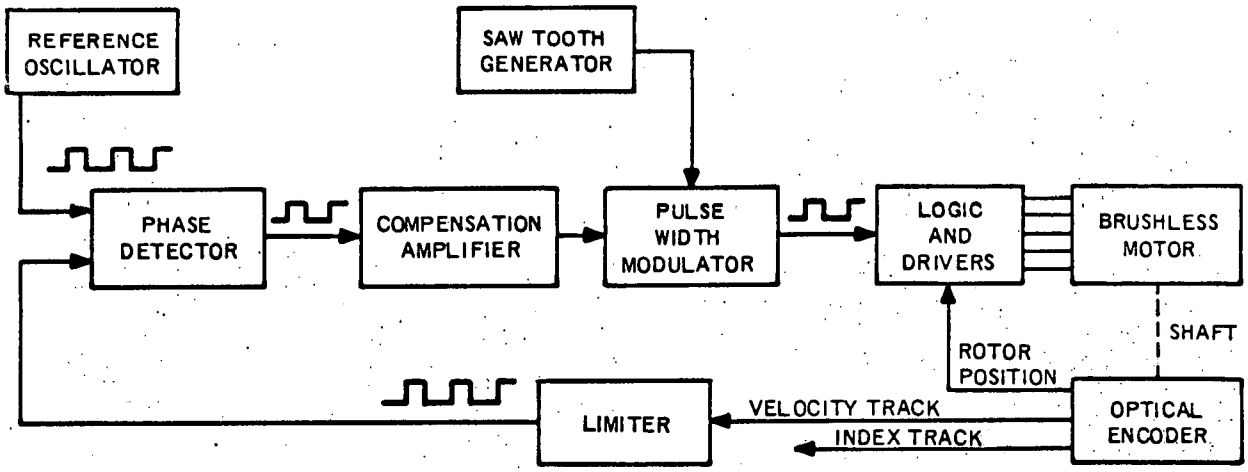

Figure VI-26. Scan Motor Drive System, Block Diagram

The motors driving the two VHRR's on the spacecraft will be phased 180 degrees with respect to each other by adding a position control function to the velocity control loop. When one radiometer is selected to provide the visible signal, the ("visible" radiometer) motor electronics will be slave phased 180 degrees with respect to the radiometer providing the IR signal. Once the 180-degree relationship is established, the control of the "visible" radiometer motor will be returned to its own velocity control loop and phase locked to the spacecraft clock derived frequencies. An error detection circuit assures that the 180-degree relationship is maintained. An error in phase will automatically cause the "visible" radiometer to rephase.

6. Mechanical Design

The VHRR has four general mechanical areas within the one unit.

- Scan Drive Assembly
- Optics assembly
- Calibration target assemblies
- Electronics packages

The scan drive assembly consists of the scan mirror and the drive motor. The beryllium scan mirror is designed to operate at more than twice the present 400 r/min rate, with no degradation in system response.

The motor that drives the scanning mirror is a brushless dc torque motor having eight poles (4-pole pairs) in a pancake configuration. Six windings are distributed in 48 slots. The motor has a torque sensitivity of 9 oz-in per ampere, with maximum stall torque of 20 oz-in. At -10°C, the predicted torque to drive the rotating assembly is 2.0 oz-in, which indicates a torque margin of 9:1 at this extreme case.

Use of this motor eliminates five bearings and several gear trains that would be required if a synchronous motor were used.

A view of the motor is shown in Figure VI-27. The spindle is mounted in two preloaded bearings located near the center of the rotating mass. A labyrinth seal is provided at each end of the bearing housing. The bearings are lubircated with G300 silicon grease. This simplification is permitted since gears are not used and a vapor lubrication system is not necessary. The lubricant has been tested for 9600 hours at a pressure of 2×10^{-8} mm Hg and temperatures to 220°F with

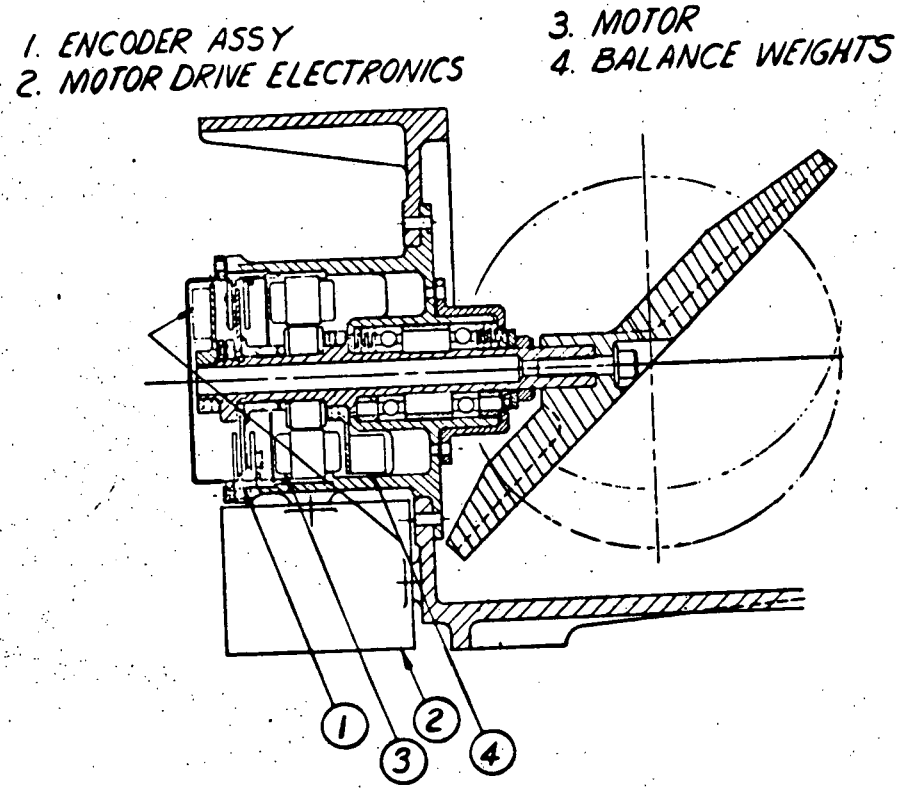

Figure VI-27. Brushless Dc Torque Motor Drive

negligible degradation of the bearings, according to information supplied by the manufacturer, General Electric, and as subsequently verified by a report published by the Lockheed Company Missile and Space Division.

The primary optics are housed in a magnesium barrel with any metallic constraint of the fused-silica optical elements carefully avoided. The primary mirror is located in a bore in the housing which is slightly oversize to allow for thermal variations. A groove is cut around the bore and after the mirror is positioned the groove is filled with RTV 566 through four filling ports. The silastic material flows around the groove, filling also the clearance between the housing and the O.D. of the mirror.

The secondary mirror is bonded into the mounting spider using a strain-free adhesive. A thin-wall invar tube separates the primary mirror and the secondary spider. The tube slides in the telescope housing with a small clearance to allow different thermal expansion rates. Invar, having a near-zero coefficient of expansion, maintains the critical separation between the two mirrors over the specified temperature range. End constraint to the assembly is provided by an "O" ring in the face of a metal clamp plate.

Following the optical assembly and alignment, the clearance around the invar tube is filled with RTV 566 to avoid metallic contact during vibration, preserving the integrity of the assembly.

The sensor housing locates accurately over the telescope housing. The spectral beam splitter, relay optics and electronics module are contained in the sensor housing assembly. A mirror mount, located in the bore of the housing, positions the dichroic beamsplitter and mirror. Axial and rotational adjustments are provided in the mirror mount to align the two channels. The first element of the relay system is mounted in the tube shield leading to the passive cooler, and has focusing provisions. The cooler assembly containing the relay optics and the detector is rigidly attached to the mounting-bracket extensions on the sensor casting.

The 300°K solar calibration target and the 240°K target comprise the calibration target assemblies. The 300°K solar calibration target is mounted in the scan cavity on the side towards the spacecraft thermal fence. In this location the target is illuminted during a portion of the orbit by direct sun light.

The 240°K target is a detachable part of the scanner unit. This target is radiation cooled to approximately 240°K. The actual temperature of the target is measured by temperature sensors and telemetered over the regular housekeeping telemetry system. The target consists of an aluminum plate covered with second surface mirrors. It is conductively coupled to the outer housing of the detector cooler through the structure of a 35 square inch second surface mirror which is capable

of maintaining both target and detector housing below 250°K. The target, mirror, and detector housing are all conductively isolated from the radiometer, and insulated, except for control surfaces, from the space environment by the same multifoil insulation as used on the TIROS M spacecraft. The 240°K target fits into the scanning cavity of the radiometer.

The electronics modules are mounted on the radiometer unit to form a one piece assembly. Two separate modules house the electronics. The detector and signal electronics are in the first unit which is attached to the sensor housing. The module is housed in an aluminum can measuring 8 × 5 × 3 inches. Five double-sided and one multilayer printed circuit boards are mounted in an elastic suspension system which provides positive vibration isolation for the board-mounted electronics. The boards engage card-edge connectors which provide an interconnection plane between the boards. All external connections are through Cannon gold-plated "D"-type connectors, mounted to the housing and hardwired to the module connector board.

The motor electroncis are housed in the second module. The packaging concept for this module is identical to the first module. A 6 × 2 × 2.5 inch can is mounted adjacent to the motor drive housing to minimize wire lengths. Three double-sided printed circuit boards contain the motor drive circuit components.

The weight of the VHRR is estimated at less than 20 pounds.

D. VERTICAL TEMPERATURE PROFILE RADIOMETER

1. Introduction

The vertical temperature profile radiometer (VTPR) is designed to make radiance measurements in the 15-micron carbon dioxide band that will permit ground computer calculation of the vertical temperature profile from the earth's surface to an altitude of 100,000 feet. An 11-micron clear window radiance measurement and a 19-micron rotational water vapor band measurement are used in conjunction with six carbon dioxide measurements to evaluate the amount of cloud cover. The radiometer step scans the earth scene below the satellite across the orbit track over an angle of ± 31.45 degrees with respect to the Nadir. Since daylight radiance measurements have the same accuracy as those made at night in this spectral region, the measurements are made on a continuous basis, day and night, over the complete earth.

Two VTPR's are carried on each spacecraft to provide fully redundant sensors for the system. Each VTPR consists of an optical system, a detector and associated electronics, and a scanning mirror drive system, all housed in one package. The VTPR is mounted within the spacecraft structure in a manner which permits the instrument to scan an unobstructed "crosstrack" field-of-view of ± 31.45 degrees from a nominal altitude of 790 nautical miles.

As each spot is scanned, the optical system collects, filters, and detects the radiation from the earth in eight spectral intervals for the same spot. Image motion compensation is used in order to obtain data from each of the eight spectral filters for each spot scanned. The associated electronics amplifies the video signal and synchronizes it with the spacecraft digital data processor.

Periodically (every 10 to 20 minutes), or upon ground command, the VTPR enters a self-calibrate mode in which its sensors view space (about 4°K) and an internal target (about 300°K, but whose exact temperature is telemetered), and in which a voltage calibration is inserted. The self-calibrate mode may be inhibited by ground command. The VTPR will return to the self-calibrate mode within 1 minute after receipt of a Calibrate Enable command.

Telemetry circuits provide information for determining the calibration reference and for monitoring the operating conditions of the radiometer.

2. System Characteristics

a. SCAN MODE

(1) SCAN MIRROR DRIVE (MECHANICAL)

A single-faced, pivoted mirror, driven by a stepper motor, deflects the radiometer's instantaneous field-of-view across (perpendicular to) the orbit plane. The total ±31.45 degree "crosstrack" field of view is covered in 23 discrete steps established by the stepper cam. The 23 cam "plateaus" are designed such that the stepper motor can overshoot its homing point by a maximum of 1.75 degrees without causing any angular deviations of the mirror. Radiometric data is sampled in each of eight spectral regions while the mirror remains on one plateau. (See paragraphs 2.a(2) and 3.) On the 24th step of the cam, the cam follower drives over a "cliff" and causes the scan mirror to retrace to the low point of the cam. The retrace takes the equivalent of 2 more spots.

In order to keep the cam follower on the cam surface at all times, a spring provides a 2.5 inch-ounce torque to the mirror in the appropriate direction. This generates a requirement for retrace damping to cushion the impact of the scan mirror on the mechanical stop at the end of its retrace. However, the implementation of such damping must not prohibit the scan mirror from pivoting about an axis orthogonal to the scan axis so as to view cold space and the calibration patch during the time of inflight calibration.

The required retrace damping is achieved using an Aeroflex TQ-10W torquer, with a mechanical linkage that allows the torquer motor to be mounted on the baseplate without interfering with the calibration sequence. In this configuration, retrace damping is accomplished by applying a torque to the mirror that counteracts

the torque produced by the 2.5 inch-ounce spring on the scanning mirror. The torquer, which is activated by the signal from a reed switch identifying the beginning of the scan retrace, applies damping torque for a fixed time (established by empirical tests). By reducing the voltage input versus time, the torque is then allowed to decay slowly. In this way, the mirror is allowed to approach its stop slowly, in a controlled manner.

(2) SCAN MODE OUTPUT DATA

During each of the 23 data steps, the viewed spot of the earth is sampled over eight discrete IR filtered spectral intervals. Each of these samples is called a filter. (See paragraph 3.c for filter characteristics.)

The analog data obtained for each filter is digitized and stored in an output register as a 15-bit word. Ten bits are used for data and 5 bits for a self-contained position identification code. The data is clocked out at a 512 pps rate by the spacecraft, LSB first, with the identification bits coming at the end. A 16th bit is added by the digital data processor (DDP) in the spacecraft as a parity bit. The digital data stream is recorded and subsequently transmitted to the ground via the S-band link.

The VTPR output line format is shown in Figure VI-28 and can be broken down as follows:

- 4.8 lines per minute (12.5 sec. per line)
- 25 spots per line (23 data and 2 retrace)
- 0.5 second per spot
- 8 filters per spot
- One word per filter

b. CALIBRATION MODE

A method of periodically checking the calibration of the radiometer while in orbit has been provided. Upon ground command, or once every ten to 20 minutes (depending upon the selected calibration mode), immediately after the completion of a line, the radiometer automatically enters a self-calibration mode. This mode consists of the voltage and temperature measurements shown in the calibration data sequence of Figure VI-29. After a single series (total time of 37.5 seconds), the calibration ends and the data mode is reentered for another ten to twenty minutes.

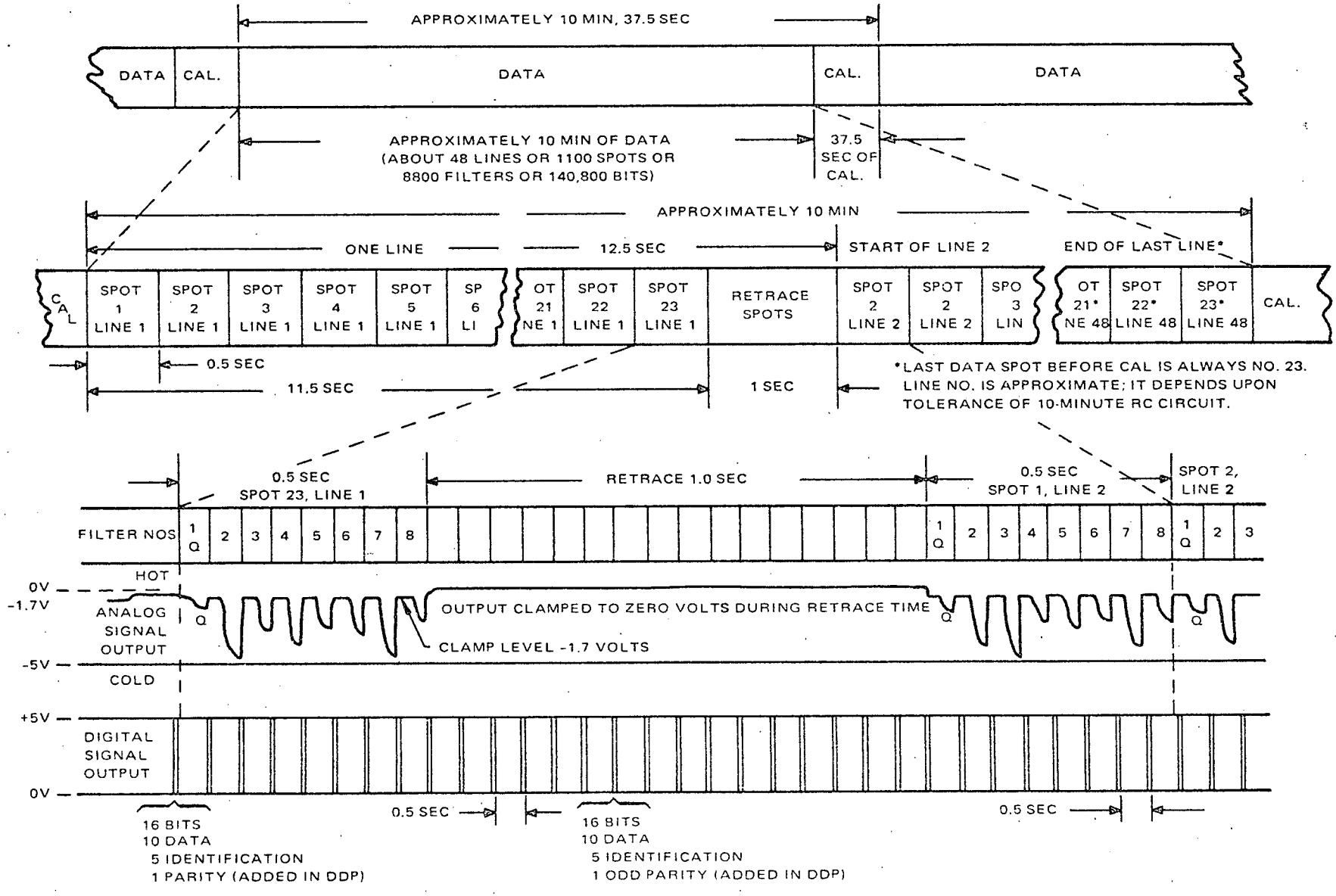

Figure VI-28. VTPR Outputs

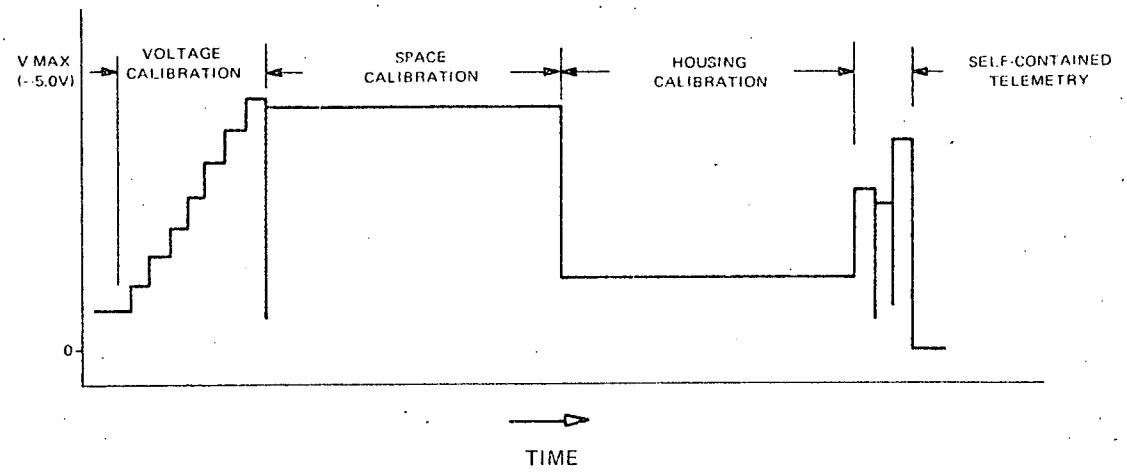

Figure VI-29. Full Calibration Sequence

(1) CALIBRATION DATA

The following calibration data is generated during the calibration sequence, digitized, and inserted in the data stream in place of the thermal video.

- Voltage calibration (electrical). An eight-step staircase, increasing in amplitude, is generated electrically at the start of the calibration sequence. Each step has a 500 millisecond duration, with voltage levels as shown in Table VI-4. The staircase is inserted into the signal near the output of the detector.
- Space calibration. During the space calibration (16 seconds), the scan mirror is pivoted 60 degrees from the local vertical to allow the detectors to view deep space at approximately 4°K. This temperature is used as a black level reference.
- Patch calibrations. For the next 16 seconds, the scan mirror is pivoted 130 degrees so that the detectors view a blackened portion of the radiometer housing at approximately 300°K. This temperature is measured to an absolute accuracy of 0.1°C. The temperature of the patch is also sensed electrically to an accuracy of 0.1°C by a linear temperature telemetry sensor.
- Other self-contained telemetry. During the last 1.5 seconds of the calibration sequence, the output of three temperature sensors is digitized and inserted in the data stream in place of the sensor data. The temperatures of the patch, shroud, and detector are each monitored for a half second period to an accuracy of 0.1°C.

TABLE VI-4. VOLTAGE CALIBRATION LEVELS

Step Number	Voltage (volts)	Tolerance (volts)
1	-1.80	±0.05
2	-2.23	±0.05
3	-2.66	±0.05
4	-3.09	±0.05
5	-3.52	±0.05
6	-3.95	±0.05
7	-4.38	±0.05
8	-4.81	±0.05

(2) CALIBRATION MIRROR DRIVE (MECHANICAL)

Feuralon sleeve bushings are used for the pivoted mirror which must operate in the space vacuum. In operation, the pivoted scan mirror must move between the fixed angular positions named above.

- Measurement position. Parallel to the local vertical.
- The space calibration and electrical calibration position. 60 degrees from the local vertical.
- The radiometric calibration position. 130 degrees from the local vertical.

The scan mirror is pivoted by an Aeroflex TQ-R5-W torquer, which provides ± 70 degrees angular travel without the use of brushes or twisting wires, and provides 4 inch-ounces of output torque over this range with only 4 watts input. A spiral spring is used to return the pivoted mirror to its measurement position at the end of each calibration sequence.

The angular orientations of the pivoted mirror for the measurement position and for the radiometric calibration position are accurately established by mechanical stops. However, the space calibration/electrical calibration position must be maintained with reasonable accuracy at an elevation angle of 60 degrees from local vertical to prevent the VTPR field-of-view from seeing the horizon edge of the earth or the radiometer housing. This middle-position angular orientation

accuracy is achieved by a "movable center stop" technique which operates as described in the following paragraphs.

A spiral spring having an essentially constant 1 inch-ounce torque over a 90 degree angular travel applies this 1 inch-ounce torque in a counterclockwise direction to the pivoted mirror-Aeroflex torquer assembly. With no voltage applied to the torquer, this spring holds the pivoted mirror against one mechanical limit stop in the measurement position. For the space calibration sequence, a voltage is applied to the Aeroflex torquer which produces a torque of approximately 1.25 inch-ounce. This will cause the pivoted mirror to slew over by 60 degrees until it hits the movable mechanical stop which, in turn, is held against a fixed stop by a linear expansion spring. This linear spring is set so that it exerts a counterclockwise torque on the movable stop of 1 inch-ounce. Therefore, it can be readily seen that, for the space calibration sequence, the mirror will be accurately maintained at a plus 60 degrees elevation angle, because the combined counterclockwise torque produced by the spiral spring and the linear spring is 2 inch-ounces while the clockwise torque (T_c) produced by its voltage input is $1 < T < 2$ inch-ounce. Since the movable stop is restrained from counterclockwise movement by a fixed stop, this mechanically establishes the space orientation to within ±0.1 degree without requiring tight tolerances on either the spiral spring or the linear spring or the voltage input to the torquer.

For the radiometric calibration sequence, a voltage is applied to the torquer which will generate more than 2.5 inch-ounce of clockwise torque, thus pushing over the movable stop until the fixed stop in the radiometric calibration position is reached. The linear spring is so arranged as to produce a "semi-toggle" action which will tend to assist the mirror in reaching the second stop. However, it will not prevent the mirror from returning to its measurement position when all clockwise torque is removed from the torquer. In order to cushion the impact on the measurement stop during the retrace period, the applied voltage to the torquer will be reduced exponentially (capacitor discharge) so as to cause the retrace to occur at a relatively small angular velocity.

c. SYSTEM OUTPUTS

The VTPR provides both a digital and analog thermal video output signal, as well as telemetry outputs, test point voltages, and mirror and filter synchronization signals.

(1) SENSITIVITY AND RADIOMETRIC ACCURACY

The relative error between any two spectral channels has a one sigma value less than or equal to 0.25 erg/(cm^2 sec sr cm^{-1}) except for the channel at 668.5 cm^{-1} which may have an error, relative to the other channels, with a one sigma value less than or equal to 0.5 erg/(cm^2 sec sr cm^{-1}).

The absolute error of any channel has a one sigma value less than or equal to 1.0 erg/(cm^2 sec sr cm^{-1}).

(2) DYNAMIC RANGE

The radiometer is capable of providing calibrated radiance measurements of surface temperatures ranging between 0 and 220 ergs/ (sec cm^2 sr cm^{-1}). (Approximately 4° to 340°K.)

(3) THERMAL VIDEO CHANNEL OUTPUTS

The analog channel output signal is composed of the amplified and clamped detector output thermal video which is periodically mixed with the voltage calibration and temperature sensor voltage. The thermal video part of this signal is composed of the signals resulting from the earth scan. During the calibration mode, the thermal video is a measurement of the space above the horizon, and the inside of the radiometer housing (patch) as appropriate. Only one of the signal components will appear at the output at a time. The analog output signal is obtained after amplification, but before the analog-to-digital converter. The analog data can be transmitted in real time via the beacon link (160 Hz bandwidth) for engineering evaluation.

The digital channel output is a digitized replica of the analog channel output. The digital output level is time-phased to the word enable signals from the spacecraft's digital data processor (DDP). The line format of the output data is discussed in section 2.a(2), and shown in Figure VI-28.

Dual buffered digital outputs are used. There is sufficient isolation between these outputs to assure that a short or open circuit on one line will not compromise the performance of the second line.

All digital data is non-return to zero (NRZ), with a +5 volt output level denoting a data "one" and 0 volts denoting a data "zero." Between words, the VTPR digital output is zero volts.

(4) SYNCHRONIZING SIGNALS

A scan flyback signal is generated at the transition that occurs when a scan line is completed and the mirror starts to fly back to start another scan line. This signal occurs during the first 500 milliseconds of the flyback and is repetitive to 12.500 ± 0.001 seconds.

(5) TELEMETRY

Three self-contained telemetry signals (patch, shroud, and detector temperatures) are monitored, digitized, and inserted in the thermal video signal. The remaining "housekeeping telemetry" is supplied directly to the spacecraft

telemetry commutator. This telemetry includes the electronics temperature, electronics input power, calibration mode verification, chopper and filter wheel PRP monitors, and patch calibration status.

3. Optical System

The VTPR optics consists of a scanning mirror, a telescope, a rotating series of optical filters, a chopper, and a detector. The radiation from the scene is focused by a spherical mirror onto the detector after passing through a chopper and a filter. The spot-chopper-filter phasing is such that the scan mirror steps from one position (spot) to another just before the Q-branch filter is put into the optical path.

Figure VI-30 shows the configuration of the instrument. The optics are composed of a single Cassegrainian-type optical telescope with an f/3 optical speed and an entrance aperture of 2.6 inches diameter. This spherical-spherical system (i.e., spherical primary and spherical secondary) results in a worst-case optical aberration of approximately 3.4 milliradians at the corners of the field. The relatively slow f/3 optical speed, chosen for the primary, minimizes the spectral spreading produced by having rays of variable angles of incidence impinging upon the optical filters. With an f/3 convergent bundle, the maximum spectral spreading produced by the unobscured bundle is 1 cm^{-1}. The primary is fabricated using an electro-form technique because this results in the lowest over-all cost and, more importantly, maximizes the space allowable behind the primary mirror for placement of the chopper and filter wheel in the prime focus.

The field lens-pyramid configuration images the secondary mirror on the image polyhedron. This serves to minimize adequately the amount of stray optical rays from outside the VTPR field-of-view, which can reach the detector without requiring the use of additional black baffles. (Black baffles in the primary optics of the VTPR are not desirable since the baffles are "radiometrically chopped". If their temperature changes or is unknown, their emission could cause serious radiometric errors.)

a. FILTER WHEEL AND CHOPPER

Situated near the focal plane of the primary optical system is a two-bladed black chopper and an eight-element filter wheel. The chopper and filter wheel are geared together and driven by a chopper motor and gear box similar to that used in the NIMBUS MRIR. The "wick" lubrication technique is used on the drive motor and bearings. The chopper rotates at 8 rotations per second. The chopper is mechanically phased to the filter wheel so that it covers the 0.22- x 0.23-inch (2.136 degree x 2.236 degree) instantaneous field stop while the field stop views the demarcation zone between two adjacent filters. The chopper thus provides a 308°K reference for that period. In other words, the time that

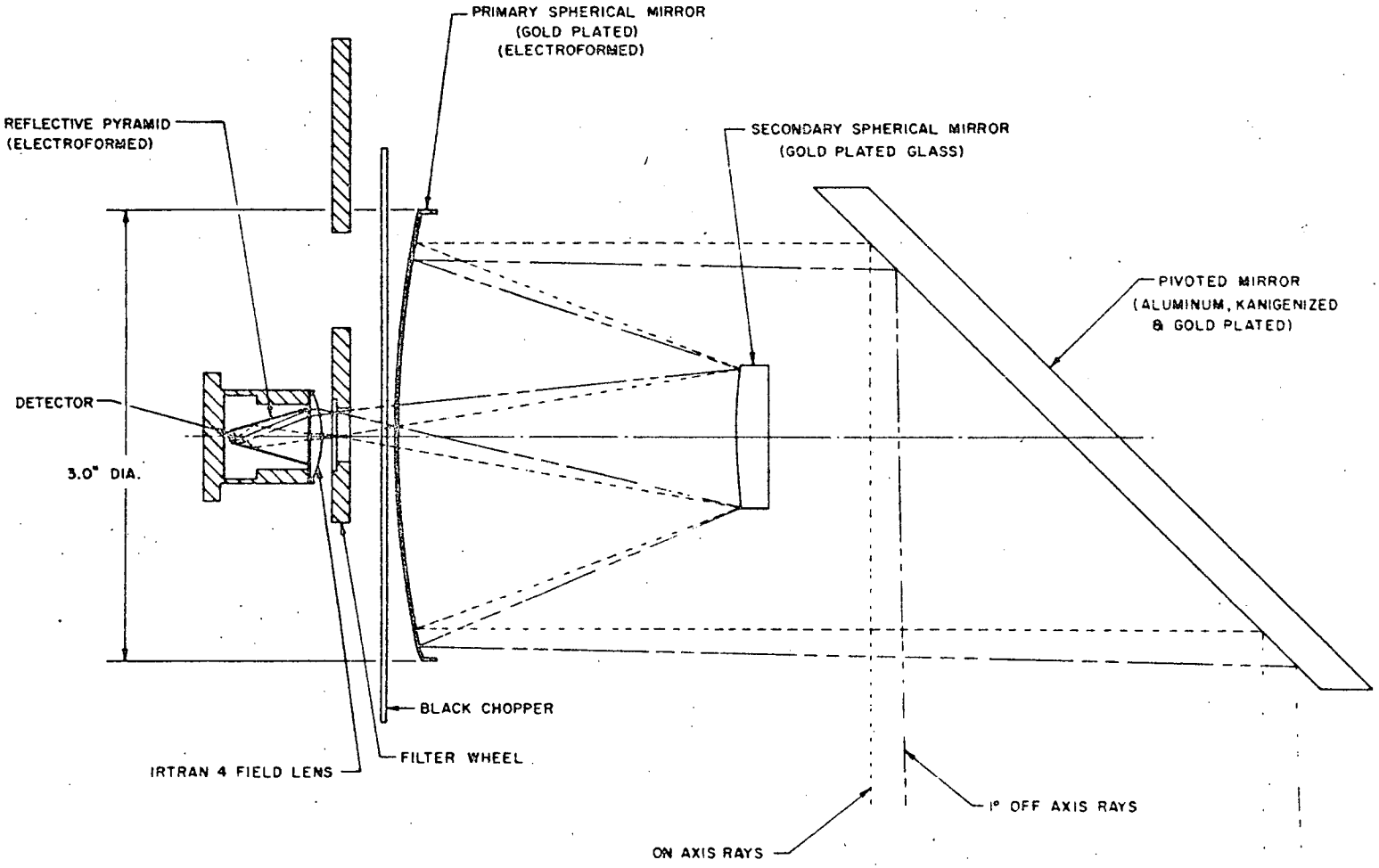

Figure VI-30. VTPR Optics

the chopper is in front of the field stop is set equal to the time taken by the field stop to effectively "move" from a position fully within one filter to a position fully within the successive filter. This raises the chopping frequency of the system to 16 Hz, where the 1/f noise component of the system is considerably less than would be the case if a 308°K reference were provided only once per 8 filters.

The filter wheel is situated in the focal plane and is temperature controlled, since the center wavelengths of all filters shift by approximately 0.1 cm^{-1} per °C. To accomplish this, the filter wheel must be enclosed by a radiative heating shroud. Furthermore, the chopper, which is also shrouded to stabilize its temperature, must be situated ahead of the filter in the optical path. Both of these elements are situated behind the primary mirror. The IR filters are used to limit the spectral bandwidth. The transmission characteristics of these filters are shown in Table VI-5.

b. FIELD-OF-VIEW

The field-of-view can be considered in three parts; the "elemental field-of view, the "scanned field-of-view", and the "calibrate field-of-view."

The "elemental field-of-view" is defined as the solid angle bounded by the points where the detector voltage response to a point source is 1 percent of the maximum obtained when the source is located on the axis defined by the telescope assembly and the scan mirror plane. The dimensions of the "elemental field-of-view" of the primary optics are 2.236 by 2.236 degrees, of which, at any time, a 2.136 by 2.236-degree field is viewed. The viewed field dimensions result from the use of an image motion compensation (IMC) technique, combined with the use of 8 filter channels in the VTPR. The IMC assures that the 8 filter sampled areas are superimposed to within 1 percent for a spot duration.

The "scanned field-of-view" will cover the earth scan angle range of 31.45 ±2 degrees in 23 steps from the nadir point in a cross track direction. The distance between two contiguous spots is 2 degrees, 44 ± 5 minutes, including mechanical jitter.

4. Operation of Electrical Circuits

An electrical block diagram of the VTPR is shown in Figure VI-31. A brief description of the electrical circuits is given in the following paragraphs. More detailed information can be found in the Barnes Engineering Design Evaluation Reports, issued in October, 1969, Part IV, Description of Operation.

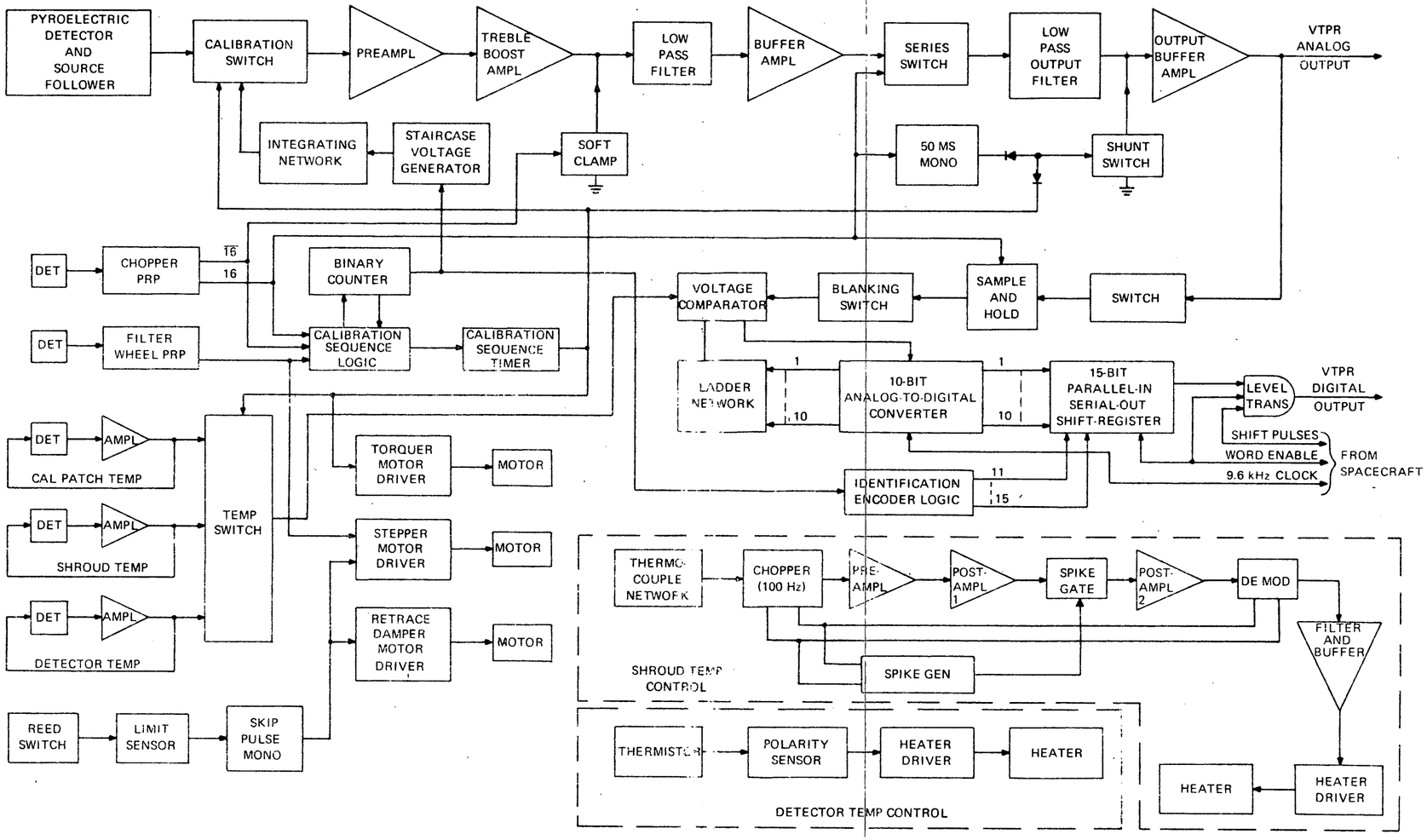

Figure VI-31. VTPR Block Diagram of Electrical Circuits

TABLE VI-5. RADIOMETER FILTER CHARACTERISTICS AT 35°C

Filter No.	Center of Spectral Response (cm^{-1})	Bandwidth and Tolerance		Relative Sensitivity
		50% Response (cm^{-1})	10% Response (cm^{-1})	(erg/sec cm^2 sr cm^{-1})
1 (Q Branch)	668.5 ± 0.5	3.5 ± 0.5	10.5 ± 1.5	0.50
2	677 $^{+2}_{-1}$	10.0 ± 2.5	20 ± 5	0.25
3	695 ± 1	10.0 ± 2.5	20 ± 5	0.25
4	708 ± 1	10.0 ± 2.0	20 ± 4	0.25
5	725 ± 1	10.0 $^{+1.0}_{-2.0}$	20 $^{+2}_{-4}$	0.25
6	747 $^{+2}_{-1}$	10.0 ± 2.5	20 ± 5	0.25
7	535 ± 1	10.0 $^{+1.0}_{-2.0}$	20 $^{+2}_{-4}$	0.25
8	835 ± 1	8.0 ± 1.0	16 ± 2	0.25

a. DATA CHANNEL

The output of the pyroelectric detector is fed into a low noise, low leakage field effect transistor (FET) source follower, which is in the same housing as the pyroelectric detector. A 10^{12} ohm resistor is placed across the detector to reduce the effects of FET leakage current on its bias point. The output of the source follower is fed into the preamplifier.

The circuit configuration of the pyroelectric detector provides for automatic repoling of the detector in case of an extreme temperature rise (greater than 47°C) in the ambient environment. Repoling is achieved since the circuit normally maintains a fixed bias voltage across the pyroelectric element.

The preamplifier consists of a discrete four-transistor stage utilizing an extremely low-noise FET as the input transistor. The input transistor has a measured noise figure of less than 1 dB at the VTPR chopping frequency of 16 Hz. The midband gain of the preamplifier is set to 40, with a low frequency break at 0.08 Hz.

During the electrical calibration sequence, the staircase generator output is fed through the signal electronics, and the coupling of the pyroelectric detector signals into the preamplifier is inhibited. As a result, the electrical calibration signals fed into the preamplifier are not affected by the radiometric input. The output of the preamplifier is fed into the treble boost amplifier.

The treble boost amplifier consists of a unity gain operational amplifier and feedback network wh ich provides the required frequency response characteristic (6 dB per octave rise to 700 Hz, followed by a 6 dB peroctave rolloff). The output of the treble boost amplifier is then fed into a soft clamp.

The purpose of the soft clamp is to clamp the signal output of the treble boost amplifier to ground when the input radiance is the same as that of the black chopper. This is achieved by; closing the soft clamp switch every time the detector sees the chopping wheel and allowing an integrating capacitor in the low pass filter to chage the resulting signal voltage, and by opening the clamp switch every time the detector views the scene.

The output of the soft clamp feeds a low pass RC filter with a break point at 16 Hz. The reason for this circuit configuration and for the shunt switch across the integrating capacitor is to reduce the cross coupling error between adjacent filter channels and thus ease the ground data reduction complexity.

The output of the soft clamp is buffered by a unity gain operational amplifier. In addition to the shunt switches, a series switch is also provided, following the buffer amplifier. The switch is opened when the shunt switch is closed and vice versa. As a result of this complementary action, no noise is fed into the following low pass output filter, when the detector is not viewing the earth.

The low pass output filter (quasi-sample and hold circuit) is an RC network with a 90 millisecond time constant, whose value was obtained by optimizing the VTPR signal-to-noise ratio. The output of the low pass output filter is shorted to ground during two events. During the calibration sequence, the temperature sensor readout input causes a 3 second short. The second input comes from the output of a 50 millisecond monostable multivibrator, which is triggered by the 16 pulse-per-second output of the chopping wheel phase reference pickup (PRP). This causes the shorting switch to close for 12.5 milliseconds, thus permiting the quasi-sample and hold circuit to hold the last value of each integrated signal for an additional 37.5 milliseconds.

The Output Buffer Amplifier isolates the output filter from the VTPR analog output, and also is used as a gain stage and signal limiter.

b. CALIBRATION SEQUENCE LOGIC

The calibration sequence timer count is established by the 2 pulse-per-second output from the filter wheel PRP. At 600 seconds, the torquer driver changes the position of the mirror from the measurement position to the space calibration position. Simultaneously, the electrical calibration staircase voltage is processed through the data channel. After 4 seconds, the staircase is replaced by the space calibration input, which lasts an additional 16 seconds.

After 20 seconds of the calibration period, the mirror shifts from the space calibration position to the patch calibration position. At the end of the 16-second patch calibration, the torquer returns to its measurement position. Simultaneously, the shorting switch at the input to the output buffer is activated, and the shroud temperature is inserted for 0.5 second. The detector and cooling patch temperatures are inserted at 36.5 and 37.0 seconds, respectively, of the calibration period.

c. STAIRCASE GENERATOR

The purpose of the staircase generator is to provide a signal which can be used for electrical calibration.

The staircase generator consists of a three-stage binary counter, an FET decoder matrix, and a constant resistance ladder network. Either -5.5 volts or ground appears on each of the inputs to the constant resistance ladder network. Since the voltage at each input is a function of the number in binary counter No. 1, the output of the constant resistance ladder network is also proportional to that number. In particular, with a voltage reference of -5.5 volts, the ladder output will change from zero to -4.8 volts in 0.69-volt steps, as counter No. 1 counts from 0 to 7.

Each level of the staircase waveform is 0.5 seconds in duration and is chopped into 8 pulses of equal amplitude. This chopping is done to simulate a constant radiance input to the detector for the 4-second electrical calibration interval.

d. DIGITAL DATA INTERFACE

The VTPR analog data is presented to the input of the sample and hold circuit which is activated by clock A. Clock A is derived from the chopper wheel PRP and occurs at a repetition rate of 16 pulses per second. Its pulse width is set at 1 millisecond. As a result of this clock input, the sample and hold output is updated to a new level. The sample and hold output rises from the old to the new level in 1 millisecond and is maintained constant at that level for 62.5 milliseconds.

Each sample and hold output level, which corresponds to the radiance seen in each filter region, is in turn quantized into 1023 levels by the 10-bit analog-to-digital converter at 9.6 kHz. This frequency is obtained from the spacecraft. The logic arrangement insures that the digitization of the analog input data does not start until the sample and hold circuit has reached its new level. An end-of-conversion pulse appears at the output of the analog-to-digital converter at the trailing edge of the 10th clock input.

When the end-of-conversion pulse appears at the load command input, the converted 10-bit word is "dumped" into the 15-bit parallel data input/serial data output shift register. The five remaining available bits in the shift register, I_1 through I_5, are generated in the identification encoder logic. These bits are also read in in parallel. The output of the identification encoder logic is a 5-bit digital word which provides 31 identification combinations.

e. THERMAL CONTROL

There are two shroud temperature sensors (thermistor beads) embedded at two points on the filter-chopper heating shroud. The outputs of each of these sensors are averaged together and converted into a voltage in the temperature-to-voltage buffer amplifier. Similarly, the two additional detector and the two additional calibration patch temperature sensor outputs are each averaged and fed into separate buffer amplifiers. In addition, each voltage output of each buffer amplifier is fed into a "single-pole, triple-throw switch." Each input to this switch is presented to the summing point of the output buffer amplifier for 1 second. As a result, the outputs of the temperature sensors are displayed on the analog signal output for a total of 3 seconds every 600 seconds, and are digitized and telemetered to ground for use in the VTPR data reduction.

The shroud and detector temperatures are each individually maintained by their own heater-controller system.

f. PHASE REFERENCE PICKUP CIRCUITS (PRP)

The phase reference pickup circuits generate the basic timing for the entire VTPR instrument.

This function is achieved by mounting a gallium arsenide infrared (IR) emitting diode so that its output is chopped by the chopping wheel (i.e., 16 times per second). In addition, another gallium arsenide IR emitting diode is positioned so that its output is chopped twice per second by the filter wheel. Each of these chopped signals is detected by a silicon photo-FET in a Schmitt trigger circuit, whose output represents the PRP output.

g. POWER SUPPLY

The power supply uses two dc-to-ac inverters. Each inverter has two outputs, each of which feeds a full-wave bridge rectifier and capacitor filter. Each of three of the four filter outputs (unregulated dc) feeds a corresponding voltage regulator. The dc output of these regulators is adjusted to +15 Vdc, -15 Vdc, and -27 Vdc, respectively. The fourth filter output is used to power the gallium arsenide IR emitting diodes used in PRP circuits.

An additional voltage regulator is used to provide the -5.5 volt reference level required for the staircase generator described previously. The input for this regulator is the -15 volts.

h. TORQUER DRIVE

The purpose of the torquer driver is to provide the appropriate signal to the torquer to change the position of the mirror during the course of the measurement sequence. During the normal measurement sequence, the two series FET switches are open. As a result, no voltage is applied to the torquer. At the appropriate time during the calibration sequence, one switch is closed, thus applying a voltage to the amplifier circuit from the voltage divider. This input voltage develops a voltage across the torquer and causes it to change its position.

Similarly, at the appropriate time, switch A is opened and switch B is closed.

The voltage divider is designed so that when switch B is closed, a voltage is developed on the torquer which saturates it. As a result, should switch A and B be closed simultaneously, the torquer will always go to its B position. Thus, a possible mirror position ambiguity is avoided.

i. SCAN DRIVE

The basic timing for the cam scanning electronics is derived from the filter wheel PRP. This PRP generates pulses that occur at a rate of 2 pulses per second. These pulses are fed into one input of AND gate No. 2. During the measurement sequence, the other inputs to AND gate No. 2 are at a "1" level; therefore, the output of AND No. 2 is a pulse train whose period corresponds to that of the Q Branch PRP (500 milliseconds). These pulses are then shaped and amplified to a suitable level for application to the clock input of the stepper motor driver.

The stepper motor driver consists, in part, of three monostable multivibrators and two transistor switches. These circuits are used to sequence the input voltage to the stepper motor in accordance with the pattern shown in Figure VI-32 to conserve power and to provide overshoot compensation on each step of the cam. In addition, other circuitry is included to provide the appropriate power sequence to each of the three motor windings such that the motor steps in a counterclockwise direction every time the clock input is at a logic "1" level. Since the cam is mechanically coupled to the stepping motor, it advances to its next position accordingly.

The cam makes one complete rotation in 24 steps. On the leading edge of the 24th Q branch PRP pulse, which corresponds to what would be the 24th step, the

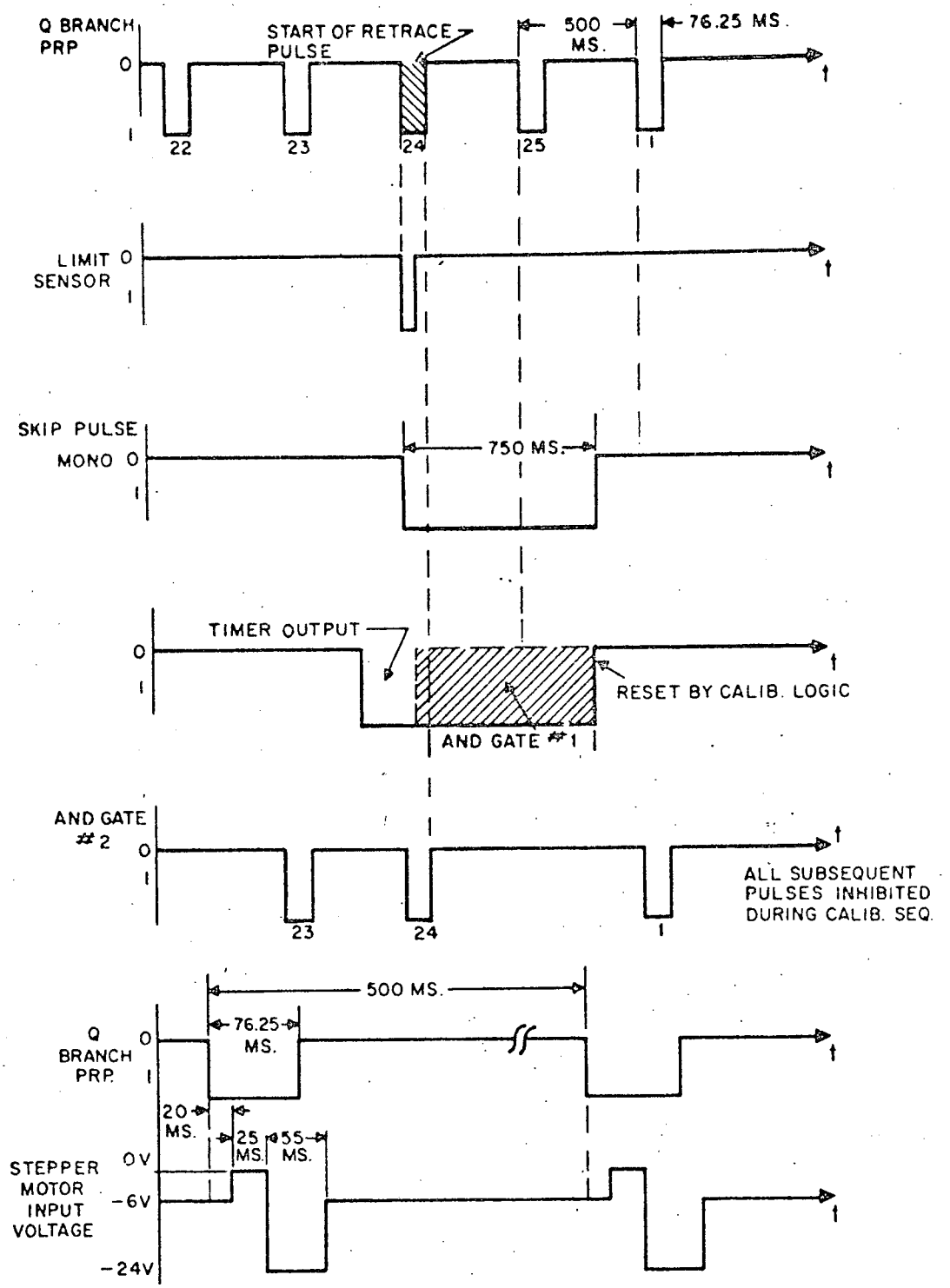

Figure VI-32. Cam Scanning Electronics, Timing Diagram

cam follower goes over the heel of the cam and, in so doing, triggers the end-of-line sensor. This action initiates the beginning of the scan retrace.

The end-of-line sensor consists of two redundant read switches connected in parallel and a transistor-resistor biasing network. The output of the end-of-line sensor triggers the "skip pulse" monostable multivibrator, which in turn causes AND gate No. 2 to inhibit the next (25th) Q branch PRP pulse from being fed into the pulse shaper. Thus, a total of one second is allowed for retrace time. During this time the stepper motor is inhibited from moving to its next position.

In addition to driving the stepper motor, the "skip pulse" monostable multivibrator also drives the retrace damper motor with its associated drive, the existing calibration sequence timer with its associated logic, and the frame counter.

E. SOLAR PROTON MONITOR

1. Introduction

The solar proton monitor (SPM) is designed to measure proton and high-energy electron flux levels at the spacecraft altitude. The SPM data is routed to the digital data processor (DDP). Time code insertion and other functions required to supplement the raw SPM data are implemented by the DDP. The operation of the DDP is covered in Section VII of this report.

In addition to the digital data processed by the DDP, real-time readout of the SPM data is provided via the beacon transmitter.

The SPM will be used, in conjunction with other satellite-borne and ground-based sensors, to provide warnings of solar proton storms.

With the exception of the data sync modification, the SPM is identical to the unit used on the TIROS M spacecraft.

2. Sensor Assembly

a. GENERAL

One surface of the sensor bracket contains four sensors (1, 2, 3 and 6) which point away from the earth at all times in the normal ITOS D and E orbit. The other surface contains two additional sensors (4 and 5) which are oriented to point along the orbit normal. Table VI-6 lists the sensors and their characteristics. Two of the sensors (5 and 6) contain two detector elements each, which are used to detect particles at several different energy levels. The other four

TABLE VI-6. SOLAR PROTON MONITOR DETECTOR CHARACTERISTICS

Detector and Word Designation (j)	Energy Range (MeV) (a)			Absorber	Field of View	Look Direction	Geometric Factor (cm^2 ster)	Accumulation Time (sec)	Duty Cycle (percent)	Word Number (h)	Logic (i)	Discrimination Levels (MeV)
	Protons	Alphas	Electrons									
1	≧60	≧ 240	>8	4.98g/cm^2Cu (dome) (c)	2π ster	Zenith	6.28	12.5	100	6	---	0.15
2	≧30	≧120	>2.15	1.42g/cm^2Cu (dome) (c)	2π ster	Zenith	6.28	12.5	100	11	---	0.15
3	≧10	≧40	>60	0.17g/cm^2Al (dome) (c)	2π ster	Zenith	0.791	12.5	100	16	---	0.30
41	2.09-2.37		≧0.140	16.7 mg/cm^2 Ni (d)	Cone 6.5 degrees half angle 0.040 ster	Perpendicular to orbit plane	2.74×10^{-3}	3.125	50 (g)	2,12	D_1D_2	D_1 = 0.10
42	>2.37		[≧0.770] low eff					3.125	50 (g)	7,17	D_2	D_2 = 0.75
51 (61)	0.27-0.56	0.48-0.78	[>200] low eff	0.222 mg/cm^2 Ni (e)	Cone 20 degrees half angle 0.38 ster	Detector 5, perpendicular to orbit plane; detector 6, zenith	0.38	1.25(1.25)f	10 (10)	3 (13)	A_1A_2B	A_1 = 0.20
52 (62)	0.56-1.05	0.78-1.28	---					1.25 (1.25)	10 (10)	4 (14)	A_2A_3B	A_2 = 0.50
53 (63)	1.05-3.2	1.28 4.1	---					1.25 (1.25)	10 (10)	5 (15)	A_3A_4B	A_3 = 1.0
54 (64)	3.2-60	>12.5	---					1.25 (1.25)	10 (10)	8 (18)	A_1B	A_4 = 4.0
55 (65)	---	12.5-32	---					1.25 (1.25)	10 (10)	9 (19)	A_4B	B = 0.30 (same for detectors 5 and 6)
56 (66)	60-86 +bkgd (b)	bkgd (b)	---					1.25 (1.25)	10 (10)	10 (20)	A_1B	

NOTES:
(a) Primary contributor over polar caps during solar proton event is underlined.
(b) Background (bkgd) is count from particles penetrating shielding (present to some extent in all channels).
(c) Shielding (except for dome) is ≧60 MeV proton equivalent of Cu.
(d) Shielding (except for aperture) is ≧50 MeV proton equivalent of Cu.
(e) Shielding (except for aperture) is ≧30 MeV proton equivalent of Cu.
(f) 6 channels of detector 5 accumulated simultaneously during words 1 and 2.
6 channels of detector 6 accumulated simultaneously during words 11 and 12.
(g) 41 and 42 each sampled twice per 12-second frame.
(h) Word order in output data is for real-time (and record) modes; on playback, it is reversed. Word 1 in real time is the Barker code.
(i) Refer to RCA logic diagram 1976102.
(j) First number indicates the detector; the second number is the energy range. Detectors 5 & 6 have different look directions.

sensors contain the equivalent of single-element detectors with fixed thrshold levels. Three of the single-element sensors are proton sensors, while the fourth is used to monitor electron fluxlevels.

High-energy trapped electrons within the Van Allen belts will contaminate the data from the proton detectors while the electron detector output is at a very high count rate due to electrons alone. In the geomagnetic polar regions, however, there are few electrons in the response range of any detector and, as a result, good proton data may be obtained. The cutoff in data from the electron detector will be used to define the edges of the trapping regions.

The sensor elements are essentially reverse-biased large-area silicon diodes, analogous to an ionization chamber in which the usual gas has been replaced with a semiconducting solid. The applied reverse-bias develops a depletion region in which charges (electron-hole pairs) are produced by ionizing charged particles. The charge carrier formation is proportional to the particle energy if the particle is completely stopped within the detector. The signal versus incident energy relationship is shown in Figure VI-33 for electrons, protons and α-particles. It can be seen from this representative figure that particle-type identification can be made by selective use of pulse-height discrimination levels. It is also apparent that channels may contain signals resulting from incidence of more than one type of particle. The expected population over the polar regions following solar-flare events is given in Table VI-6 for each readout channel.

The charge output from the sensors is collected on a capacitor in a charge-sensitive preamplifier to produce a voltage step proportional to the incident particle energy. This signal is amplified and used to feed pulse-height discriminators for detection. Combinations of electronic discriminator levels and detector shielding thicknesses are employed to define the energy response of each detector.

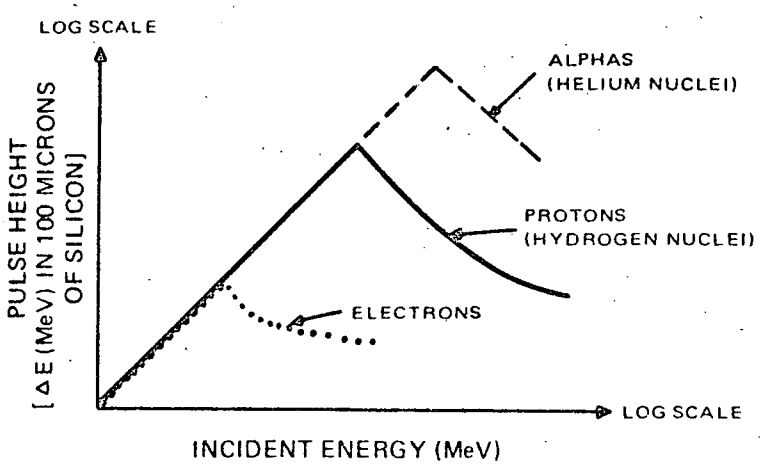

Figure VI-33. Detector Response to Protons, Electrons, and Alpha Particles

b. SENSORS

(1) PROTON SENSORS 1 AND 2 ($E_p > 60$ MeV AND $E_p > 30$ MeV)

Each of these two higher energy channels consists of three 700-micron-thick silicon surface barrier detectors mounted on orthogonal axes and surrounded by a hemispherical shield, as shown in Figure VI-34(a). The three detector outputs are wired in parallel to provide a fairly uniform cross-section over a complete hemisphere.

The only difference between these two sensors is the thickness of the shielding dome, its thickness being by far the most important factor in determining the energy threshold of the detectors. Sensor 1 detects proton particles with energy 60 MeV or greater, and sensor 2 detects protons at 30 MeV or greater.

(2) PROTON SENSOR 3 ($E_p > 10$ MeV)

This detector consists of a lithium-drifted silicon detector in the shape of a 3-millimeter cube and surrounded by a thin aluminum shield. Figure VI-34(b) shows a cross-section diagram of this unit. The dimensions of this detector are small due to the large proton flux in the energy range $E_p > 10$ MeV that is possible following solar-flare events. At lower latitudes, electron contribution will be a major portion of this detector's data.

(3) ELECTRON SENSOR ($100 < E_e < 750$ keV)

The electron sensor consists of a single detector wafer inside a shielding mount with an opening aperture that defines the sensor look-angle. A thin light-shield prevents extraneous signals should the detector look towards the sun. A cross-section of this detector is given in Figure VI-34(c). The thermistor located in the base of sensor 4 is used to determine the temperature of the assembly. The difference in temperature between detectors should be small. The operation of the electron detector is different from the operation of the other sensors in that the last amplifier output has two pulse-height discriminators, designated upper-level and lower-level, which feed an anticoincidence circuit. The function of the anticoincidence circuit is to produce a pulse output if only the lower-level discriminator is triggered but not to produce an output if both the upper- and lower-level discriminators fire. The anticoincidence circuit output and upper-level discriminator output are subcommutated into one data accumulator, which is read out four times each frame.

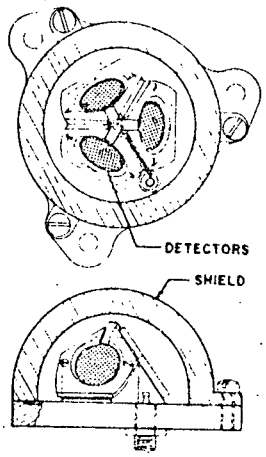

(a) Proton Sensors 1 and 2

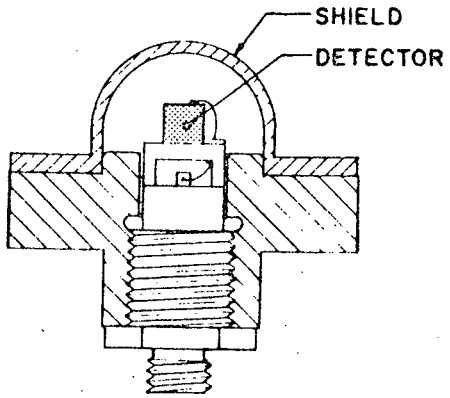

(b) Proton Sensor 3

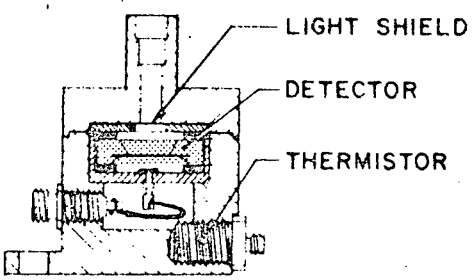

(c) Electron Sensor 4

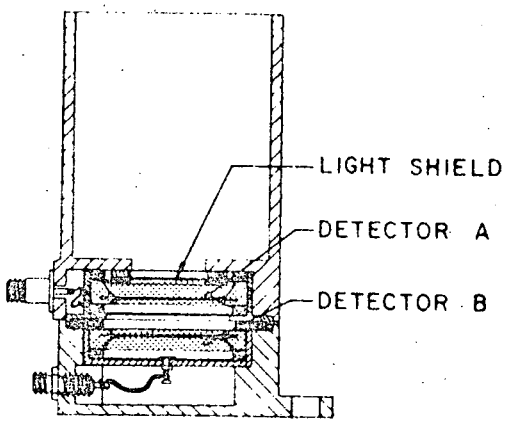

(d) Dual Channel Proton Sensors 5 and 6

Figure VI-34. SPM Sensor Units

(4) DUAL CHANNEL PROTON SENSORS (5 and 6)

Sensors 5 and 6 are identical except for orientation on the sensor bracket. This unit, shown in Figure VI-34(d), is a telescopic arrangement of two surface barrier devices; a 100-micron-thick detector (A), backed up by a 200-micron-thick detector, (B). Discriminator levels and the logic applied are given in Table VI-6, yielding the energy ranges shown. These sensors will provide data on lower energy proton fluxes beginning at 270 keV and extending up to 60 MeV, as well as α-particles from 12.5 to 32 MeV. The data from these detectors is subcommutated into two amplifier channels, one for both front-detector elements and the other for both rear-detectors. The outputs from the discriminator units for these chains are routed to the low energy channel pulse handling logic. The front and rear detector arrangement is used to determine direction and energy level of incident particles. For example, a particle detected in both the front and rear detectory by coincidence methods is defined as coming through the opening aperture with an energy level with a given range, whereas a particle detected only in the rear detector probably came in through the shielding due to the geometric properties of the sensor and the detectors and is used in determining background rates. Of course the response from the front detector follows the relationship shown in Figure VI-33.

3. Data Processing Electronics

a. GENERAL

The data processing circuits are contained in a 5.5 pound unit, 6.23 inches high, 6.2 inches wide, and 6.0 inches deep. This unit contains all circuits for processing the SPM sensor outputs; it consisting basically of the amplifier-discriminator chains for each data channel, the data encoder which compresses and formats the SPM information, and the power supply which generates the dc voltages required by the electronics and the bias voltages for the detectors.

Each SPM output is accumulated in a 20-stage counter with a capacity of 2^{19} or 1,015,808 bits. At the end of each accumulation, the 20-bit data word is converted to a 9-bit floating point binary format by breaking the number into a characteristic (N) and mantissa (M) so that the data has the form $M2^N$. In the SPM subsystem, N is limited to 4 bits, and M to 5 bits, which yields a resultant accuracy of 1 part in 2^5 (or approximately 3 percent), and a count capacity of 2^{19}. There are 20 words in a data frame, of which 19 are data words of 9-bit floating point binary codes each. The data words are preceded by a frame synchronization word. A unique (Barker) code is used which can be recognized even under highly adverse signal-to-noise conditions. Thus frame sync can be maintained even under such conditions.

The SPM data is simultaneously available in two forms. The primary data format is an NRZ code which is supplied to the DDP. As an alternative means of transmitting the SPM data to the ground, the 3900-Hz SCO of the 136.77-MHz beacon will transmit the RB code supplied by the SPM unless a higher priority function has been commanded. The required interconnection is accomplished by latching relays. When this alternative is in use, real-time SPM data is radiated by the beacon continuously, except for brief interruptions for command verification and (when commanded) housekeeping telemetry. In this manner, it is possible to use STADAN and other receiving sites to acquire SPM data.

b. AMPLIFIER-DISCRIMINATOR CHAINS

The charge output from each solid-state detector is transferred to a voltage output by the charge-sensitive preamplifier, amplified twice, and then detected in a discriminator unit. RC double differentiation is used between amplifier stages to allow for fast counting rates with minimum offset. The pulse output from the last amplifier is detected by a discriminator (which is adjustable to allow trim of the entire system) that produces a standard pulse for counting.

c. PULSE-HANDLING LOGIC

The pulse-handling logic is used to separate the signals from sensors 5 and 6 into the energy ranges given in Table VI-6 by sampling the discriminator outputs for pulse-height information and by performing coincidence measurements between them. The discriminators that feed the pulse handling logic causes 5 flip-flops to be set, according to the input pulse height. An output from the coincidence gate sets another flip-flop. These flip-flops serve as 1-bit buffer registers.

d. DATA COMMUTATOR AND ACCUMULATOR CONTROL

This unit determines the input data source and the readout sequence for the seven data accumulators. Sensors 1, 2 and 3 are read out once per frame. The two data words from sensor 4 are each read out twice per frame, while the six output lines from the pulse-handling logic are read-out twice per frame also. The data from the pulse-handling logic is from detector 5 for the first set of readings each frame, and from detector 6 for the second set.

The data commutator and accumulator control is driven by the 16-Hz signal from the spacecraft clock via a countdown chain made up of a divide-by-9 shift register and a divide-by-20 counter. The divide-by-9 shift-register is wired to generate a Barker code that is shifted into the data stream once each 20 words and used as the synchronization pattern. The output from the divide-by-9 register also triggers the processor control into operation once each output word. The divide-by-20 counter provides the address for controlling the frame of 20 words.

e. DATA ACCUMULATOR

The 20-bit scaler is free to count input pulses continuously. When the register is to be read out, the input data is first inhibited in the accumulator control, a transfer pulse is applied to the output gates, and the register is then reset to zero. All gate outputs from the seven accumulators are wired "OR" into the 20 parallel output lines.

f. FLOATING POINT COMPRESSOR

The floating point compressor is made up of the 20-bit shift register and the divide-by-16 counter. The 20-bit register is transfer loaded from one of the seven 20-bit accumulators for each readout. After transfer, the data in the register is shifted until a "1" is in the most significant digit or until 15 shifts have occurred. The number of shifts denotes the value of the characteristic. The five most significant bits in the 20-bit shift register are the mantissa of the count.

g. PROCESSOR CONTROL

The processor control generates the shift-pulse train and the input inhibit, data transfer, and accumulator reset pulses for each word. A 1 MHz clock generator is used to produce the processor control pulse rate. This control unit is triggered into operation by the word "clock" from the divide-by-9 register and triggered "off" by the data in the word being processed.

h. DATA SYNC (BOX) MODIFICATION

The data sync modification (DSB) has been added to the solar proton monitor to interface it with the digital data processor on ITOS D and E. The DSB takes nonreturn-to-zero (NRZ) input from the SPM, formats it into a 15-bit NRZ digital word, and stores it until commanded by the DDP to shift the word out. The DSB logic is shown in Figure VI-35.

The 16 Hz timing signal clocks bits into the Modulo 9 and Modulo 20 counter until the counters are full, thus triggering the end-of-frame signal (EF). The clocking of bits is continued until the Barker word is recognized. The Barker word recognition, plus the EF signal, inhibits the 16-Hz signal to the SPM clock. The DDP frame start signal resets the EF, and the SPM clock gates open again. Clock pulses are then used to transfer the data stored in the 9-bit shift register of the SPM into the 9-bit shift register in the DSB. At the same time, in parallel, the Modulo 9 counter is filled. When it is full (9 counts), the SPM clock is stopped while the data is transferred into the output register.

The output register is a 15-bit register in which 6 bits are always wired to give "0's."

When a word enable signal is directed to the SPM, the DDP shift pulse (512 bits-per-second) signal is used to clock the data out of the output register. This word enable signal also resets a gate, enabling the SPM clock once again.

i. REAL TIME OUTPUT

The return-to-bias (RB) output, which was previously available from the SPM, is used for the real-time output. This signal, which contains four characteristic and five mantissa bits, is shifted out of the SPM at a 16-Hz rate by the SPM clock. This clock is stopped after each word (9 bits) to wait for the word enable signal. The interruption is equal to the period of one clock bit.

The signal is shifted out of the SPM and transmitted over the beacon with the least significant bit first.

j. REMOTE OUTPUT

The output from the data sync modification to the DDP is the remote output. The output signal is gated by the word-enable signal and clocked by the DDP shift pulse signal at a 512-bit-per-second rate.

The data output is a nonreturn-to-zero code (NRZ) of 15 data bits in length. The least significant bit is shifted out first. Only 9 bits of the data are meaningful. The remaining 6 bits are "0" used to fill out the word.

Twenty words make up the SPM frame. The first word, in real time, is the Barker word. This means that, on playback of the stored DDP data, the last word of SPM data in a frame is the Barker word.

k. POWER AND TELEMETRY

The SPM electronics unit contains an SPM ON/OFF latching relay (operated from the CDU), which controls SPM power application in accordance with ground commands. The -24.5 volt input is converted into eight other dc voltages (varying between -6 and +300 volts) by an internal dc-to-dc converter. Fusing for the SPM is provided in the power supply electronics.

Two telemetry points are available. One is derived from the converter and its presence denotes that the relay is in the "SPM ON" state and the dc-to-dc converter is producing an output. Absence of telemetry indicates that the relay is in the "SPM OFF" state, that the fuse has blown, or that the converter is inoperative. A thermistor is attached to the sensor bracket to provide sensor bracket temperature telemetry.

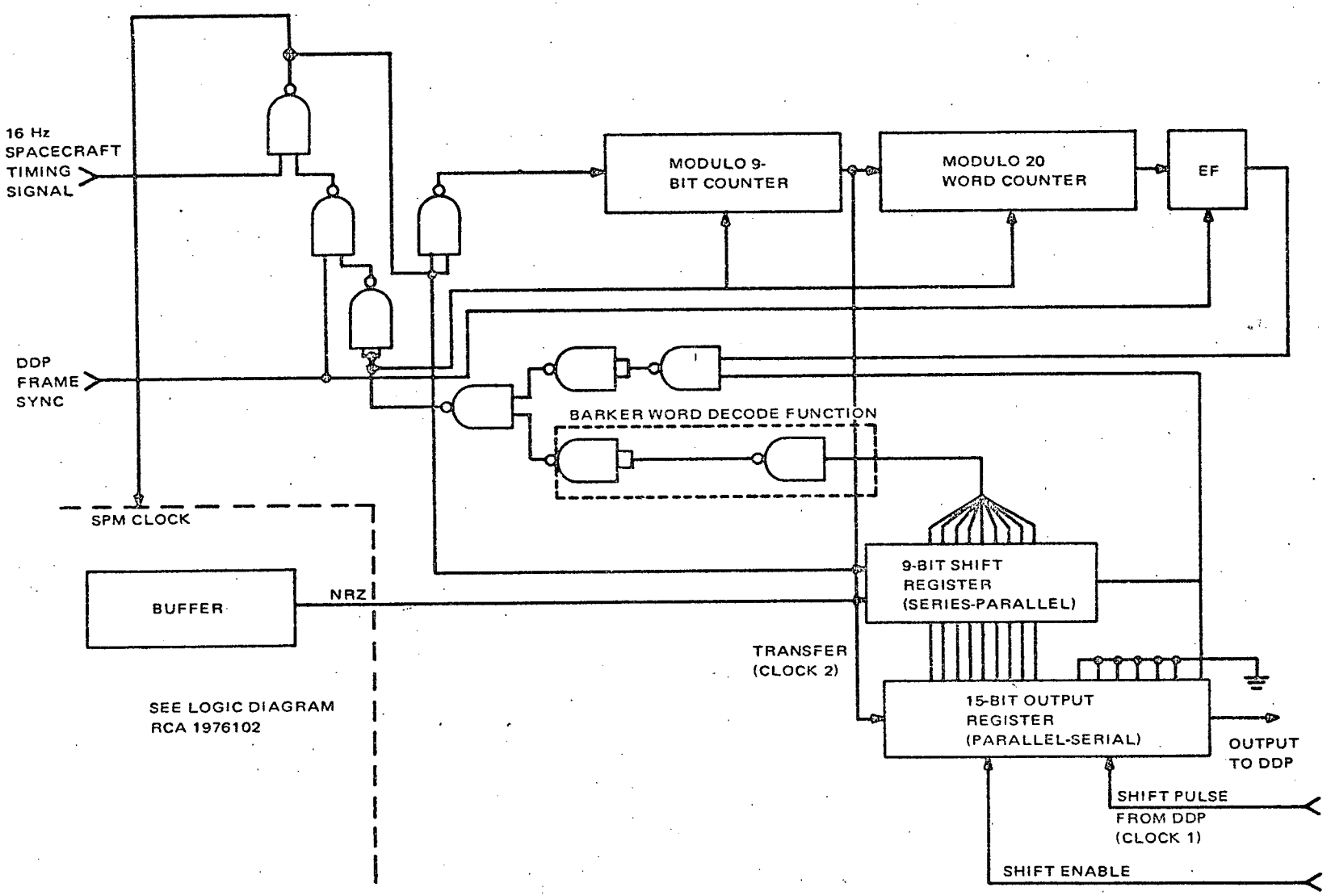

Figure VI-35. Data Sync Modification (SPM)

SQT 74529R

U.S. DEPARTMENT OF COMMERCE
National Technical Information Service
5285 Port Royal Road
Springfield, Virginia 22151

Date: June 25, 1973

Reply to Attn of: 954.01

Subject: NASA Document Discrepancy Report 73-258

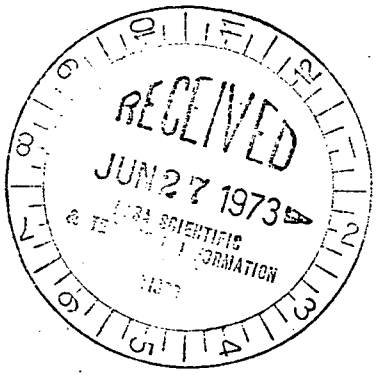

To: Mr. E. E. Baker
Deputy General Manager
Informatics TISCO
P. O. Box 33
College Park, Maryland 20740

Re: N 73-18863

[X] 1. Page(s) are missing from microfiche and paper copy. Please provide a complete copy. Pages VI-45 and VI-47.

[ ] 2. Portions of this document are illegible when reproduced. Please provide a reproducible copy.

[ ] 3. A microfiche reproduction is not legible. The case file was not received. Please provide at least an acceptable microfiche.

[ ] 4. Incorrectly priced at _____. It should be _____ for _____ pages. However, price will remain as announced in STAR.

[X] 5. Case file returned herewith. When correction has been made please return to NTIS or if corrections cannot be made note NASA records that the case file was returned.

[ ] 6. Other:

Sincerely,

Barbara Reed

Phone: 703 -321-8517

VH/BR/djr

Response

Before After
___ Issue Ch. of Status ___
Code XN/XN/Y Code
___ Comp. Ser.-No Act. ___
___ Delay Ch. OF Status
___ Post(ed) on Form 107 ___

PLEASE ATTACH COPY OF THIS LETTER WITH YOUR RESPONSE